

VRIJE
UNIVERSITEIT
BRUSSEL

A search for flavour changing neutral currents involving a top quark and a Z boson, using the data collected by the CMS experiment at a centre-of-mass energy of 13 TeV

Isis Van Parijs

**Proefschrift ingediend met het oog op het behalen van de academische graad
Doctor in de Wetenschappen.**

Published in Faculteit Wetenschappen & Bio-ingenieurswetenschappen
Vrije Universiteit Brussel
At 21 November 2017.

Responsible Contact: Isis Van Parijs
Supervisor: Prof. Jorgen D'Hondt
Interuniversity Intitute for High Energy Physics

Doctoral examination commission:

Chair:	Prof. Dr. B. Craps	Vrije Universiteit Brussel
Supervisor:	Prof. Dr. J. D'Hondt	Vrije Universiteit Brussel
Secretary:	Prof. Dr. S. Buitink	Vrije Universiteit Brussel
Other:		
DNTK:	Prof. Dr. P. Van Mulders	Vrije Universiteit Brussel
DSCH:	Prof. Dr. S. Ballet	Vrije Universiteit Brussel
External	Prof. Dr. B. Fuks	University Pierre and Marie Curie (Paris VI)
External:	Prof. Dr. A. Onofre	LIP and University do Minho

Date of Hand-in: 13 November 2017
Date of Private Defense: 21 December 2017

© 2017 Isis Van Parijs

All rights reserved. No parts of this book may be reproduced or transmitted in any form or by any means, electronic, mechanical, photocopying, recording, or otherwise, without the prior written permission of the author.

Contents

Introduction	vii
1 Theoretical basis	1
1.1 Elementary particles and forces	1
1.2 Standard Model Lagrangian, connecting fields with particles	3
1.3 Flavours in the SM	5
1.4 The top quark in the SM	7
1.5 Effective field theories	10
1.6 Motivation for new physics	14
1.7 An effective approach beyond the SM: FCNC involving a top quark	15
1.8 Experimental constraints on top-FCNC	18
2 Experimental set-up	23
2.1 The Large Hadron Collider	23
2.2 The Compact Muon Solenoid	27
2.2.1 CMS coordinate system	28
2.2.2 Towards the heart of CMS	29
2.2.3 Data acquisition	37
2.2.4 Phase 1 upgrades	37
2.2.5 CMS computing model	39
3 Analysis techniques	41
3.1 Hadron collisions at high energies	41
3.2 Event generation	44
3.2.1 Fundamentals of simulating a proton collision	44
3.2.2 Programs for event generation	44
3.2.3 Generating FCNC top-Z interactions	46
3.2.4 Generating SM background events	48
3.3 Multivariate analysis techniques: Boosted Decision Trees	50
3.4 Statistical methodology	52
4 Event reconstruction and identification	55
4.1 Object Reconstruction	55
4.1.1 Charged particle tracks	57

4.1.2	Following the Muon's Footsteps	57
4.1.3	The path of the Electron	57
4.1.4	Primary Vertex Reconstruction	58
4.1.5	Calorimeter clusters	58
4.2	Particle flow identification	59
4.3	Pileup mitigation and luminosity measurement	59
4.4	Physics object reconstruction and identification	60
4.4.1	Muons	60
4.4.2	Electrons	62
4.4.3	Jets	63
4.4.4	Jets from b fragmentation	66
4.4.5	Missing transverse energy	68
4.5	Summary of corrections	69
5	Event selection and categorisation	71
5.1	Baseline event selection and filters	71
5.1.1	Event cleaning	74
5.1.2	Estimation of the trigger efficiency	75
5.1.3	Corrections	77
5.1.4	Reconstruction of kinematic variables	81
5.2	Analysis Strategy	82
5.3	Data driven NPL background simulation	82
5.4	Statistical independent regions	84
5.4.1	WZCR	85
5.4.2	TTCR and STCR	86
5.4.3	TTSR and STSR	86
6	The search for FCNC involving a top quark and a Z boson	87
6.1	Construction of template distributions	87
6.1.1	Distributions of the BDT variables	87
6.1.2	BDTs	91
6.1.3	Transverse mass in WZCR	96
6.2	Systematic uncertainties	97
6.2.1	Effect of systematic uncertainties on the transverse mass distribution	99
6.2.2	Effect of the systematic uncertainties on the multivariate discriminator distributions	100■
6.3	Limit setting procedure validation	102■
6.4	Results and discussion	103■
6.4.1	One dimensional limits	111■
6.4.2	Two-dimensional limits	114■
7	Conclusion and prospects	117■
7.1	Conclusion	117■
7.2	Prospects	118■
Appendices		119■

A Trigger scale factors	123■
B Transfer factors	125■
C Details about the BDTs	127■
D Limit setting details	145■
D.1 BDT input variables for the tZc interaction	145■
D.2 Effect of the systematic uncertainties	146■
D.3 Postfit distributions	153■
D.3.1 Nuisance parameters	153■
D.3.2 Postfit yields	158■
Summaries	163■
Bibliography	169■
Acknowledgments	183■

Introduction

The Standard Model of particle physics is the theory of fundamental particles and their interactions. This theory has been experimentally confirmed and all its predicted particles have been found. Despite its many successes, the Standard Model has its shortcomings and can not explain phenomena such as neutrino masses, dark matter, dark energy or gravity. The heaviest particle in the Standard Model is the top quark and physicists believe that it has an enhanced sensitivity to various new particles and interactions suggested by beyond the Standard Model theories. Its lifetime is so short that it doesn't form bound states, making it possible to study the bare quark. Furthermore, the top quark has a distinct signature since it almost exclusively decays to a W boson and a bottom quark. This makes the top quark the ideal candidate to directly study quark properties. On top of this, many beyond the Standard Model physics phenomena are investigated by measuring the production rate of top quarks by studying the Wtb vertex and interactions that are heavily suppressed in the Standard Model are researched. The Large Hadron Collider is a top quark factory, producing a large number of events containing top quarks. At the proton collision points, experiments are placed to study these collisions. The work presented in the thesis uses the data collected by one of such an experiment, the Compact Muon Solenoid, and investigates flavour changing neutral currents.

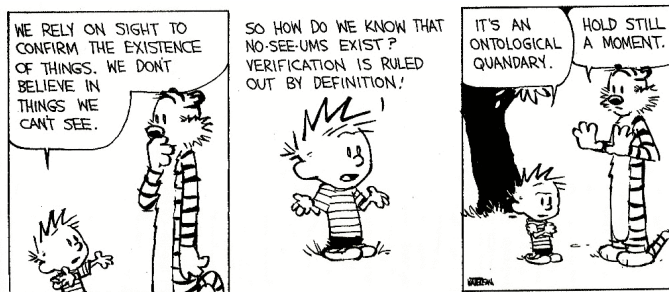
In the 1960s, the charged current process occurring when a charged kaon decaying to muon ($K^+ \rightarrow \mu^+ \nu_\mu$) was a well known process. The neutral current process $K_L^0 \rightarrow \mu^+ \mu^-$ was however not observed. This suppression of neutral currents with respect to charged currents was baffling the physicists of that time. At that time, only three different quarks were known and although the existence of a fourth quark was proposed, there was no evidence for it yet. The GIM mechanism [1], proposed in 1970, was the theory providing a satisfying explanation for the suppression of neutral current processes compared to charged current processes, via a fourth quark with specific couplings to the other quarks. This brought a revolution in physics, and the GIM mechanism combined with then already existing measurements provided indirect observation of the charm quark before it was directly observed in J/Ψ meson decay [2]. This confirmed that flavour changing neutral currents, that change the flavour of a fermion without altering its electric charge, are highly suppressed in the Standard Model.

The first evidence for flavour changing neutral currents was provided in 2005 by the CDF experiment [3], by looking at $B_s^0 \rightarrow \phi\phi$ decays. However, it was the large production rate of b hadrons at the LHC that made it possible for the LHCb and CMS collaboration to measure the FCNC decays of b hadrons [4]. Their combined data provided the first discovery of FCNC decays

with the $B_s^0 \rightarrow \mu^- \mu^+$ decay. This observation agreed with the Standard Model prediction and has put stringent limits on many beyond the Standard Model theories. Recent reinterpretations for bottom to strange quark transitions in 2005, have even found strong hints for a new physics particle [5].

The search presented in this thesis is performed on data collected by the Compact Muon Solenoid experiment at a centre-of-mass energy of 13 TeV, resulting in 35.9 fb^{-1} of integrated luminosity. The anomalous coupling of a Z boson to a top quark and an up or charm quark are being investigated for three lepton signatures. In the Standard Model, the branching fraction for a top quark decaying into a charm or up quark and a Z boson of the order of 10^{-14} [13, 14]. Several extensions of the Standard Model however enhance the FCNC branching fractions and can be probed at the LHC [13] and provide interactions resulting in flavour changing single top quark production through a tZq vertex. Up to this moment, the searches performed on top quark related flavour changing neutral currents are done at the Tevatron by the CDF [6] and D0 [7] collaborations, as well as at the LHC by the ATLAS [8, 9] and CMS [10–12] collaborations. Their limits are still far from the sensitivity of the Standard Model predictions, leaving a large phase space to reveal or exclude new physics phenomena.

The first chapter of this thesis introduces the Standard Model of particle physics as well as a brief introduction into effective field theories. The end of this chapter focusses on flavour changing neutral currents involving top-Z-quark interactions and gives an overview of the current experimental limits. The second chapter gives a description of the Large Hadron Collider at CERN, as well as the CMS experiment. Its coordinate system, hardware, and data acquisition are discussed. The analysis techniques used for the search presented in this thesis are discussed in the third chapter. Here, the simulation of proton collisions is explained, and an introduction is given to Boosted Decision Trees as well as the statistical methodology used for the search. In the fourth chapter, the reconstruction and identification of particles within CMS is explained. At the end, an overview is given of the corrections that one needs to apply for making the simulation agree with data. The event selection and categorisation used for the search are explained in the fifth chapter. Here the analysis strategy is set and the statistical independent regions are defined. In chapter six, the templates that are used for the limits are discussed and the results are presented. The final chapter concludes the search and an outlook to the future is given.



Theoretical basis

1

The Standard Model (SM) [15] is a name given in the 1970s to a theory describing the fundamental particles and their interactions. This quantum field theory describes the particles and their interactions as fields and has successfully incorporated three of the four fundamental forces in the universe. In [Section 1.1](#), the particle content of the SM is summarised, while [Section 1.2](#) describes the SM Lagrangian and its symmetries. In [Section 1.3](#), the flavour content of the SM is highlighted, and [Section 1.4](#) focusses on the top quark in the SM.

The successful theory of the SM has some shortcomings which are discussed in [Section 1.6](#) and lead to searches for a more general theory. One of such is using an effective field theory (EFT) approach [16] to search for new physics in a model independent way. In [Section 1.7](#) an EFT model focussing on flavour changing neutral currents (FCNC) involving a top quark is presented. Its current experimental constraints are given in [Section 1.8](#).

1.1 Elementary particles and forces

The interactions in nature can be described by four forces, the strong force, the electromagnetic (EM) force, the weak force and the gravitational force. These interactions happen via particles with an integer spin known as bosons. The strong interaction is mediated by eight gluons g , while the electromagnetic force is mediated by photons γ , and the weak force by Z and W^\pm bosons. In [Table 1.1](#), the forces and their characteristics are shown. The gravitational force is the only force not included in the SM and can be neglected for energies lower than the Planck scale (1.22×10^{19} GeV).

Table 1.1: The four forces of nature and their characteristics.

	Range	Mediator
Strong force	10^{-15} m	8 gluons
Electromagnetic force	∞	photon
Weak force	10^{-18} m	W^\pm , Z bosons
Gravitational force	∞	unknown

The fermions are the particles that make up the visible matter in the universe. They carry half integer spin and can be subdivided into leptons and quarks, where leptons do not interact strongly. Each fermion has a corresponding anti-fermion which has the same mass and is oppositely charged. The electron e is the first elementary particle discovered [17] and belongs to the first generation of leptons together with the electron neutrino ν_e . The second generation comprises the muon μ and muon neutrino ν_μ , whereas the third generation consists of the tau τ and tau neutrino ν_τ . The neutrinos are neutral particles, while the other leptons have charge $\pm q_e$ with q_e representing the elementary charge of 1.602×10^{-19} C. The masses of charged leptons differ by four orders of magnitude between the first and third generations. In the SM the neutrinos are assumed to be massless, nonetheless it is experimentally established that neutrinos do have a tiny non-zero mass [18, 19]. In Table 1.2, the leptons and their properties in the SM are summarised.

Table 1.2: The properties of the leptons in the three generations of the SM [20], where q_e represents the elementary charge.

	Generation	Particle	Mass	Charge
First		e^-	0.511 MeV	$-q_e$
		ν_e	≈ 0	0
Second		μ^-	106 MeV	$-q_e$
		ν_μ	≈ 0	0
Third		τ^-	1777 MeV	$-q_e$
		ν_τ	≈ 0	0

The quarks are also divided into three generations. Unlike the leptons, they carry colour charge and can interact via the strong interaction. The top quark, discovered in 1995 at the Tevatron [21, 22], is the heaviest SM particle with a mass¹ measured to be $173.34 \pm 0.27(\text{stat}) \pm 0.71(\text{syst})$ GeV [23]. The quarks and their properties are summarised in Table 1.3. In nature, only colour neutral objects can exist. This has as consequence that quarks are bound through gluons into mesons (quark+anti-quark) and baryons (three quarks). These mesons and baryons are mostly short-lived and unstable particles that rapidly decay through W^\pm and Z bosons. The only known stable baryon is the proton, made up of two up quarks and one down quark.

The scalar boson, commonly known as the Higgs boson, is the last piece of the SM discovered in 2012 [24, 25]. It is responsible for the masses of the W^\pm and Z boson, and that of the fermions.

¹In this thesis all masses and energies are expressed in natural units, where the speed of light and \hbar are taken to be equal to one.

Table 1.3: The properties of the quarks in the three generations of the SM [20], where q_e represents the elementary charge.

	Generation	Particle	Mass	Charge
First		up u	$2.2^{+0.6}_{-0.4}$ MeV	$\frac{2}{3} q_e$
		down d	$4.7^{+0.5}_{-0.4}$ MeV	$-\frac{1}{3} q_e$
Second		charm c	1.28 ± 0.03 GeV	$\frac{2}{3} q_e$
		strange s	96^{+8}_{-4} MeV	$-\frac{1}{3} q_e$
Third		top t	173.1 ± 0.6 GeV	$\frac{2}{3} q_e$
		bottom b	$4.18^{+0.04}_{-0.03}$ GeV	$-\frac{1}{3} q_e$

1.2 Standard Model Lagrangian, connecting fields with particles

The SM is a quantum field theory and thus describes the dynamics and kinematics of particles and forces by a Lagrangian \mathcal{L} . The theory is based on the $SU(3)_C \times SU(2)_L \times U(1)_Y$ gauge symmetry, where $SU(2)_L \times U(1)_Y$ describes the electroweak interaction and $SU(3)_C$ the strong interaction. The indices refer to colour C, the left chiral nature of the $SU(2)_L$ coupling L, and the weak hypercharge Y. Its Lagrangian is constructed such that symmetries representing physics conservation laws such as conservation of energy, momentum and angular momentum are contained. The symmetries under local gauge transformations are sustained by demanding gauge invariance².

The $U(1)_Y$ group has one generator Y with an associated gauge field B_μ . The three gauge fields W_μ^1 , W_μ^2 , and W_μ^3 , are associated to $SU(2)_L$ with three generators that can be written as half of the Pauli matrices:

$$T_1 = \frac{1}{2} \begin{pmatrix} 0 & 1 \\ 1 & 0 \end{pmatrix}, \quad T_2 = \frac{1}{2} \begin{pmatrix} 0 & -i \\ i & 0 \end{pmatrix}, \quad T_3 = \frac{1}{2} \begin{pmatrix} 1 & 0 \\ 0 & -1 \end{pmatrix}. \quad (1.1)$$

The generators T^a satisfy the Lie algebra:

$$[T_a, T_b] = i\epsilon_{abc} T^c \text{ and } [T_a, Y] = 0, \quad (1.2)$$

where ϵ_{abc} is an antisymmetric tensor. The gauge fields of $SU(2)_L$ only couple to left-handed fermions as required by the observed parity violating nature of the weak force. The $SU(3)_C$ group represents quantum chromodynamics (QCD). It has eight generators corresponding to eight gluon fields $G_\mu^{1\dots 8}$. Unlike $SU(2)_L \times U(1)_Y$, $SU(3)_C$ is not chiral.

Under $SU(3)_C$ quarks are colour triplets while leptons are colour singlets. This implies that the quarks carry a colour index ranging between one and three, whereas leptons do not take part

²Different field configurations of unobservable fields can result in identical quantities. Transformations between such configurations are called gauge transformation and the absence of change in the measurable quantities is a characteristic called gauge invariance.

in strong interactions. Based on the chirality, the quarks and leptons are organized in doublets or singlets. Each generation i of fermions consists of left-handed doublets and right-handed singlets:

$$l_{L,i} = \begin{pmatrix} e_{L,i} \\ \nu_{L,i} \end{pmatrix}, \quad e_{R,i}, \quad q_{L,i} = \begin{pmatrix} u_{L,i} \\ d_{L,i} \end{pmatrix}, \quad u_{R,i}, \text{ and } d_{R,i} \quad (1.3)$$

The SM Lagrangian can be decomposed as a sum of four terms

$$\mathcal{L}_{\text{SM}} = \mathcal{L}_{\text{gauge}} + \mathcal{L}_f + \mathcal{L}_{\text{Yuk}} + \mathcal{L}_\phi, \quad (1.4)$$

that are related to the gauge, fermion, Yukawa and scalar sectors. The gauge Lagrangian regroups the gauge fields of all three symmetry groups, and the fermionic part consists of kinetic energy terms for quarks and leptons. The interaction between fermions and the scalar doublet ϕ gives rise to fermion masses and is described by the Yukawa Lagrangian. The scalar part of the Lagrangian is composed of a kinematic and potential component related to the scalar boson.

For the electroweak theory, two coupling constants are introduced, namely g' for $U(1)_Y$ and g for $SU(2)_L$. The physically observable gauge bosons of this theory are the photon field A_μ , the Z boson field Z_μ^0 , and the W boson fields W_μ^\pm . These are a superposition of the four gauge fields of $SU(2)_L \times U(1)_Y$:

$$\begin{aligned} A_\mu &= \sin \theta_W W_\mu^3 + \cos \theta_W B_\mu, \\ Z_\mu^0 &= \cos \theta_W W_\mu^3 - \sin \theta_W B_\mu, \text{ and} \\ W_\mu^\pm &= \sqrt{\frac{1}{2}} (W_\mu^1 \mp i W_\mu^2), \end{aligned} \quad (1.5)$$

where θ_W represents the weak mixing angle defined as $\tan \theta_W = \frac{g'}{g}$.

The coupling constant representing the strength of the QCD interactions is denoted as g_s . In QCD there is asymptotic freedom whereby the strong coupling constant becomes weaker as the energy with which the interaction between strongly interacting particles is probed increases, and stronger as the distance between the particles increases. A consequence of this is known as colour confinement, the quarks and gluons can not exist on their own and are not observed individually. They are bound in colour neutral states called hadrons, this process is known as hadronisation.

Electroweak symmetry breaking

In $\mathcal{L}_{\text{gauge}}$ and \mathcal{L}_f are no mass terms for fermions present because only singlets under $SU(3)_C \times SU(2)_L \times U(1)_Y$ can acquire a mass with an interaction of the type $m^2 \phi^\dagger \phi$ without breaking the gauge invariance. In order to accommodate mass terms for fermions and gauge fields, electroweak symmetry breaking, leading to \mathcal{L}_ϕ is introduced.

The scalar doublet is introduced in the SM as

$$\phi = \frac{1}{\sqrt{2}} \begin{pmatrix} \varphi_1 + i \varphi_2 \\ \varphi_3 + i \varphi_4 \end{pmatrix}. \quad (1.6)$$

Its field potential is of the form

$$V(\phi) = \mu^2 \phi^\dagger \phi + \lambda (\phi^\dagger \phi)^2, \quad (1.7)$$

with $\mu^2 < 0$ and λ a positive integer. This choice of parameters gives the potential a "Mexican hat" shape. It has an infinite set of minima (ground states) and by expanding the field around an arbitrary choice of ground state, the electroweak symmetry is broken (EW):

$$\phi = \begin{pmatrix} 0 \\ \frac{v}{\sqrt{2}} \end{pmatrix} + \hat{\phi}, \quad (1.8)$$

where v is the vacuum expectation value (vev), measured to be around 245 GeV and corresponds to $\sqrt{-\frac{\mu}{\lambda}}$. The scalar doublet's four degrees of freedom are reduced to three degrees of freedom that couple to the gauge fields and fix the W^+ , W^- and Z bosons. The remaining fourth degree of freedom has given rise to a physically observable particle, called the Brout-Englert-Higgs (BEH), SM scalar or Higgs boson. This spontaneous symmetry breaking leaves the gauge invariance intact and gives masses to the W^\pm and Z bosons as:

$$m_W = \frac{1}{2} v |g| \quad \text{and} \quad m_Z = \frac{1}{2} v \sqrt{g'^2 + g^2}. \quad (1.9)$$

The Brout-Englert-Higgs field couples universally to fermions with a strength proportional to their masses, and to gauge bosons with a strength proportional to the square of their masses.

1.3 Flavours in the SM

Flavour changing charged currents are introduced in 1963 by Nicola Cabibbo [26]. Via interactions with a W boson the flavour of the quarks is changed. At the time of the postulation only up, down, and strange quarks were known and the charged weak current was described as a coupling between the up quark and d_{weak} , where d_{weak} is a linear combination of the down and strange quarks, $d_{\text{weak}} = \cos \theta_c d + \sin \theta_c s$. This linear combination is a direct consequence of the chosen rotation

$$\begin{pmatrix} d_{\text{weak}} \\ s_{\text{weak}} \end{pmatrix} = \begin{pmatrix} \cos \theta_c & \sin \theta_c \\ -\sin \theta_c & \cos \theta_c \end{pmatrix} \begin{pmatrix} d \\ s \end{pmatrix} = \mathcal{R} \begin{pmatrix} d \\ s \end{pmatrix}, \quad (1.10)$$

where the rotation angle θ_c is known as the Cabibbo angle. This provides a definition for the charged weak current between u and d quarks,

$$J_\mu = \bar{u} \gamma_\mu (1 + \gamma_5) d_{\text{weak}}. \quad (1.11)$$

A consequence of Cabibbo's approach is that the s_{weak} is left uncoupled, leading to Glashow, Iliopoulos and Maiani (GIM) [1, 14, 27] to require the existence of a fourth quark with charge $\frac{2}{3}q_e$. This quark, known as the charm quark, couples to s_{weak} and a new definition of the charged weak current is modified to

$$J_\mu = (\bar{u} \quad \bar{c}) \gamma_\mu (1 + \gamma_5) \mathcal{R} \begin{pmatrix} d \\ s \end{pmatrix} = \bar{U} \gamma_\mu (1 + \gamma_5) \mathcal{R} D. \quad (1.12)$$

The neutral weak current is defined as

$$J_3 = \bar{U} \gamma_\mu (1 + \gamma_5) [\mathcal{R}, \mathcal{R}^\dagger] D, \quad (1.13)$$

and is diagonal in flavour space. This has as consequence that no flavour changing neutral currents occur at tree-level interactions [15] in the SM.

Kobayashi and Maskawa generalised the Cabibbo rotation matrix to accommodate a third generation of quarks. The result is a 3×3 unitary matrix known as the CKM matrix \mathcal{V}_{CKM} , responsible for the mixing of weak interaction states of down-type quarks:

$$\begin{pmatrix} d_{\text{weak}} \\ s_{\text{weak}} \\ b_{\text{weak}} \end{pmatrix} = \begin{pmatrix} V_{ud} & V_{us} & V_{ub} \\ V_{cd} & V_{cs} & V_{cb} \\ V_{td} & V_{ts} & V_{tb} \end{pmatrix} \begin{pmatrix} d \\ s \\ b \end{pmatrix} = \mathcal{V}_{\text{CKM}} \begin{pmatrix} d \\ s \\ b \end{pmatrix}, \quad (1.14)$$

where \mathcal{V}_{CKM} is unitary ($\mathcal{V}_{\text{CKM}}^\dagger \mathcal{V}_{\text{CKM}} = \mathbb{1}$). A general 3×3 unitary matrix depends on three real angles and six phases. For the CKM matrix, the freedom to redefine the phases of the quark eigenstates can remove five of the phases, leaving a single physical phase known as the Kobayashi-Maskawa phase. This phase is responsible for the charge parity violation in the SM [28]. Each element V_{ij} of \mathcal{V}_{CKM} represents the transition probability of a quark i going to a quark j , and is experimentally determined to be [20]

$$\mathcal{V}_{\text{CKM}} = \begin{pmatrix} 0.97425 \pm 0.00022 & 0.2253 \pm 0.0008 & (4.13 \pm 0.49) \times 10^{-3} \\ 0.225 \pm 0.008 & 0.986 \pm 0.016 & (41.1 \pm 1.3) \times 10^{-3} \\ (8.4 \pm 0.6) \times 10^{-3} & (40.0 \pm 2.7) 10^{-3} & 1.021 \pm 0.032 \end{pmatrix}. \quad (1.15)$$

From Equation 1.15 follows that top quarks predominantly decay via charged weak currents to bottom quarks, with a probability consistent with unity. In the SM, FCNC can only occur via higher loop interactions which are highly suppressed. The expected transition probabilities for a top quark decaying via a FCNC interaction in the SM are given in Table 1.4, where it is clear that the FCNC top quark interactions of the SM are still beyond the reach of the sensitivity of current experiments.

Table 1.4: The predicted branching fractions \mathcal{B} for FCNC decays involving the top quark in the SM [13].

Process	\mathcal{B} in the SM	Process	\mathcal{B} in the SM
$t \rightarrow uZ$	8×10^{-17}	$t \rightarrow cZ$	1×10^{-14}
$t \rightarrow u\gamma$	4×10^{-16}	$t \rightarrow c\gamma$	5×10^{-14}
$t \rightarrow ug$	4×10^{-14}	$t \rightarrow cg$	5×10^{-12}
$t \rightarrow uH$	2×10^{-17}	$t \rightarrow cH$	3×10^{-15}

1.4 The top quark in the SM

Discovered in 1995 by the CDF and D0 collaborations at the Tevatron with proton-antiproton data [29, 30], the top quark plays an important role in studying high energy physics. Its Yukawa interaction is given by

$$\mathcal{L}_{\text{top-Yukawa}} = -\frac{\lambda_t \nu}{\sqrt{2}} \bar{t}_L t_R - \frac{\lambda_t}{\sqrt{2}} H \bar{t}_L t_R + \text{h.c.}, \quad (1.16)$$

yielding a Yukawa coupling of [20]

$$\lambda_t = \frac{\sqrt{2} m_t}{\nu} = 0.991 \pm 0.003. \quad (1.17)$$

This Yukawa coupling is very large compared to the other Yukawa couplings in the SM ($\mathcal{O}(10^{-2})$), leading to the belief that the top quark may have an important role in understanding the mechanism of electroweak symmetry breaking. On top of this, the very short lifetime of the top quark makes it an excellent candidate to study the properties of a bare quark. Its high mass, almost 40 times higher than the mass of the closest fermion in mass, leads to a large coupling with the Higgs boson and makes the top quark an interesting candidate to investigate how particles acquire mass.

The CKM matrix element V_{tb} , given in Equation 1.15, is experimentally found to be much larger than V_{ts} , V_{td} , and close to unity. The top quark decays through electroweak interactions since the W boson mass is smaller than the top quark mass and the W boson can be on shell. A consequence of this is that the top quark has a very short lifetime of only $1/\Gamma_t \approx 5 \cdot 10^{-25}$ s [20] leading to the fact that the formation of bound states involving top quarks are not allowed. This lifetime is even shorter than the typical hadronisation timescale of $1/\Lambda_{\text{QCD}} \approx 10^{-23}$ s, prohibiting gluons to radiate from the top quark and keeping its spin coherent. Since the electroweak interactions have a vector-axial vector (V-A) coupling structure³, the top quark spin orientation can be derived from the angular distributions of its decay products. This makes it possible to study the polarisation of top quarks from the angular distributions in various processes.

The massiveness of the top quark leads to the fact that a large amount of energy is needed to create one. This is only the case for high energy collisions such as those happening in the Earth's upper atmosphere when cosmic rays collide with particles in air, or by particle accelerators. The production of top quarks happens in two ways: single via the electroweak interaction or in pairs via the strong interaction. At hadron colliders, the dominant production mechanism is top quark production via gluon ($gg \rightarrow t\bar{t}$) or quark fusion ($q\bar{q} \rightarrow t\bar{t}$). In Figure 1.1, the different top quark pair production mechanisms are shown. The production channel of gluon fusion is the main contributor to the top quark pair cross section at the LHC compared to quark fusion at the Tevatron. The $gg \rightarrow t\bar{t}$ process contributes 80-90% to the total top quark pair cross section in the LHC centre-of-mass energy regime of 7-14 TeV [20]. In Table 1.5 the predicted top quark pair production cross sections are given for the LHC and the Tevatron, while in Figure 1.2, a

³In the SM a vector - axial vector coupling structure $(\gamma^\mu - \gamma^\mu \gamma^5)$ is predicted that only permits left-handed fermions or right-handed anti fermions to interact with a spin-1 particle.

summary plot of the LHC and Tevatron top quark pair cross section measurements as a function of the centre-of-mass energy can be found. These measurements are found to be in agreement with their SM predictions.

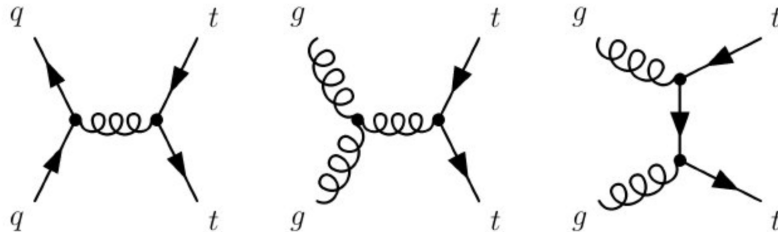


Figure 1.1: Leading order diagrams of the top quark pair production. Gluon fusion (right and middle) are the dominant processes at the LHC, while quark fusion (left) is the dominant one at the Tevatron.

Table 1.5: Predictions on the top quark pair production cross sections at next-to-next-to-leading order with next-to-next-to-leading log soft gluon resummation per centre-of-mass energy [20]. The first uncertainty is from scale dependence, while the second uncertainty originates from parton density functions.

Experiment	Top quark mass	Centre-of-mass energy	Cross section (pb)
Tevatron	$m_t = 173.3 \text{ GeV}$	$\sqrt{s} = 1.96 \text{ TeV}$	$\sigma_{\bar{t}t} = 7.16^{+0.11+0.17}_{-0.20-0.12}$
LHC	$m_t = 173.2 \text{ GeV}$	$\sqrt{s} = 7 \text{ TeV}$	$\sigma_{\bar{t}t} = 173.6^{+4.5+8.9}_{-5.9-8.9}$
LHC	$m_t = 173.2 \text{ GeV}$	$\sqrt{s} = 8 \text{ TeV}$	$\sigma_{\bar{t}t} = 247.7^{+6.3+11.5}_{-8.5-11.5}$
LHC	$m_t = 173.2 \text{ GeV}$	$\sqrt{s} = 13 \text{ TeV}$	$\sigma_{\bar{t}t} = 816.0^{+19.4+34.4}_{-28.6-34.4}$

The singly produced top quarks are produced via the electroweak interaction. These production mechanisms are subdivided at leading order into three main channels based on the virtuality ($Q^2 = -p_\mu p^\mu$) of the exchanged W boson. In Figure 1.3, the corresponding Feynman diagrams are shown. The single top quark production cross sections, given in Table 1.6, are smaller than the top quark pair production cross sections since the electroweak coupling strength is smaller than the strong coupling strength. In addition, for the single top quark production, there is the need of sea quarks (b, \bar{q}) in the initial states for which the parton density functions increase less steeply at low momentum fractions compared to the gluon parton density functions.

The production via the t -channel has a virtuality of the W boson $Q^2 > 0$, making it space-like. It is produced via the scattering of the W boson of a bottom quark coming from a proton or from gluon splitting ($g \rightarrow b\bar{b}$). It has the highest single top quark cross section in proton collisions and the top quark production is roughly twice as large than the antitop quark. This is a consequence of the up-down valence quark composition of the proton. This feature makes the t -channel sensitive to the parton density functions of the proton. The s -channel is the production mechanism with the smallest cross section. Here the W boson is time-like ($Q^2 < 0$) which requires the W boson to have a large virtuality to produce the heavier top quark. It is produced

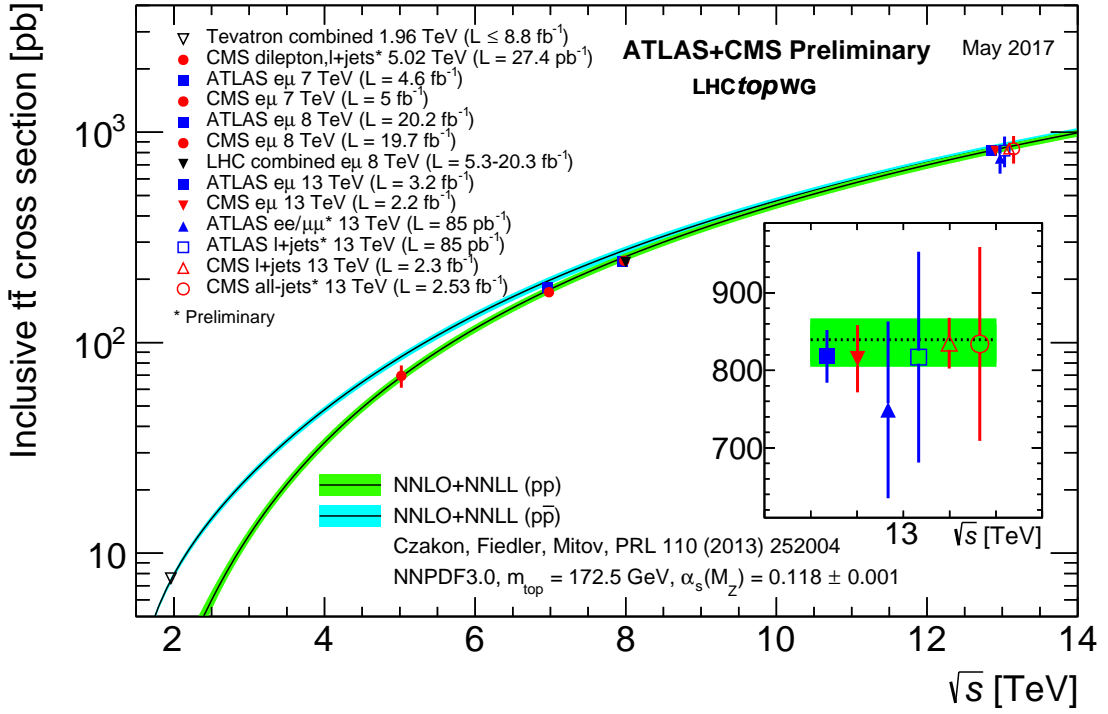


Figure 1.2: Summary of the LHC and the Tevatron measurements of the top quark pair production cross section as function of the centre-of-mass energy compared with the next-to-next-to-leading order QCD calculation. The theory bands are the uncertainties due to renormalization and factorisation scales, parton density functions and the strong coupling. The mass of the top quark is assumed to be 172.5 GeV. Measurements for the same centre-of-mass energy are slightly off-set for clarity. Figure taken from [31].

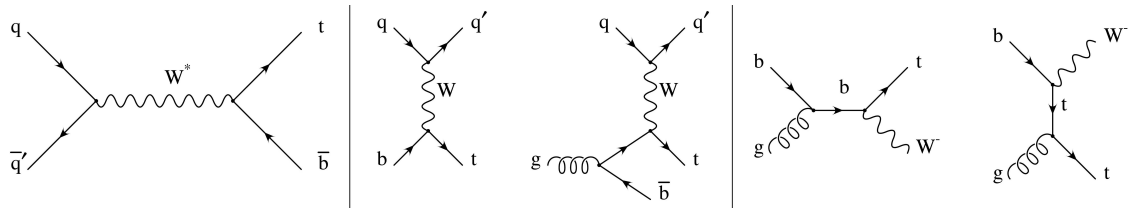


Figure 1.3: Leading order Feynman diagrams of the electroweak production of single top quarks in the s -channel (left), t -channel (middle), and for the tW associated production. Figure taken from [32].

from two quarks belonging to the same isodoublet (e.g. $u\bar{d}$) and subsequently decays to $t\bar{b}$. This process gets enhanced by many beyond the Standard Model scenarios via the addition of new heavy particles such as W' . The tW -channel has a top quark produced in association with a W boson produced on shell $Q^2 = -m_W^2$. This mode is negligible at the Tevatron, but of relevant size at the LHC. The tW -channel is sensitive to new physics affecting the Wtb vertex. The single top quark production cross section measurements by the CMS collaboration can be found in Figure 1.4 and are not showing any significant deviations from their SM predictions.

Table 1.6: Predictions on the single top quark production cross sections at next-to-leading order per centre-of-mass energy [20]. The uncertainties from scale dependence and from parton density functions are combined in quadrature or given separately (scale + PDF). For the t -channel the relative proportions to t and \bar{t} are 65% and 35%. For the s -channel this is respectively 69% and 31%. The tW -channel has an equal proportion of top and antitop quarks. For Tevatron, the top quark mass is assumed to be 173.3 GeV, while the LHC predictions use $m_t = 172.5$ GeV [20, 33].

Collider	Centre-of-mass energy	Cross section $\sigma_{t+\bar{t}}$ (pb)		
		t -channel	s -channel	tW -channel
Tevatron	$\sqrt{s} = 1.96$ TeV	$2.06^{+0.13}_{-0.13}$	$1.03^{+0.05}_{-0.05}$	—
LHC	$\sqrt{s} = 7$ TeV	$63.89^{+2.91}_{-2.52}$	$4.29^{+0.19}_{-0.17}$	$15.74^{+0.40+1.10}_{-0.40-1.14}$
LHC	$\sqrt{s} = 8$ TeV	$84.69^{+3.76}_{-3.23}$	$5.24^{+0.22}_{-0.20}$	$22.37^{+0.60+1.40}_{-0.60-1.40}$
LHC	$\sqrt{s} = 13$ TeV	$216.99^{+9.04}_{-7.71}$	$10.32^{+0.40}_{-0.36}$	$71.7^{+1.80+3.40}_{-1.80-3.40}$

1.5 Effective field theories

Problems can be simplified if one looks at the relevant scale of the process that one want to investigate, for example the chemical properties of an hydrogen atom can be described without any knowledge of quark interactions inside the proton. In this case, the proton can be considered the elementary object (indivisible) due to the fact that the binding energy of the constituents is much bigger than the energy of the electron in orbit around the proton. Effective field theories are based on this kind of separation of different energy scales in a system [35]. Effective field theories can be used for theories where the perturbative expansion cannot be trusted, e.g. QCD at low energy, or as bottom up approach to look for new physics in a model independent way. The latter is the way effective field theory will be used throughout this thesis.

The main idea behind effective field theory is easily explained via the example of the Fermi theory. Fermi explained in 1933 [36] the β -decay as a product of currents:

$$\mathcal{L}_{\text{EFT}}^{\text{Fermi}} = -\frac{G_F}{\sqrt{2}} J^\mu J_\mu^\dagger, \quad (1.18)$$

where G_F is the Fermi coupling constant, measured to be $G_F \approx 1.17 \times 10^{-5}$ GeV $^{-2}$. The current J_μ can written as the sum of an hadronic J_μ^h and leptonic J_μ^l current, where for simplicity only the leptonic current discussed.

$$J_\mu^l = \sum_i \bar{\nu}_i \gamma_\mu (1 - \gamma_5) l. \quad (1.19)$$

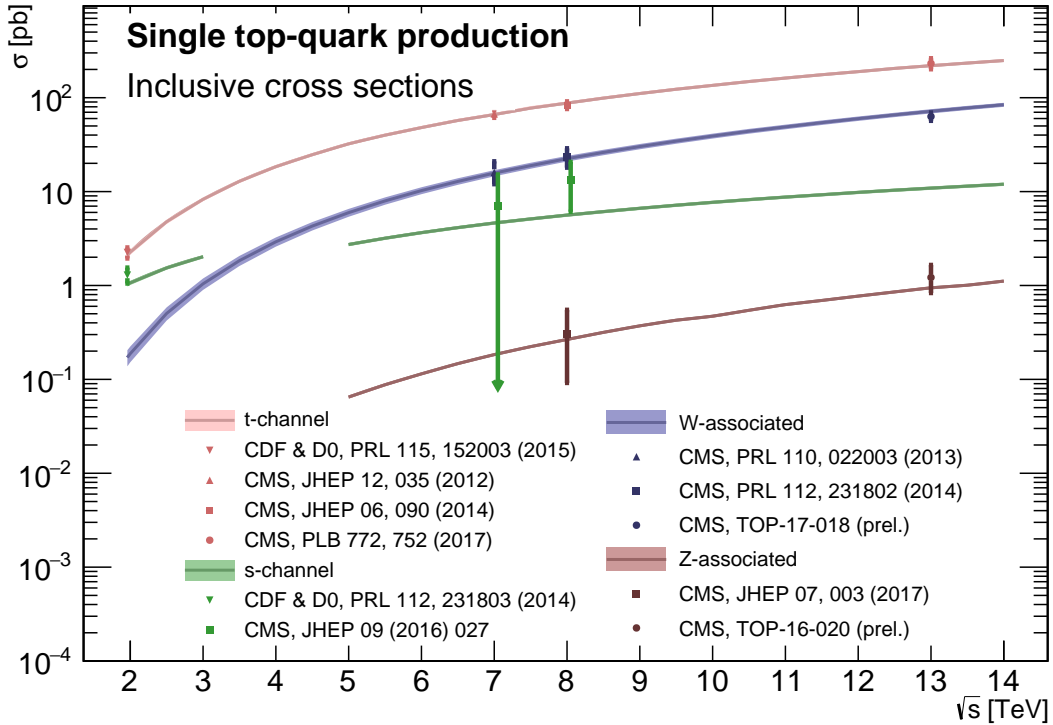


Figure 1.4: Summary of the measurements of the single top quark production cross section as function of the centre-of-mass energy. Figure taken from [34].

Historically, charged currents were flavour universal and the later discovered parity violation of the weak interaction led to the V-A structure. After this, the $SU(2)_L$ symmetry was postulated and the existence of neutral currents was predicted. The effective Lagrangian used then (given in Equation 1.18), could nowadays be build starting from $SU(2)_L$ symmetries only.

The muon decay can be computed from two different starting points. The effective Fermi Lagrangian provides the decay width of the muon into an electron and two neutrinos

$$\Gamma(\mu \rightarrow e \bar{\nu}_e \nu_\mu) \approx \frac{1}{96\pi^3} \frac{m_\mu^2}{\Lambda_F^4}, \quad (1.20)$$

where Λ_F is the energy scale defined as

$$\frac{G_F}{\sqrt{2}} = \frac{1}{\Lambda_F^2}. \quad (1.21)$$

From muon decay measurements, the value of Λ_F is determined to be $\Lambda_F \approx 348$ GeV [35]. From the SM Lagrangian, one could also calculate the muon decay. Considering that the momenta involved are small compared to the W boson mass, the propagator's denominator

can be expanded as [15]

$$\frac{1}{p^2 - m_W^2} = -\frac{1}{m_W^2} - \frac{p^2}{m_W^4} + \dots \quad (1.22)$$

Looking at the first term, and identifying

$$\frac{g^2}{8m_W} = \frac{1}{\Lambda_F^2}, \quad (1.23)$$

one sees that this corresponds with [Equation 1.20](#), thus the effective Lagrangian in [Equation 1.18](#) is the first term of the expansion in $\frac{1}{m_W^2}$ applied on the full Lagrangian.

An effective theory is thus a Taylor expansion in the ratio of two scales and the only remnants of the full theory at low energies are the symmetries and the values of the coupling constants. If the expansion parameter is small, one can truncate the series leading to the Lagrangian containing a finite number of free coefficients, making predictions possible. The error on these predictions is then of the order as the truncated piece.

The SM can be seen as an effective theory applicable up to energies not exceeding a scale Λ . Therefore, remnants should still be valid and the theory above that scale should have a gauge group containing $SU(3)_C \times SU(2)_L \times U(1)_Y$ and all the SM degrees of freedom, as well as reduce to the SM at lower energies. The general SM Lagrangian becomes then

$$\mathcal{L}_{SM+EFT} = \mathcal{L}_{SM}^{(4)} + \frac{1}{\Lambda} \sum_k C_k^{(5)} Q_k^{(5)} + \frac{1}{\Lambda^2} \sum_k C_k^{(6)} Q_k^{(6)} + \mathcal{O}\left(\frac{1}{\Lambda^3}\right), \quad (1.24)$$

where $Q_k^{(n)}$ are dimension- n operators (currents) and $C_k^{(n)}$ the corresponding dimensionless coupling constants, so-called Wilson coefficients. The Wilson coefficients are determined by the underlying high energy theory.

In the Warsaw basis [37], a set of independent operators of dimension 5 and 6 are built out of the SM fields and are consistent with the SM gauge symmetries and is fully derived in Ref. [37]. In general the various measurements show a good agreement with the SM predictions and by lack of deviations from the SM, limits on the anomalous couplings can be derived. The estimated coupling strengths per operator contributing to single top quark production obtained from various measurements at the LHC and Tevatron are shown in [Figure 1.5](#) for which the conventions are discussed in Ref. [38]. These results are consistent with the SM expectation for which those operators vanish.

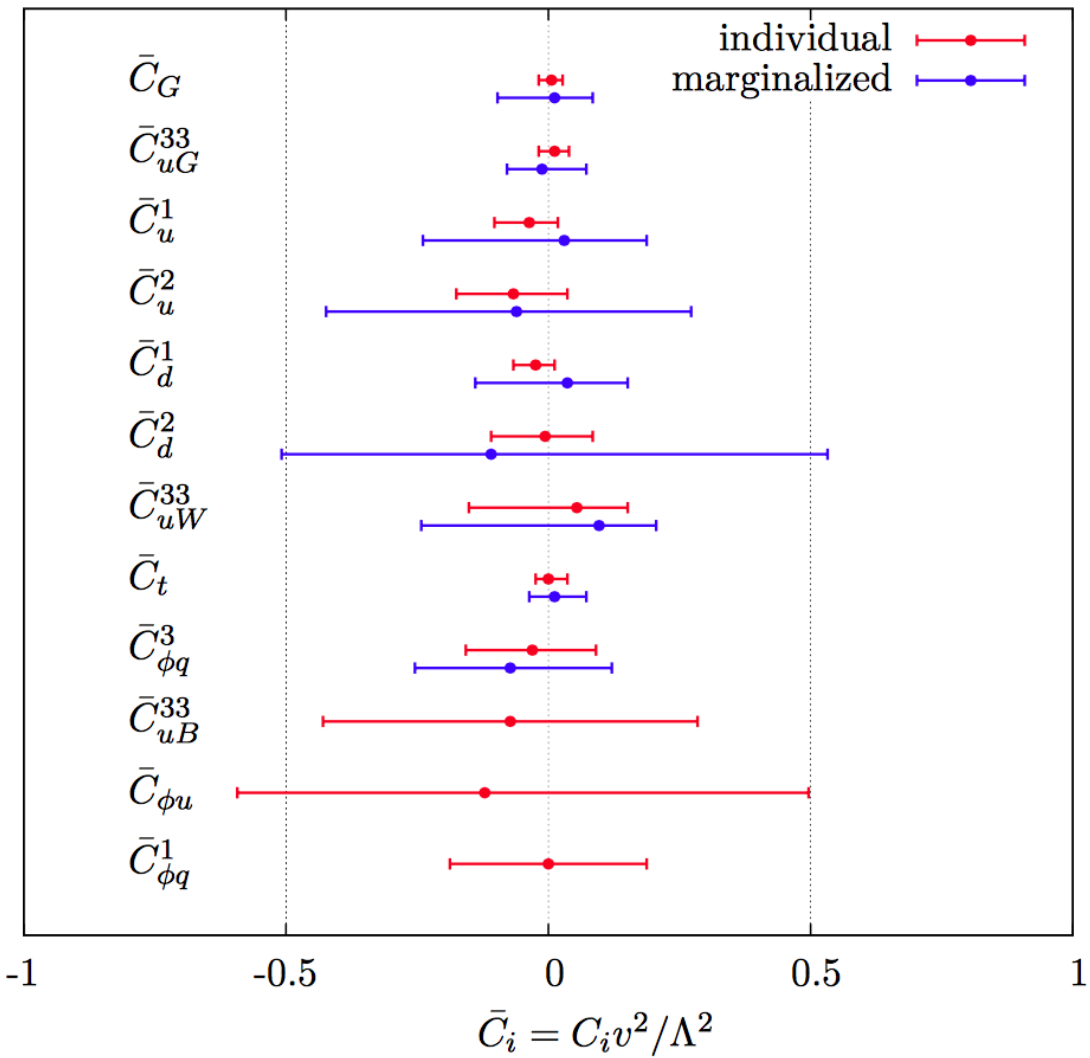


Figure 1.5: Global fit results of top quark effective field theory to experimental data including all constrained operators at dimension six. For the operators, the Warsaw basis of [37] is used. The bounds are set on the Wilson coefficients of various operators contributing to top quark production and decay in two cases (red) all other coefficients set to zero, or (blue) all other coefficients marginalized over. Figure taken from [39].

1.6 Motivation for new physics

Many high energy experiments confirm the success of the SM. In particular the scalar boson, the cornerstone of the SM, has consecrated the theory. Unfortunately there are also strong indications that the SM ought to be a lower energy expression of a more global theory. The existence of physics beyond the SM (BSM) [40] is strongly motivated. These motivations are based on direct evidence from observation such as the existence of neutrino masses, the existence of dark matter and dark energy, or the matter-antimatter asymmetry, and also from theoretical problems such as the hierarchy problem, the coupling unification or the large numbers of free parameters in the SM.

In the SM, the neutrinos are assumed to be massless, while experiments with solar, atmospheric, reactor and accelerator neutrinos have established that neutrinos can oscillate and change flavour during flight [18, 19]. These oscillations are only possible when neutrinos have masses. The flavour neutrinos (ν_e , ν_μ , ν_τ) are then linear expressions of the fields of at least three mass eigenstate neutrinos ν_1 , ν_2 , and ν_3 .

The ordinary or baryonic matter described by the SM describes only 5% of the mass (energy) content of the universe. Astrophysical evidence indicated that dark matter is contributing to approximately 27% and dark energy to 68% of the content of the universe. From the measurements of the temperature and polarizations anisotropies of the cosmic microwave background by the Planck experiment [41], the density of cold non baryonic matter is determined. Cold dark matter is assumed to be only sensitive to the weak and gravitational force, leading to only one possible SM candidate: the neutrino. However, these are too light to account for the vast amount of dark matter and other models are needed. Dark energy is assumed to be responsible for the acceleration in the expansion of the universe [42].

At the Big Bang, matter and antimatter are assumed to be produced in equal quantities. However, it is clear that we are solely surrounded by matter. In 1967, Sakharov identified three mechanisms that are necessary to obtain a global matter antimatter asymmetry [43]. These mechanisms are those of baryon and lepton number violation, that at a given moment in time there was a thermal imbalance for the interactions in the universe, and there is charge C and charge parity CP violation⁴.

The large number of free parameters in the SM comes from the nine fermion masses, three CKM mixing angles and one CP violating phase, one EM coupling constant g' , one weak coupling constant g , one strong coupling constant g_s , one QCD vacuum angle, one vacuum expectation value, and one mass of the scalar boson. This large number of free parameters leads to the expectation of a more elegant and profound theory beyond the SM.

The hierarchy problem [44] is related to the huge difference in energy between the weak scale and the Planck scale. The vev of the Brout-Englert-Higgs field determines the weak scale that is approximately 246 GeV. The radiative corrections to the scalar boson squared mass m_H^2 , coming from its self couplings and couplings to fermions and gauge bosons, are quadratically

⁴The rate of a process $i \rightarrow f$ can be different from the CP-conjugate process: $\tilde{i} \rightarrow \tilde{f}$. The SM includes sources of CP-violation through the residual phase of the CKM matrix. However, these could not account for the magnitude of the asymmetry observed.

proportional to the ultraviolet momentum cut-off Λ_{UV} . This cut-off is at least equal to the energy to which the SM is valid without the need of new physics. For the SM to be valid up to the Planck mass, the correction to m_H^2 becomes thirty orders of magnitude larger than m_H^2 . This implies that an extraordinary cancellation of terms should happen. This is also known as the naturalness problem of the H boson mass.

The correction to the squared mass of the scalar boson coming from a fermion f , coupling to the scalar field ϕ with a coupling λ_f is given by

$$\Delta m_H^2 = -\frac{|\lambda_f|^2}{8\pi^2} \Lambda_{\text{UV}}^2, \quad (1.25)$$

while the correction to the mass from a scalar particle S with a mass m_S , coupling to the scalar field with a Lagrangian term $-\lambda_S |\phi|^2 |S|^2$ is

$$\Delta m_H^2 = \frac{|\lambda_S|^2}{16\pi^2} \left(\Lambda_{\text{UV}}^2 - 2m_S^2 \ln \left(\frac{\Lambda_{\text{UV}}}{m_S} \right) + \dots \right). \quad (1.26)$$

As one can see the correction term to m_H^2 is much larger than m_H^2 itself. By introducing BSM physics models that introduce new scalar particles at the TeV scale that couple to the scalar boson one can cancel the Λ_{UV}^2 divergence and avoid this fine-tuning.

The choice of the $SU(3)_C \times SU(2)_L \times U(1)_Y$ symmetry group itself as well as the separate treatment of the three forces included in the SM raises concern. The intensity of the forces show a large disparity around the electroweak scale, but have comparable strengths at higher energies. The electromagnetic and weak forces are unified in a electroweak interaction, but the strong coupling constant does not encounter the other coupling constants at high energies. In order to reach a grand unification, the running of couplings can be modified by the addition of new particles in BSM models.

1.7 An effective approach beyond the SM: FCNC involving a top quark

The closeness of the top quark mass to the electroweak scale led physicists to believe that it is a sensitive probe for new physics. Studying its properties is therefore an important topic of the experimental program at the LHC. Several extensions of the SM enhance the FCNC branching fractions and can be probed at the LHC [13], from which some of them are shown in [Table 1.7](#). Previous searches have been performed at the Tevatron by the CDF [6] and D0 [7] collaborations, and at the LHC by the ATLAS [8, 9, 45–47] and CMS [10–12, 48, 49] collaborations.

The impact of BSM models can be written in a model independent way by means of an effective field theory valid up to an energy scale Λ . The leading effects are parametrized by a set of fully gauge symmetric operators that are added to the SM Lagrangian and can be reduced to a minimal set of operators as seen in [Equation 1.24](#). For simplicity, the assumption is made

Table 1.7: The predicted branching fractions \mathcal{B} for FCNC interactions involving the top quark in some BSM models [13]: quark singlet (QS), generic two Higgs doublet model (2HDM) and the minimal supersymmetric extensions to the SM (MSSM).

Process	QS	2HDM	MSSM
$t \rightarrow uZ$	$\leq 1.1 \times 10^{-4}$	—	$\leq 2 \times 10^{-6}$
$t \rightarrow u\gamma$	$\leq 7.5 \times 10^{-9}$	—	$\leq 2 \times 10^{-6}$
$t \rightarrow ug$	$\leq 1.5 \times 10^{-7}$	—	$\leq 8 \times 10^{-5}$
$t \rightarrow uH$	$\leq 4.1 \times 10^{-5}$	$\leq 5.5 \times 10^{-6}$	$\leq 10^{-5}$
$t \rightarrow cZ$	$\leq 1.1 \times 10^{-4}$	$\leq 10^{-7}$	$\leq 2 \times 10^{-6}$
$t \rightarrow c\gamma$	$\leq 7.5 \times 10^{-9}$	$\leq 10^{-6}$	$\leq 2 \times 10^{-6}$
$t \rightarrow cg$	$\leq 1.5 \times 10^{-7}$	$\leq 10^{-4}$	$\leq 8 \times 10^{-5}$
$t \rightarrow cH$	$\leq 4.1 \times 10^{-5}$	$\leq 10^{-3}$	$\leq 10^{-5}$

that new physics effects are exclusively described by dimension-6 operators, thus neglecting neutrino physics. In the fully gauge symmetric case, the EFT Lagrangian is then given by

$$\mathcal{L}_{\text{SM+EFT}} = \mathcal{L}_{\text{SM}} + \sum_i \frac{\bar{c}_i}{\Lambda^2} O_i + \mathcal{O}\left(\frac{1}{\Lambda^3}\right), \quad (1.27)$$

where the Wilson coefficients \bar{c}_i depend on the considered theory and on the way that new physics couples to the SM particles. Taking into account that Λ is large, contributions suppressed by powers of Λ greater than two are neglected. Additionally, all four fermion operators are omitted for the rest of this thesis. The Warsaw basis is adopted for the independent effective operators [37], parametrising the new physics effects relevant for the flavour changing neutral current interactions of the top quark as,

$$\begin{aligned} \mathcal{L}_{\text{EFT}}^t = & \frac{\bar{c}_{uG}}{\Lambda^2} \Phi^\dagger \cdot [\bar{Q}_L \sigma^{\mu\nu} \mathcal{T}_a u_R] G_{\mu\nu}^a + \frac{\bar{c}_{uB}}{\Lambda^2} \Phi^\dagger \cdot [\bar{Q}_L \sigma^{\mu\nu} u_R] B_{\mu\nu} + \frac{2\bar{c}_{uW}}{\Lambda^2} \Phi^\dagger T_i \cdot [\bar{Q}_L \sigma^{\mu\nu} u_R] W_{\mu\nu}^i \\ & + i \frac{\bar{c}_{hu}}{\Lambda^2} \left[\Phi^\dagger \overleftrightarrow{D}_\mu \Phi \right] [\bar{u}_R \gamma^\mu u_R] + i \frac{\bar{c}_{hq}^{(1)}}{\Lambda^2} \left[\Phi^\dagger \overleftrightarrow{D}_\mu \Phi \right] [\bar{Q}_L \gamma^\mu Q_L] \\ & + i \frac{4\bar{c}_{HQ}^{(3)}}{\Lambda^2} \left[\Phi^\dagger T_i \overleftrightarrow{D}_\mu \Phi \right] [\bar{Q}_L \gamma^\mu T^i Q_L] + \frac{\bar{c}_{uh}}{\Lambda^2} \Phi^\dagger \Phi \Phi^\dagger \cdot [\bar{Q}_L u_R] + \text{h.c.}, \end{aligned} \quad (1.28)$$

with all flavour indices implied. The left handed $SU(2)_L$ doublet of the quark fields is denoted by Q_L , the up-type right handed fields by u_R , the down-type right handed fields by d_R , the $SU(2)_L$ doublet of the Higgs field by Φ , the field strength tensors as

$$\begin{aligned} B_{\mu\nu} &= \partial_\mu B_\nu - \partial_\nu B_\mu, \\ W_{\mu\nu}^k &= \partial_\mu W_\nu^k - \partial_\nu W_\mu^k - g \epsilon_{ij}^k W_\mu^i W_\nu^j, \\ G_{\mu\nu} &= \partial_\mu G_\nu^a - \partial_\nu G_\mu^a + g_s f_{bc}^a G_\mu^b G_\nu^c, \end{aligned} \quad (1.29)$$

denoting the structure constant of the $SU(3)_C$ group as f_{bc}^a and the structure constant of the $SU(2)_L$ group as ϵ_{ij}^k . The gauge covariant derivatives are also standard defined as

$$D_\mu \Phi = \partial_\mu \Phi - \frac{1}{2} i g' B_\mu \Phi - i g T_k W_\mu^k \Phi \quad (1.30)$$

with the conventions of [Section 1.2](#). The representation matrices T of $SU(2)_L$ are defined in [Equation 1.1](#), while the representation matrices \mathcal{T} of $SU(3)_C$ are the Gell-Mann matrices [15]. The hermitian derivative operator is defined as

$$\Phi^\dagger \overleftrightarrow{D} \Phi = \Phi^\dagger D^\mu \Phi - D_\mu \Phi^\dagger \Phi. \quad (1.31)$$

After electroweak symmetry breaking, the operators induce [13, 50] both corrections to the SM couplings and new interactions at tree level such as FCNC interactions. The FCNC interactions of the top quark that are not present in the SM are given by

$$\mathcal{L}_{\text{EFT}}^t = \frac{\sqrt{2}}{2} \sum_{q=u,c} \left[g' \frac{\kappa_{tyq}}{\Lambda} A_{\mu\nu} \bar{t} \sigma^{\mu\nu} (f_{\gamma q}^L P_L + f_{\gamma q}^R P_R) q \right. \quad (1.32)$$

$$+ \frac{g}{2 \cos \theta_W} \frac{\kappa_{tzq}}{\Lambda} Z_{\mu\nu} \bar{t} \sigma^{\mu\nu} (f_{Zq}^L P_L + f_{Zq}^R P_R) q \quad (1.33)$$

$$+ \frac{\sqrt{2}g}{4 \cos \theta_W} \zeta_{tzq} \bar{t} \gamma^\mu (\tilde{f}_q^L P_L + \tilde{f}_q^R P_R) q Z_\mu \quad (1.34)$$

$$+ g_s \frac{\kappa_{tgq}}{\Lambda} Z_{\mu\nu} \bar{t} \sigma^{\mu\nu} (f_{gq}^L P_L + f_{gq}^R P_R) q G_{\mu\nu}^a \quad (1.35)$$

$$+ \eta_{Hqt} \bar{t} (\hat{f}_q^L P_L + \hat{f}_q^R P_R) q H + \text{h.c.} \Big], \quad (1.36)$$

where the value of the FCNC couplings at scale Λ are represented by κ_{tzq} , κ_{tgq} , κ_{tyq} , ζ_{tzq} , and η_{Hqt} . These are assumed to be real and positive, with the unit of GeV^{-1} for κ_{txq}/Λ and no unit for ζ_{xqt} and η_{xqt} . In the equation, $\sigma^{\mu\nu}$ equals to $\frac{i}{2} [\gamma^\mu, \gamma^\nu]$, and the left- and right-handed chirality projector operators are denoted by P_L and P_R . The electromagnetic coupling constant is denoted by g' , the strong interaction coupling is denoted as g_s , while the electroweak interaction is parametrised by the coupling constant g and the electroweak mixing angle θ_W . The complex chiral parameters are normalized according to $|f_{xq}^L|^2 + |f_{xq}^R|^2 = 1$, $|\tilde{f}_q^L|^2 + |\tilde{f}_q^R|^2 = 1$, and $|\hat{f}_q^L|^2 + |\hat{f}_q^R|^2 = 1$. In the expression for $\mathcal{L}_{\text{EFT}}^t$, the unitary gauge is adopted and the scalar field is expanded around its vacuum expectation value v with H being the SM scalar boson. The field strength tensors of the photon A_μ , the gluon field $G_\mu^{1\dots 8}$, and the Z boson Z_μ^0 are defined as

$$\begin{aligned} A_{\mu\nu} &= \partial_\mu A_\nu - \partial_\nu A_\mu, \\ Z_{\mu\nu} &= \partial_\mu Z_\nu - \partial_\nu Z_\mu, \text{ and} \\ G_{\mu\nu} &= \partial_\mu G_\nu^a - \partial_\nu G_\mu^a + g_s f_{bc}^a G_\mu^b G_\nu^c. \end{aligned} \quad (1.37)$$

The massive Z boson will appear in both the Z_μ^0 field as well as the covariant derivative, leading to an extra Z-vertex in $\mathcal{L}_{\text{EFT}}^t$. Furthermore, due to the electroweak symmetry breaking, there are two coupling constants arising in the Lagrangian.

The relations between the Wilson coefficients in (1.28) and the coupling strengths of the interactions in Equation 1.36 can be derived. The 14 effective operators are mapped onto 10 free parameters providing a more minimal parametrisation of the anomalous interactions of the top quark:

$$\begin{aligned}
 \kappa_{tgq} f_{gq}^L &= \frac{\nu}{g_s \Lambda} [\bar{c}_{uG}]_{i3}^*, & \kappa_{tgq} f_{gq}^R &= \frac{\nu}{g_s \Lambda} [\bar{c}_{uG}]_{3i}, \\
 \kappa_{t\gamma q} f_{\gamma q}^L &= \frac{\nu}{g' \Lambda} [\cos \theta_W \bar{c}_{uB} - \sin \theta_W \bar{c}_{uW}]_{i3}^*, & \kappa_{t\gamma q} f_{\gamma q}^R &= \frac{\nu}{g' \Lambda} [\sin \theta_W \bar{c}_{uB} - \cos \theta_W \bar{c}_{uW}]_{3i}, \\
 \kappa_{tZq} f_{Zq}^L &= -\frac{2\cos \theta_W \nu}{g \Lambda} [\sin \theta_W \bar{c}_{uB} + \cos \theta_W \bar{c}_{uW}]_{i3}^*, & \kappa_{tZq} f_{Zq}^R &= -\frac{2\cos \theta_W \nu}{g \Lambda} [\cos \theta_W \bar{c}_{uB} + \sin \theta_W \bar{c}_{uW}]_{3i}, \\
 \zeta_{tZq} \tilde{f}_{Zq}^L &= -\frac{2\nu^2}{\Lambda^2} [(\bar{c}_{hq}^{(1)} - \bar{c}_{hq}^{(3)})_{i3} + (\bar{c}_{hq}^{(1)} - \bar{c}_{hq}^{(3)*})_{3i}], & \zeta_{tZq} \tilde{f}_{Zq}^R &= -\frac{2\nu^2}{\Lambda^2} [(\bar{c}_{hu})_{i3} + (\bar{c}_{hu})_{3i}^*], \\
 \eta_{tHq} \hat{f}_{Hq}^L &= \frac{3\nu^2}{2\Lambda^2} [\bar{c}_{uh}]_{i3}^*, & \eta_{tHq} \hat{f}_{Hq}^R &= \frac{3\nu^2}{2\Lambda^2} [\bar{c}_{uh}]_{3i}.
 \end{aligned} \tag{1.38}$$

1.8 Experimental constraints on top-FCNC

Experimental particle physicists commonly put limits on the branching fractions which allow an easier interpretation across different EFT models by use of the branching fraction

$$\mathcal{B}(t \rightarrow qX) = \frac{\delta_{tXq}^2 \Gamma_{t \rightarrow qX}}{\Gamma_t}, \tag{1.39}$$

where $\Gamma_{t \rightarrow qX}$ represents the FCNC decay width⁵ for a coupling strength $\delta_{tXq}^2 = 1$, and Γ_t the full decay width of the top quark. In the SM, supposing a top quark mass of 172.5 GeV, the full width becomes $\Gamma_t^{\text{SM}} = 1.32 \text{ GeV}$ [51].

Searches for top-FCNC usually adopt a search strategy depending on the experimental set-up and the FCNC interaction of interest, looking either for FCNC interactions in the production of a single top quark or in its decay for top quark pair interactions. In Figure 1.6, these two cases are shown for the tZq vertex.

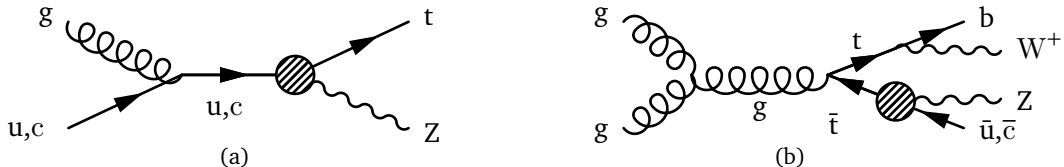


Figure 1.6: Feynman diagrams for the processes with a tZq FCNC interaction, where the FCNC interaction is indicated with the shaded dot. (a) Single top quark production through an FCNC interaction. (b) Top quark pair production with an FCNC induced decay.

The observation of top-FCNC interactions has yet to come and experiments have so far only been able to put upper bounds on the branching fractions. An overview of the best current limits

⁵The decay width of a certain process represents the probability per unit time that a particle will decay. The total decay width, defined as the sum of all possible decay widths of a particle, is inversely proportional to its lifetime.

is given in [Table 1.8](#). In [Figure 1.7](#) a comparison is shown between the current best limits set by ATLAS and CMS with respect to several BSM model benchmark predictions. From there one can see that FCNC searches involving a Z or H boson are close to excluding or confirming several BSM theories. In [Figure 1.8](#), the searches performed by CMS are summarised. For the tZq vertex, the current most stringent limit is set by the ATLAS collaboration at a centre-of-mass of 13 TeV [[47](#)]. The observed (expected) limits at 95% CL are $\mathcal{B}(t \rightarrow uZ) < 1.7 \times 10^{-4}$ (2.4×10^{-4}) and $\mathcal{B}(t \rightarrow cZ) < 2.3 \times 10^{-4}$ (3.2×10^{-4}). The most stringent limit from the CMS collaboration comes from Ref. [[10](#)] where both single top quark and top quark pair are studied. The observed (expected) limits at 95% CL for a centre-of-mass of 8 TeV for the FCNC tZq interaction by CMS are $\mathcal{B}(t \rightarrow uZ) < 2.2 \times 10^{-4}$ (2.7×10^{-4}) and $\mathcal{B}(t \rightarrow cZ) < 4.9 \times 10^{-4}$ (12×10^{-4}). In [Figure 1.9](#), the summary of the 95% confidence level observed limits on the branching fractions of the top quark decays to a charm or up quark and a neutral boson is given, considering the results from the HERA, the LEP, the Tevatron, and the LHC.

Table 1.8: Overview of the most stringent observed and expected experimental limits on top-FCNC branching fractions \mathcal{B} at 95% confidence level.

Process	Search mode	Observed \mathcal{B}	Expected \mathcal{B}	Experiment	
$t \rightarrow uZ$	top quark pair decay	1.7×10^{-4}	2.4×10^{-4}	ATLAS	[47]
$t \rightarrow u\gamma$	single top quark production	1.3×10^{-4}	1.9×10^{-4}	CMS	[12]
$t \rightarrow ug$	single top quark production	4.0×10^{-5}	3.5×10^{-5}	ATLAS	[9]
$t \rightarrow uH$	top quark pair decay	2.4×10^{-3}	1.7×10^{-3}	ATLAS	[46]
$t \rightarrow cZ$	top quark pair decay	2.3×10^{-4}	3.2×10^{-4}	ATLAS	[47]
$t \rightarrow c\gamma$	single top quark production	2.0×10^{-3}	1.7×10^{-3}	CMS	[12]
$t \rightarrow cg$	single top quark production	2.0×10^{-4}	1.8×10^{-4}	ATLAS	[9]
$t \rightarrow cH$	top quark pair decay	2.2×10^{-3}	1.6×10^{-3}	CMS	[46]

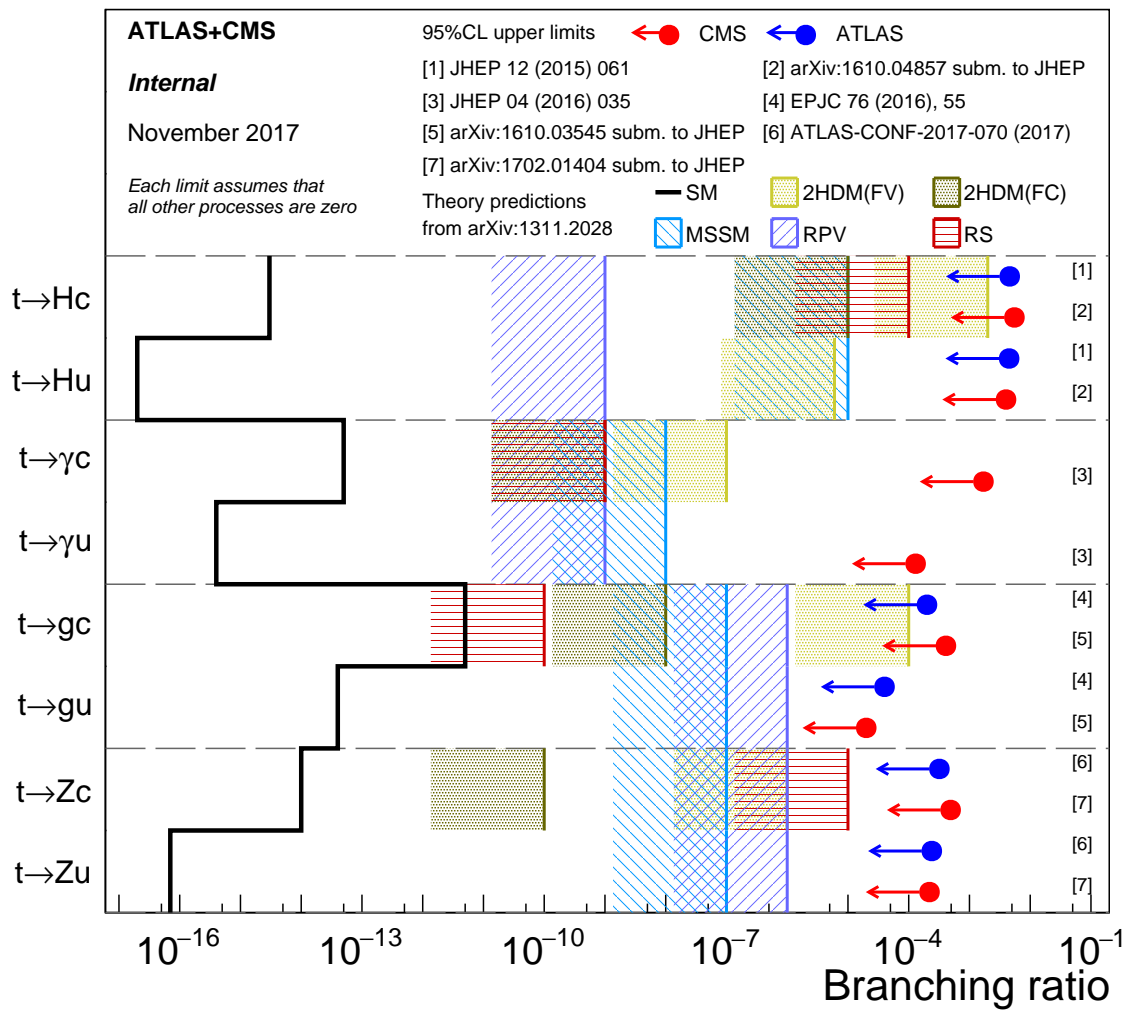


Figure 1.7: Current best limits set by CMS and ATLAS for top-FCNC interactions. Figure adapted from [34].

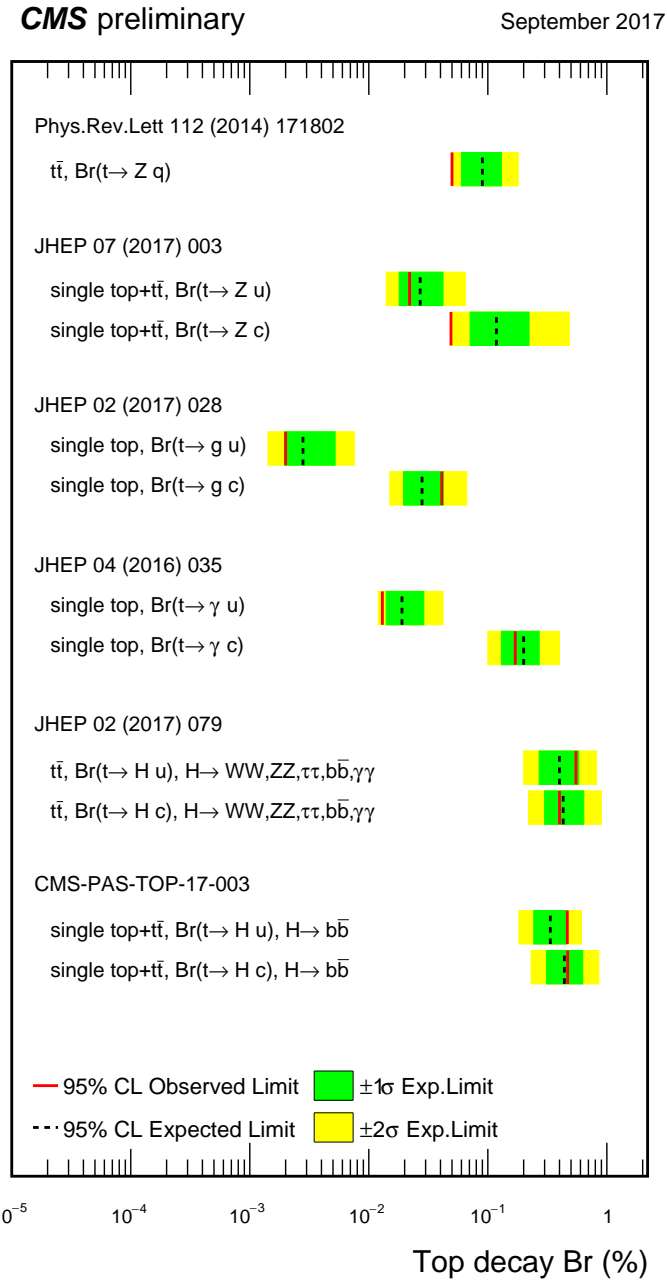


Figure 1.8: Summary of the FCNC branching fractions from CMS searches at 8 TeV. Figure taken from [34].

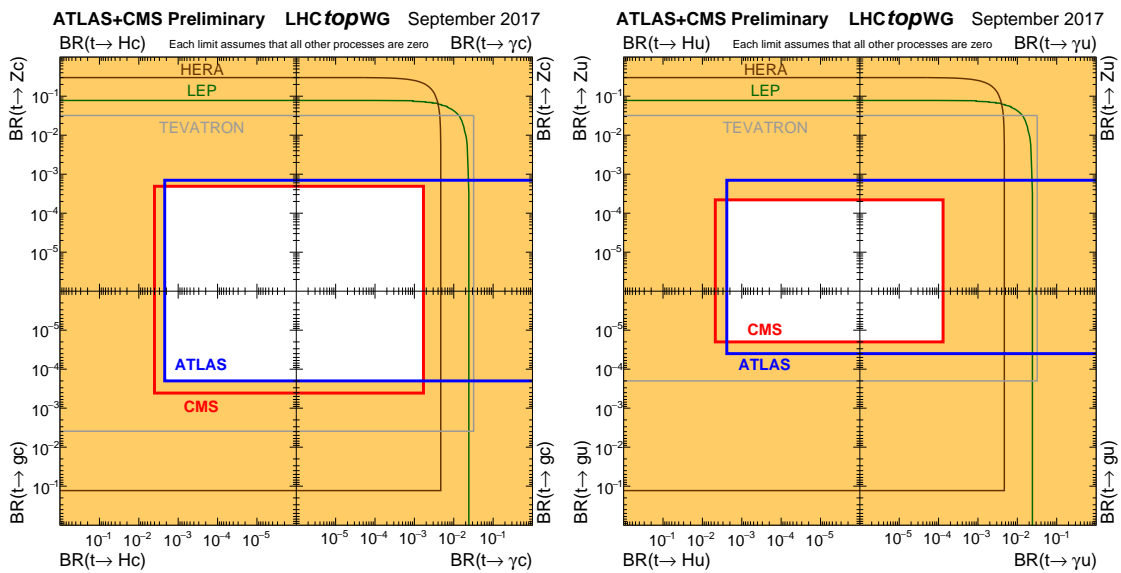


Figure 1.9: Summary of the current 95% confidence level observed limits on the branching fractions of the top quark decays via flavour changing neutral currents to a charm (left) or up (right) quark and a neutral boson. The coloured lines represent the results from HERA (the most stringent limits between the ones obtained by the H1 and ZEUS collaborations, in brown), LEP (combined ALEPH, DELPHI, L3 and OPAL collaborations result, in green), TEVATRON (the most stringent limits between the ones obtained by the CDF and D0 collaborations, in grey). The yellow area represents the region excluded by the ATLAS and the CMS Collaborations. Figure taken from [31].

Experimental set-up 2

A key objective of the Large Hadron Collider (LHC) was the search for the Brout-Englert-Higgs boson. The Large Electron Positron (LEP) [52] and Tevatron [53] experiments established that the mass of the scalar boson has to be larger than 114 GeV [54, 55], and smaller than approximate 1 TeV due to unitarity and perturbativity constraints [56]. On top of this, the search for new physics such as supersymmetry or the understanding of dark matter were part of the motivation for building the LHC. Since the start of its operation, the LHC is pushing the boundaries of the Standard Model, putting the most stringent limits on physics beyond the Standard Model as well as precision measurements of the parameters of the Standard Model. A milestone of the LHC is the discovery of the scalar boson in 2012 by the two largest experiments at the LHC [24, 25].

This chapter is dedicated to the experimental set-up of the LHC and the Compact Muon Solenoid (CMS) experiment. Section 2.1 describes the LHC and its acceleration process for protons to reach their design energies. The CMS experiment and its components are presented in Section 2.2. The upgrades performed during the long shutdown in 2013 are discussed in Section 2.2.4. The data acquisition of CMS is presented in Section 2.2.3, while the CMS computing model is shown in Section 2.2.5.

2.1 The Large Hadron Collider

The LHC has started its era of cutting edge science on 10 September 2008 [57] after approval by the European Organisation of Nuclear Research (CERN) in 1995 [58]. Installed in the previous LEP tunnel, the LHC consists of a 26.7 km quasi ring, that is installed between 45 and 170 m under the French-Swiss border amidst Cessy (France) and Meyrin (Switzerland). Built to study rare physics phenomena at high energies, the LHC can accelerate mainly two types of particles, protons and lead ions Pb^{45+} , and provides collisions at four interaction points, where the particle bunches are crossing. Experiments for studying the collisions are installed at each interaction point.

As can be seen in Figure 2.1, the LHC is the last element in a chain that creates, injects and accelerates protons. The starting point is the ionisation of hydrogen, creating protons that are injected in a linear accelerator (LINAC 2). Here, the protons obtain an energy of 50 MeV. They

continue to the Proton Synchrotron Booster (PSB or Booster), where the packs of protons are accelerated to 1.4 GeV and each pack is split up in twelve bunches with 25 or 50 ns spacing. The Proton Synchrotron (PS) then increases their energy to 25 GeV before the Super Proton Synchrotron (SPS) increases the proton energy up to 450 GeV. Each accelerator ring expands in radius in order to reduce the energy loss of the protons by synchrotron radiation¹. Furthermore, the magnets responsible for the bending of the proton trajectories have to be strong enough to sustain the higher proton energy. Ultimately, the proton bunches are injected into opposite directions into the LHC, where they are accelerated to 3.5 TeV (in 2010 and 2011), 4 TeV (in 2012 and 2013) or 6.5 TeV (in 2015-2017) [59].

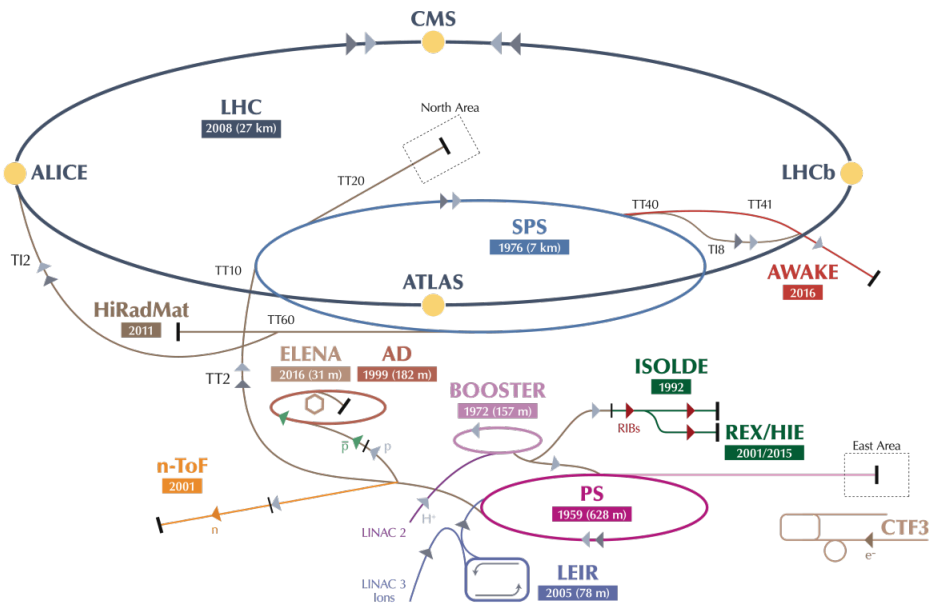


Figure 2.1: Schematic representation of the accelerator complex at CERN [60]. The LHC (dark blue) is the last element in chain of accelerators. Protons are successively accelerated by LINAC 2, the Booster, the Proton Synchrotron (PS) and the Super Proton Synchrotron (SPS) before entering the LHC.

In Figure 2.2 the LHC programme is shown. the first data collisions, so-called Run 1 period, lasted from 2008 until 16 February 2013 after which the CERN accelerator complex shut down for two years of planned maintenance and consolidation during so-called long shutdown 1 (LS1). On 23 March 2015, the new data taking period known as Run 2 started. With a brief end of the year extended technical stop (EYETS) at the end of 2016. The main activities carried out during the EYETS were the maintenance of systems such as the cryogenics, the cooling, electrical systems, etc.; the replacement of the magnet, as well as a de-cabling and cabling campaign on the SPS[61]. Run 2 will last until July 2018 when the long shutdown 2 (LS2) will begin for 2 years. The main goal of this shutdown is the LHC injectors upgrade (LUI), but also maintenance and consolidation will be performed. Furthermore, preparations for the High

¹This energy loss is proportional to the fourth power of the proton energy and inversely proportional to the bending radius.

Luminosity LHC (HL-LHC), which will start in 2024, will be done. More information about phase 1 upgrades during LS1 and the EYETS in 2016 is given in [Section 2.2.4](#).

Before the start of the LHC in 2010, the previous energy record was held by the Tevatron collider at Fermilab, colliding protons with antiprotons at $\sqrt{s} = 1.96$ TeV. When completely filled, the LHC nominally contains 2220 bunches in Run 2, compared to 1380 in Run 1.

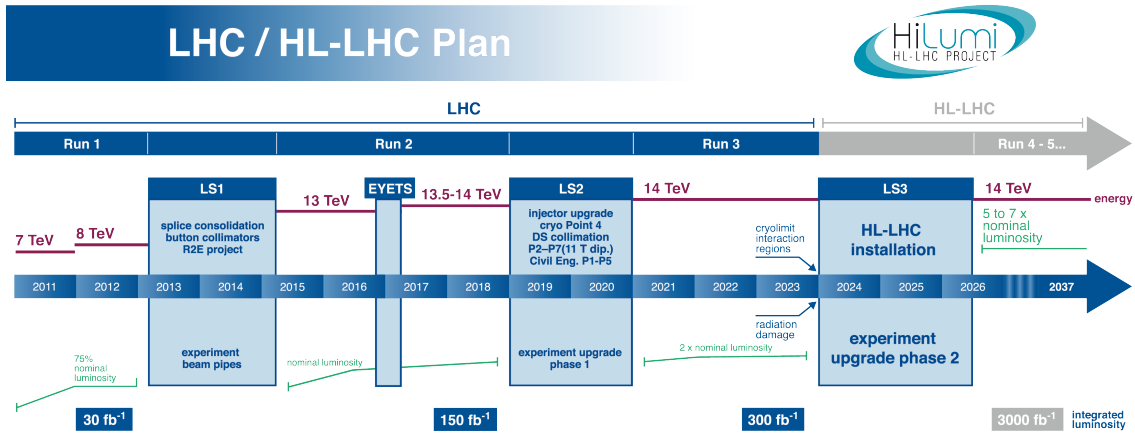


Figure 2.2: The HL-LHC timeline. Figure taken from [62].

Inside the LHC ring [63], the protons are accelerated by the means of radio frequency cavities, while 1232 dipole magnets of approximately 15 m long, each weighing 35 t ensure the deflection of the beams. The two proton beams circulate in opposite direction in separate pipes inside of the magnet. Through the use of a strong electric current in the coils of the magnet, magnetic fields are generated and cause the protons to bend in the required orbits. In order for the coil to become superconducting and able to produce a strong magnetic field of 8.3 T, the magnet structure is surrounded by a vessel. This vessel is filled with liquid Helium making it possible to cool down the magnet to 1.9 K. In order to get more focussed and stabilised proton beams, additional higher-order multipole and corrector magnets are placed along the LHC beam line.

The LHC is home to seven experiments, each located at an interaction point:

- A Toroidal LHC ApparatuS (ATLAS) [64] and the Compact Muon Solenoid (CMS) [65] experiments are the two general purpose detectors at the LHC. They both have a hermetic, cylindrical structure and were designed to search for new physics phenomena along with precision measurements of the Standard Model. The existence of two distinct experiments allows cross-confirmation of any discovery.
- A Large Ion Collider Experiment (ALICE) [66] and the LHC Beauty (LHCb) [67] experiments are focusing on specific phenomena. ALICE studies strongly interacting matter at extreme energy densities where a quark-gluon plasma forms in heavy ion collisions (Pb-Pb or p-Pb). LHCb searches for differences between matter and antimatter with the focus on b quark physics.

- The forward LHC (LHCf) [68] and the TOTal cross section, Elastic scattering and diffraction dissociation Measurement (TOTEM) [69] experiments are two smaller experiments that focus on head-on collisions. LHCf consists of two parts placed before and after ATLAS and studies particles created at very small angles. TOTEM is placed in the same cavern as CMS and measures the total proton-proton cross section and studies elastic and diffractive scattering.
- The Monopoles and Exotics Detector At the LHC (MoEDAL) [70] experiment is situated near LHCb and tries to find magnetic monopoles.

For the enhancement of the exploration of rare events and thus enhancing the number of collisions, high beam energies as well as high beam intensities are required. The luminosity [71] is a measurement of the number of collisions that can be produced in a detector per square meter and per second and is the key role player in this enhancement. The LHC collisions create a number of events per second given by

$$N_{\text{event}} = L\sigma_{\text{event}}, \quad (2.1)$$

where σ_{event} is the cross section of the process of interest and L the machine instantaneous luminosity. This luminosity depends only on the beam parameters and is for a Gaussian beam expressed as

$$L = \frac{1}{4\pi} N_b n_b f_{\text{rev}} \frac{N_b}{\epsilon_n} \left(1 + \left(\frac{\theta_c \sigma_z}{2\sigma^*} \right)^2 \right)^{-\frac{1}{2}} \frac{\gamma_r}{\beta^*}. \quad (2.2)$$

The number of particles per bunch is expressed by N_b , while n_b is the number of bunches per beam, f_{rev} the revolution frequency, γ_r the relativistic gamma factor, ϵ_n the normalized transverse beam emittance - a quality for the confinement of the beam, β^* the beta function at the collision point - a measurement for the width of the beam, θ_c the angle between two beams at the interaction point, σ_z the mean length of one bunch, and σ^* the mean height of one bunch. In Equation 2.2, the blue part represents the stream of particles, the red part the brilliance, and the green part the geometric reduction factor due to the crossing angle at the interaction point.

The peak design luminosity for the LHC is $10^{34} \text{ cm}^{-2}\text{s}^{-1}$, which leads to about 1 billion proton interactions per second. In 2016, the LHC was around 10% above this design luminosity [72]. The luminosity is not a constant in time since it diminishes due to collisions between the beams, and the interaction of the protons and the particle gas that is trapped in the centre of the vacuum tubes due to the magnetic field. The diffusion of the beam degrades the emittance and therefore also the luminosity. For this reason, the mean lifetime of a beam inside the LHC is around 15 h. The integrated luminosity - the luminosity provided in a certain time range - recorded by CMS and ATLAS over the year 2016 is given in Figure 2.3. In Run 2, the peak luminosity is $13\text{-}17 \times 10^{33} \text{ cm}^{-2}\text{s}^{-1}$ compared to $7.7 \times 10^{33} \text{ cm}^{-2}\text{s}^{-1}$ in Run 1. The recorded luminosity is validated for physics analysis keeping 35.9 fb^{-1} during 2016 data taking.

Multiple proton-proton interactions can occur during one bunch crossing, referred to as pileup. On average, the number of pileup events is proportional to the luminosity times the total inelastic proton-proton cross section. In 2016, an average of about 27 of pileup interactions has been observed in 13 TeV proton collisions at the interaction point of CMS. For 2012, this number was about 21 pileup interactions for 8 TeV collisions.

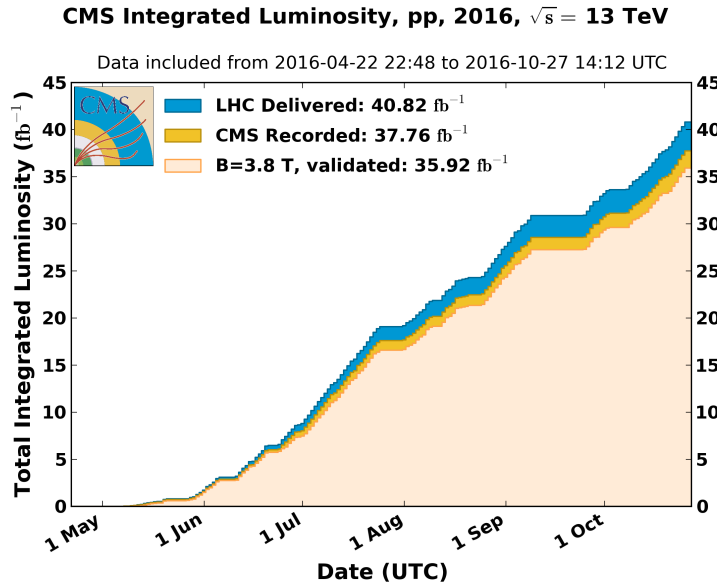


Figure 2.3: Cumulative off-line luminosity measured versus day delivered by the LHC (blue), and recorded by CMS (orange), and certified as good physics analysis during stable beams (light orange) during stable beams and for proton collisions at 13 TeV centre-of-mass energy in 2016. [73].

2.2 The Compact Muon Solenoid

At one of the collision points of the LHC, the CMS detector [74–76] is placed. Weighing 14 000 t, this cylindrical detector is about 28.7 m long and 15 m in diameter. It has an onion like structure of several specialised detectors and contains a superconducting solenoid with a magnetic field of 3.8 T. Since the LHC produces collisions in a hadronic environment, the main backgrounds of rare physics processes are multi-jet processes produced by the strong interaction. Therefore, good identification, momentum resolution, and charge determination of muons, electrons and photons are one of the main goals of the CMS detector. Additionally, a good charged particle momentum resolution and reconstruction efficiency in the inner tracker provides identification for jets coming from b quarks or tau particles. Also the electromagnetic resolution for an efficient photon and lepton isolation as well as a good hadronic calorimeter for the missing transverse energy² were kept into account while designing CMS. In Figure 2.4, an overview of the CMS detector is shown.

²The missing transverse energy comes from an imbalance in the transverse plane. This will be discussed in Chapter 4.

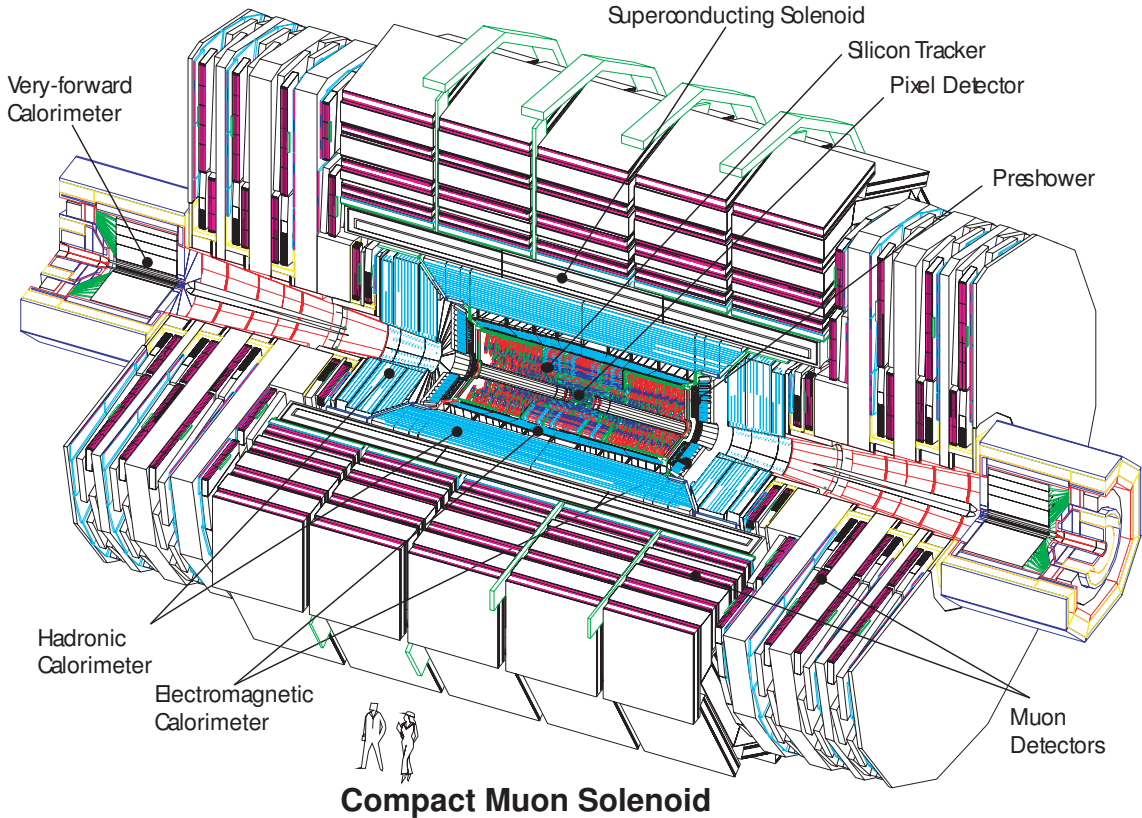


Figure 2.4: Mechanical layout of the CMS detector. Figure taken from [77].

2.2.1 CMS coordinate system

The coordinate system used by CMS can be found in [Figure 2.5](#). The origin of the right handed orthogonal coordinate system is chosen to be the point of collisions. The x-axis points towards the centre of the LHC ring such that the y-axis points towards the sky, and the z-axis lies tangent to the beam axis. Since the experiment has a cylindrical shape, customary coordinates are used to describe the momentum \vec{p} : the distance $p = |\vec{p}|$, the azimuthal angle³ $\phi \in [-\pi, \pi]$, the pseudo-rapidity⁴ η :

$$\eta = -\ln\left(\tan\left(\frac{\theta}{2}\right)\right). \quad (2.3)$$

For the energies considered at the LHC, where $E \gg m$, the pseudo-rapidity is a good approximation of the rapidity y

$$y = \frac{1}{2} \ln\left(\frac{E + p_z}{E - p_z}\right), \quad (2.4)$$

where the difference of rapidities of two particles is invariant under a Lorentz boost in the z-direction.

³The azimuthal angle is the angle between the x-axis and the projection in the transverse plane of the momentum \vec{p} , denoted as \vec{p}_T .

⁴The pseudo rapidity is expressed by the polar angle θ between the direction of \vec{p} and the beam.

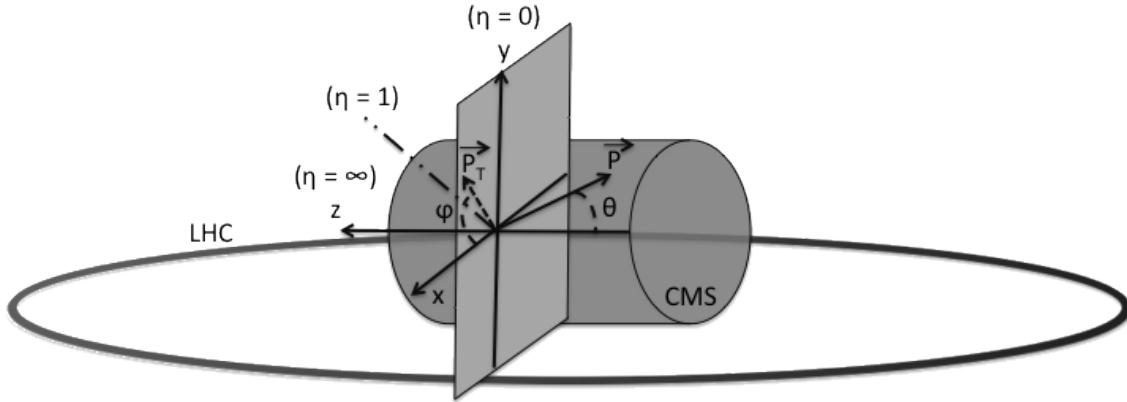


Figure 2.5: Representation of the coordinate system used by CMS. The point of origin is put at the collision point. The x-axis points towards the centre of the LHC ring such that the z-axis lies tangent to the beam axis.

2.2.2 Towards the heart of CMS

The CMS detector can be divided into two parts. A central barrel is placed around the beam pipe ($|\eta| < 1.4$), and two plugs (endcaps) ensure the hermeticity of the detector. In [Figure 2.4](#) and [Figure 2.6](#) the onion like structure of the CMS detector is visible. The choice of a solenoid of 12.9 m long and 5.9 m diameter gives the advantage of bending the particle trajectories in the transverse plane. The hadronic calorimeter ([Section 2.2.2.3](#)), the electromagnetic calorimeter ([Section 2.2.2.4](#)) and the tracker ([Section 2.2.2.5](#)) are within the solenoid ([Section 2.2.2.2](#)), while the muon chambers ([Section 2.2.2.1](#)) are placed outside the solenoid. The data used for the search presented in this thesis is collected after the long shutdown 1. After discussing each part of CMS in their Run 1 configuration, [Section 2.2.4](#) elaborates on their different upgrades for the data collected in Run 2.

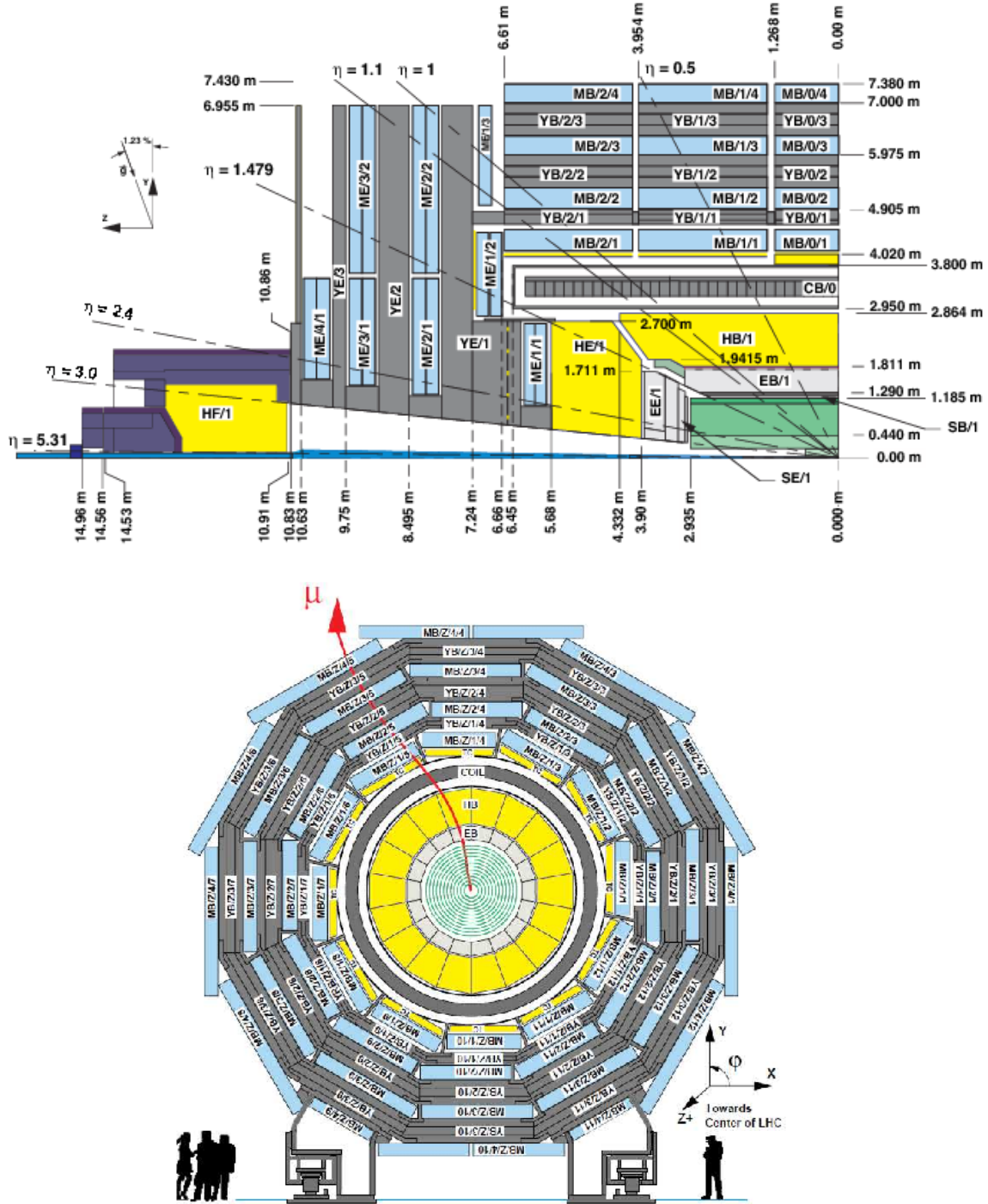


Figure 2.6: Schematic view of the CMS detector in the Run 1 configuration. The longitudinal view of one quarter of the detector is given at the top, while the transversal view is shown at the bottom. The muon system barrel elements are denoted as $MBZ/N/S$, where $Z = -2 \dots +2$ is the barrel wheel number, $N = 1 \dots 4$ the station number and $S = 1 \dots 12$ the sector number. Similarly, the steel return yokes are denoted as $YBZ/N/S$. The solenoid is denoted as $CB0$, while the hadronic calorimeter is denoted as HE (endcap)/ HB (barrel)/ HF (forward) and the electromagnetic calorimeter as EE (endcap)/ EB (barrel). The green part represents the tracking system (tracker + pixel). Figure taken from [78].

2.2.2.1 Muon system

The outermost part of CMS consists of the muon system. The magnet return yoke is interleaved with gaseous detector chambers for muon identification and momentum measurement. The barrel contains muon stations arranged in five separate iron wheels, while in the endcap four muon stations are mounted onto three independent iron discs on each side. Each barrel wheel has 12 sectors in the azimuthal angle.

The muon system is divided into three parts, shown in [Figure 2.7](#). The muon rate and neutron induced backgrounds are small and the magnetic field is very low for the barrel, thus CMS can use drift tube (DT) chambers. For the endcaps however, the muon and background flux is much higher and there is a need to use cathode strip chambers (CSC) which are able to provide a faster response, higher granularity and have a better resistance against radiation. In order to form a redundant trigger system, resistive plate chambers (RPC) are added. This makes a total of 250 DT, 540 CSC and 610 RPC chambers. In [Figure 2.6](#) the arrangement is shown.

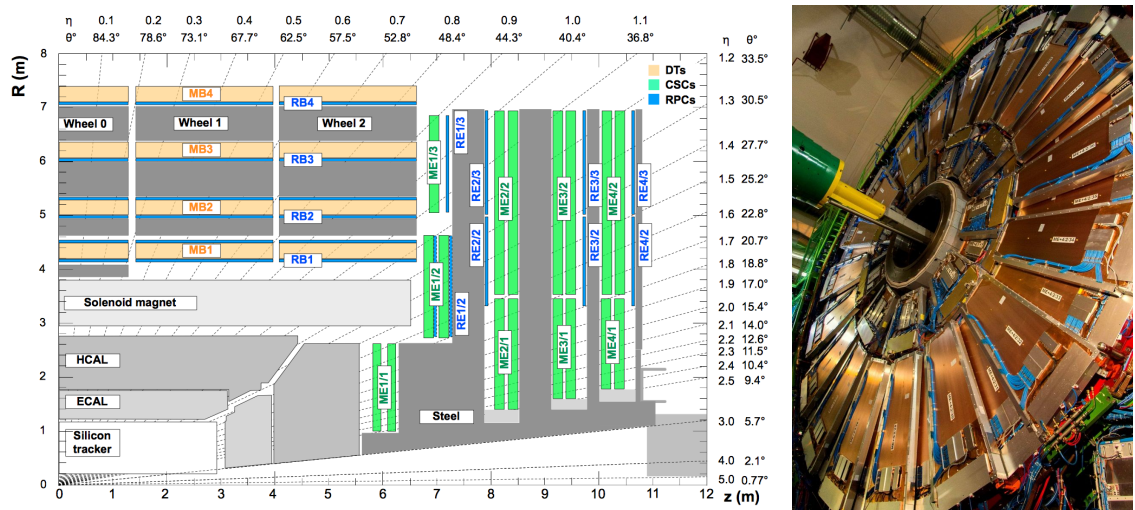


Figure 2.7: (Left) Schematic view of one quarter of the CMS muon system in the Run 1 configuration. The cathode strip chambers (CSC) are shown in green, the drift tubes (DT) are shown in yellow, while the resistive plate chambers (RPC) are shown in blue. Figure taken from [78]. (Right) Cathode strip chambers (ME+4/2 chambers on YE+3). Photo taken from [79].

Providing a measurement for $|\eta| < 1.2$, the DT chambers in the barrel are on average $2 \times 2.5 \text{ m}^2$ in size and consist of 12 layers of DT cells⁵ arranged in three groups of four. The $r\phi$ coordinate is provided by the two outside groups, while the middle group measures the z coordinate. For the outer muon station, the DT chambers contain only 8 layers of DT cells, providing a muon position in the $r\phi$ plane. There are four CSC stations in each endcap, providing muon measurements for $0.9 < |\eta| < 2.4$. These CSCs are multi-wired proportional chambers that consist of 6 anode wire planes crossed by 7 copper strips cathode panels in a gas volume. The r coordinate is provided by the copper strips, while the ϕ coordinate comes from the anode wires, giving a two dimensional position measurement. There are six layers of RPCs

⁵The DT cells are 4 cm wide gas tubes with positively charged stretched wires inside.

in the barrel muon system and one layer into each of the first three stations of the endcap. They are made from two high resistive plastic plates with an applied voltage and separated by a gas volume. Read-out strips mounted on top of the plastic plates detect the signal generated by a muon passing through the gas volume. The RPCs provide a fast response with a time resolution of 1 ns and cover a range of $|\eta| < 1.8$.

The muon system provides triggering on muons, identifying muons and improves the momentum measurement and charge determination of high p_T muons. On top of the muon system, a fraction of the muon energy is deposited in the electromagnetic calorimeter, the hadronic calorimeter, and outer calorimeter. The high magnetic field enables an efficient first level trigger and allows a good momentum resolution of $\Delta p/p \approx 1\%$ for a p_T of 100 GeV and $\approx 10\%$ for a p_T of 1 TeV. There is an efficient muon measurement up to $|\eta| < 2.4$.

2.2.2.2 Solenoid

Making use of the knowledge of previous experiments like ALEPH and DELPHI at LEP and H1 at HERA, CMS chose for a large super conducting solenoid with a length of 12.9 m and a inner bore of 5.9 m [76]. With 2168 turns, a current of 18.5 kA resulting in a magnetic field of 3.8 T, and a total energy of 2.7 GJ, a large bending power can be obtained for a modestly-sized solenoid. In order to ensure a good momentum resolution in the forward regions, a favourable length/radius was necessary. In [Figure 2.8](#), a photo of the CMS solenoid is shown.

The solenoid uses a high-purity aluminium stabilised conductor with indirect cooling from liquid helium, together with full epoxy impregnation. A four-layer winding is implemented that can withstand an outward pressure of 64 atm. The NbTi cable is co-extruded by pure aluminium that acts as a thermal stabilizer and has an aluminium alloy for mechanical reinforcement. The return of the magnetic field is done by five wheels, noted by YB in [Figure 2.6](#).

2.2.2.3 Hadronic calorimeter

The hadronic calorimeter (HCAL) is dedicated to precisely measure the energy of charged and neutral hadrons via a succession of absorbers and scintillators. This makes it crucial for physics analyses with hadronic jets or missing transverse energy. The HCAL barrel extends between $1.77 < r < 2.95$ m, where r is the radius in the transverse plane with respect to the beam. Due to space limitations, the HCAL needs to be as small as possible and is made from materials with short interaction lengths⁶. On top of this, the HCAL should be as hermetic as possible and extend to large absolute pseudo rapidities such that it can provide a good measurement of the missing transverse energy.

The quality of the energy measurements is dependent on the fraction of the hadronic shower that can be detected. Therefore, the HCAL barrel (HB) inside the solenoid is reinforced by an outer hadronic calorimeter between the solenoid and muon detectors (HO, see [Figure 2.9](#)), using the solenoid as extra absorber. This increases the thickness to 12 interaction lengths. The HB

⁶Here the interaction length is the nuclear interaction length and this is the length needed for absorbing 36.7% of the relativistic charged particles. For the electromagnetic calorimeter this is defined in radiation length X_0 . The radiation length is the mean distance over which a high energy electron loses all but $1/e$ of its energy by bremsstrahlung.

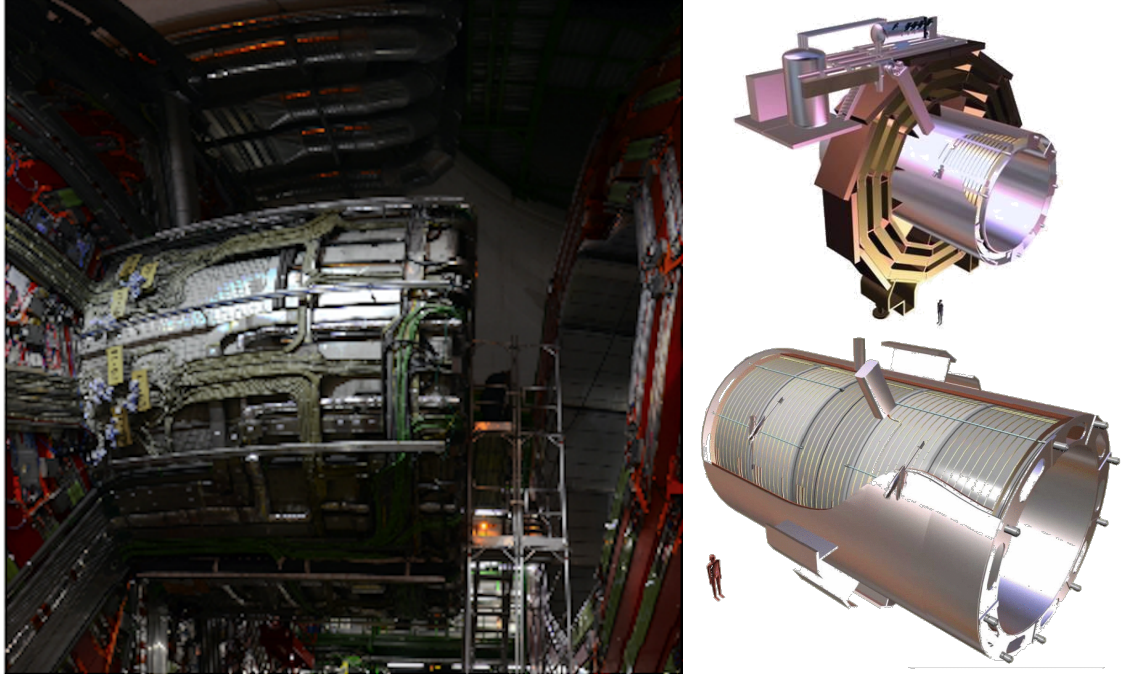


Figure 2.8: (Left) CMS solenoid during the long shutdown in 2013. (Right) An impression of the solenoid magnet taken from [80].

and HO provide measurements for $|\eta| < 1.3$, while an endcap on each side (HE, $1.3 < |\eta| < 3$) and a forward calorimeter (HF, $3.0 < |\eta| < 5.2$) extend the pseudo rapidity range.

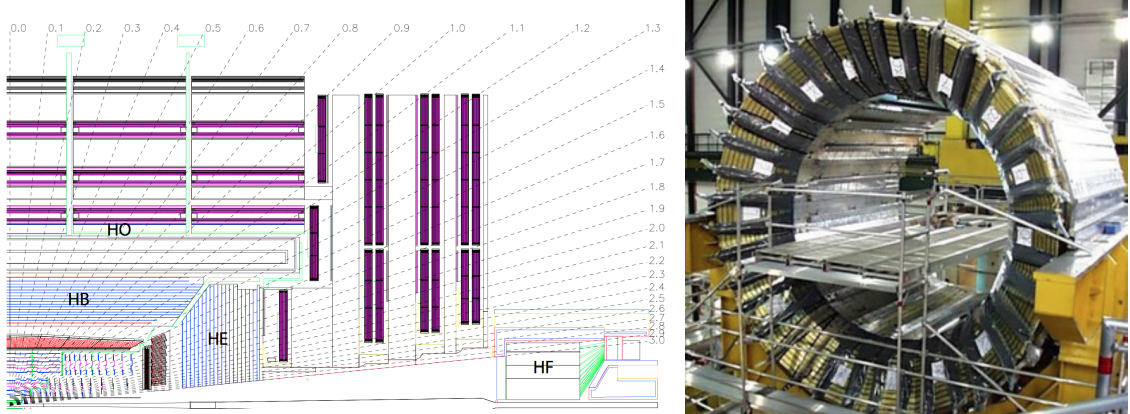


Figure 2.9: (Left) Longitudinal view of the CMS detector showing the locations of the HB, HE, HO, and HF calorimeters. Figure taken from [65]. (Right) CMS barrel calorimeter. Photo taken from [81].

The HB is made of 16 absorber plates where most of them are built from brass and others are made from stainless steel and is about five to ten interaction lengths thick. It is divided in $\eta \times \phi$ towers and contains 2592 read-out channels. The HO complements the HB and extends the reach up to twelve interaction lengths. This subsystem contains 2160 read-out channels. The HE is also composed of brass absorber plates and has a thickness corresponding to approximately

ten interaction lengths, with 2592 read-out channels. The HF experiences intense particle fluxes with an expected energy of 760 GeV deposited on average in a proton interaction at a centre-of-mass of 14 TeV, compared to 100 GeV in the rest of the detector. Therefore, these are Cherenkov light detectors made of radiation hard quartz fibres. The main causes of such large energy events are high energy muons and charged particles from late showering hadrons. The HF represents 1728 read-out channels.

The HCAL and electromagnetic calorimeter combined, can measure the hadron energy with a resolution $\Delta E/E \approx 100\% \sqrt{E[\text{GeV}]} + 5\%$.

2.2.2.4 Electromagnetic calorimeter

The electromagnetic calorimeter (ECAL) is designed to measure the energy of photons and electrons and covers $|\eta| < 3$. It is an hermetic, homogeneous detector and consists of 75 848 lead tungstate (PbWO_4) crystals. These crystals have a fast response time - 80% of the light is emitted within 25 ns- and are radiation hard. The electromagnetic showers produced by passing electrons or photons, ionize the crystal atoms which emit a blue-green scintillation light, that is collected by silicon avalanche photodiodes (APDs) in the barrel and vacuum phototriodes (VPTs) in the endcaps. The crystals and the APD response are sensitive to temperature changes and require a stable temperature.

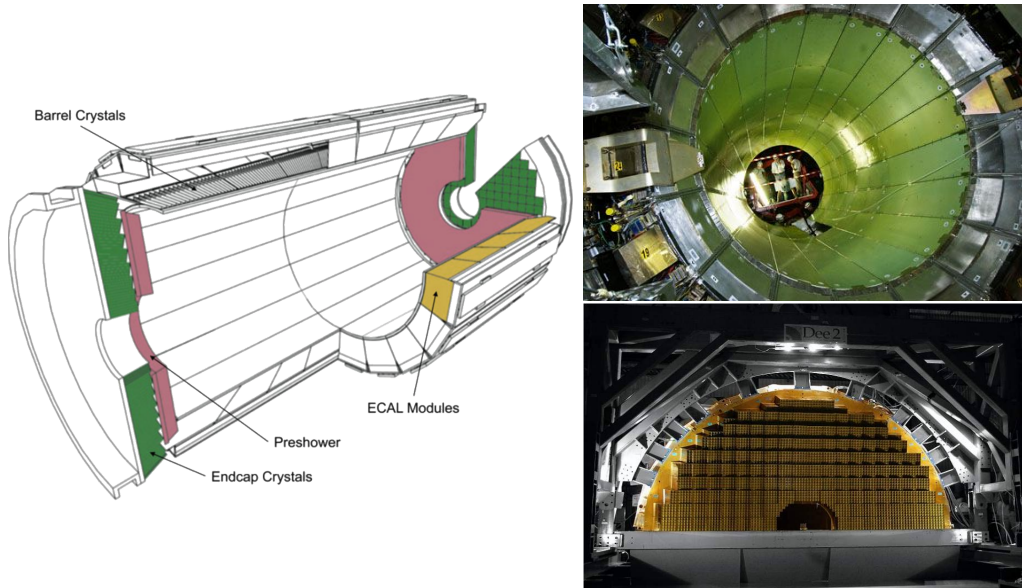


Figure 2.10: (Left) Schematic cross section of the electromagnetic calorimeter taken from [65]. (Right top) The ECAL barrel during construction [83]. (Right bottom) One half of an EE [84].

There are three parts: a central barrel (EB), an endcap region (EE) and a preshower (ES) (Figure 2.10). The EB has an inner radius of 129 cm and corresponds to a pseudo rapidity of $0 < |\eta| < 1.479$. At a distance of 314 cm from the vertex and covering a pseudo rapidity of $1.479 < |\eta| < 3.0$, are the EE. They consist of semi-circular aluminium plates from which structural units of 5×5 crystals (super crystals) are supported. The ES is placed in front of

the crystal calorimeter over the endcap pseudo rapidity range with two planes of silicon strip detectors as active elements.

The electromagnetic shower will typically involve more than one channel. More than 90% of the energy of a 35 GeV electron or photon is contained in a 5×5 matrix of crystals. Therefore, a clustering algorithm is performed in order to associate the energy deposits to the particles impinging the calorimeter. The achieved precision [85] for the barrel is 2×10^{-3} rad in ϕ and 10^{-3} in η . For the endcaps this is 5×10^{-3} rad in ϕ and 2×10^{-3} in η . The energy is reconstructed by a supercluster algorithm, taking into account energy radiated via bremsstrahlung or conversion [65]. The energy resolution is given by

$$\frac{\sigma(E)}{E} = \frac{2.8\%}{\sqrt{E}} \oplus \frac{0.128}{E(\text{GeV})} \oplus 0.3\%, \quad (2.5)$$

in the absence of a magnetic field, where the contributions come from the stochastic, noise and constant terms respectively. The dominating term is the constant term ($E_{\text{shower}} \approx 100$ GeV) and thus the performance is highly dependent on the quality of calibration and monitoring.

2.2.2.5 Inner tracking system and operations

The tracking system (tracker) [86] is the detecting unit closest to the point of interaction. Responsible for the reconstruction of trajectories from charged particles with $|\eta| < 2.5$ that are bent by the magnetic field, it provides a measurement of the momentum. The tracker is also responsible for the determination of the interaction point or vertex. It should be able to provide high granularity as well as fast read-out, and be able to endure high radiation. For these reasons, the CMS collaboration chose silicon detector technology.

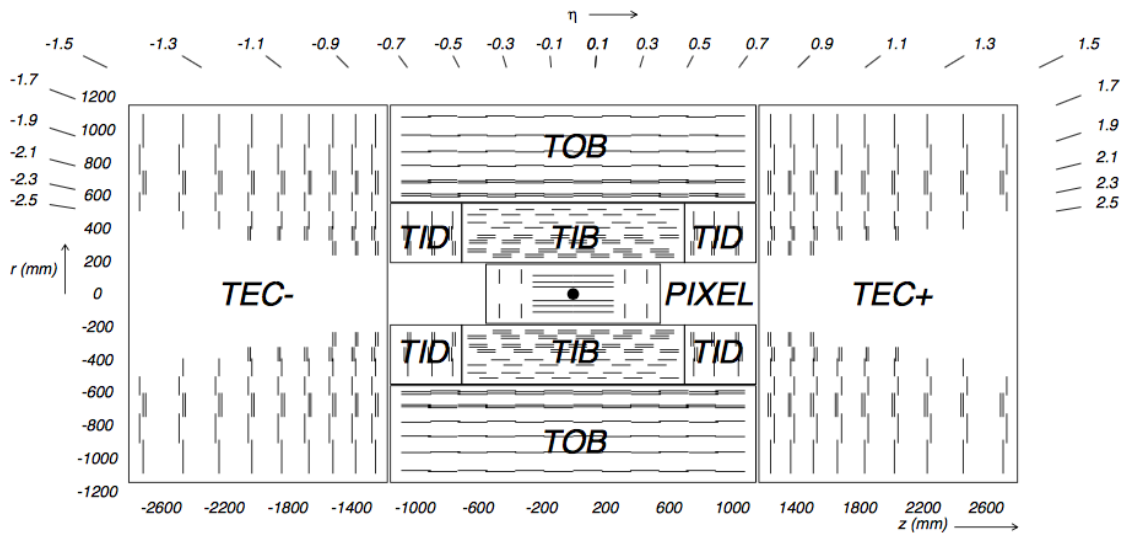


Figure 2.11: Schematic cross section through the CMS tracker. Each line represents a detector module. Double lines indicate back-to-back modules that deliver stereo hits. The tracker inner barrel (TIB) and inner discs (TID) are set around the pixel detector. The tracker outer Barrel (TOB) and endcaps (TEC) form the outer layers. Figure taken from [65].

The tracking system consists of a cylinder of 5.8 m long and 2.5 m in diameter. It is immersed in a co-axial magnetic field of 3.8 T provided by the solenoid. As shown in Figure 2.11, the tracker is built up from a large silicon strip tracker with a small silicon pixel tracker inside. The inner pixel region ($4.4 < r < 10.2$ cm), gets the highest flux of particles. Therefore, pixel silicon sensors of $100 \times 150 \mu\text{m}^2$ are used. It consists of three cylindrical barrels that are complemented by two discs of pixel modules at each side. The silicon strip tracker ($20 < r < 116$ cm) has three subdivisions. The Tracker Inner Barrel and Discs (TIB, TID, see Figure 2.13) are composed of four barrel layers accompanied by three discs at each end. The outer part of the tracker - Tracker Outer Barrel (TOB) - consists of 6 barrel layers. In the outer discs, there are nine discs of silicon sensors, referred to as Tracker End Caps (TEC).

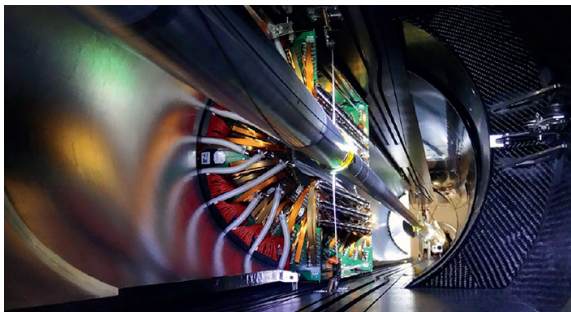


Figure 2.12: The pixel barrel being re-installed after the Long Shutdown in 2015, around the beam pipe at CMS [87].



Figure 2.13: First half of the inner tracker barrel, consisting of three layers of silicon modules [88].

The pixel detector, shown in Figure 2.12, has 1440 modules that cover an area of about 1 m^2 and have 66 million pixels. It provides a three-dimensional position measurement of the hits arising from the interaction from charged particles with the sensors. In transverse coordinate ($r\phi$), the hit position resolution is about $10 \mu\text{m}$, while $20\text{-}40 \mu\text{m}$ is obtained in the longitudinal coordinate (z). The sensor plane position provides the third coordinate. The TIB/TID, shown in Figure 2.13, delivers up to four $r\phi$ -measurements using $320 \mu\text{m}$ thick silicon micro-strip sensors. These sensors are placed with their strips parallel to the beam axis in the barrel and radial in the discs. In the TIB, the first two layers have a strip pitch of $80 \mu\text{m}$, while the remaining two have a strip pitch of $120 \mu\text{m}$. This leads to a respective single point resolution of $23 \mu\text{m}$ and $35 \mu\text{m}$. For the TID, the pitch varies between $100 \mu\text{m}$ and $141 \mu\text{m}$. The TOB provides six $r\phi$ -measurements with a single point resolution of $53 \mu\text{m}$ in the first four layers, and $35 \mu\text{m}$ in the last two layers. It consists of $500 \mu\text{m}$ thick microstrip sensors with strip pitches of $183 \mu\text{m}$ (first 4 layers) or $122 \mu\text{m}$ (last two layers). The TEC provides up to 9 ϕ -measurements via 9 discs consisting of up to 7 rings of silicon microstrip sensors of $97 \mu\text{m}$ to $184 \mu\text{m}$ average pitch.

A second coordinate measurement (z in the barrel, r on the discs) is provided through the use of a second micro strip detector module mounted back-to-back with a stereo angle of 100 mrad. This is done on the modules in the first two layers and rings of the TIB, TID, and TOB, as well as rings 1, 2, and 5 of the TECs (double lines in Figure 2.11). The resolution in the z direction is approximately $230 \mu\text{m}$ in the TIB and $530 \mu\text{m}$ in the TOB, and is varying with pitch in the TID and TEC. To allow overlay and avoid gaps in acceptance, each module is shifted slightly in r or z with respect to its neighbouring modules within a layer. With this detector lay-out,

at least nine points per charged particle trajectory can be measured in an $|\eta|$ range up to 2.4, where at least four of them being two dimensional. The CMS silicon tracker provides 9.3 million read-out channels and covers an active area of about 198 m^2 .

2.2.3 Data acquisition

At a design luminosity of $10^{34} \text{ cm}^{-2}\text{s}^{-1}$, the proton interaction rate exceeds 1 GHz. Given the large size of an event (about 1 MB), the high crossing rate, and that typically tens of collisions happen at the same time, it is impossible for the CMS experiment to store all the data generated. In order to deal with the large amount of data, a two level trigger system has been put in place. The first level (Level-1) is a custom hardware system, while a second high level trigger (HLT) is software based, running on a large farm of computers.

CMS Level-1 Trigger

The Level-1 Trigger has to be a flexible, maintainable system, capable of adapting to the evolving physics programme of CMS [89]. Its output rate is restricted to 100 kHz imposed by the CMS read-out electronics. It is implemented by custom hardware and selects events containing candidate objects - e.g. ionization deposits consistent with a muon, or energy clusters corresponding to an electron / photon / tau lepton / missing transverse energy / jet. Collisions with large momenta can be selected with the use of the scalar sum of the transverse momenta of the jets.

By buffering the raw data from the CMS subdetectors in front-end drivers, the Level-1 Trigger has a pipeline memory of 3.2 μs to decide whether to keep an event or reject it. The trigger primitives (TP) from the calorimeters and muon detectors are processed in several steps and combined into a global trigger. This information is then combined with the input from the other subsystems for the HLT. The separate inputs are synchronized to each other and the LHC orbit clock and sent to the global trigger module. Here, Level-1 Trigger algorithms are performed within 1 μs to decide whether to keep the event.

CMS HLT Trigger

The HLT is an array of commercially available computers with a programmable menu that has an output rate of on average 400 Hz for off-line event storage. The data processing is based on an HLT path. This is a set of algorithmic steps to reconstruct objects to define selection criteria. Here, the information of all subdetectors can be used to perform algorithms on higher level reconstructed objects.

2.2.4 Phase 1 upgrades

Before the start of taking collision data for 13 TeV operations on 3 June 2015, CMS had a long shutdown (LS1) [90]. During this shutdown, the section of the beryllium beam pipe within CMS was replaced by a narrower one. This operation required the pixel detector to be removed and reinserted into CMS. During Run 2, higher particle fluxes with respect to Run 1 are expected. To avoid longterm damage caused by the intense particle flux at the heart of CMS, the tracker has been made ready to operate at much lower temperature than during Run

1. The electromagnetic calorimeter preshower system was damaged during Run 1, therefore the preshower discs were removed, repaired and reinstalled successfully inside CMS in 2014. To help the discrimination between interesting low momentum muons coming from collisions and muons caused by backgrounds, a fourth triggering and measurement station for muons was added in each of the endcaps. Several new detectors were installed into CMS for measuring the collision rate within the detector and to monitor beam related backgrounds.

During the LS1, the muon system underwent major upgrades [91, 92]. In the fourth station of each endcap, the outermost rings of CSC and RPC chambers were completed, providing an angular coverage of $1.2 < |\eta| < 1.8$ for Run 2, increasing the system redundancy, and allowing tighter cuts on the trigger quality. In order to reduce the environmental noise, outer yoke discs have been placed on both sides for the endcaps. At the innermost rings of the first station, the CSCs have been upgraded by refurbishing the read-out electronics to make use of the full detector granularity instead of groups of three as was the case for Run 1.

Since the HF experiences intense particle fluxes, it became clear during Run 1 that the glass windows of the PMTs need replacing. For the ECAL in Run 1, the energy reconstruction happened via a weighted sum of the digitized samples [93]. For Run 2 however, the reconstruction had to be made more resistant for out-of-time pileup and a multi-fit approach has been set into place. In this approach, the pulse shape is modelled as a sum of one in-time pulse plus the out-of-time pulses [85]. The energy resolution is better than 2% in the central barrel region and 2-5 % elsewhere.

During the first data taking period of the LHC (2010 to 2013), the tracker operated at +4°C. With the higher LHC beam intensities from 2015 onwards, the tracker needs to be operated at much lower temperatures. The reason for this is that with intense irradiation, the doping concentration changes, the leakage current increases proportional to the fluence and the charge collection efficiency decreases due to charge trapping. Mostly the leakage current (I) is affected by the temperature change:

$$I \propto T^2 e^{-\frac{E_g}{2kT}}, \quad (2.6)$$

where T is the operating temperature, E_g the band gap and k the Boltzmann constant. There is approximately a factor 15 between the leakage currents at room temperatures and at -10 °C.

During the LS1, the CMS cooling plant was refurbished [94] and the fluorocarbon cooling system overhauled. To help suppressing the humidity inside the tracker, new methods for vapour sealing and insulation were applied. Furthermore, several hundred high-precision sensors are used to monitor the humidity and temperature. In order to get as dry air as possible, a new dry-gas plant provides eight times more dry gas (air or nitrogen) than during the first run, and allows regulation of the flow. As a final addition, the cooling bundles outside the tracker are equipped with heater wires and temperature sensors in order to maintain safe operations above the cavern dew point. For the data taking during Run 2, the tracker is operated at -15 °C.

In Run 2, with the increase in centre-of-mass energy and a higher luminosity, a larger number of simultaneous inelastic collisions per crossing is expected with respect to Run 1. For this, the CMS Level-1 has been upgraded [95]. All hardware, software, databases and the timing control

system have been replaced for Run 2, where the main changes are that the muon system now uses the redundancy of the muon detector system earlier to make a high resolution muon trigger. Other upgrades are also performed, including providing the global trigger with more Level-1 Trigger algorithms.

After the first half of Run 2, during EYETS, the innermost part of detection in CMS (pixel detector) was replaced, enhancing the particle tracking capabilities of CMS. The data used in the framework of this thesis however is from before this upgrade. More information on the Pixel upgrade can be found in Refs. [96, 97].

2.2.5 CMS computing model

The selected data is stored, processed and dispersed via the Worldwide Large Hadron Collider Computing Grid (WLCG) [98, 99]. This has a tiered structure that functions as a single, coherent system.

At CERN and the Wigner Research Centre for physics, a single Tier-0 is located. The raw data collected by the experiments is archived here, and a first reconstruction of the data is done. This data is then already in a file format usable for physics analysis. Furthermore, it is able to reprocess data when new calibrations become available. The Tier-0 site distributes this data to a total of 14 Tier-1 centres. They carry out data reprocessing and store real data as well as simulated data. The Tier-1 further distributes the data to over 150 Tier-2 centres. These make the data accessible for physics analysis and are also being used for the production of simulated data. The data is made accessible for physicists around the world. For CMS, the Tier-0 site at CERN reconstructs the full collision events and the backup of the data is sent to seven Tier-1 computer centres in France, Germany, Italy, Spain, Taiwan, UK, and the US. At the Tier-1 sites the events are again reconstructed using refined calibration constants. The patterns are created and the more complex events are sent to forty Tier-2 centres for specific analysis tasks.

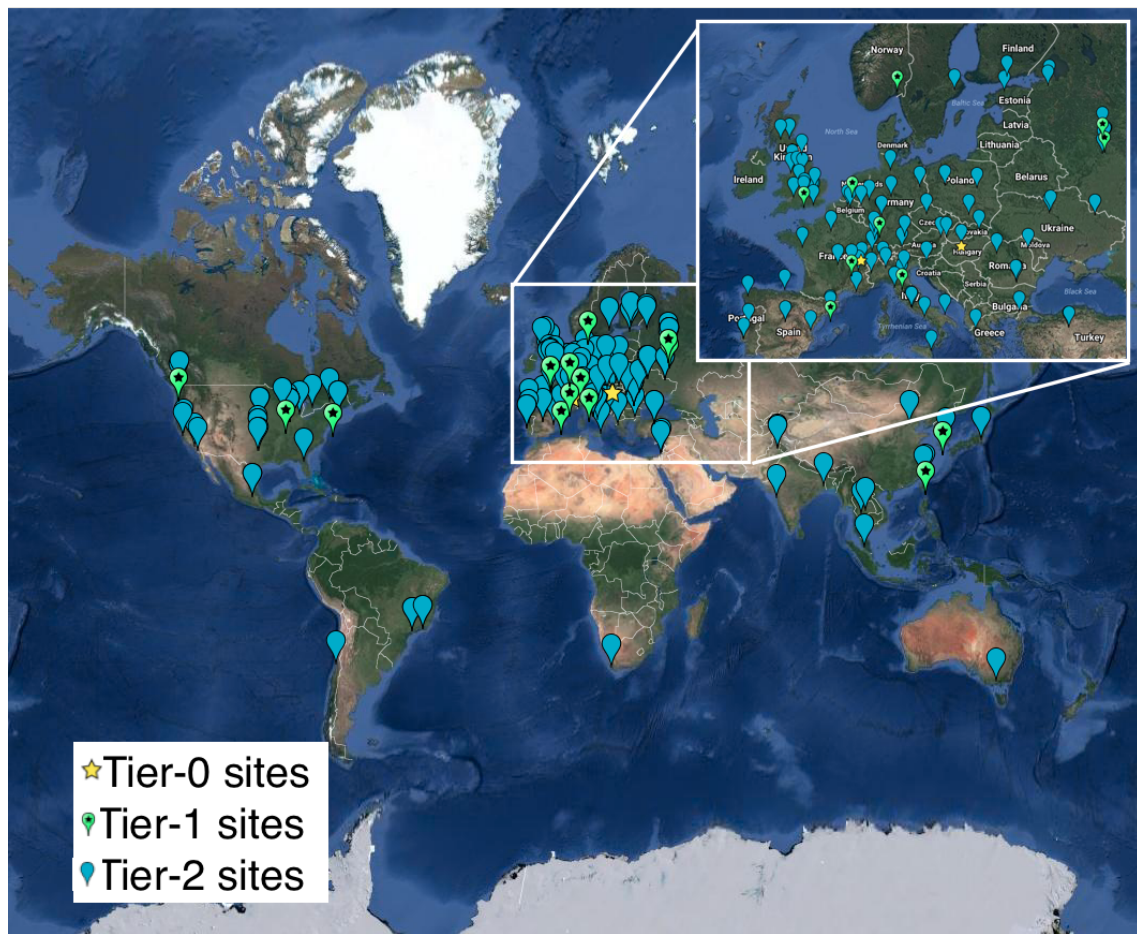


Figure 2.14: Worldwide LHC Computing Grid in 2017 [100].

Analysis techniques

3

In order to study the collisions coming from high energy experiments, many tools have been developed. In [Section 3.1](#), the physics of hadron collision at high energies are presented. These insights are used to generate events via Monte Carlo event generators, explained in [Section 3.2](#). Machine learning helps to differentiate between signal- and background-like events. In [Section 3.3](#), the multivariate technique of boosted decision trees is explained. This yields powerful discriminants for separating signal and background events and provides distributions for template-based maximum likelihood fits. The fitting method used in the search presented in this thesis is discussed in [Section 3.4](#).

3.1 Hadron collisions at high energies

All partons can be approximated as free when there is sufficiently high momentum transfer in hadron collisions. This makes it possible to treat a hadron-hadron scattering as a single parton-parton interaction. The momentum of the parton can then be expressed as a fraction of the hadron momentum

$$\vec{p}_{\text{parton}} = x \vec{p}_{\text{hadron}}, \quad (3.1)$$

where x is referred to as the Björken scaling variable. The interaction $p_A p_B \rightarrow X$ can then be factorised in terms of partonic cross sections $\hat{\sigma}_{ij \rightarrow X}$ [101]

$$\sigma_{p_A p_B \rightarrow X} = \sum_{ij} \iint dx_1 dx_2 f_i^A(x_1, Q^2) f_j^B(x_2, Q^2) d\hat{\sigma}_{ij \rightarrow X}, \quad (3.2)$$

where i and j are the partons resolved from protons A and B. The parton density functions (PDF) are denoted as $f_i(x_j, Q^2)$, and Q^2 is the factorisation scale more commonly denoted as μ_F . This factorisation scale represents the energy at which the hadronic interaction can be expressed as a product of the partonic cross section and the process independent PDF. In [Figure 3.1](#), the kinematic regions in x and μ_F are shown for fixed target and collider experiments.

The parton density functions (PDF) [102–104] represent the momentum distribution of the proton amongst its partons at an energy scale μ_F . These functions are obtained from global fits to data since they can not be determined from first principles. From measurements on deep

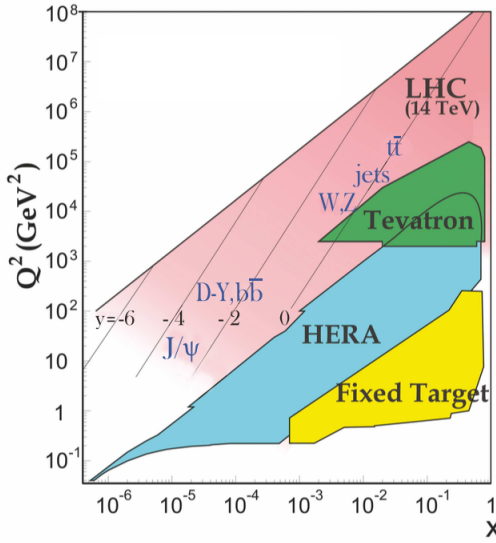


Figure 3.1: Kinematic regions in momentum fraction x and factorisation scale Q^2 probed by fixed-target and collider experiments. Some of the final states accessible at the LHC are indicated in the appropriate regions, where y is the rapidity. In this figure, the incoming partons have $x_{1,2} = (M/14 \text{ TeV})e^{\pm y}$ with $Q = M$ where M is the mass of the state shown in blue in the figure. For example, exclusive J/ψ and Υ production at high $|y|$ at the LHC may probe the gluon PDF down to $x \sim 10^{-5}$. Figure taken from [20].

inelastic scattering using lepton-proton collision by the HERA collider [105], supplemented with proton-antiproton collisions from the Tevatron [106], and proton collision data from the ATLAS, CMS and LHCb collaborations at the LHC (Run 1) [107] the PDFs are determined and included in global PDF sets known as the PDF4LHC recommendation [104]. Their measurement at scale μ_F is extrapolated to higher energies by use of the DGLAP equations [108]. Once these PDFs are known, the cross section of a certain process can be calculated and used as input for the Monte Carlo generators used to make the simulated data samples at the LHC. In the framework of this thesis, the NLO PDF4LHC15_100 set is used. This set is an envelope of three sets: CT14, MMHT2014 and NNPDF3.0 [104]. As illustration, the dependency of the PDFs on the momentum fraction x is shown for the NNPDF3.0 set on hadronic scale $\mu_F^2 = 10 \text{ GeV}^2$ and LHC scale $\mu_F^2 = 10^4 \text{ GeV}^2$ in Figure 3.2. The gluon density dominated for most values of the momentum fraction, implying that it is easier to probe gluons than the quarks. When the Björken scale is set to one, the parton densities of the valence quarks of the proton, up and down quarks, dominate over the gluon density. The sea quarks originating from gluon splitting, the charm, anti-up, and anti-down quarks, have lower densities in general for the proton. The resolution scale Q^2 is typically taken to be the energy scale of the collision. For the top quark pair production a scale of $Q^2 = (350 \text{ GeV})^2$ is chosen, meaning that the centre-of-mass energy of the hard interaction is about twice the top quark mass. The uncertainty on the parton distributions is evaluated using the Hessian technique [109], where a matrix with a dimension identical to the number of free parameters needs to be diagonalised. In the case of PDF4LHC15_100 set, this translates into 100 orthonormal eigenvectors and 200 variations of the PDF parameters in the plus and minus direction.

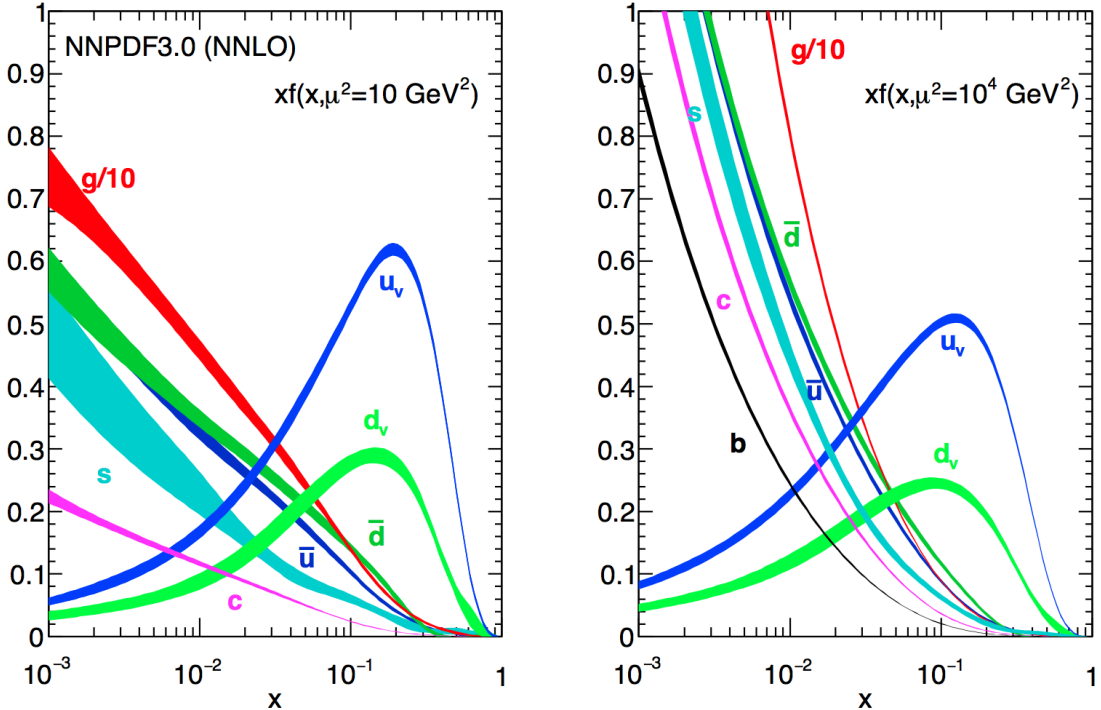


Figure 3.2: The momentum fraction x times the parton distribution functions $f(x)$, where $f = u_v, d_v, \bar{u}, \bar{d}, s, c$, or g as a function of the momentum fraction obtained in the NNLO NNPDF3.0 global analysis at factorisation scales $\mu^2 = 10 \text{ GeV}^2$ (left) and $\mu^2 = 10^4 \text{ GeV}^2$ (right), with $\alpha_s(M_Z^2) = 0.118$. The gluon PDF has been scaled down by a factor of 0.1. Figure taken from [20].

Quantum fluctuations can cause divergences at high energies. This is solved by introducing a renormalization scale μ_R to redefine physical quantities, making the theory still able to describe the experimental regime. A consequence of this method is that the coupling constants will run as a function of μ_R . Beyond the renormalization scale, the high energy effects such as the loop corrections to propagators (self energy) are absorbed in the physical quantities through a renormalization of the fields. In particular, the running behaviour of the strong coupling constant¹ α_S is found to be

$$\alpha_S = \frac{\alpha_S(\mu_0^2)}{1 + \alpha_S(\mu_0^2) \frac{33-2n_f}{12\pi} \ln\left(\frac{|\mu_R^2|}{\mu_0^2}\right)}, \quad (3.3)$$

with n_f the number of quarks and μ_0 the reference scale at which the coupling is known. The current world average of the strong coupling constant at the Z boson mass is $\alpha_S(\mu_R = m_Z) = 0.1181 \pm 0.0011$ [20]. From Equation 3.3 one can see easily that the coupling strength decreases with increasing renormalization scale, this is known as asymptotic freedom. Additionally, following the behaviour of $\alpha_S(\mu_R^2)$, a limit $\Lambda_{\text{QCD}} \approx 200 \text{ MeV}$ is found for which α_S becomes larger than one. Under this limit, the perturbative calculations of observables can no longer be done.

¹The strong coupling constant is defined as $\alpha_S = \frac{g_S^2}{4\pi}$.

Cross sections can be written in terms of interacting vertices contributing to the matrix element (ME) originating from elements of a perturbative series [110], allowing them to be expanded as a power series of the coupling constant α

$$\sigma = \sigma_{\text{LO}} \left(1 + \left(\frac{\alpha}{2\pi} \right) \sigma_1 + \left(\frac{\alpha}{2\pi} \right)^2 \sigma_2 + \dots \right). \quad (3.4)$$

Leading order (LO) accuracy contains the minimal amount of vertices in the process, then depending on where the series is cut-off one speaks of next-to-leading order (NLO), or next-to-next-to-leading order (NNLO) accuracy in α . Predictions including higher order corrections tend to be less affected by theoretical uncertainties originating from a variation of the chosen renormalization and factorisation scales.

3.2 Event generation

In order to compare reconstructed data with theoretical predictions, collision events are generated and passed through a simulation of the CMS detector and an emulation of its read-out. For the detector simulation, a so-called Full Simulation package [111, 112] based on the Geant4 toolkit [113] is employed. This allows detailed simulations of the interactions of the particles with the detector material.

3.2.1 Fundamentals of simulating a proton collision

The generation of $\text{pp} \rightarrow \text{X}$ events is subdivided into sequential steps [114–116], as shown in Figure 3.3.

The interaction of two incoming protons is often soft and elastic leading to events that are not interesting in the framework of this thesis. More intriguing are the hard interactions between two partons from the incoming protons. The event generation starts from the matrix elements of a hard scattering process of interest. The corresponding cross section integral is sampled using Monte Carlo techniques and the resulting sample of events reflects the probability distribution of a process over its final state phase space. A parton shower (PS) program is then used to simulate the hadronisation of final state partons, coming from the sample of events of the hard interaction, into hadrons which then decay further. On top of this, radiation of soft gluons or quarks from initial or final state partons is simulated. These are respectively referred to as initial state radiation (ISR) or final state radiation (FSR). The contributions from soft secondary interactions, the so-called underlying event (UE), and colour reconnection effects are also taken into account. A brief overview of the programs used for the event generation of the signal and main background processes used in the search presented in this thesis, is given in Section 3.2.2.

3.2.2 Programs for event generation

The FEYNRULES package [117] allows for the calculation of the Feynman rules in momentum space for any quantum field theory model. By use of a Lagrangian, the set of Feynman rules associated with this Lagrangian is calculated. Via the Universal FeynRules Output (UFO) [118] the results are then passed to matrix element generators.

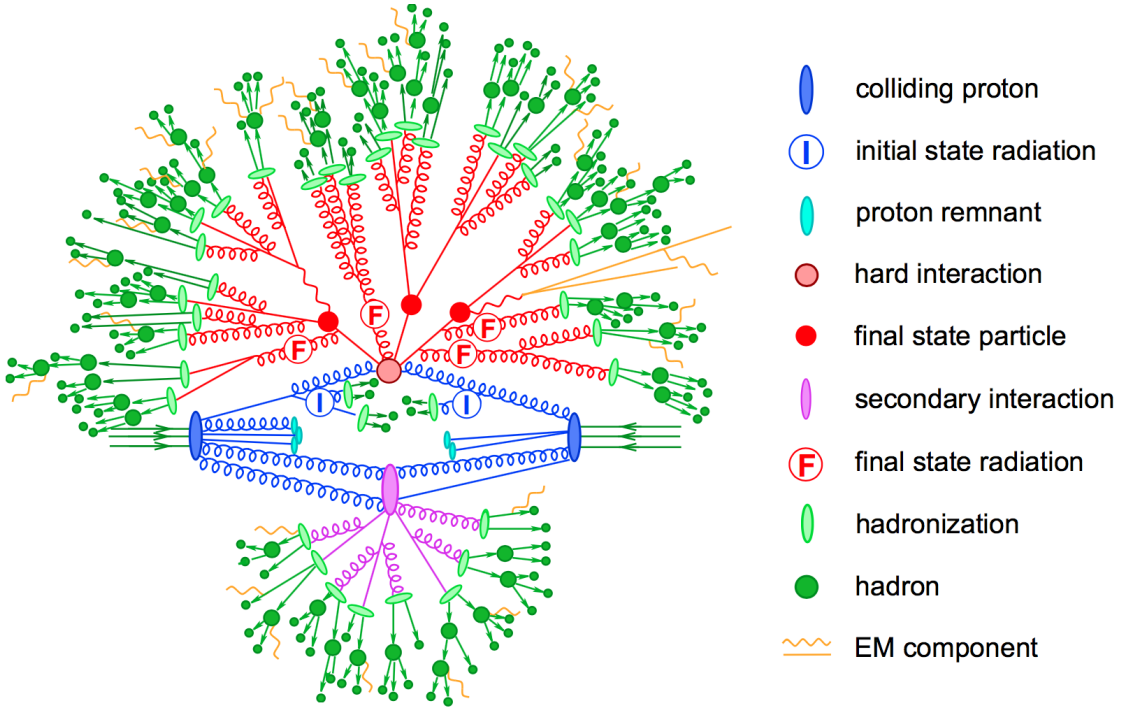


Figure 3.3: Sketch of a hadron collision as simulated by a Monte-Carlo event generator. The red blob in the centre represents the hard collision, surrounded by a tree-like structure representing Bremsstrahlung as simulated by parton showers. The purple blob indicates a secondary hard scattering event. Parton-to-hadron transitions are represented by light green blobs, dark green blobs indicate hadron decays, while yellow lines signal soft photon radiation. Figure taken from [116].

The MadGraph program [119] is used to interpret the physics model and calculate the corresponding Feynman diagrams and matrix elements. After this, MadEvent [120] is used to calculate the corresponding partons. These generated parton configurations are then merged with Pythia [121, 122] parton showers using the MLM merging scheme [123].

The MadGraph5_aMC@NLO program [124] combines the LO MadGraph [119] and the aMC@NLO program into a common framework. This combination supports the generation of samples at LO or NLO together with a dedicated matching to parton showers using the MC@NLO [125] or FxFx [126] schemes respectively. The FxFx scheme produces a certain fraction of events with negative weights originating from the subtraction of amplitudes that contain additional emissions from the NLO matrix element to prevent double-counting.

The POWHEG box (versions 1 and 2) [127–132] contains predefined implementations of various processes at NLO. It applies the POWHEG method for ME- to PS- matching, where the hardest radiation generated from the ME has priority over subsequent PS emission to remove the overlap with the PS simulation.

The JHU generator (version 7.02) [133–136] is used to generate the parton level information including full spin and polarization correlations. It is commonly used for studying the spin and parity properties of new resonances such as $ab \rightarrow X \rightarrow VV$, where $V = Z, W, \gamma$.

The generation of events from processes involving the production and decay of resonances creates a computational heavy load, especially at NLO. The narrow width approximation assumes that the resonant particle is on-shell. This factorizes the production and decay amplitude, allowing to perform the simulation of the production and decay of heavy resonances like top quarks or Higgs bosons to be performed in separate steps. The MadSpin program [137] extends this approach and accounts for off-shell effects through a partial reweighting of the events. Additionally, spin correlation effects between production and decay products are taken into account.

The Pythia program (versions 6 and 8) [121, 122] generates events of various processes at LO. However, more commonly it is only used for its PS simulation and is then used after other LO and NLO event generators to perform subsequent parton showering, hadronisation, and simulation of the underlying event. In this thesis the underlying event tunes [138] are the CUETP8M2T4, CUETP8M1 and CUETP8M2.

The detector response is simulated via the Geant4 [113] program. This program tracks the particles through the detector material via a detailed description of the detector and generates several hits throughout several sensitive layers. In addition, the response of the detector electronics to these hits are simulated.

3.2.3 Generating FCNC top-Z interactions

The FCNC processes are generated by interfacing the Lagrangian in Equation 1.36 with MadGraph5_aMC@NLO by means of the FeynRules package and its Universal FeynRules Output format. The complex chiral parameters are arbitrary chosen to be $f_{Xq}^L = 0$ and $f_{Xq}^R = 1$.

NOTE: RH and LH gave the same resulting variables and RH is easier to simulate since those are singlets under SU2 (no doublet with b)

The processes are generated with the MadGraph5_aMC@NLO (version 2.2.2) and showered with Pythia. The signal consists of two components: events describing the top quark pair production followed by a FCNC decay of one top quark ($t \rightarrow Zq$), and events with the FCNC single top quark production ($Zq \rightarrow t$) for which the top quark decays according to the SM. The leading order generation of the single top quark FCNC process $tZ+0,1$ jet including a merging technique can not be done since $tZ+1$ jet also contains contributions from top quark pair FCNC where one quark is decaying in tZ . Therefore, single top quark and top quark pair processes are generated independently, where the single top quark process is generated without the extra hard jet, and the top quark pair FCNC process is generated with up to two extra jets.

The signal rates are estimated by use of the MadGraph5_aMC@NLO program for estimating the partial widths. The anomalous couplings are left free to float for this estimation, and only one coupling is allowed to be non-vanishing at a time. The results are presented in Table 3.1.

The anomalous single top quark cross sections are calculated by convolution of the hard scattering matrix elements with the LO order set of NN23L01 [139] partons densities. The NLO effects are modelled by multiplying each LO cross section by a global k -factor. The LO single top quark production cross section and the global k -factors for the top-Z production are shown in Table 3.2. The hard scattering events are then matched to parton showers to Pythia to account for the simulation of the QCD environment relevant for hadronic collisions.

Table 3.1: Leading order partial widths related to the anomalous decay modes of the top quark, where the new physics scale Λ is given in GeV.

Anomalous coupling	vertex	Partial decay width (GeV)
κ_{tZq}/Λ	tZu	$1.64 \times 10^4 \times (\kappa_{tZu}/\Lambda)^2$
	tZc	$1.64 \times 10^4 \times (\kappa_{tZc}/\Lambda)^2$
ζ_{tZq}	tZu	$1.69 \times 10^{-1} \times (\zeta_{tZu})^2$
	tZc	$1.68 \times 10^{-1} \times (\zeta_{tZc})^2$

Table 3.2: Leading order single top quark production cross section at a centre-of-mass of 13 TeV for $pp \rightarrow tZ$ or $\bar{t}Z$, where the new physics scale is given in GeV. The NLO k -factors [140] are given in the last column.

Anomalous coupling	vertex	Cross section (pb) $pp \rightarrow t + pp \rightarrow \bar{t}$	$\sigma_{pp \rightarrow \bar{t}}/\sigma_{pp \rightarrow t}$	NLO k -factor
κ_{tZq}/Λ	tZu	$1.92 \times 10^7 \times (\kappa_{tZu}/\Lambda)^2$	0.12	1.40
	tZc	$2.65 \times 10^6 \times (\kappa_{tZc}/\Lambda)^2$	0.50	1.40
ζ_{tZq}	tZu	$8.24 \times 10 \times (\zeta_{tZu})^2$	0.14	1.40
	tZc	$1.29 \times 10 \times (\zeta_{tZc})^2$	0.50	1.40

The top quark pair cross sections are derived from the SM $t\bar{t}$ cross section, calculated with MadGraph5_aMC@NLO at NLO at a centre-of-mass of 13 TeV ($\sigma_{t\bar{t}}^{\text{SM,NLO}} = 6.741 \times 10^2 \text{ pb}$), and considering the decay $t\bar{t} \rightarrow (bW^\pm)(Xqt)$. The branching fraction $\mathcal{B}(t \rightarrow bW^\pm)$ is assumed to be equal to one and the FCNC branching fraction is calculated as

$$\mathcal{B}(t \rightarrow qX) = \frac{\Gamma_{t \rightarrow qX}}{\Gamma_t^{\text{SM}} + \Gamma_t^{\text{FCNC}}} \approx \frac{\Gamma_{t \rightarrow qX}}{\Gamma_t^{\text{SM}}}, \quad (3.5)$$

where $\Gamma_{t \rightarrow qX}$ is given in Table 3.1, $\Gamma_t^{\text{SM}} = 1.32 \text{ GeV}$ [51], and the assumption $\Gamma_t^{\text{FCNC}} \ll \Gamma_t^{\text{SM}}$ is made. In Table 3.3 the resulting NLO cross sections for the top-Z FCNC interactions are given.

Table 3.3: Next to leading order top quark pair cross section for the top-Z FCNC interactions $t\bar{t} \rightarrow (bW^\pm)(X_{qt})$ with a full leptonic decay at a centre-of-mass of 13 TeV, where $\sigma_{pp \rightarrow t\bar{t}}^{\text{SM,NLO}} = 6.741 \times 10^2 \text{ pb}$, $\mathcal{B}(Z \rightarrow \ell\bar{\ell}) = 3.36 \times 3 \times 10^{-2}$, and $\mathcal{B}(W \rightarrow \ell\nu) = 10.80 \times 3 \times 10^{-2}$.

Anomalous coupling	vertex	Process	Cross section (pb)
κ_{tZq}/Λ	tZu	$t\bar{t} \rightarrow (b\ell^+\nu)(\bar{u}\ell^+\ell^-)$	$2.727 \times 10^5 \times (\kappa_{tZu}/\Lambda)^2$
		$t\bar{t} \rightarrow (\bar{b}\ell^-\bar{\nu})(u\ell^+\ell^-)$	$2.727 \times 10^5 \times (\kappa_{tZu}/\Lambda)^2$
	tZc	$t\bar{t} \rightarrow (b\ell^+\nu)(\bar{c}\ell^+\ell^-)$	$2.726 \times 10^5 \times (\kappa_{tZc}/\Lambda)^2$
		$t\bar{t} \rightarrow (\bar{b}\ell^-\bar{\nu})(c\ell^+\ell^-)$	$2.726 \times 10^5 \times (\kappa_{tZc}/\Lambda)^2$
ζ_{tZq}	tZu	$t\bar{t} \rightarrow (b\ell^+\nu)(\bar{u}\ell^+\ell^-)$	$2.807 \times (\zeta_{tZu})^2$
		$t\bar{t} \rightarrow (\bar{b}\ell^-\bar{\nu})(u\ell^+\ell^-)$	$2.807 \times (\zeta_{tZu})^2$
	tZc	$t\bar{t} \rightarrow (b\ell^+\nu)(\bar{c}\ell^+\ell^-)$	$2.807 \times (\zeta_{tZc})^2$
		$t\bar{t} \rightarrow (\bar{b}\ell^-\bar{\nu})(c\ell^+\ell^-)$	$2.807 \times (\zeta_{tZc})^2$

3.2.4 Generating SM background events

The SM tZq sample is generated using the MadGraph5_aMC@NLO generator at leading order accuracy. The t̄Z and triboson samples were generated using the MadGraph5_aMC@NLO generator, interfaced through the dedicated MC@NLO matching scheme. The WZ+jets and t̄W samples are produced with up to one additional parton at next-to-leading order accuracy using MadGraph5_aMC@NLO and using FxFx approach for matching and merging. The samples of t̄H, WW, ZZ, and single top quark production channels are generated with the POWHEG box. The JHU generator is used for the tqH sample, while the tWZ sample is generated using MadGraph5_aMC@NLO at leading order. All events are interfaced to Pythia to simulate parton shower, hadronisation, and underlying event. Additionally, MadSpin is used for the tZq, WZ+jets, t̄Z, t̄W, tWZ, and triboson samples.

The complete list of SM samples is given in Table 3.4, along with their cross sections at a centre-of-mass of 13 TeV. The cross sections without a reference are coming from the generator with which the sample has been made, for some of them the uncertainties are provided by the Generator Group [142]. For each MC sample, the integrated luminosity that the sample represents is estimated as the number of simulated events divided by the cross section of the generated process. This luminosity is then matched to integrated luminosity of 35.9 fb^{-1} represented by the data used for analysis. For processes generated with MadGraph5_aMC@NLO, the effective number of simulated events is used, taking into account positive and negative event weights. In Figure 3.4, a summary is given of the SM cross section measurements performed by the CMS collaboration. These cross sections are all in agreement with their SM predictions.

Table 3.4: SM MC samples used in this analysis with their corresponding cross section at a centre-of-mass of 13 TeV and MadGraph5_aMC@NLO correction C when applicable. The generators used for each sample are indicated and the simulation of the parton shower, hadronisation, and underlying event is done by Pythia version 8.22 [122] for all samples.

Process	Generator	Cross section (pb)	C	Ref.
$WZ \rightarrow 3\ell\nu$	MadGraph5_aMC@NLO+MadSpin	5.26	1.61	[142]
tZq with $Z \rightarrow \ell^+\ell^-$	MadGraph5_aMC@NLO+MadSpin	0.0758	3.77	[142]
tqH with $H \rightarrow ZZ \rightarrow \ell^+\ell^-\ell^+\ell^-$	JHU	$8.80 \cdot 10^{-6}$	-	[142]
$t\bar{t}W$ +jets with $W \rightarrow \ell\nu$	MadGraph5_aMC@NLO+MadSpin	0.2043 ± 0.0020	1.94	[142]
$t\bar{t}Z \rightarrow 2\ell + 2\nu + \text{other}$, with $m_{\ell\ell} > 10$ GeV	MadGraph5_aMC@NLO+MadSpin	0.2529 ± 0.0004	2.15	[142]
$t\bar{t}H$, no $b\bar{b}$ decays	POWHEG	0.2151	-	[142]
$t\bar{t}H$, $b\bar{b}$ decays	POWHEG	0.2934	-	[142]
$WW \rightarrow 2\ell 2\nu$	POWHEG	12.178	-	[143]
$ZZ \rightarrow 4\ell$	POWHEG	0.3366	-	[142]
WZZ	MadGraph5_aMC@NLO+ MadSpin	0.05565	1.14	[142]
ZZZ	MadGraph5_aMC@NLO	0.01398	1.17	[142]
single top quark tWZ , with $Z_\mu \rightarrow \ell^+\ell^-$	MadGraph5_aMC@NLO(LO)+MadSpin	0.001123	-	[142]
single top quark t-channel \bar{t}	POWHEG+MadSpin	$44.33^{+1.76}_{-1.49}$	-	[142]
single top quark t-channel t	POWHEG+MadSpin	$26.38^{+1.32}_{-1.18}$	-	[142]
single top quark $\bar{t}W$	POWHEG	35.85 ± 0.90 (scale) ± 1.70 (PDF)	-	[142]
single top quark tW	POWHEG	35.85 ± 0.90 (scale) ± 1.70 (PDF)	-	[142]
$t\bar{t}$	POWHEG	$831.76^{+19.77+35.06}_{-29.20-35.06}$	-	[142]
$Z/\gamma^* + \text{jets}$, with $m_{\ell\ell} > 50$ GeV	MadGraph5_aMC@NLO	$3 \times (1921.8 \pm 0.6 \pm 33.2)$	1.49	[142]
$Z/\gamma^* + \text{jets}$, with 10 GeV $< m_{\ell\ell} < 50$ GeV	MadGraph	18610	-	[142]

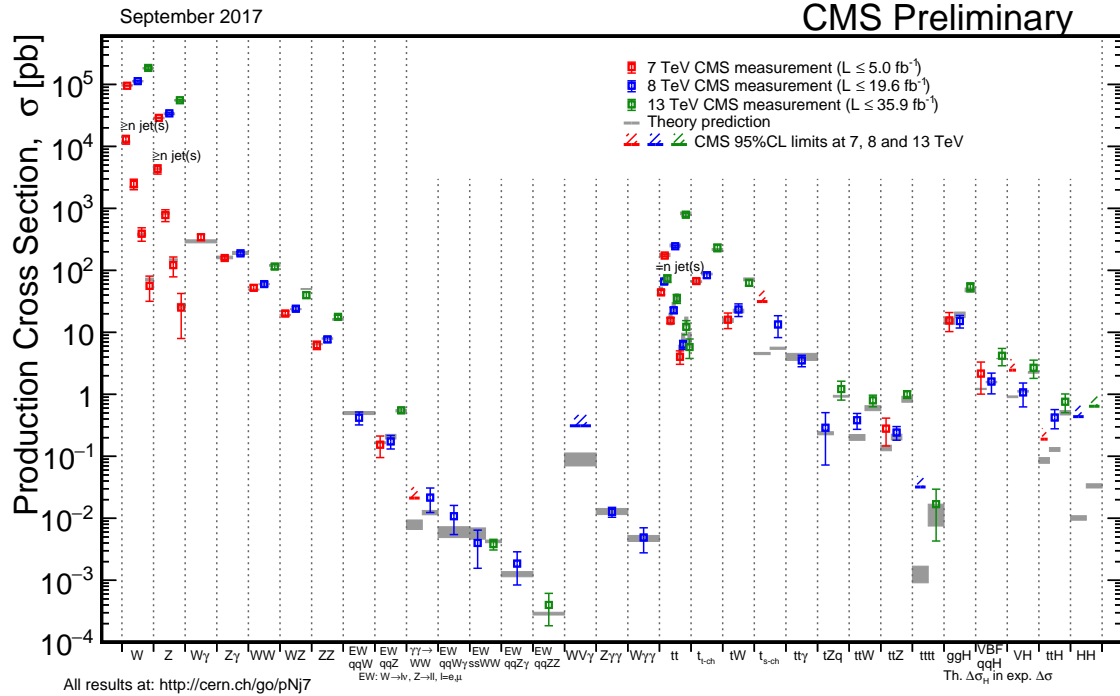


Figure 3.4: Summary of the SM cross section measurements performed by the CMS collaboration. Figure taken from [34].

3.3 Multivariate analysis techniques: Boosted Decision Trees

The need for processing large quantities of data and discriminating between events with largely similar experimental signatures makes multivariate analysis (MVA) a largely used method in the physics community. Multivariate classification methods based on machine learning techniques are a fundamental ingredient to most analyses. The advantage of using a MVA classifier is that it can achieve a better discrimination power with respect to a simpler analysis based on individual selection criteria or poorly discriminating variables. A risk of using MVA classifiers is overtraining. This happens when there are too many model parameters of an algorithm adjusted to too few data points. This leads to an increase in the classification performance over the objectively achievable one.

There are many software tools that exist for MVA. In this thesis, the Tool for Multivariate Analysis (TMVA) [144] is used. This software is an open source project included into ROOT [145]. By training on events for which the classification is known, a mapping function is determined that describes a classification or an approximation of the underlying behaviour defining the target value (regression). Boosted decision trees (BDT) are employed for the classification of events as implemented in the TMVA framework [144]. This multivariate technique is based on a set of decision trees where each tree yields a binary output depending on the fact that an event is signal- or background-like. This has as advantage that several discriminating variables can be combined into a powerful one-dimensional discriminant D.

The decision tree is constructed by training on a dataset for which the outcome is already provided, such as simulation datasets with signal and background processes (supervised learning). Different trees can be combined into a forest where the final output is determined by the majority vote of all trees, so-called boosting. This stabilises the decision trees against statistical fluctuations and makes it possible to keep the decision trees very shallow, making the method more robust against overtraining. Examples of such boosting algorithms are Adaptive Boosting (AdaBoost) and Gradient Boosting [146]. For the search presented in the following chapters, Gradient boost is used with a learning rate of 0.2-0.3 and the depth of the tree is set to three. Additionally, the Gradient boost is used in combination with bagging, so-called stochastic gradient boosting. Bagging smears the statistical fluctuations in the training data and therefore stabilises the response of the classifier and increases the performance by eliminating overtraining. More information about stochastic gradient boosting can be found in Ref. [147].

The discriminating power of a BDT is assessed by analysing the receiver operating characteristic (ROC) curve. This curve represents the background rejection over the signal efficiency of the remaining sample. The area under the curve (AUC) is compared to random guessing in order to identify the best classifier. When the multivariate discriminator has no discriminating power, the resulting AUC will be 0%, while 50% means fully separated event classes. In Figure 3.5 examples of ROC curves are shown.

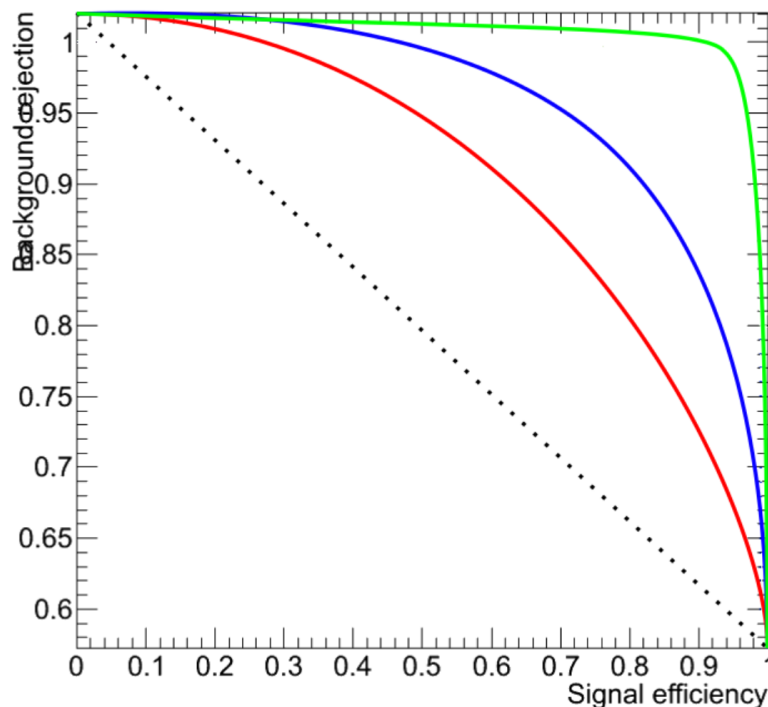


Figure 3.5: Example of ROC curves. In this example, the green method is better than the blue one, which is better than the red one. The dashed line represents a case where there is no separation. Figure taken from [148].

3.4 Statistical methodology

The search performed in the framework of this thesis requires the simultaneous analysis of data from different decay channels. The statistical methodology used for this search is developed by the ATLAS and CMS collaborations in the context of the LHC Higgs Combination group [149–152]. The Higgs Combined Tool [153] is a RooStats [154] framework which runs different statistical methods. In this section, only the statistical tools necessary for the performed search are described [150].

The event yields of signal and background processes are denoted as s and b respectively. These represent event counts in multiple bins or unbinned probability density functions. By use of simulation, predictions on both signal and background yields are made. The multiple uncertainties on these predictions are accounted for by introducing nuisance parameters θ such that $s = s(\theta)$ and $b = b(\theta)$.

The Bayesian and modified classical frequentist statistical approaches are used in high energy physics to characterise the absence of a signal. The level of incompatibility of data with a signal hypothesis is quantified in terms of confidence levels (CL). The convention is to require a 95% CL for excluding a signal. In general, limits are not set on the signal cross section directly, but are set on the signal strength modifier μ . The signal strength modifier is defined such that it equally changes all the cross sections of all production mechanisms of the signal by the same scale.

In this thesis, the modified frequentist approach [155, 156] for confidence levels that adopts the classical frequentist method to allow nuisance parameters, is used. It constructs a likelihood $\mathcal{L}(\text{data}|\mu, \theta)$ is as

$$\mathcal{L}(\text{data}|\mu, \theta) = \text{Poisson}(\text{data}|\mu s(\theta) + b(\theta)) \text{ pdf}(\tilde{\theta}|\theta). \quad (3.6)$$

The probability density function $\text{pdf}(\tilde{\theta}|\theta)$ describes all sources of uncertainty. In this thesis, all sources of uncertainties are assumed to be either 100% correlated or uncorrelated. When uncertainties are partially correlated, they are broken down to subcomponents that fit those requirements. This allows to include all constraints in the likelihoods in a clean factorised form.

A systematic uncertainty $\text{pdf}(\theta|\tilde{\theta})$ for the nuisance θ with nominal value $\tilde{\theta}$ is used. It reflects the degree of belief of what the true value of the θ is. In this thesis, the approach from the Higgs Combined Tool is used where the pdfs $\rho(\theta|\tilde{\theta})$ are re-interpreted as posteriors of real or imaginary measurements $\tilde{\theta}$

$$\rho(\theta|\tilde{\theta}) \sim \text{pdf}(\tilde{\theta}|\theta) \pi_\theta(\theta), \quad (3.7)$$

where $\pi_\theta(\theta)$ is the hyper prior for the (imaginary) measurements. The pdfs used by the Higgs Combine Tool are described in Ref. [152].

The data in Equation 3.6 represents either the actual observation or pseudo-data to construct sampling distributions. For a binned likelihood, the Poisson probabilities to observe n_i events in bin i is given as

$$\text{Poisson}(\text{data}|\mu s(\theta) + b(\theta)) = \prod_i \frac{(\mu s_i(\theta) + b_i(\theta))^{n_i}}{n_i!} e^{-\mu s_i(\theta) - b_i(\theta)}. \quad (3.8)$$

At the LHC, the test statistic is defined as

$$q_\mu = -2 \ln \frac{\mathcal{L}(\text{data} | \mu, \hat{\theta}_\mu)}{\mathcal{L}(\text{data} | \hat{\mu}, \hat{\theta}_\mu)}, \quad (3.9)$$

where the likelihood is maximised in the numerator (maximum likelihood estimator, MLE) for a given μ and (pseudo) data at $\hat{\theta}_\mu$, while $\hat{\mu}$ combined with $\hat{\theta}$ defines the point for which the likelihood reaches its global maximum. The estimated signal strength modifier $\hat{\mu}$ can not become negative since a signal rate is positive defined by physics. Furthermore, an upper constraint on the MLE $\hat{\mu} \leq \mu$ is imposed.

The signal is excluded at $1 - \alpha$ confidence level when

$$\text{CLs} = \frac{P(q_\mu \geq q_\mu^{\text{obs}} | \mu s + b)}{P(q_\mu \geq q_\mu^{\text{obs}} | b)} \leq \alpha, \quad (3.10)$$

with $P(q_\mu \geq q_\mu^{\text{obs}} | \mu s + b)$ the probability to observe a value of the test statistic at least as large as the one observed in data q_μ^{obs} , under the signal plus background ($s + b$) hypothesis, and $P(q_\mu \geq q_\mu^{\text{obs}} | b)$ for the background only (b) hypothesis. These probabilities are defined as

$$\begin{aligned} p_\mu &= P(q_\mu \geq q_\mu^{\text{obs}} | \mu s + b) = \int_{q_\mu^{\text{obs}}}^{\infty} f(q_\mu | \mu, \hat{\theta}_\mu^{\text{obs}}) dq_\mu, \\ 1 - p_b &= P(q_\mu \geq q_\mu^{\text{obs}} | b) = \int_{q_{\mu=0}^{\text{obs}}}^{\infty} f(q_\mu | \mu = 0, \hat{\theta}_{\mu=0}^{\text{obs}}) dq_\mu, \end{aligned} \quad (3.11)$$

where p_μ and p_b are the p-values associated to the two hypothesis, and $f(q_\mu | \mu, \hat{\theta}_\mu^{\text{obs}})$ and $f(q_\mu | \mu = 0, \hat{\theta}_{\mu=0}^{\text{obs}})$ are the probability density functions of the signal plus background and background only hypothesis constructed from toy Monte Carlo pseudo data. These are generated with nuisance parameters fixed to $\hat{\theta}_{\mu=0}^{\text{obs}}$ (background only) and $\hat{\theta}_\mu^{\text{obs}}$ (signal plus background). The 95% CL level upper limit on μ is achieved by adjusting μ until $\text{CL} = 0.05$, this is the so-called observe limit. The expected median upper limit and the $\pm 1\sigma$ and $\pm 2\sigma$ bands for a hypothesis is generated by a large set of pseudo data and calculate the CLs and the value of μ at 95% CL for each of them. A cumulative probability distribution can be build by starting the integration from the side corresponding to low event yields. The median expected value, so-called expected limit at 95% CL, is where the cumulative distribution function crosses the 50% quantile. The $\pm 1\sigma$ (68%) and $\pm 2\sigma$ (95%) bands on the expected limit are defined by the crossings of the 16% and 84%, and 2.5% and 97.5% quantiles.

In order to significantly reduce computing time, the Asymptotic CL method is used. This method avoids an ensemble of toy Monte Carlo samples and instead replaces it by one representative dataset, called Asimov dataset. This dataset is constructed such that all observed quantities are set equal to their MLE values ($\hat{\theta}_{\text{Asimov}} = \theta_0$). More information about this procedure can be found in Refs. [150].

Event reconstruction and identification

4

The simulated data after the detector simulation described in [Section 3.2](#), has the exact same format as the real collision data recorded at the CMS experiment. Therefore the same software can be used for the reconstruction of both simulation and real data. In [Section 4.1](#), the object reconstruction is explained. After reconstructing the objects, they are connected to physics objects, which need to be identified ([Section 4.2](#)) and corrected for pileup ([Section 4.3](#)). The objects used for physics analysis have extra requirements as shown in [Section 4.4](#). A summary of all the corrections applied to data and simulation is given in [Section 4.5](#).

4.1 Object Reconstruction

In [Figure 4.1](#), the particle interaction in a transverse slice of the CMS detector is shown. When a particle enters the detector, it first enters the tracker where charged particle trajectories, so-called tracks, and origins, so-called vertices, are reconstructed from signals or hits in the sensitive layers. The magnetic field bends the charged particles making it able to measure the electric charges and momenta of charged particles. The electrons and photons are absorbed in the ECAL and the corresponding electromagnetic showers are detected as clusters of energy in adjacent cells. From this, the energy and the direction of the particles can be determined. The charged and neutral hadrons can also initiate a hadronic shower in the ECAL that is fully absorbed in the HCAL. The clusters from these showers are also used to estimate the energy and direction. Muons and neutrinos pass through the calorimeters without little to no energy loss and the neutrinos even escape the CMS detector undetected while muons produce hits in the muon detectors.

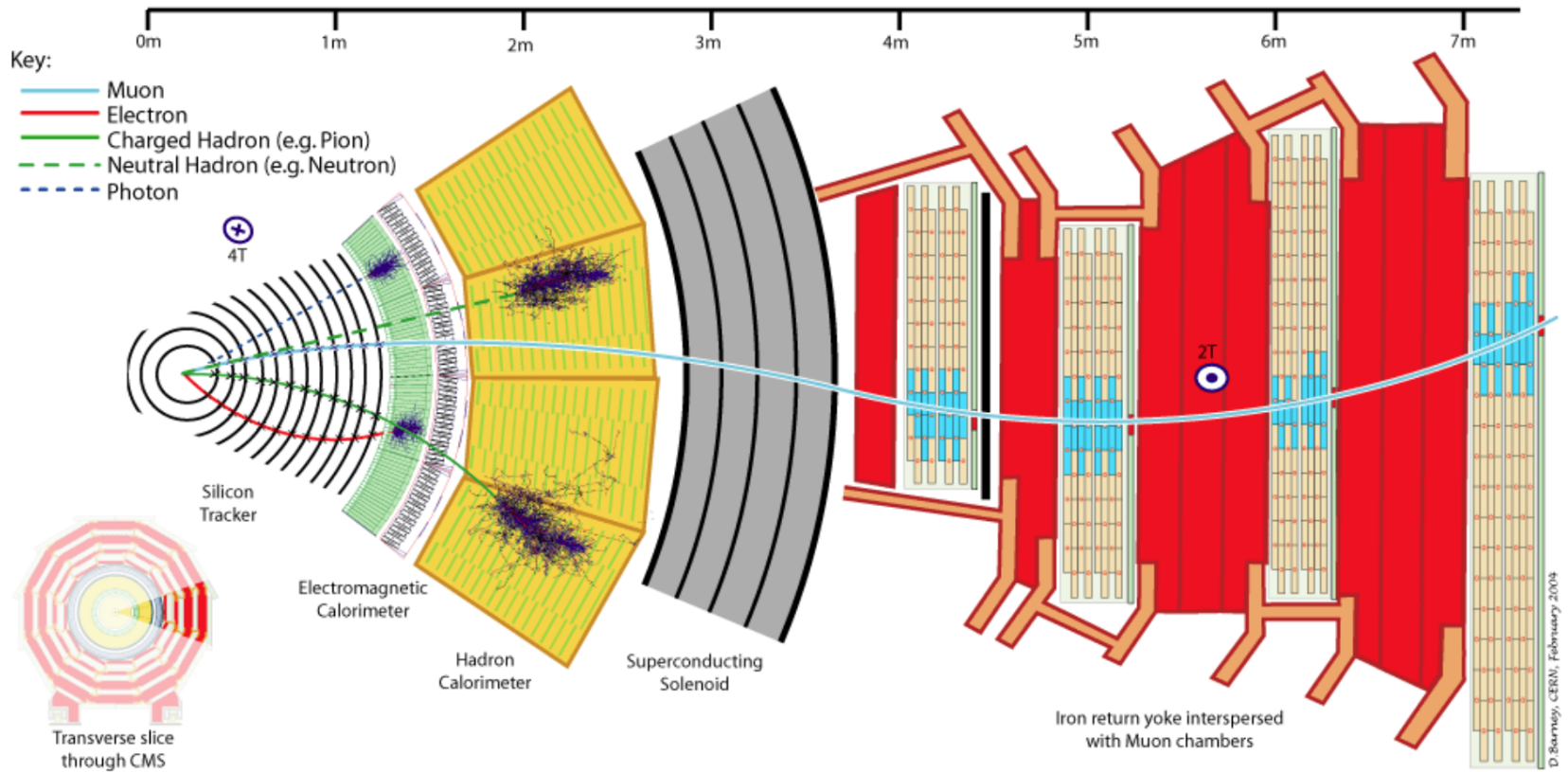


Figure 4.1: Cross-section of the CMS detector with all parts of the detector labelled. This sketch shows the specific particle interactions from a beam interaction region to the muon detector. The muon and charged pion are positively charged, the electron is negatively charged. Figure taken from [157].

The particle flow (PF) [157] reconstruction algorithm correlates the tracks and clusters from all detector layers with the identification of each final state particle, and combines the corresponding measurements to reconstruct the properties. The muon is identified by a track in the inner tracker, connected to a track in the muon detector as described in Section 4.1.2. The electrons are identified by a track and an ECAL cluster, not connected to an HCAL cluster as described in Section 4.1.3. The ECAL and HCAL clusters without a track link identify the photons and neutral hadrons, while the addition of the tracker determines the energy and direction of a charged hadron (Section 4.1.5).

NOTE: Ik kan hier stoppen en 4.1.1, 4.1.2, 4.1.3.4.1.4 volledig schrappen (dus enkel primary vertex houden)

4.1.1 Charged particle tracks

An iterative tracking algorithm is responsible for the reconstruction of the tracks made by charged particles in the inner tracking system. Each iteration consists of four steps [76]: the track-seed generation, the pattern recognition algorithm, removal of track-hit ambiguities and a final track fit. The pattern recognitions done by use the Kalman filter method [158, 159] which takes into account the magnetic field and multiple scattering effects. All hits that are unambiguously associated to the final track are removed from the list of available hits. In order to associate the remaining hits, the procedure is repeated with looser track reconstruction criteria. The use of the iterative track reconstruction procedure has a high track finding efficiency, where the fake track reconstruction rate is negligible.

4.1.2 Following the Muon's Footsteps

The muon reconstruction [160] has three subdivisions: local reconstruction, regional reconstruction and global reconstruction. The local reconstruction is performed on individual detector elements such as strip and pixel hits in the inner tracking system, and muon hits and/or segments in the muon chambers. Independent tracks are reconstructed in the inner tracker - called tracker tracks - and in the muon system, called standalone muon tracks. Based on these tracks, two reconstructions are considered: Global Muon reconstruction and Tracker Muon reconstruction. The first is an outside-in approach starting from a standalone muon track while the second uses an inside-out approach starting from tracker tracks. For low transverse momenta ($p_T \lesssim 5$ GeV), the tracker muon reconstruction is more efficient than the global muon approach. This is due to the fact that tracker muons only require a single muon segment in muon system, while the global muon approach requires typically segments in at least two muon stations. These tracker muons are used for identifying muons from the hadronisation of b or c quarks. The global muon approach typically improves the tracker reconstruction for $p_T \gtrsim 200$ GeV.

4.1.3 The path of the Electron

Standard tracking algorithms are based on Kalman filtering which assume that the energy loss is Gaussian distributed. Since the electron tracks are increasingly curved in the magnetic field as a function of its flight distance, these standard tracking algorithms are not suitable to fit the electron tracks and different filtering algorithm. The Gaussian sum filter (GSF) [161] is used instead.

In CMS, the electrons are reconstructed in two ways. The older ECAL based tracking is developed to identify high energetic isolated electrons. This tracking algorithm starts from

ECAL clusters with a transverse energy above 4 GeV and extrapolates from these cluster the position of the hits in the tracker. Another, tracker based algorithm uses all the tracks with a p_T higher than 2 GeV found with iterative tracking as seeds. The electron seeds from the ECAL- and tracker-based procedures are merged into a unique collection and are then refitted by using the summed Gaussian distributions as uncertainty per hit in the track fit. The electron efficiency is measured in 8 TeV proton collision data to be better than 93% for electrons with an ECAL supercluster energy of $E_T > 20$ GeV [162]. For electrons with an $E_T > 25$ GeV in 13 TeV proton collision data, the efficiency is about 96%[163].

4.1.4 Primary Vertex Reconstruction

The primary vertex (PV) reconstruction is able to measure the location of all proton interaction vertices in each event consisting of the signal vertex and all vertices from pileup events. First, tracks are selected to be consistent with being produced promptly in the primary interaction [86]. Then the tracks are grouped according to the z coordinate of their closest approach to the beam line [164] and a vertex fitting algorithm [165] is performed. The primary vertex is found as the vertex corresponding to the highest sum of squared track transverse momenta and is taken to be the main interaction point. The resolution on the primary vertex is about 14 μm in $r\phi$ and about 19 μm in the z direction for primary vertices with the sum of the track $p_T > 100$ GeV for 2016 data taking.

4.1.5 Calorimeter clusters

The energy and direction of stable neutral particles such as photons and neutral hadron are reconstructed using a cluster algorithm. This algorithm also separates neutral particles from charged hadron energy deposits, and reconstructs and identifies electrons and their bremsstrahlung photons. Furthermore, the cluster algorithm is contributing to the energy measurements of charged hadrons that don't have accurate tracks parameters, e.g. for low quality and high transverse momentum tracks. The clustering is performed separately in each subdetector: ECAL barrel and endcaps, HCAL barrel and endcaps, and the two preshower layers. The HF has no clustering algorithm since the electromagnetic or hadronic components give rise to an HF EM or HF HAD cluster.

The clustering algorithm consist of different steps. First seeds are identified when cells have an energy larger than the seeding threshold and larger than their neighbouring cells. Then topological clusters are made by accumulating cells that share at least a corner with a cell already in the cluster and an energy above a cell threshold set to twice the noise level. The third step is an expectation maximization algorithm that reconstructs the cluster [157] and assumes that the energy deposits are Gaussian distributed. The calorimeter clusters are used for reconstructing photons and neutral hadrons. The clusters that are not in the vicinity of the extrapolated charged tracks are identified as neutral hadrons or photons. If the energy deposits are in vicinity of charged tracks, such is the case for charged hadrons, the neutral particle energy deposit is measured as an excess over the charged particle deposit.

4.2 Particle flow identification

The several PF elements from the various CMS subdetectors are connected through a link algorithm. This algorithm tests any pair of elements in an event, only considering nearest neighbours in the $\eta\phi$ -plane. The quality of the link is determined via the distance between the two elements and PF blocks of elements are formed from elements with a direct link or indirect link through common elements. The identification and reconstruction follows a particular order in each PF block. After each identification and reconstruction the corresponding PF elements (tracks and clusters) are removed from the PF block.

The muons are the first to be identified and reconstructed. These are reconstructed if their momenta are compatible with corresponding track only momenta. Then the electron and its corresponding brehmstrahung photons, are identified and reconstructed by using the GSF tracking. At the same time, the energetic and isolated photons are identified as well. The remaining elements in the PF block are subjected to a cross identification of charged hadrons, neutral hadrons, and photons that arise from parton fragmentation, hadronisation, and decays in jets. The charged hadron candidate is made from the remaining candidates that have a charged particle track associated with them. Then the charged particle energy fraction is subtracted from the calibrated energy of the linked calorimeter clusters and the remaining energy is assigned to the neutral energy. Depending on the excess of neutral energy in the ECAL and HCAL clusters, a photon or a neutral hadron is assigned respectively. The pseudorapidity range of the inner tracker limits the information on the particles charge to $|\eta| < 2.4$. Outside this range a simplified identification is done for hadronic and electromagnetic candidates only.

4.3 Pileup mitigation and luminosity measurement

For the 8 TeV dataset, an average of about 21 pileup interactions happen per bunch cross section. For the dataset taken at 13 TeV, the number of pileup interactions increases to about 27 interactions per bunch crossing. These interactions are spread around the beam axis around the centre of the CMS coordinate system and follow a normal distribution with a standard deviation of about 5 cm [157]. The number of pileup interactions is estimated from the number of interaction vertices reconstructed from charged particle tracks, or from the instantaneous luminosity of the given bunch crossing with dedicated detectors and the inelastic proton-proton crossing. The luminosity of the CMS interaction point is estimated from measuring certain process rates with luminometers such as the pixel detector, HF calorimeter, and the pixel luminosity telescope [166]. The instantaneous luminosity from recorded process rate R is then determined as

$$Ldt = \frac{Rdt}{\sigma_{fid}}, \quad (4.1)$$

where $\sigma_{fid} = \sigma \times A$ corresponds to the fiducial cross section recorded in the luminometer acceptance A which is determined using van der Meer scans [167]. The overall uncertainty on the luminosity measurement is estimated to be 2.5%.

The luminosity is used to infer the number of pileup interactions in data, which can be used to correct the predefined pileup interactions in simulation. Then an event weight can be derived

from the ratio of the distributions of pileup interactions in data and simulation. For 13 TeV collisions, the inelastic cross section is measured to be 71.3 ± 3.5 mb [168]. However a better agreement in data and simulation for the pileup sensitive variables, such as the number of primary vertices, is found with a lower cross section of 69.2 mb with an uncertainty of 4.6%.

4.4 Physics object reconstruction and identification

The particle flow objects are used for building physics objects that are used for analysis. Analyses use jets, muons, electrons, photons, taus and missing transverse momentum \vec{p}_T with extra, analysis dependent requirements. In the following section, only the physics objects used throughout this thesis are discussed.

4.4.1 Muons

The muon candidates used for analysis in this thesis correspond to the tight and loose working point. Detailed reports on the performance can be found in [169].

The tight working point rejects objects wrongly reconstructed as muons from hadron showers that reach the muon system (punch-throughs), by requiring that the global muon fit includes at least one valid hit in the muon chambers for which at least two muon segments in two muon stations are present. Furthermore, the muon tracks should have a global fit yielding a goodness-of-fit of $\chi^2/\text{ndof} < 10$. Requiring at least one pixel hit in the muon track suppresses the decay of muons in flight. Also a minimum of five hits in the tracker is required. Cosmic muons and muons originating from pileup interactions are rejected by constricting the distance of the muon with respect to the primary vertex by putting limits on $d_{x,y} < 2$ mm and $d_z < 5$ mm. Also muons according to the loose muon working point will be used in the thesis. These are either global muons or tracker muons reconstructed from the particle flow muon object. In Table 4.1, the muon requirements for the muons used throughout this thesis are summarised. In Figure 4.2, the muon efficiencies for data and simulation are presented. These efficiencies are estimated from tag-and-probe methods [169]. Overall, the efficiency is about 95-100%, with two drops due to the crack between the wheels of the DT system. The differences between data and simulation are corrected by applying p_T - and η -dependent scale factors ($\epsilon_{\text{data}}/\epsilon_{\text{MC}}$) to simulated events.

In addition to the identification criteria, the muons are required to be spatially isolated from electromagnetic and hadronic activity. The relative lepton isolation is defined as estimating the total transverse energy of the particles emitted around the direction of the lepton by defining a cone of radius ΔR in $\eta\phi$ plane around the lepton direction. Then a summed energy is calculated from the charged hadrons (CH), neutral hadrons (NH), and photons (γ), excluding the lepton itself. This sum is then corrected to remove the energy coming from pileup interactions. The relative isolation for muons \mathcal{I}_{μ} is defined as [157]:

$$\mathcal{I}_{\mu} = \frac{\sum p_T(\text{CH}) + \max(0., \sum E_T(\text{NH}), \sum E_T(\gamma) - 0.5 \times \sum E_T(\text{CH}))}{p_T(\mu)}, \quad (4.2)$$

where a cone of $\Delta R = 0.4$ is adopted and the pileup mitigation is based on the $\Delta\beta$ correction. The $\Delta\beta$ correction estimates the pileup energy as half of the contribution coming from charged

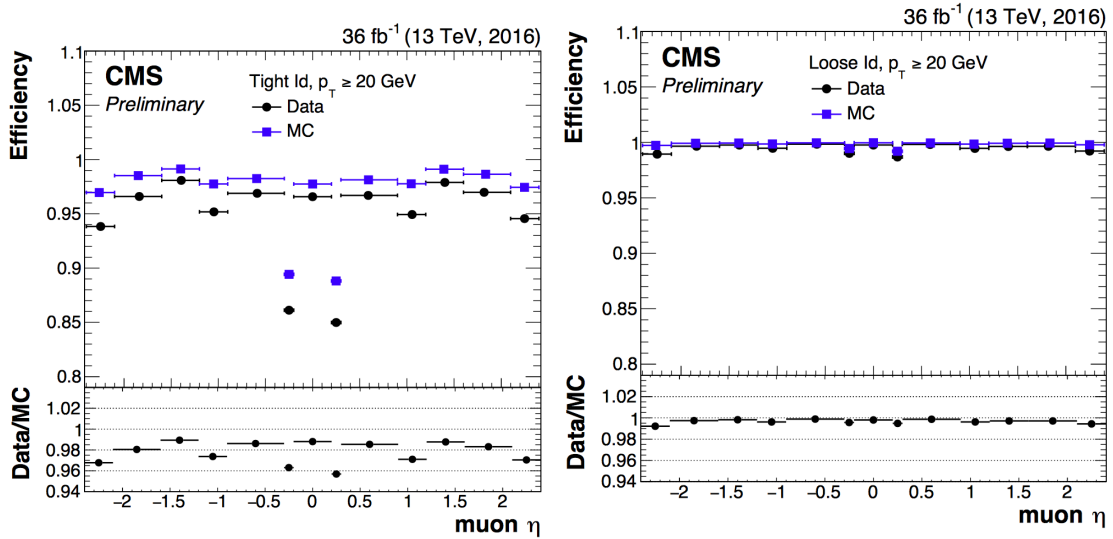


Figure 4.2: Comparison of the muon tight ID (left) and loose ID (right) efficiencies in data and simulation as a function of the pseudorapidity of the muon using the full 2016 dataset. Figure taken from [169].

hadrons. For tight ID muons, this relative isolation should $\mathcal{I}_\mu < 0.15$, while for loose muons this should be $\mathcal{I}_\mu < 0.25$. In Figure 4.3, the isolation efficiencies as a function of the pseudo rapidities using the tag and probe method are shown for the tight muon working point. The efficiencies are 85-100% and have a decline for low- p_T muons. The differences between data and simulation are accounted for by applying η - and p_T -dependent scale factors on the simulation.

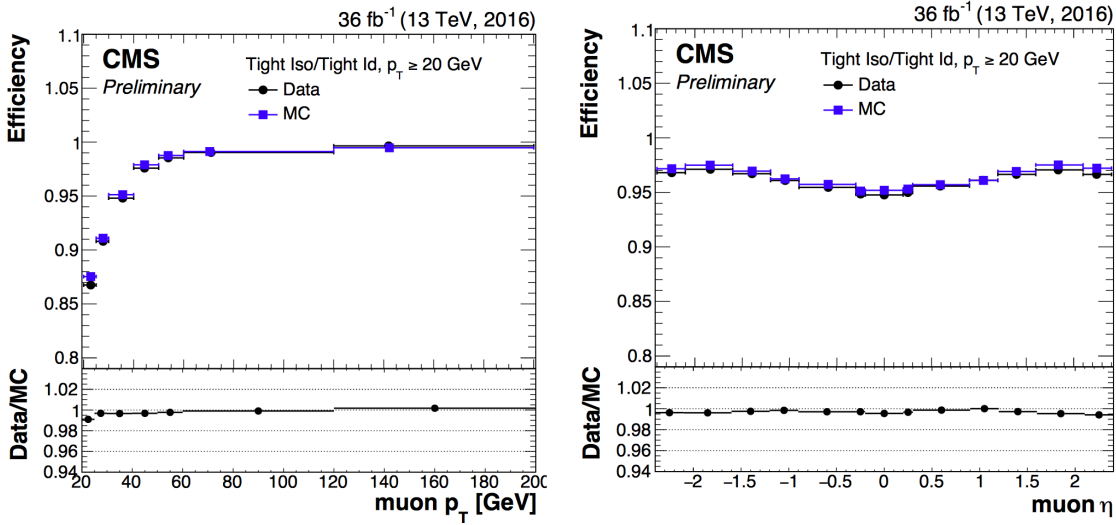


Figure 4.3: Comparison of the muon tight isolation requirement with the muon tight ID efficiencies in data and simulation as a function of the transverse momentum (left) or pseudorapidity (right) of the muon using the full 2016 dataset. Figure taken from [169].

Table 4.1: Muon requirements for the tight and loose working points, used throughout this thesis.

Properties	Loose Muons	Tight Muons
Global muon or Tracker Muon	One or the other	Both
Particle Flow muon	Y	Y
χ^2/ndof of global muon track fit	N/A	< 10
Nb. of hit muon chambers	N/A	> 0
Nb. of muon stations contained in the segment	N/A	> 1
Size of the transverse impact parameter of the track wrt. the PV	N/A	$d_{xy} < 2 \text{ mm}$
Longitudinal distance wrt. the PV	N/A	$d_z < 5 \text{ mm}$
Nb. of pixel hits	N/A	> 0
Nb. of tracker layers with hits	N/A	> 5
Relative Isolation	<0.25	<0.15

4.4.2 Electrons

The electron candidates used, correspond to the tight and veto working points. The study of the electron reconstruction and identification performance can be found in [163].

Starting from an electron PF candidate with a GSF track that is outside the barrel-endcap transition region ($1.4443 < |\eta| < 1.5660$), several requirements are set. The electron track should not have more than one (two or three) missing hit(s) in the innermost layer for the tight (veto) working point. This dismisses electrons from photon conversions. Additionally, a photon conversion veto is applied by testing if a pair of electron tracks is originating from a common displaced vertex. Furthermore, refined cuts are applied on the shower shape variables such as the difference in η or ϕ between the energy weighted supercluster position in the ECAL and the track direction at the innermost tracker position ($\Delta\eta_{\text{in}}$, $\Delta\phi_{\text{in}}$), and the ECAL crystal based shower covariance in the η direction ($\sigma_{\eta\eta}$). These cuts also include energy related variables such as the absolute difference between the inverse electron energy measured in the ECAL and the inverse momentum measured in the tracker ($|1/E - 1/p|$), and the ratio of the energy measured in the HCAL and ECAL (H/E). Unlike the muon case, the identification criteria also contain requirements on the isolation of the electrons.

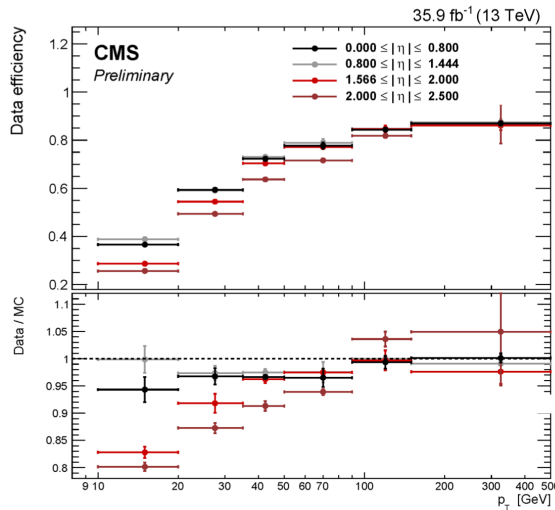
Similar to the muons, the electron relative isolation is determined from the sum of the particles in a cone around the electron itself. The cone radius used for electrons is $\Delta R = 0.3$ and a ρ correction for pileup mitigation is applied. For this correction, the expected pileup energy inside the isolation cone is estimated from the median density energy per area of pileup contamination (ρ), computed event by event, and the effective area ($A_{\text{eff.}}$) [157]. This effective area is estimated from simulation and denotes the expected amount of neutral energy from pileup interactions per ρ within the isolation cone as a function of the pseudo rapidity of the associated ECAL superclusters. Table 4.2 shows the values used for 13 TeV data. The relative electron isolation \mathcal{I}_e is calculated as

$$\mathcal{I}_e = \frac{\sum p_T(\text{CH}) + \max(0., \sum E_T(\text{NH}), \sum E_T(\gamma) - \rho \times A_{\text{eff.}})}{p_T(e)}. \quad (4.3)$$

Table 4.2: The effective areas A_{eff} used for the electron relative isolation [170].

η region	A_{eff}
$0 < \eta < 0.1752$	0.1703
$1.0 < \eta < 0.1479$	0.1715
$1.479 < \eta < 2.0$	0.1213
$2.0 < \eta < 2.2$	0.1230
$2.2 < \eta < 2.3$	0.1635
$2.3 < \eta < 2.4$	0.1937
$2.4 < \eta < 2.5$	0.2393

The efficiency of electron identification is estimated from $Z \rightarrow e^- e^+$ events via the tag-and-probe method and is shown in Figure 4.4 for the tight working point. The efficiencies reach $95 - 100\%$. The difference between data and simulation is corrected for by dedicated p_T - and η dependent scale factors as well.

**Figure 4.4:** Electron identification efficiency as function of the electron transverse momentum from the full 2016 dataset. Figure taken from [163].

4.4.3 Jets

Jets are reconstructed from all reconstructed particles without the charged hadrons associated to pileup vertices. The clustering is done via the anti- k_T algorithm [171] with a radius parameter for the cone size of the resulting jet of $R = 0.4$. More information about the jet algorithm performance can be found in Ref. [172].

The jets used for the analysis in this thesis, are identified according to the loose identification working point summarised in Table 4.4. The requirements on the jet constituents are based

Table 4.3: Electron requirements used in this analysis. The requirements are set in the barrel ($|\eta_{supercluster}| \leq 1.479$) and the endcaps ($|\eta_{supercluster}| > 1.479$).

Properties	$ \eta_{supercluster} \leq 1.479$		$ \eta_{supercluster} > 1.479$	
	Veto electron	Tight electron	Veto electron	Tight electron
$\sigma_{\eta\eta}$	< 0.0115	< 0.00998	< 0.037	< 0.0292
$ \Delta\eta_{in} $	< 0.00749	< 0.00308	< 0.00895	< 0.00605
$ \Delta\phi_{in} $	< 0.228	< 0.0816	< 0.213	< 0.0394
H/E	< 0.356	< 0.0414	< 0.211	< 0.0641
relative isolation	< 0.175	< 0.0588	< 0.159	< 0.0571
$ 1/E - 1/p $	< 0.299 GeV^{-1}	< 0.0129 GeV^{-1}	< 0.15 GeV^{-1}	< 0.0129 GeV^{-1}
expected missing inner hits	≤ 2	≤ 1	≤ 3	≤ 1
pass conversion veto	Y	Y	Y	Y

on the assumption that a proper jet originating from the hadronisation of a quark or gluon consists of multiple PF particles and types. Therefore, the jet should consist of more than one constituent, and the neutral hadron fraction and neutral EM energy fractions should be less than 99%. For the jets within the tracker acceptance ($|\eta| < 2.4$), at least one constituent has to be a charged hadron resulting in a charged hadron energy fraction above 0%. Additionally the charged EM energy fraction should be less than 99%. On top of these requirements, objects that are labelled as jets and found in vicinity of any isolated lepton, $\Delta R < 0.3$, are removed from the jet collection in that event to avoid duplications of objects.

Table 4.4: Jet criteria used throughout the thesis. The last three requirements are only for jets within the tracker acceptance.

Properties	Loose Jet ID
Neutral hadron fraction	< 0.99
Neutral EM fraction	< 0.99
Number of constituents	> 1
Charged hadron fraction	> 0
Charged multiplicity	> 0
Charged EM fraction	< 0.99

The energy of the reconstructed jets deviates from the energies of the corresponding jets clustered from the hadronisation products of true partons from simulations due to non-linear subdetector response and efficiencies. The jet energy corrections (JEC) calibrate the jets in order to have the correct energy scale and resolution. Jet energy scale corrections (JES) are determined as a function of pseudorapidity and the transverse momentum from data and simulated events by combining several channels and methods. This is extensively described in [173]. These corrections account for the effects of pileup, the uniformity of the detector response, and residual data-simulation jet energy scale differences. Furthermore, the jet energy resolution (JER) is measured in data and simulation as function of pileup, jet size and jet flavour. The performance of the jet energy corrections for the 13 TeV dataset can be found in [174].

The JEC are factorised and subsequently correct for the off-set energy due to pileup, the detector response to hadrons, and residual differences between data and simulation as a function of the jet pseudorapidity and transverse momentum. The consecutive steps of JEC are shown in Figure 4.5. The off-set corrections remove the dependency of the jet energy response of

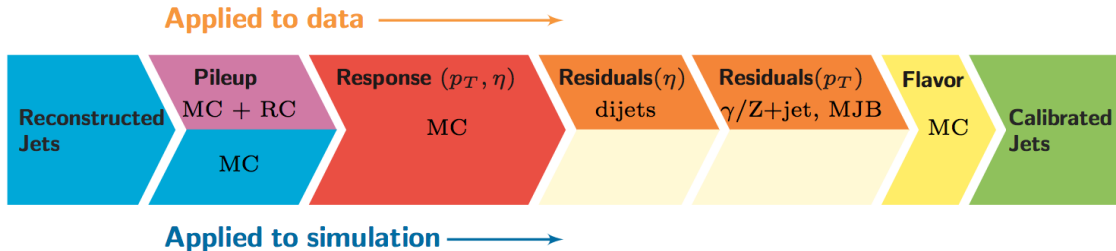


Figure 4.5: The sequence of the JEC for data and simulations. The corrections marked with MC are derived from simulation studies, while RC stands for random cone, and MJB for the analysis of multi-jet events. Figure taken from [173].

additional pileup activity. It is based on the jet area method, which uses the effective area of the jets multiplied by the average density in the event, to calculate the off-set energy to be subtracted of the jets. The correction factors are derived by comparing the jet response with and without pileup events. The residual differences between data and detector simulation are determined using the random cone method (RC). For this method, many jets are reconstructed in each event by clustering particles through placing random cones. This provides a mapping of the $\eta\phi$ -space and the average p_T of those jets gives the average energy off-set due to pileup [173]. The next level of corrections have as goal to have a uniform energy response independent of the transverse momentum or pseudorapidity of the jet. These corrections are determined from simulated events by matching the reconstructed to true particle jets and comparing their momenta. The residual corrections between data and simulation are determined by comparing the transverse momentum balance in various types of events (multi-jet, Z + jets, and γ + jets), using a reference jet in the barrel region. The jet flavour corrections are optional and not used for this thesis. More information on the jet flavour corrections can be found in [173]. For jets with a transverse momentum above 30 GeV, the uncertainties from the various corrections are 3-5% for the 13 TeV dataset [174].

After applying JEC, the transverse momentum resolution of the jet is extracted from data and simulated events. There are two methods used to rescale the reconstructed four momentum based on whether or not the simulated jet can be matched to a true jet in simulation. The factors are defined as

$$c_{\text{matched}} = 1 + \frac{p_T^{\text{reco.}} - p_T^{\text{true}}}{p_T^{\text{reco.}}} (s_{\text{JER}} - 1),$$

$$c_{\text{unmatched}} = 1 + N(0, \sigma_{\text{JER}}) \sqrt{\max(s_{\text{JER}}^2 - 1, 0)}, \quad (4.4)$$

where $N(0, \sigma_{\text{JER}})$ denotes a sample value from a normal distribution centred at zero with standard deviation the relative resolution in simulation σ_{JER} , and s_{JER} the η -dependent resolution scale factors. These scale factors are derived from data from di-jet or $\gamma + \text{jets}$ events

and analysing the p_T balance. The resolution scale factors (data/simulation) are found to be 1.1-1.2, except for the transition regions around $|\eta| = 3$ and $|\eta| = 1.4$ [174] and given in Table 4.5.

Table 4.5: Jet energy scale factors in bins of η with uncertainty

$ \eta $	SF	Uncertainty (\pm)
0-0.5	1.109	0.008
0.5-0.8	1.138	0.013
0.8-1.1	1.114	0.013
1.1-1.3	1.123	0.024
1.3-1.7	1.084	0.011
1.7-1.9	1.082	0.035
1.9-2.1	1.140	0.047
2.1-2.3	1.067	0.053
2.3-2.5	1.177	0.041

4.4.4 Jets from b fragmentation

Jets originating from the hadronisation of bottom quarks can be discriminated from jets from gluons and light-flavour quarks as well as charm quark fragmentation through the use of b-tagging. There are several algorithms developed within CMS to perform b-tagging [175, 176] on jets that fall within the pseudorapidity acceptance of the trackers. These algorithms exploit the properties of the b quark to identify the jets formed by its fragmentation. These hadrons have relative large masses, long lifetimes and daughter particles with hard momentum spectra. Additionally, their semi-leptonic decays can be exploited as well. To use b jet identification in an analysis, one needs to know its efficiency and misidentification probability. In general, these are function of the pseudorapidity and transverse momentum of the considered jet. Their performances are directly measured from data by use of b jet enriched jet samples (multi-jet or top-quark decays).

This thesis uses b jets identified by the Combined Secondary Vertex version 2 (CSVv2) algorithm [175]. This algorithm combines secondary vertices together with track based lifetime information by use of a multivariate technique. The secondary vertex is reconstructed from displaced tracks within a jet, as illustrated in Figure 4.6. The final state b quark is encapsulated in a B meson (e.g. B^\pm , B_0 , B_S) after the hadronisation. This B meson has relatively long lifetime and can travel a measurable distance from the primary vertex before decaying. After reconstruction, the secondary vertices are required to be in accordance with the B meson hypothesis based on the amount of shared tracks with the primary vertex, the invariant vertex mass to reject kaon decays, and the direction of the tracks compared to the jet axis.

The b-tagging algorithm performances are evaluated taking into account two cases: discrimination of b-tagged jets originating from charm quarks, and discrimination of b-tagged jets against jets coming from gluons or light (u, d, s) quarks. In Figure 4.7, the misidentification probabilities for different b-tagging algorithms within CMS are shown. Based on the misidentification probabilities for a certain threshold on the CSVv2 discriminator, different working points

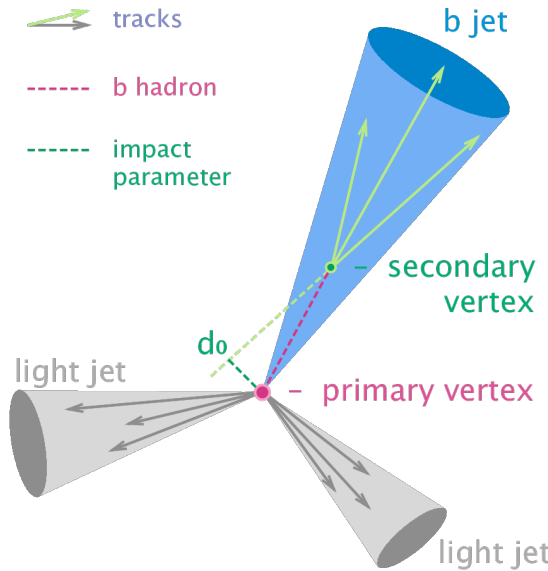


Figure 4.6: Sketch showing the common principle of the identification of b jets. Figure taken from [177].

are defined. These are shown in Table 4.6. The analysis presented in this thesis uses the loose working point which has an average efficiency of 81% and a misidentification rate of 10%.

NOTE: Find reason why I am not using cMVA, omdat CSVv2 op ttbar events is gemeten en cMVA op multijet?

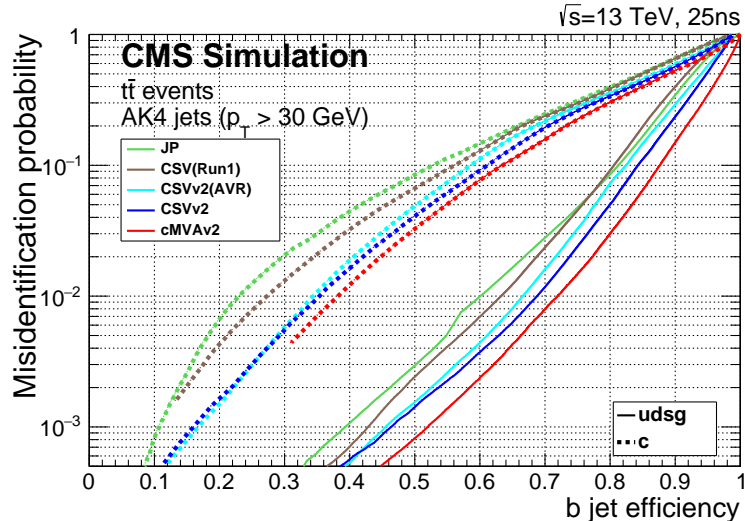


Figure 4.7: Misidentification probabilities of various b-tagging algorithms in simulation. Figure taken from [176].

The efficiency of tagging a jet as coming from a bottom quark in simulation typically deviates somewhat from data. Efficiency scale factors $\epsilon_b^{\text{data}} / \epsilon_b^{\text{MC}}$ are derived from data to account for those differences. These scale factors are η -, p_T -, and flavour dependent, where the flavour of the jet is determined from matched generated hadrons. For cut based analyses these scale

Table 4.6: Working points used for tagging jets as coming from b quarks for the CSVv2 discriminant.

WP	CSVv2 discr cut	b-tag eff.	misid. prob.
Loose (L)	> 0.5426	$\approx 81\%$	$\approx 10\%$
Medium (M)	> 0.8484	$\approx 66\%$	$\approx 1\%$
Tight (T)	> 0.9535	$\approx 46\%$	$\approx 0.1\%$

factors are applied to the b-tagging efficiencies and mistag rates according to the chosen working point [176]. For shape based analysis however, such as the one presented in this thesis, the scale factors are applied on the distribution of the b-tagging discriminator. This is the so-called IterativeFit method [178].

The uncertainties related to the IterativeFit method cover the possible shape discrepancies between data and simulation. There are two uncertainties coming from the purity of the sample based on the purity of the light flavoured (lf) and heavy flavoured (hf) jet contributions in the sample. Furthermore, the jet energy scale results in jets migrating from one p_T bin to another and has an influence on the bin dependent scale factors. Also the statistical fluctuations of the limited amount of entries in each bin are accounted for and have an influence on the scale factor uncertainties. The statistical fluctuations have four uncorrelated sources: two for heavy flavour and two for light flavour jets. The uncertainty on the scale factors for the jets originating from a charm quark (cf) is determined from the uncertainty on the scale factors from a bottom quark, and results in two independent uncertainties [178].

4.4.5 Missing transverse energy

The missing transverse momentum \vec{p}_T and energy E_T^{miss} resulting from particles that do not interact with the detector material, are calculated by balancing the vectorial sum of the transverse momenta of all particles:

$$E_T = |\vec{p}_T|, \quad \vec{p}_T = - \sum_{i=1}^{N_{\text{particles}}} \vec{p}_{T,i}. \quad (4.5)$$

The missing transverse energy is influenced by the minimum thresholds in calorimeters, the inefficiencies in the tracker, and the non-linear response of the calorimeter to hadronic particles. The bias is reduced by correcting the transverse momentum of the jets to particle jet p_T via the JEC and propagating it to the missing transverse momentum. The performance of the missing transverse energy reconstruction can be found in [179].

4.5 Summary of corrections

Throughout the chapter several corrections are introduced to improve the agreement between data and simulation. These corrections are sources of systematic uncertainties for the analysis presented in this thesis. Therefore a summary of the corrections and their associated uncertainties is provided.

Lepton scale factors The systematic uncertainty on the lepton scale factors consists of three sources: identification, isolation and tracking. The applied scale factors are varied independently within one standard deviation of their measured uncertainties to account for their systematic impact on the measurements.

Jet energy corrections The momenta of the reconstructed jets are corrected to match the expected true energy derived from the hadronisation products of partons in simulation. Furthermore, residual corrections and smearing is applied to match the overall energy scale and resolution for simulation and data. These corrections are also propagated to the missing transverse energy. The systematic uncertainties due to these scale factors are estimated by varying them within their uncertainties and repeating the measurements with recalibrated jets and missing transverse energy.

CSVv2 discriminant shape reweighting There are three sources of uncertainty contributing to the measurement of the scale factors: statistical uncertainties, jet energy scale and the purity of the sample. The jet energy scale uncertainty is 100% correlated to the jet energy uncertainties and is evaluated simultaneously. The uncertainty coming from the purity of the sample is subdivided into two uncorrelated uncertainties based on the purity of the light flavoured (lf) and heavy flavoured (hf) jet contributions in the sample. A one sigma shift in each of the two purity contributions corresponds to a higher/lower contribution in the purity of the considered flavours. The statistical uncertainties have four uncorrelated sources, two for heavy flavour and two for light flavour jets. One of the uncertainties correspond to the shift consistent with the statistical uncertainties of the sample, while the other is propagated in a way that the upper and lower ends of the distribution are affected with respect to the centre of the distribution. The uncertainty on the charm jet scale factors (cf) is obtained from the uncertainty on the heavy flavour scale factors, doubling it in size and constructing two nuisance parameters to control the charm flavour scale factors and treating them as independent uncertainties.

Pileup Varying the minimum bias cross section, used to calculate the pileup distribution by $\pm 4.6\%$, results in a systematic shift in the pileup distribution. The uncertainty is estimated by recalculating the pileup weights to the distributions associated to the minimum bias cross sections.

Luminosity The luminosity is measured with a global uncertainty of 2.5%, affecting the expected number of events.

Event selection and categorisation

5

A basic event selection is made for selecting signal like events and is discussed in [Section 5.1](#). Also the effect of the corrections applied to simulation and data, summarised in [Section 4.5](#) is shown. The analysis strategy is presented in [Section 5.2](#), defining the signal and background regions to constrain the huge SM background compared to the expected signal. [Section 5.4](#) discusses each region that is entering the analysis. On top of the use of background estimation from control regions, backgrounds that have prompt leptons contaminated by real leptons either from decays of tau leptons or from hadronized mesons or baryons (collectively commonly referred as “non-prompt leptons”) as well as by hadrons or jets misidentified as leptons are evaluated with a data-driven method discussed in [Section 5.3](#). These two classes of contamination will be referred to as not prompt-lepton (NPL) samples.

5.1 Baseline event selection and filters

In this analysis a search is performed in a final state made up of a Z boson and a top quark, associated or not with a jet, in the leptonic decay of the Z boson and the top quark. The leading order Feynman diagrams can be seen in [Figure 5.1](#) and [Figure 5.2](#). The signal considers both the single top quark FCNC (tZ in the final state) and the top quark pair FCNC (tZq with $q = c, u$ in the final state) events. Their final state signatures consist of three leptons, considering electrons or muons, and a jet originating from a b quark. For FCNC tZq , there is an additional up or charm jet. Leptons from tau decays are not vetoed and are entering the analysis via their leptonic decays. Four different lepton channels based on lepton flavour are considered: 3e, 2e1 μ , 1e2 μ , and 3 μ .

The CMS collaboration recorded in the course of 2016 proton collisions data at a centre-of-mass of 13 TeV with a total recorded integrated luminosity of 35.9 fb^{-1} . The baseline event selection has as goal to substantially reject SM background events, whilst maintaining a high signal efficiency. The CMS trigger system, described in [Section 2.2.3](#), filters out the main of the collision events from uninteresting processes, and dedicated trigger paths are defined to single out the events with our required detector signature. The trigger paths are chosen based on online triggering objects with at least one muon (M), at least one electron (E), at least two muons (MM), at least two electrons (EE), at least one muon and an electron (ME), at least three

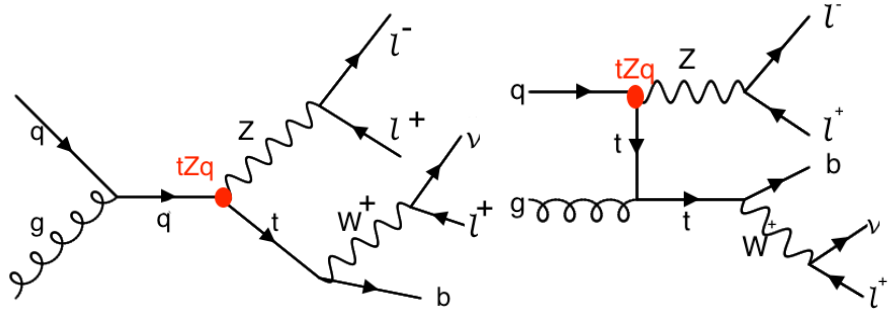


Figure 5.1: Single top quark Feynman diagrams at leading order. The vertex labelled tZq is the sought-for FCNC interaction.

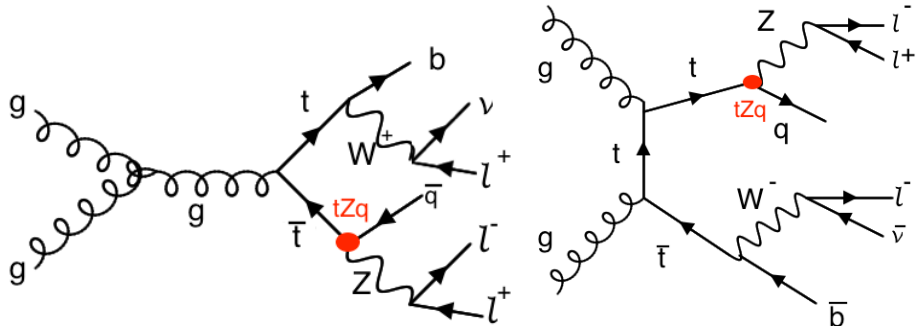


Figure 5.2: Top quark pair Feynman diagram at leading order. The vertex labelled tZq is the sought-for FCNC interaction.

muons (MMM), at least three electrons (EEE), at least two muons and one electron (MME), or at least two electrons and one muon (EEM). For the MC simulation a simple *or* of all triggers is taken and the event is considered when it passes one of the trigger paths. For data however, double counting of the same event has to be taken into account and a procedure to avoid double counting has been put into place. It consists of vetoing in a given dataset the events that are already selected in another, as given in Table 5.1.

Table 5.1: Trigger logic used to select data events in order to avoid double counting.

Dataset	Trigger Logic
1e1μ	$EM \parallel EEM \parallel MME$
2μ	$(MM \parallel MMM) \&\& !(EM \parallel EEM \parallel MME)$
2e	$(EE \parallel EEE) \&\& !(MM \parallel MMM) \&\& !(EM \parallel EEM \parallel MME)$
single μ	$M \&\& !(EE \parallel EEE) \&\& !(MM \parallel MMM) \&\& !(EM \parallel EEM \parallel MME)$
single e	$E \&\& !M \&\& !(EE \parallel EEE) \&\& !(MM \parallel MMM) \&\& !(EM \parallel EEM \parallel MME)$

For the single lepton triggers, at least one electron (muon) with a transverse momentum p_T higher than 32 (24) GeV is required. The dilepton triggers require an electron (muon)

with $p_T > 23$ GeV and a muon (electron) with $p_T > 8$ GeV, or an electron (muon) with $p_T > 23$ (17) GeV and an electron (muon) with $p_T > 12$ (8) GeV. Events collected by the trilepton triggers require an electron (muon) with $p_T > 16$ (12) GeV, a second electron (muon) of $p_T > 12$ (10) GeV, and a third electron (muon) with $p_T > 8$ (5) GeV. The mixed trilepton trigger events require two electrons (muons) with $p_T > 12$ (9) GeV and a third muon (electron) with $p_T > 8$ (9) GeV. The HLT trigger paths used in data and simulation are summarised in [Table 5.2](#).

Table 5.2: HLT trigger paths used to select data and simulation events.

Trigger path name	Trigger type
HLT_Mu23_TrkIsoVVL_Ele8_CaloIdL_TrackIdL_IsoVL_v	ME
HLT_Mu23_TrkIsoVVL_Ele8_CaloIdL_TrackIdL_IsoVL_DZ_v	ME
HLT_Mu8_TrkIsoVVL_Ele23_CaloIdL_TrackIdL_IsoVL_v	ME
HLT_Mu8_TrkIsoVVL_Ele23_CaloIdL_TrackIdL_IsoVL_DZ_v	ME
HLT_DiMu9_Ele9_CaloIdL_TrackIdL_v	MME
HLT_Mu8_DiEle12_CaloIdL_TrackIdL_v	EEM
HLT_IsoMu24_v	M
HLT_IsoTkMu24_v	M
HLT_Ele32_eta2p1_WPTight_Gsf_v	E
HLT_Mu17_TrkIsoVVL_Mu8_TrkIsoVVL_v	MM
HLT_Mu17_TrkIsoVVL_TkMu8_TrkIsoVVL_v	MM
HLT_Mu17_TrkIsoVVL_Mu8_TrkIsoVVL_DZ_v	MM
HLT_Mu17_TrkIsoVVL_TkMu8_TrkIsoVVL_DZ_v	MM
HLT_TripleMu_12_10_5_v	MMM
HLT_Ele23_Ele12_CaloIdL_TrackIdL_IsoVL_DZ_v	EE
HLT_Ele16_Ele12_Ele8_CaloIdL_TrackIdL_v	EEE

In order to ensure a full trigger efficiency, the off-line p_T thresholds are set higher than the online trigger thresholds. Selected electrons (muons) are required to have $p_T > 35$ (30) GeV and $|\eta| < 2.1$ (2.4). The electrons and muons corresponding to a tight working point, as discussed in [Section 4.4.1 \(Table 4.1\)](#) and [Section 4.4.2 \(Table 4.3\)](#), are used for analysis. Only events with exactly three leptons are being considered. Events with extra leptons according to looser working points are vetoed. The trigger efficiency estimation is described in [Section 5.1.2](#) and is approximately 100%. To ensure that all reconstructed particles considered for the analysis are corresponding to a proton interaction and remove signals from beam halo particles as well as detector noise, several filters are used. These are described in [Section 5.1.1](#).

In addition to three leptons, jets and missing transverse energy are expected from the signal signature. The jets are reconstructed using the anti- k_T algorithm with a distance parameter of 0.4, using the particle flow particles that are not identified as isolated leptons as input. The jet momentum is determined as the vectorial sum of the particles contained in the jet. Additional selection criteria are applied to each event to remove spurious jet-like features originating

from isolated noise patterns in certain hadron calorimeter regions. The jet requirements are discussed [Section 4.4.3](#). The jets are calibrated in simulation and in data separately, accounting for deposits from pileup and the non-linear detector response. Calibrated jets with $p_T > 30$ GeV and $|\eta| < 2.4$ are selected for the analysis. A selected jet may still overlap with the selected leptons, leading to a double-counting of reconstructed objects. To prevent such cases, jets that are found within a cone of $R = 0.3$ around any of the signal electrons (muons) are removed from the collection of selected jets. The jets originating from b quarks are tagged using the CSVv2 algorithm, which combines the information of displaced tracks with information of secondary vertices associated with the jet using a multivariate technique. The jets are tagged as a jet coming from a b quark (b-tagged) if the CSVv2 discriminator is above a certain threshold. This analysis uses a threshold that results in an average b-tagging efficiency of 81% and a misidentification rate of 10%. More information about b-tagging can be found in [Section 4.4.4](#).

The missing transverse momentum vector \vec{p}_T^{miss} is defined as the projection on the plane perpendicular to the beams of the negative vector sum of the momenta of all reconstructed particles in an event. Its magnitude is denoted by E_T^{miss} as shown in [Section 4.4.5](#). Its longitudinal component is calculated by limiting the lepton + neutrino to the W boson mass. In case two solutions arise, the mass closest to the known top quark mass is used.

5.1.1 Event cleaning

Some events arising from instrumental noise and beam backgrounds might end up in the data [179, 180]. Spurious deposits may appear in the ECAL from non-collision origins such as beam halo particles, or from particles hitting the sensors in the ECAL photo-detectors. Conjointly, dead ECAL cells can cause artificial missing transverse energy. Also the HCAL can cause spurious energy from particle interactions with the light guides and the photomultiplier tubes of the HF, as well as noisy hybrid photo diodes. In CMS, different algorithms, so-called filters, are developed to identify and suppress these events.

The ECAL electronics noise and spurious signals from particle interactions with photo detectors are mostly removed via topological and timing-based selection using ECAL information only. The remaining effects such as anomalously high energy crystals and the lack of information for channels due to inefficiencies in the read-out are removed through dedicated events filters. Five ECAL endcap supercrystals have been identified for giving anomalously high energies due to high amplitude pulses in several channels at once, and are masked. Furthermore, the crystal read-out from a small amount of ECAL towers is not available. However, their trigger primitive information is still available making it possible to estimate the magnitude of unmeasured energy and when the value is too large, the event is filtered out.

The machine induced particles via beam-gas / beam-pipe/... interactions, that are flying with the beam, affect the physics analysis. They leave a calorimeter deposit along a line at constant ϕ in the calorimeter, and interactions in the CSCs will often line up with this deposit. This can be seen in [Figure 5.3](#). Therefore, events containing such beam halo particles are removed from the selection with the CSC Beam Halo Filter. This filter uses information related to the geometric quantities, energy deposits, and timing signatures. For 2016 proton collision data, the filter rejects 85% in a halo-enriched sample, whereas the mistag probability determined from simulation is found to be less than 0.01%.

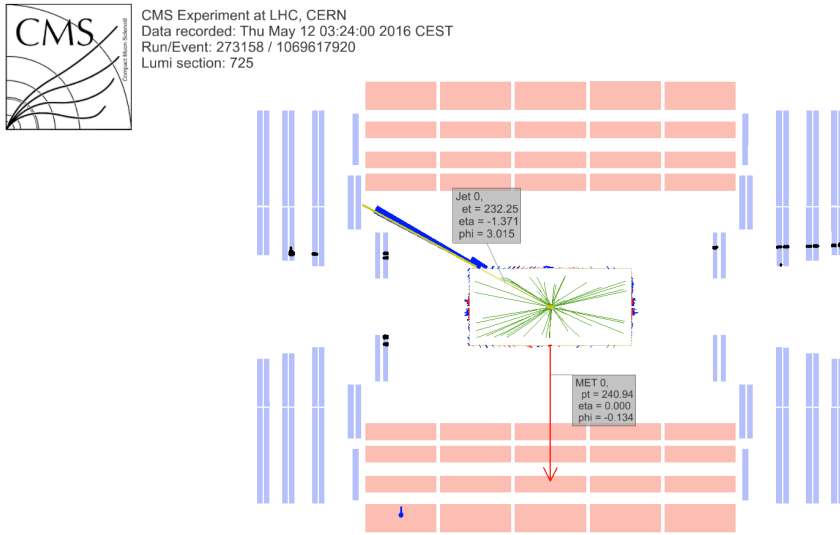


Figure 5.3: Event display of a beam halo event with collinear hits in the CSC (black), missing transverse energy of 250 GeV and a jet of 232 GeV. The hadronic deposit is spread in η , but narrow in ϕ . Figure taken from [179].

Furthermore, there is anomalous high missing transverse energy coming from low quality muons that lead to high- p_T tracks, but are considered not good by the particle flow algorithm. These low quality tracks will be mislabelled as charged hadrons and will therefore be used in the calculation of the missing transverse energy. By investigating the purity of the reconstructed tracks and the relative transverse momentum error of the muons, these events can be filtered out.

Supplementary to previous filters, only events where the first primary vertex is a well reconstructed primary vertex are selected. The reconstructed primary vertex should have at least five degrees of freedom, the longitudinal distance from the beam spot is maximally 24 cm ($d_z < 24$ cm), and the transversal distance from the beam spot is maximally 2 cm ($d_{xy} < 2$ cm).

5.1.2 Estimation of the trigger efficiency

The trigger efficiency in data is estimated using a data sample collected using unprescaled E_T^{miss} triggers. These allow events with a missing transverse energy higher than 110 GeV (120 GeV) and a scalar sum of the transverse momenta of the reconstructed PF jets $H_T^{\text{trig.}}$ of at least 300 GeV (120 GeV), or a calorimeter (PF) E_T^{miss} higher than 200 GeV (300 GeV). For an HB-HE cleaned event, the PF missing transverse energy threshold is lowered to 170 GeV. These trigger paths are summarised in Table 5.3 and chosen to be completely uncorrelated with the lepton triggers given in Table 5.2.

The trigger efficiency is studied on the main background, namely WZ+jets, with all corrections applied. For this study, the events passing a three lepton cut and at least one jet are being used.

Table 5.3: Unprescaled E_T^{miss} HLT trigger paths for estimating the trigger efficiency. An *or* of the triggers is used to select events.

Trigger path	Requirement
HLT_PFHT300_PFMET110_v*	PF $E_T^{\text{miss}} > 110 \text{ GeV}$, PF $H_T^{\text{trig.}} > 300 \text{ GeV}$
HLT_MET200_v*	calorimeter $E_T^{\text{miss}} > 200 \text{ GeV}$
HLT_PFMET300_v*	PF $E_T^{\text{miss}} > 300 \text{ GeV}$
HLT_PFMET120_PFT120_IDTight_v*	PF $E_T^{\text{miss}} > 120 \text{ GeV}$, PF $H_T^{\text{trig.,tightWP}} > 120 \text{ GeV}$
HLT_PFMET170_HBHECleaned_v*	PF $E_T^{\text{miss}} > 170 \text{ GeV}$, cleaned for HB/HE anomalous signals

The corresponding efficiencies are then calculated as

$$\epsilon_{\text{data}} = \frac{\text{Nb. of events passing lepton and MET triggers}}{\text{Nb. of events passing MET triggers}} \quad (5.1)$$

$$\epsilon_{\text{MC}} = \frac{\text{Nb. of events passing lepton triggers}}{\text{Nb. of total events}} \quad (5.2)$$

The resulting efficiencies and scale factors can be found in [Table 5.4](#), where the scale factors are defined as

$$SF = \frac{\epsilon_{\text{data}}}{\epsilon_{\text{MC}}} \quad (5.3)$$

More detailed scale factors and efficiencies can be found in [Appendix A](#).

Table 5.4: Trigger scale factors for each lepton channel, after three lepton plus jets selection, in the Z mass window, by counting the number of events.

all	3 μ	3e	2e1 μ	1e2 μ
1.0000	1.0000	0.9541	1.0006	1.0004

The trigger efficiencies are also measured in function of the p_T of the leptons for which the distributions can be found in [Figure 5.4](#). The trigger efficiencies are measured to be nearly 100% for both simulation and data. The results are dominated by statistics and assigning a large uncertainty to the trigger efficiency based on the dataset collected by E_T^{miss} triggers, would be over conservative. A one percent uncertainty on the trigger selection for the 2e1 μ and 3 μ final states, and 5% for the 3e and 1e2 μ final states is assigned instead. No scale factors will be applied on simulation as they are close to unity. Control plots are made in the dilepton region to validate all corrections applied to simulation.

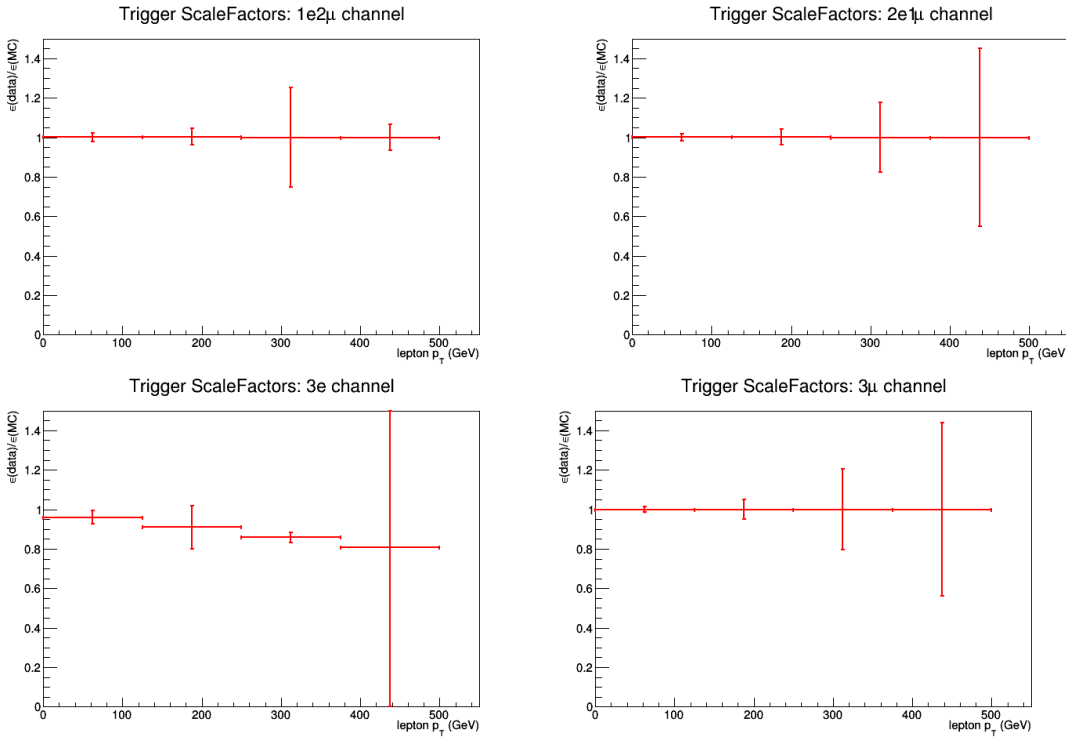


Figure 5.4: The trigger scale factors measured as a function of lepton p_T , using the dataset collected by E_T^{miss} triggers and WZ simulation, after a 3 lepton and jets selection, in the Z mass window. All corrections to simulation are applied. Left, upper: 1e2μ channel. Right, upper: 2e1μ channel. Left, lower: 3e channel. Right, lower: 3μ channel.

5.1.3 Corrections

Mismatches between data and simulation are corrected via the use of scale factors. These are elaborately discussed in [Section 4.4](#). In this section a short overview of the applied corrections is given, and their effect on a dilepton selection is shown.

Pileup reweighting

In data, the number of interactions per bunch crossing (pileup) is calculated with a minimum bias cross section of 69.2 mb. The number of simulated pileup events is then reweighed to match the expected number of pileup events in data. Pileup reweighting manifests itself as an altered shape of the number of reconstructed primary vertices as can be seen in [Figure 5.5](#).

Note that [Figure 5.5](#) indicates that even after pileup reweighting, the primary vertex multiplicity is not well described by simulation. This is a known effect, and using a minimum bias cross section with a slightly lower value is found to better describe the data. However, the b-tagging scale factors are only provided for the nominal inelastic cross section, and thus this value is used.

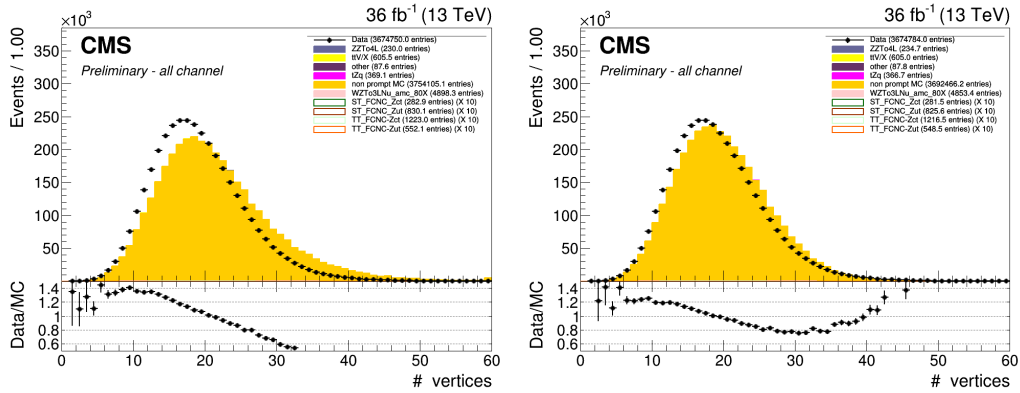


Figure 5.5: The number of primary vertices before (left) and after (right) pileup reweighting. After a dilepton plus jets selection, in the Z mass window.

Lepton scale factors

The efficiency to select leptons is different in simulation (ϵ_{MC}) compared to the data (ϵ_{data}). This is corrected by applying lepton scale factors (SF) to the simulation that are defined as

$$SF = \frac{\epsilon_{\text{data}}}{\epsilon_{\text{MC}}}. \quad (5.4)$$

These scale factors are measured for the identification, isolation, tracking and trigger efficiencies of the objects as a function of p_{T} and η (see [Section 4.4.1](#) and [Section 4.4.2](#)). Multiplying these scale factors for each lepton provides an overall efficiency:

$$SF_{\text{global}}^{\mu} = \prod_{\text{i}}^{\#\mu} SF_{\text{ID}}^{\mu}(p_{\text{T}}, \eta) SF_{\text{Iso.}}^{\mu}(p_{\text{T}}, \eta) SF_{\text{Trig.}}^{\mu}(p_{\text{T}}, \eta) SF_{\text{Track}}^{\mu}(p_{\text{T}}, \eta), \quad (5.5)$$

$$SF_{\text{global}}^e = \prod_{\text{i}}^{\#e} SF_{\text{ID}}^e(p_{\text{T}}, \eta) SF_{\text{Iso.}}^e(p_{\text{T}}, \eta) SF_{\text{Trig.}}^e(p_{\text{T}}, \eta) SF_{\text{Track}}^e(p_{\text{T}}, \eta). \quad (5.6)$$

The effect of the scale factors can be found in [Figure 5.7](#) for the electron scaling and in [Figure 5.6](#) for the muons. The trigger efficiencies are estimated in [Section 5.1.2](#).

Additionally, corrections are made for the energy resolution of the leptons. For the electrons, energy smearing and regression is applied [181]. The energy regression uses the detector information to correct the electron energy in order to have the best energy resolution by correcting local energy containment, material effects, etc.. The energy scale and smearing is done in order to bring the data energy scale to simulation level. It smears the simulation energies to have identical energy resolution in simulation and data. For the muons, the p_{T} is corrected using the Rochester method [182, 183]. This correction removes the bias of the muon p_{T} from any detector misalignment or any possible error of the magnetic field. The effect of the Rochester correction can be found in [Figure 5.8](#).

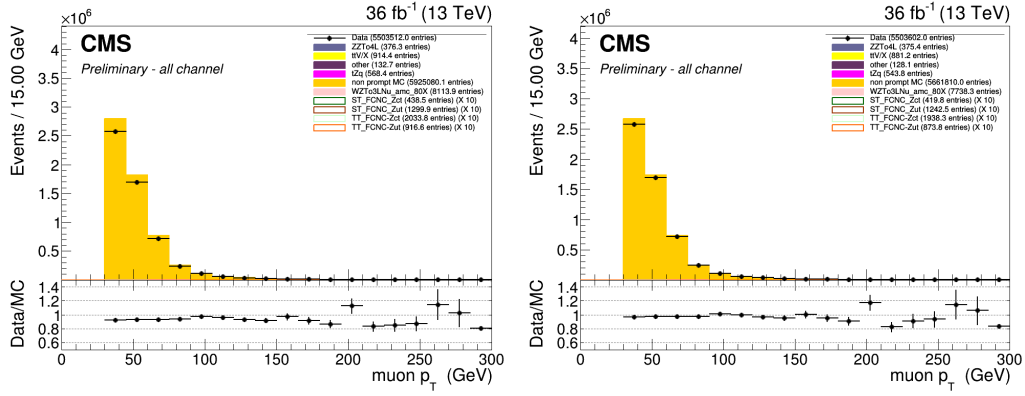


Figure 5.6: The p_T of the muons before (left) and after (right) muon scale factors. After a dilepton plus jets selection, in the Z mass window. Both after the Rochester correction.

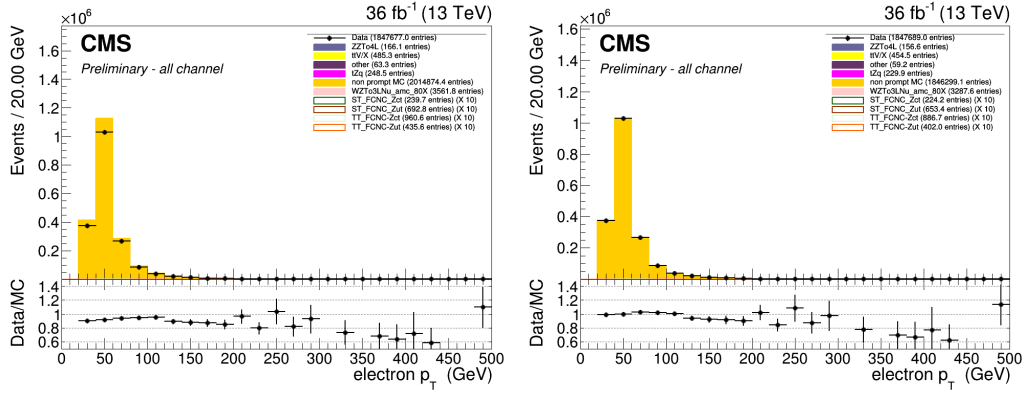


Figure 5.7: The p_T of the electrons before (left) and after (right) electron scale factors. After a dilepton plus jets selection, in the Z mass window. Both after energy scale corrections and smearing.

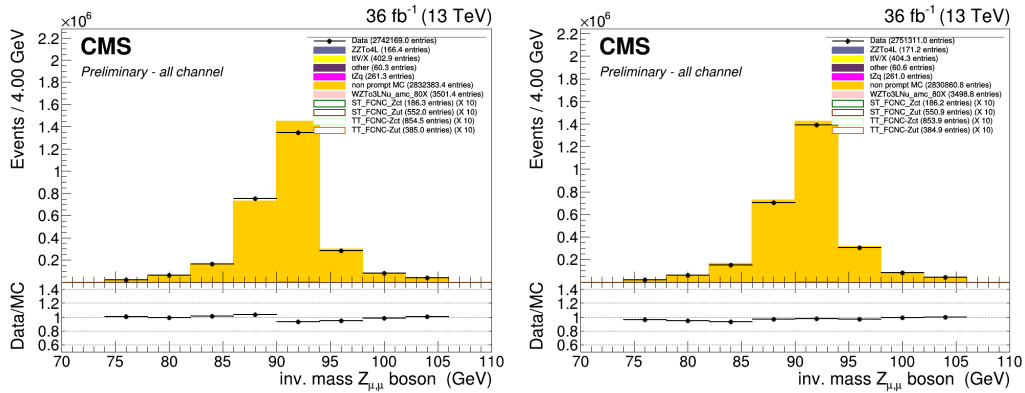


Figure 5.8: The mass of the Z boson consisting of the muons before (left) and after (right) the rochester correction. After a dilepton plus jets selection, in the Z mass window.

CSVv2 shape correction

In order to make the shape of the CSVv2 b-tagging discriminant in simulation agree with data, jet-by-jet based scale factors are applied. These scale factors are a function of the p_T , η and CSVv2 value of the jet as discussed in Section 4.4.4. The effect of these scale factors can be found in Figure 5.9.

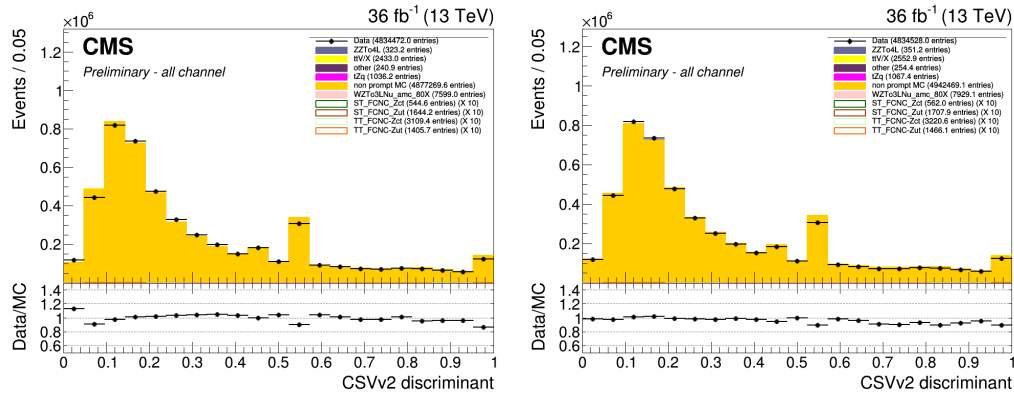


Figure 5.9: The CSVv2 discriminant of the jets before (left) and after (right) b-tag scale factors. After a dilepton plus jets selection, in the Z mass window.

Jet energy

The jet energy in data and simulation is corrected by the measured energy response of the detector. This provides p_T - and η dependent scale factors and are directly taken from the frontier condition database as discussed in Section 4.4.3. The effect of the jet energy corrections can be found in Figure 5.10 and Figure 5.11.

NOTE: Fix
jer plot

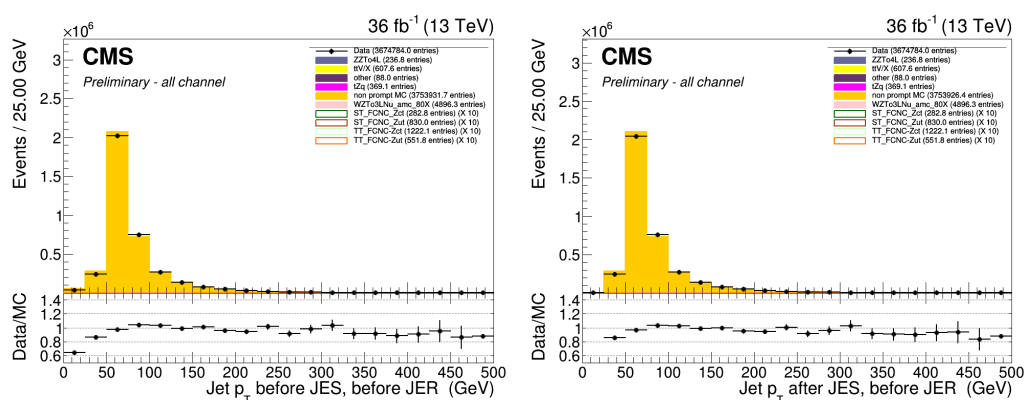


Figure 5.10: The p_T of the jets before (left) and after (right) jet energy scale corrections. After a dilepton plus jets selection, in the Z mass window.

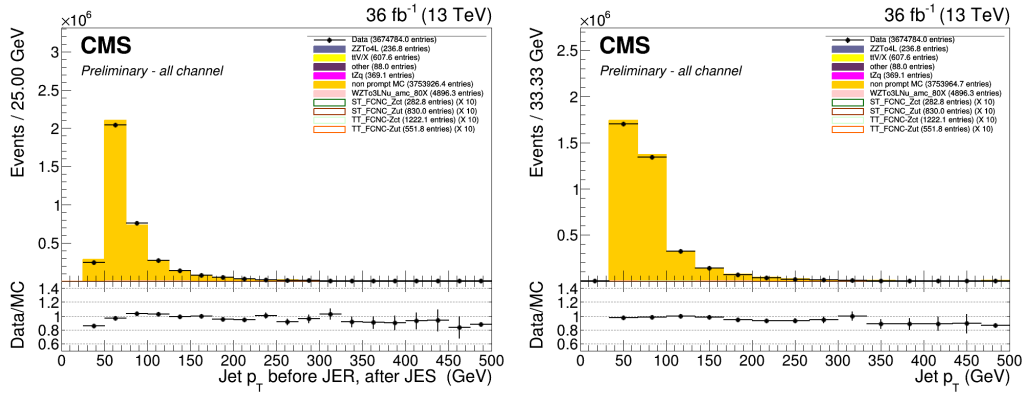


Figure 5.11: The p_T of the jets before (left) and after (right) jet energy resolution smearing. After a dilepton plus jets selection, in the Z mass window.

Missing transverse energy

The energy scale and resolution corrections applied to the jets are propagated back to the missing transverse energy as discussed in Section 4.4.5. This rebalances the transverse net momentum of the event and improves the missing transverse energy resolution itself.

5.1.4 Reconstruction of kinematic variables

The variables used for the training are related to the reconstructed leptons, jets, Z boson and top quark candidates. The Z boson is reconstructed as the sum of the four vectors of the two same flavour leptons of opposite sign giving the closest value to the Z mass. The third remaining lepton is assigned as the lepton coming from the W boson decay. The reconstruction of the SM top quark candidate is more difficult and done by summing the third lepton, the SM b jet and the neutrino (E_T^{miss}). The SM b jet is assigned to the jet with the highest CSVv2 discriminant. The longitudinal momentum of the neutrino is calculated by putting a constraint on the lepton + neutrino system with the W mass. In case two solutions are found for the p_z^{ν} component, the one that gives the reconstructed mass (lepton + neutrino + b jet) to the known top quark mass, is used. The FCNC top quark is reconstructed by summing the reconstructed Z boson and the jet giving the mass closest to the top mass, from the jet collection from which the SM b jet is removed.

The reconstructed objects are validated using simulation by matching the reconstructed objects to their generated counterpart by minimizing ΔR . The efficiencies derived from the simulated signal samples and the SM tZq background process can be found in Table 5.5 and Table 5.6.

Table 5.5: Efficiencies of assigning the correct leptons in the analysis.

	FCNC tZq	FCNC tZ	SM tZq
W lepton	99%	98%	97%
leptons from the Z boson	99%	98%	97%
all leptons in the decay	99%	98%	97%

Table 5.6: Efficiencies of assigning the correct jets in the analysis.

	FCNC tZq	FCNC tZ	SM tZq
SM b jet	99%	98%	80%
c jet	71%	N/A	50%
u jet	83%	N/A	54%

5.2 Analysis Strategy

The analysis strategy uses five statistically independent regions to extract limits, using a likelihood fit of various observables. Two signal regions, the tZ (STS)R and tZq (TTS)R signal regions, are constructed using the jet multiplicity, focussed on each signal signature (see [Table 5.9](#)). In order to constrain the rate of WZ+jet events as well as that of NPL backgrounds, three control regions are defined. The WZ control region (WZCR) focusses on NPLs originating from Z/γ^* + jets and simultaneously constrains the WZ+jets background rate. The NPL backgrounds coming from a $t\bar{t}$ process are constrained by two control regions, TTCR and STCR, one for each signal region (TTSR and STSR). In the STSR and TTSR, multivariate discriminants based on Boosted Decision Trees (BDT) (see [Section 3.3](#)) are used to respectively discriminate FCNC tZ and FCNC tZq from backgrounds. In the WZCR, a discriminating variable between the two backgrounds, WZ+jets and NPLs, is used. In TTCR and STCR, the dominating process is the $t\bar{t}$ process, and its rate is estimated by subtracting all other background predictions from data. A simultaneous global fit using the Higgs Combined Tool ([Section 3.4](#)) is performed taking into account each region (STS, TTS, WZCR, TTCR and STCR) for the four different lepton channels.

5.3 Data driven NPL background simulation

One of the most important backgrounds consists of events with not prompt leptons. These are mostly instrumental backgrounds and are therefore very difficult to model. The NPL background is estimated from data for both its shape and its normalisation.

The NPL background originates from hadronic objects wrongly reconstructed as leptons, real leptons coming from the semi-leptonic decay of a b or c hadron, or real leptons coming from the conversion of photons that pass the identification and isolation requirements. The dominant source of these NPLs depends on the flavour of the leptons and therefore the events with a not prompt muon (NP μ) are treated differently than those with a not prompt electron (NPe). For muons, the dominant source is the semi-leptonic decay of heavy flavour hadrons, while for electrons, the dominant sources are hadrons and photon conversions.

The backgrounds causing NPL contributions are mostly $Z/\gamma^* + \text{jets}$ (Drell–Yan) and $t\bar{t} + \text{jets}$ dilepton processes, and in a smaller amount WW processes. All of these backgrounds contain two real leptons and one NPL. Due to the fact that the probability for a lepton to be a NPL is small, backgrounds containing two or more NPL are neglected in this search. The assumption is made that for $Z/\gamma^* + \text{jets}$ the two leptons compatible with a Z boson decay are the real leptons, and the additional lepton is coming from a NPL source, while for $t\bar{t} + \text{jets}$ the NPL is associated to the Z boson. This assumption has been validated using a Monte Carlo simulation.

The NPL sample is constructed from data by requiring exactly three leptons, from which two are considered real isolated leptons and the third lepton is identified as a NPL. This NPL is created by loosening its identification and inverting its isolation criteria. The full requirements on the not prompt leptons are given in [Table 5.7](#) and [Table 5.8](#). For NPes, a large fraction is coming from misidentified photons. These are removed by applying a tighter cut on the $1/E - 1/p$ variable, and by limiting the isolation values to be smaller than one.

Table 5.7: Non prompt electron requirements used in this analysis. The requirements are set in the barrel ($|\eta_{\text{supercluster}}| \leq 1.479$) and the end caps ($|\eta_{\text{supercluster}}| > 1.479$).

Properties	$ \eta_{\text{supercluster}} \leq 1.479$	$ \eta_{\text{supercluster}} > 1.479$
$\sigma_{\eta\eta}$	< 0.011	< 0.0314
$ \Delta\eta_{\text{in}} $	< 0.00477	< 0.00868
$ \Delta\phi_{\text{in}} $	< 0.222	< 0.212
H/E	< 0.298	< 0.101
relative isolation	$\geq 0.0588 \& < 1$	$\geq 0.0571 \& < 1$
$ 1/E - 1/p $	$< 0.0129 \text{ GeV}^{-1}$	$< 0.0129 \text{ GeV}^{-1}$
expected missing inner hits	≤ 1	≤ 1
pass conversion veto	Y	Y
p_T	$> 35 \text{ GeV}$	$> 35 \text{ GeV}$

Table 5.8: Non prompt muon requirements used in the analysis.

Properties	modified Loose Muon WP
Global muon or Tracker Muon	Both
Particle Flow muon	Y
χ^2/ndof of global muon track fit	N/A
Nb. of hit muon chambers	N/A
Nb. of muon stations contained in the segment	N/A
Size of the transverse impact parameter of the track wrt. PV	N/A
Longitudinal distance wrt. PV	N/A
Nb. of pixel hits	N/A
Nb. of tracker layers with hits	N/A
Relative Isolation	≥ 0.15
p_T	$> 30 \text{ GeV}$

5.4 Statistical independent regions

The regions are defined as in [Table 5.9](#) after a common selection of exactly three leptons containing one opposite sign same flavour pair that is assigned to the Z boson, at least one jet and at the most three jets, and the transverse mass of the W boson to be maximal 300 GeV. The transverse mass $m_T(W)$ is reconstructed using

$$m_T(W) = \sqrt{(p_T(l_W) + p_T(v_W))^2 - (p_x(l_W) + p_x(v_W))^2 - (p_y(l_W) + p_y(v_W))^2}. \quad (5.7)$$

Table 5.9: The statistically independent regions used in the analysis.

	WZCR	STSR	TTSR	STCR	TTCR
Number of jets	≥ 1	1	≥ 2	1	≥ 2
Number of b jets	0	1	≥ 1	1	≥ 1
$ m_Z^{\text{reco}} - m_Z < 7.5 \text{ GeV}$	Yes	Yes	Yes	No	No
$ m_Z^{\text{reco}} - m_Z < 30 \text{ GeV}$	Yes	Yes	Yes	Yes	Yes
Number of leptons	3	3	3	3	3

Additional leptons with a looser identification are vetoed in order to reduce the contamination of backgrounds with four or more leptons in the final state, e.g. ZZ, t̄Z, and t̄tH. The most important backgrounds are the ones that contain three prompt leptons in the final state. These are mainly WZ+jets, t̄Z and SM tZq. For these backgrounds, the three lepton topology is identical to the FCNC signal: two opposite sign leptons of the same flavour decaying from the Z boson, and a third additional, high p_T lepton coming from the W boson decay.

For the FCNC tZ final state, one b jet coming from the SM top decay is expected. For the FCNC tZq, an additional light jet is expected. In the t̄Z final state, two b jets are present in the final state. However, due to inefficiencies of the b-tagging algorithm, one of the two b jets may be identified as a light quark jet, giving the same final state as the FCNC tZq final state. For the WZ+jets final states, one of the b jets produced by gluon splitting, can be b-tagged or light flavour jets coming from the WZ+jets production can be mis-tagged as b jets. The SM tZq final state expects the same signal as FCNC tZq.

The NPL events give a significant background contribution. This background is mainly coming from $Z/\gamma^* + \text{jets}$ and $t\bar{t} + \text{jets}$ processes (in a less significant way, also WW contributes), which have very high cross sections and cause a large number of NPL background events compared to the signal.

In order to reduce the large uncertainties in backgrounds, five independent regions are used as defined in [Table 5.9](#). In [Figure 5.12](#), the strategy and usage of each region is illustrated.

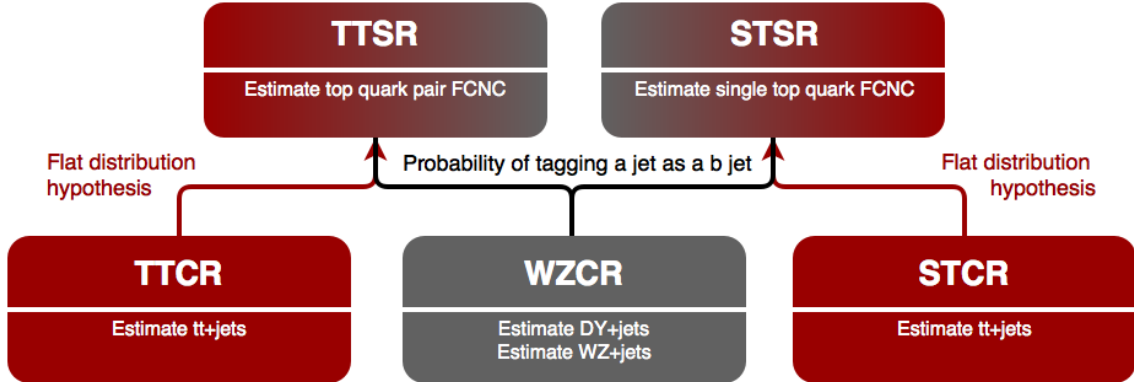


Figure 5.12: The strategy used for this search. The WZCR region is used to estimate the WZ+jets background process as well as the NPL background coming from the $Z/\gamma^* + \text{jets}$ process. The TTCR and STCR regions are used to estimate the contributions of the NPL background coming from the $t\bar{t} + \text{jets}$ process.

5.4.1 WZCR

The WZCR is constructed by vetoing events with jets tagged as being a b jet, making it statistically independent from the signal regions where at least one b-tagged jet is required. In this region, a fit is performed on the transverse mass of the W boson, in order to estimate the NPL yield coming from $Z/\gamma^* + \text{jets}$ and the WZ+jets backgrounds.

A transfer factor is used to account for going from a region without b-tagged jets to a region with exactly, or at least, one b-tagged jet. For this, the probability of tagging at least one jet with the CSVv2 algorithm at the loose working point is used to calculate the expected number of events, N_b , after b-tagging:

$$N_b = \frac{\sum_{\text{events}} \mathcal{P}_b}{\text{total nb of events}}, \quad (5.8)$$

where \mathcal{P}_b is the probability that an event survives the b-tagging requirement,

$$\begin{aligned} \mathcal{P}_b &= 1 - P(\text{event doesn't survive b tag}), \\ &= 1 - \left(\prod_b P(\text{b not b-tagged}) \prod_c P(\text{c not b-tagged}) \prod_{\text{uds}} P(\text{light not b-tagged}) \right), \end{aligned} \quad (5.9)$$

with the products going over all b-, c-, and light jets. The jet flavour is determined by means of matching the reconstructed jet to the generated quarks, based on the distance in the $\eta\phi$ plane. In order to estimate the probability for exactly one b-tagged jet, the expected number of events is corrected by the fraction of events with exactly one jet in the WZCR. The resulting transfer factors are given in [Appendix B](#). The yield of WZ+jets events in the signal region estimated using the above described transfer factor, and the yield calculated with simulated events, are in agreement.

5.4.2 TTCR and STCR

The TTCR and STCR are constructed with the same selection criteria as TTSR and STSR, but are outside the Z mass window (sidebands):

$$7.5 \text{ GeV} < |m_Z^{\text{reco}} - m_Z| < 30 \text{ GeV}, \quad (5.10)$$

where m_Z^{reco} is the reconstructed mass of the Z boson in the event, and m_Z the mass of the Z boson. These regions are dominated by $t\bar{t}$ +jets (see Appendix B) and are used to estimate the NPL coming from $t\bar{t}$ +jets in the STSR and TTSR. Since there aren't enough events entering these regions, no shapes are used in the fit. The distribution of the mass of the Z boson is flat for $t\bar{t}$ +jets events, as shown in Figure 5.13, and thus the number of expected events, N_s , in the signal regions estimated from the number of expected events, N_c , in the control region is obtained as

$$N_s = \frac{15}{60 - 15} N_c. \quad (5.11)$$

The resulting transfer factors are given in Appendix B. The expected yield in the signal region estimated from the TTCR (STCR) is in agreement with the yield calculated from simulated events.

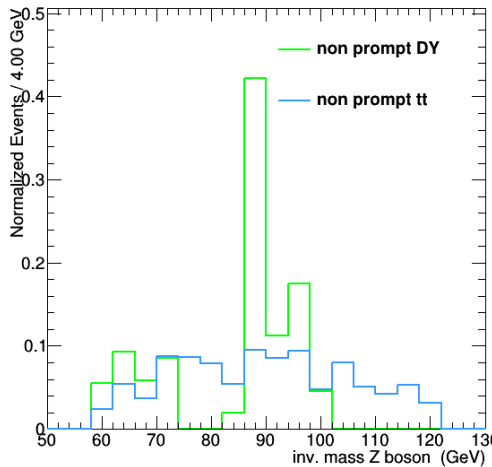


Figure 5.13: The normalized distribution for $Z/\gamma^* + \text{jets}$ and $t\bar{t} + \text{jets}$ events before dividing the events in to regions, after $|m_Z^{\text{reco}} - m_Z| < 30 \text{ GeV}$. All lepton channels combined.

5.4.3 TTSR and STSR

The TTSR is defined to target top quark pair FCNC (tZq), while the STSR focusses on single top quark FCNC (tZ). They have NPL contributions coming from $Z/\gamma^* + \text{jets}$ and $t\bar{t} + \text{jets}$ events. In this region, the data driven NPL template is split into two templates, based on the presence of the NPL in the Z boson. The NPL associated with W boson is assigned to $Z/\gamma^* + \text{jets}$ and estimated in the WZCR, while the NPL associated with Z boson is assigned to $t\bar{t} + \text{jets}$ and estimated in the TTCR and STCR.

The search for FCNC involving a top quark and a Z boson

6

6.1 Construction of template distributions

There were no selection criteria found to make a clear rejection of the background events without sacrificing a significant amount of signal. For this reason, a multivariate approach using Boosted Decision Trees that combines several discriminating variables in the TMVA framework is used. For the training, the BDTs are trained against all backgrounds, where the NPL background is not taken into account. The BDT settings avoid over-training and maintain a good discriminating power against all backgrounds. The background and signal yields follow the relative fractions predicted by the simulation.

The prefit distributions of the variables used for creating the multivariate discriminator are given in [Section 6.1.1](#). The resulting multivariate discriminator are shown in [Section 6.1.2](#). The technical details of the BDTs can be found in [Appendix C](#).

6.1.1 Distributions of the BDT variables

The variables used to construct the BDTs include the angles, distances, masses and transverse momenta:

1. pseudo rapidity of the SM top: TTSR + STSR tZu, STSR tZc
2. invariant mass of the W lepton and the SM b jet: TTSR + STSR tZu, TTSR + STSR tZc
3. $\Delta\Phi$ between the W lepton and the SM b jet: TTSR + STSR tZu, STSR tZc
4. minimal ΔR between the W lepton and jets: TTSR tZu
5. invariant mass of the Z boson: TTSR tZu, TTSR tZc
6. $\Delta\Phi$ between the W lepton and the Z boson: TTSR + STSR tZu, TTSR tZc
7. ΔR between the W lepton and the SM b jet: TTSR + STSR tZu, TTSR tZc

8. number of CSVv2 medium WP b jets: TTSR tZu, TTSR tZc
9. invariant mass of the FCNC top: TTSR tZu, TTSR tZc
10. ΔR between the Z boson and the FCNC light jet: TTSR tZu, TTSR tZc
11. ΔR between the FCNC light jet and the SM b jet: TTSR tZu, TTSR tZc
12. charge of the W lepton times the absolute pseudo rapidity of the W lepton: STSR tZu
13. CSVv2 discriminant of the highest p_T jet: STSR tZu, STSR tZc
14. total Ht of the leptons: STSR tZu
15. the p_T of the W lepton times its charge: STSR tZu
16. total invariant mass of the leptons: STSR tZc
17. ΔR between the W lepton and Z boson: TTSR +STSR tZc
18. total invariant mass of the event: TTSR tZc
19. CSVv2 discriminant of the FCNC light jet: TTSR tZc
20. ΔR between the SM b jet and Z boson: TTSR tZc

The normalised distributions of the BDT input variables for the tZu vertex in the TTSR and STSR are shown without the contribution of the NPL background. The distributions for the tZc vertex distributions can be found in [Appendix D.1](#).

NOTE:
Beschrijf
plotjes

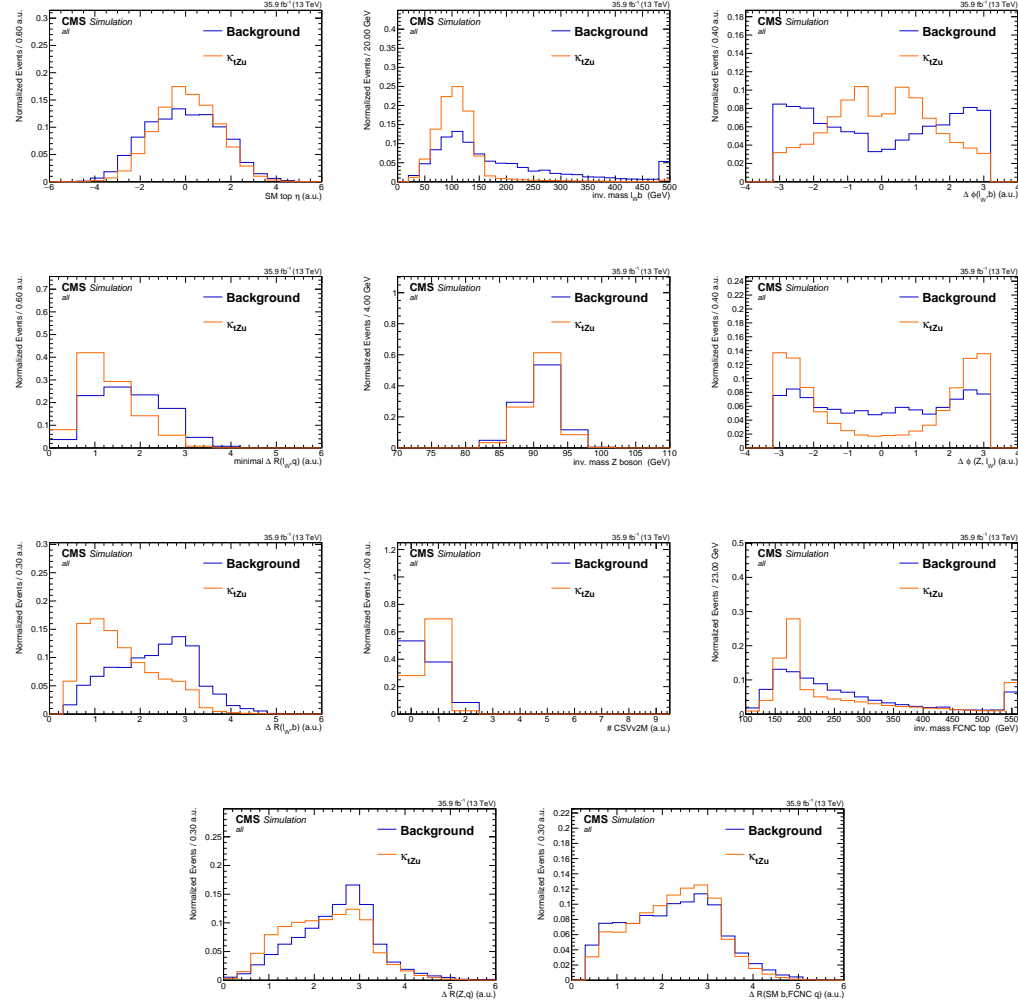


Figure 6.1: The normalised input variables for reconstructing the multivariate discriminator in the TTSR for the tZu vertex.

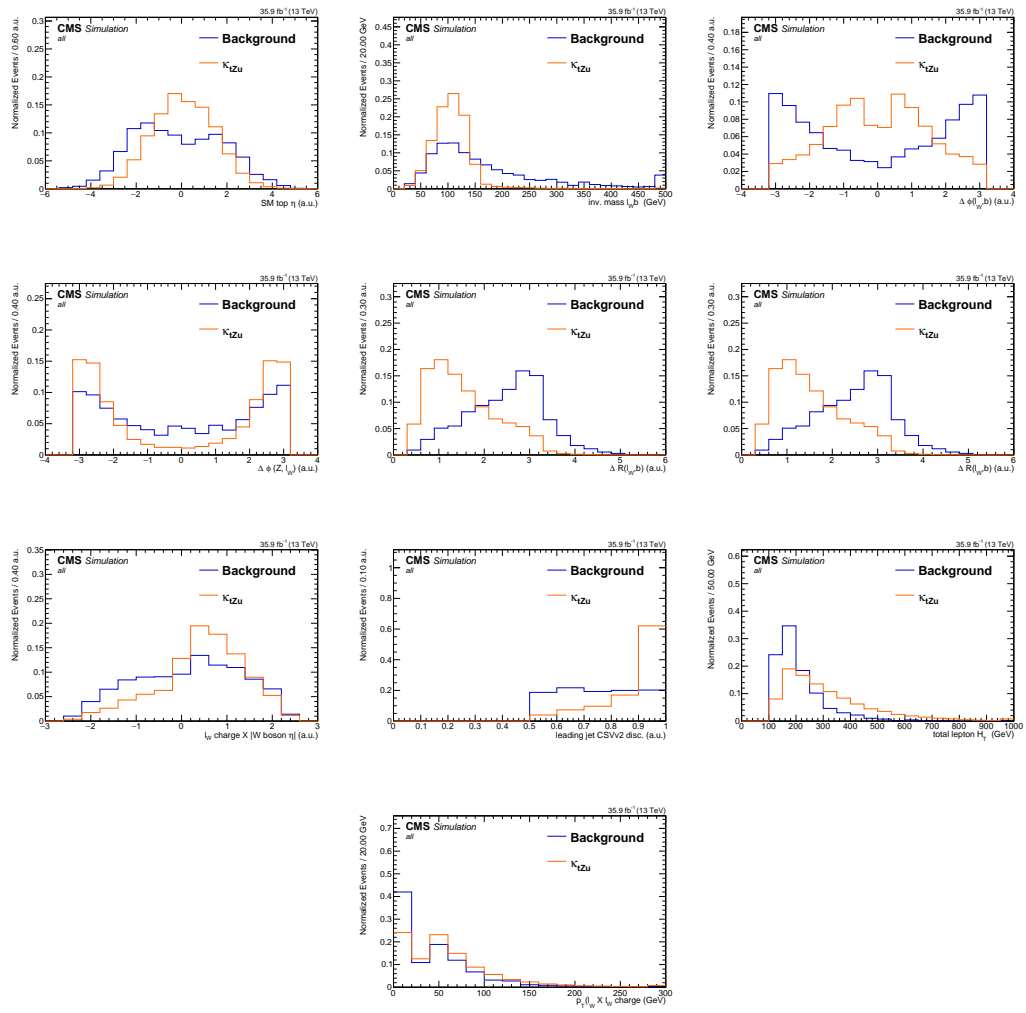


Figure 6.2: The normalised input variables for reconstructing the multivariate discriminator in the STSR for the $t\bar{Z}u$ vertex.

6.1.2 BDTs

The normalised distributions of the multivariate discriminator, including the NPL background are shown in this section.

NOTE:
Beschrijf
plotjes

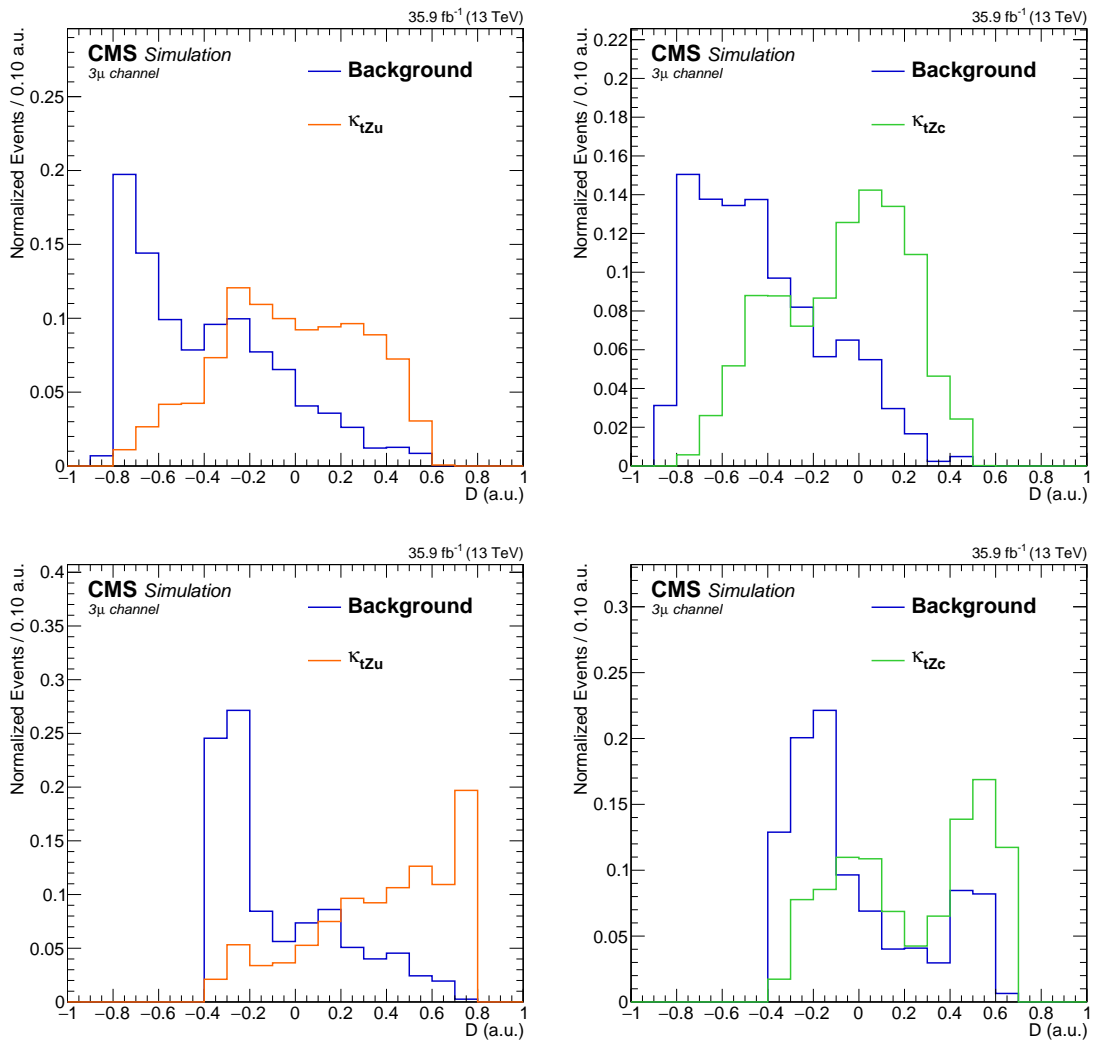


Figure 6.3: Normalised distributions of the discriminating variable before the fit, 3μ lepton channel.
Upper left: TTSR tZu , upper right: TTSR tZc ; lower left: STSR tZu , lower right: STSR tZc .

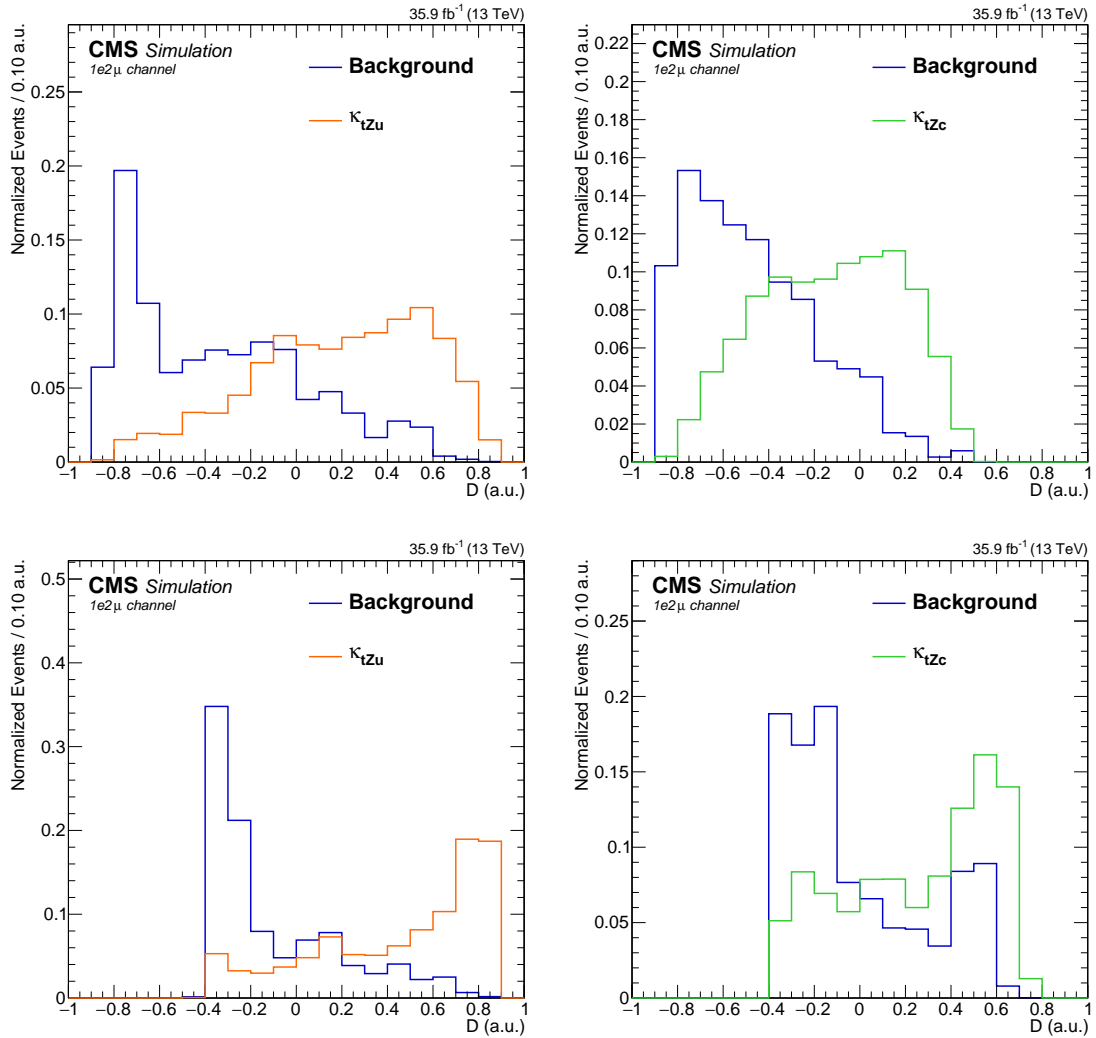


Figure 6.4: Normalised distributions of the discriminating variable before the fit, $1e2\mu$ lepton channels.
Upper left: TTSR tZu, upper right: TTSR tZc; lower left: STSR tZu, lower right: STSR tZc.

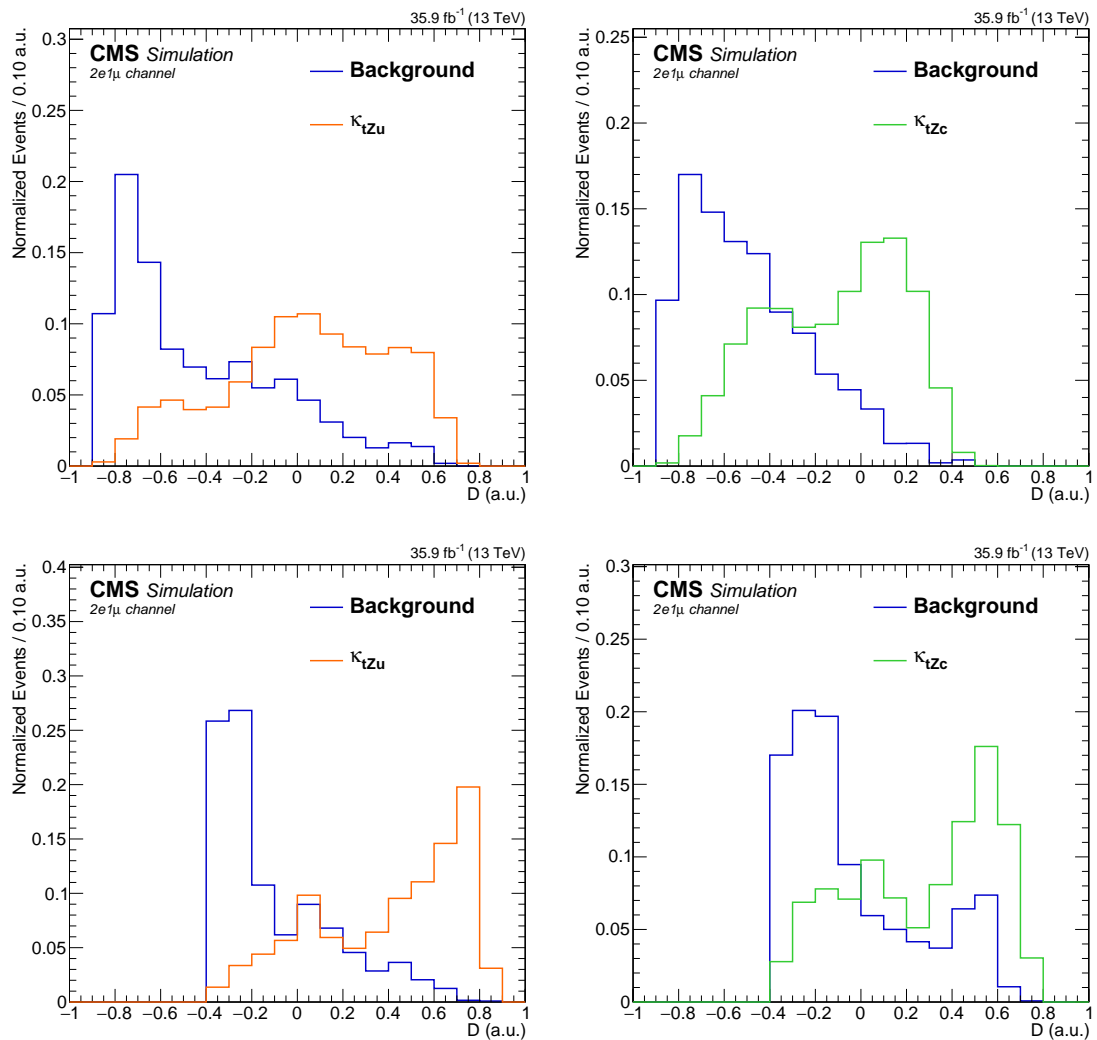


Figure 6.5: Normalised distributions of the discriminating variable before the fit, 2e1 μ lepton channel.
Upper left: TTSR tZu, upper right: TTSR tZc; lower left: STSR tZu, lower right: STSR tZc.

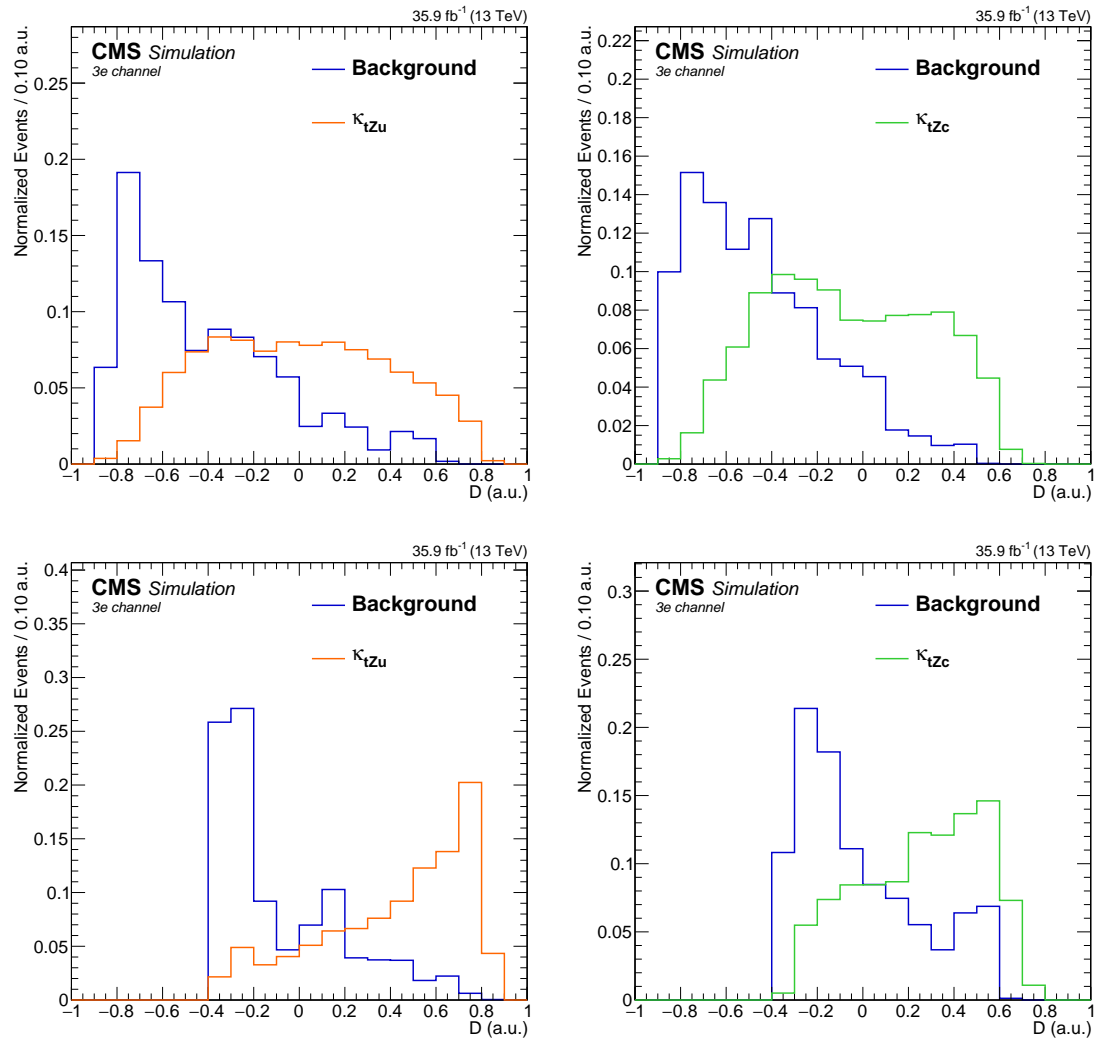


Figure 6.6: Normalised distributions of the discriminating variable before the fit, 3e lepton channel. Upper left: TTSR tZu , upper right: TTSR tZc ; lower left: STSR tZu , lower right: STSR tZc .

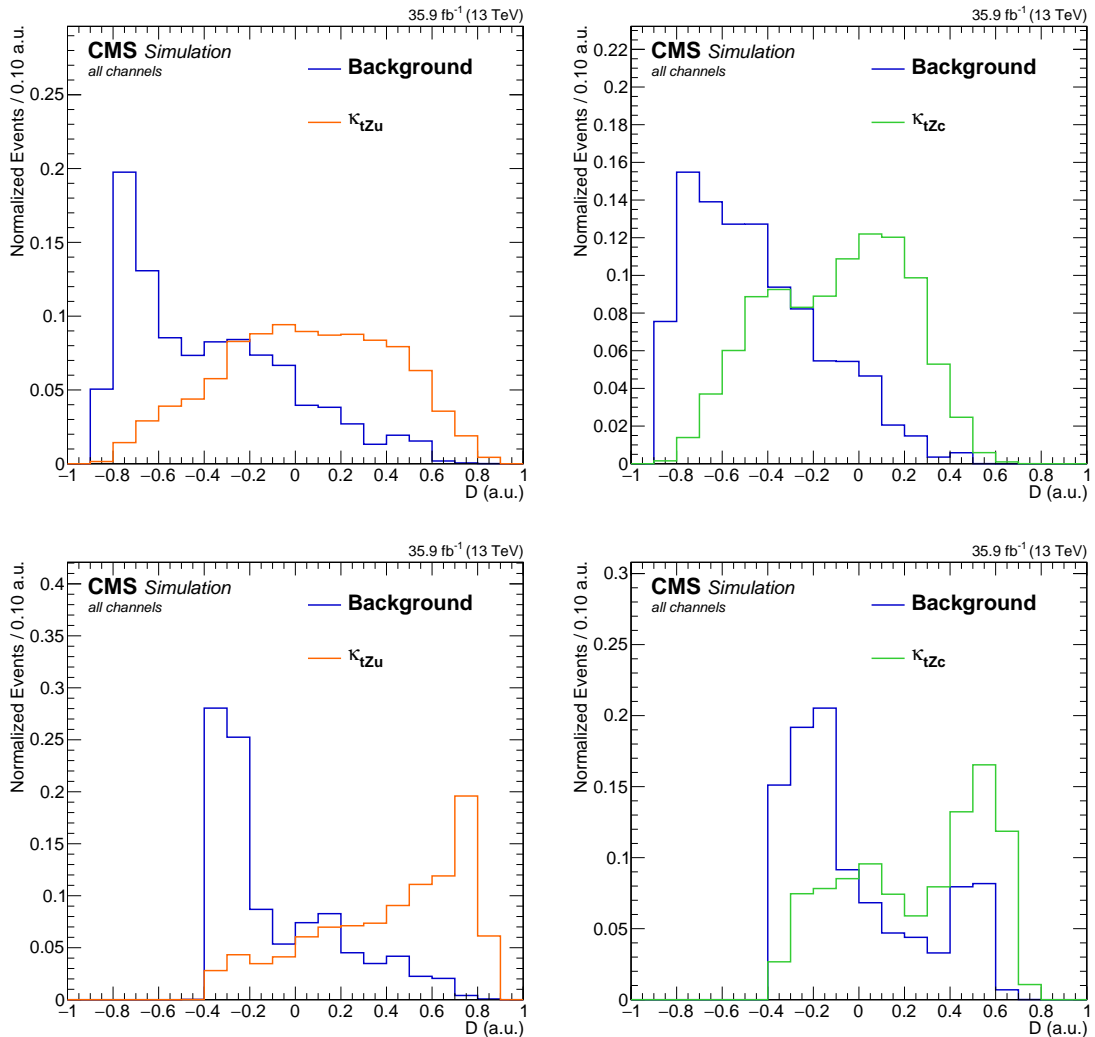


Figure 6.7: Normalised distributions of the discriminating variable before the fit, all different lepton channels together. Upper left: TTSR tZu, upper right: TTSR tZc; lower left: STSR tZu, lower right: STSR tZc.

6.1.3 Transverse mass in WZCR

The WZCR is used to estimate the contribution from $WZ + \text{jets}$ and NPL background. In this region, a fit is performed on the transverse mass distribution of the W boson. The prefit normalised templates are given in this section.

NOTE:
beschrijf
plotjes

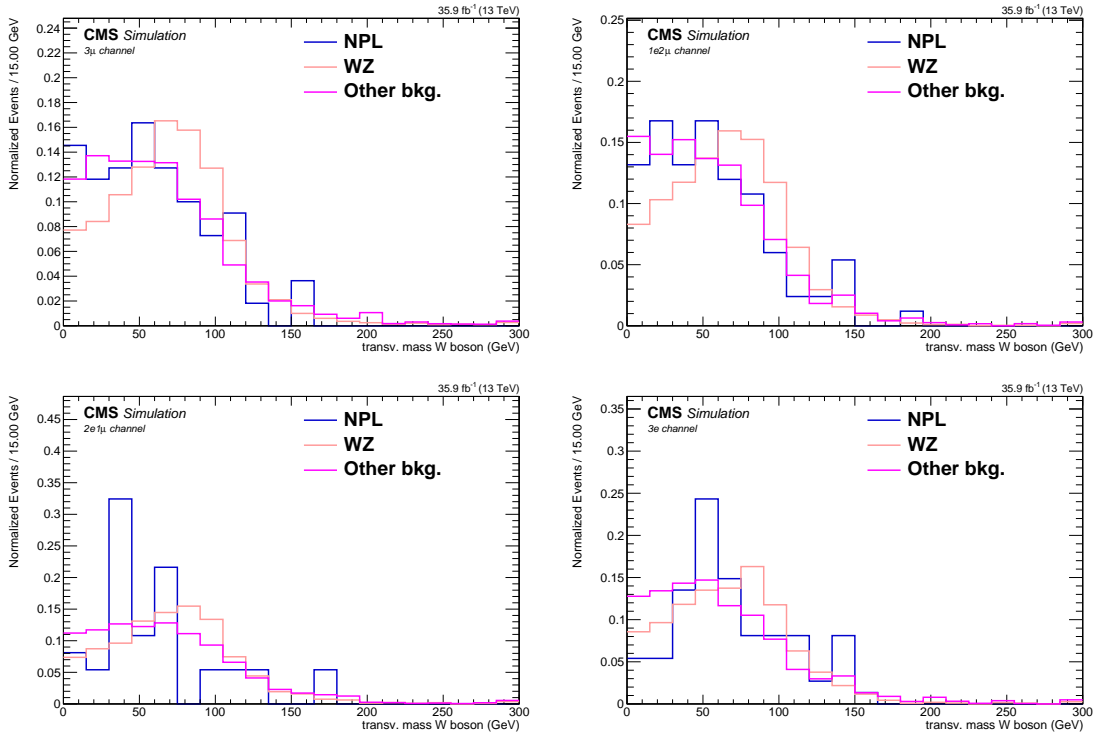


Figure 6.8: The normalised distribution of the transverse mass of the W boson in the WZCR, before the fit. Left: 3μ , left-middle: $1e2\mu$, right-middle: $2e1\mu$, and right: $3e$ lepton channel.

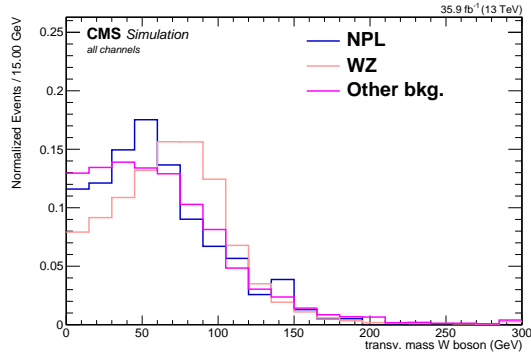


Figure 6.9: The normalised distribution of the transverse mass of the W boson in the WZCR, before the fit. All different lepton channels together.

6.2 Systematic uncertainties

The systematic uncertainties entering the analysis are coming from different sources. The experimental uncertainties arise from the reconstruction of the objects and are discussed in [Section 4.4](#). These influence the number of events passing the selection, so-called normalisation uncertainties, or the relative occupancies of the distributions, so-called shape uncertainties. The normalisation uncertainties coming from reconstruction include the uncertainty of 2.5% on the measured integrated luminosity and the efficiency of the trigger logic used for the analysis which has a 1% (5%) uncertainty on the 3μ and $1e2\mu$ ($2e1\mu$ and $3e$) channels. The pileup distribution is calculated via the minimum bias cross section which has a 4.6% uncertainty. This uncertainty results in a systematic shift in the pileup distribution and its shape effect is estimated by recalculating the pileup distribution for each variation of the minimum bias cross section. The shape uncertainties also include the uncertainties coming from the applied lepton scale factors. Their systematic uncertainty originates from three sources: identification, isolation and tracking. The uncertainties arising from jet energy corrections require a recalculation of all jet related kinematic observables and its effect is propagated to the missing transverse energy. The reweighting of the CSVv2 discriminant is also a source of uncertainty. There are three sources of uncertainty contributing to the measurement of the b-tag related scale factors: statistical uncertainties, jet energy scale and the purity of the sample. These result in eight uncorrelated contributions.

Since the NPL sample is artificially made from data by inverting the isolation of the third lepton. Its effect has to be estimated. The shape uncertainty one the NPL processes is obtained by varying the isolation inversion with respect to tight working point to the loose working point for electrons and muons at the same time. This found to have negligible effect. The uncertainty on the normalisation of the overall NPL yield is taken as 50% in accordance with the SM tZq search [\[184\]](#).

The uncertainty on the expected yield of the simulated backgrounds is taken to be 30% of the yield such that it covers all uncertainties at next to leading order accuracy. Theory uncertainties originating from the modelling of the main backgrounds are estimated to account for the effect on the shape of the distributions from the choice of parton density functions, and renormalization (μ_R) and factorization (μ_F) scales. The effect of the renormalization (μ_R) and factorization (μ_F) scales is estimated by varying each independently and correlated up and down by a factor of two, where the anti-correlated variations are dropped. The envelope of these variations is used as an uncertainty. The uncertainties coming from the parton density functions used for simulation are estimated using the PDF4LHC recipe [\[185\]](#), which combines the MMHT14, CT14, and NNPDF3.0 PDF sets [\[185\]](#). The theory uncertainties are considered for the main backgrounds coming from simulation: WZ+jets, ZZ+jets, $t\bar{t}Z$, and tZq. This is found to have a negligible effect.

The way the uncertainties are treated as nuisance parameters is summarized in [Table 6.1](#). The effect of systematic uncertainties that are treated as shape uncertainties is shown in [Section 6.2.1](#) and [Section 6.2.2](#).

NOTE: INCLUDE EFFECT PDF AND FACT/RENO

Table 6.1: Uncertainties used in this analysis. The column labelled type represents how the uncertainty is treated for the fit.

Source	Systematic input	Type
nonprompt muon norm.	50%	normalisation
nonprompt electron norm.	50%	normalisation
background $t\bar{t}Z$ norm.	30%	normalisation
background WZ norm.	30%	normalisation
background tZq norm.	30%	normalisation
background ZZ norm.	30%	normalisation
background other MC norm.	30%	normalisation
trigger	1% (5%)	normalisation
lepton identification	$\pm\sigma(p_T, \eta)$	shape
JES	$\pm\sigma(p_T, \eta)$	shape
JER	$\pm\sigma(p_T, \eta)$	shape
b-tagging	$\pm\sigma(p_T, \eta)$	shape
pileup	$\pm\sigma$ of min. bias cross section	shape
PDF	PDF4LHC recipe	shape
luminosity	2.5%	normalisation
renorm. and fact. scales	varying indep. and corr.	shape

6.2.1 Effect of systematic uncertainties on the transverse mass distribution

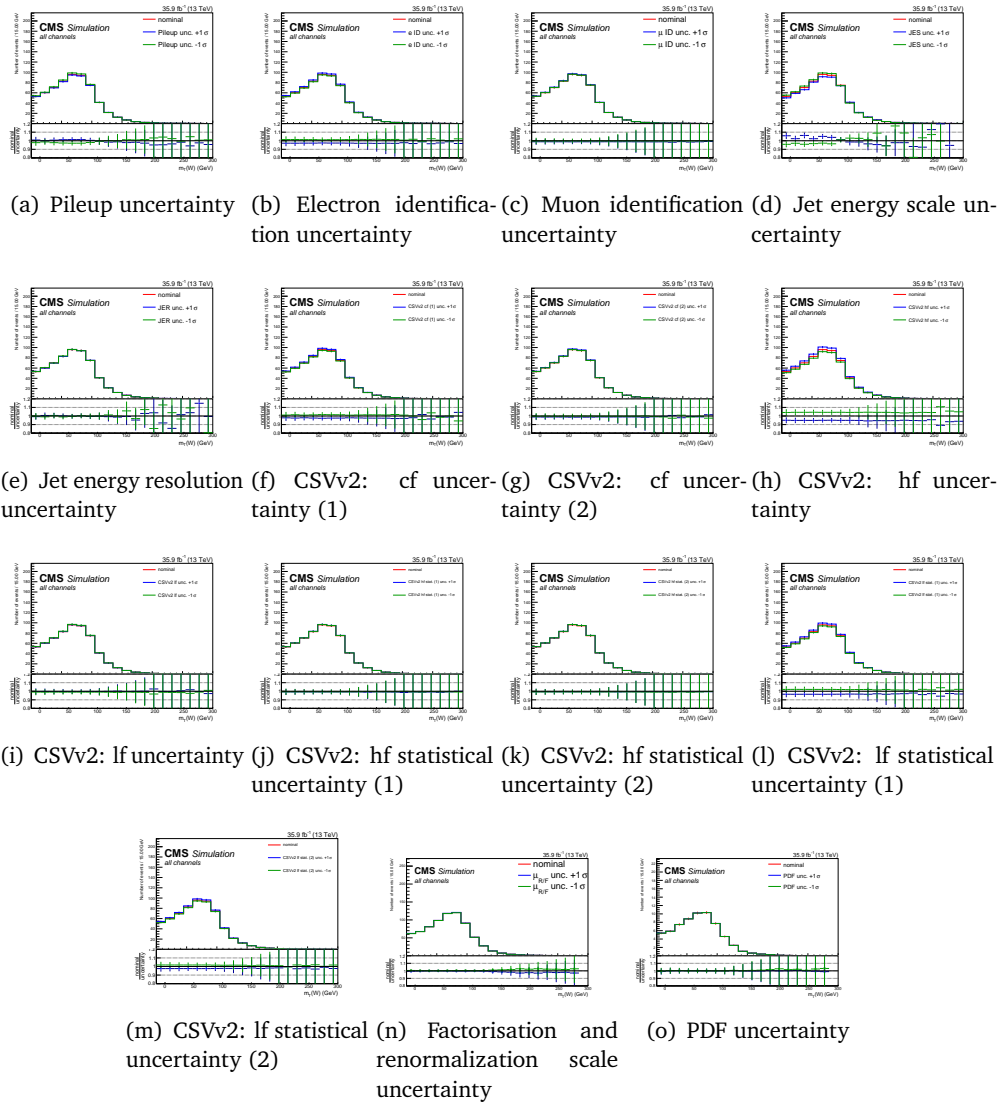


Figure 6.10: Distribution of the nominal values and shift due to systematic uncertainties for the transverse mass of the W boson in the WZCR for the WZ process. All lepton channels summed.

6.2.2 Effect of the systematic uncertainties on the multivariate discriminator distributions

The effect of the systematic uncertainties on the multivariate discriminator in the STSR involving the tZu vertex is shown. Other regions are shown in [Appendix D.2](#).

NOTE: Besprek plottjes

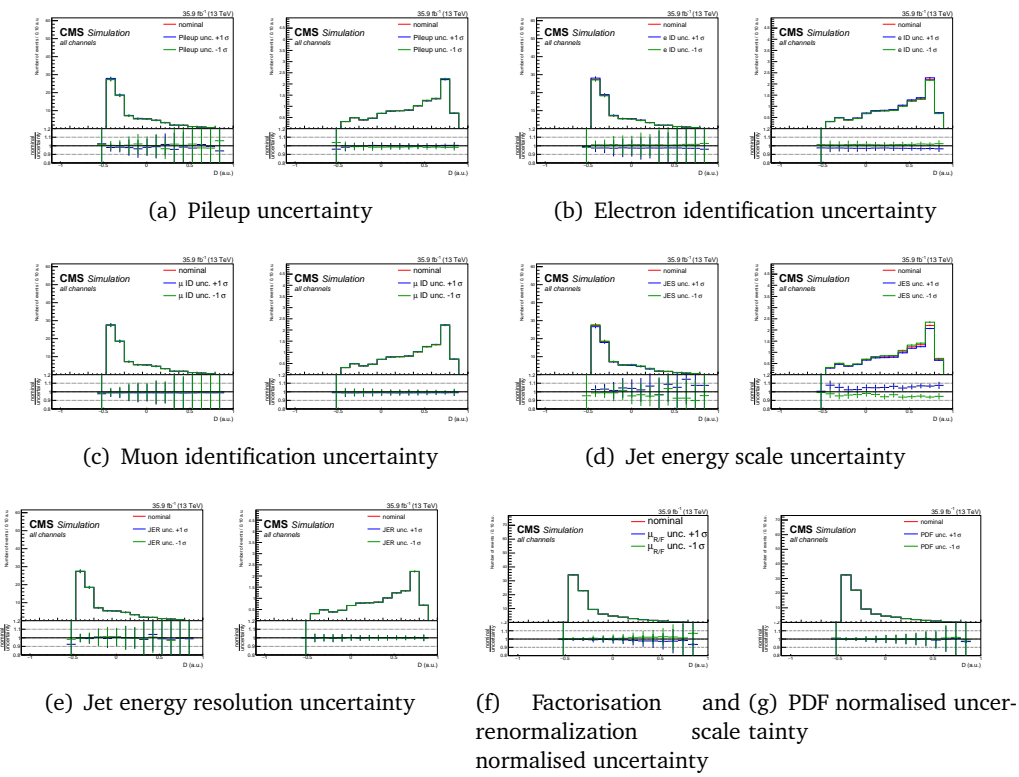


Figure 6.11: Distribution of the nominal values and shift due to systematic uncertainties for the transverse mass of the W boson in the STSR for the WZ process and FCNC signal involving a tZu vertex. All lepton channels summed. Part one.

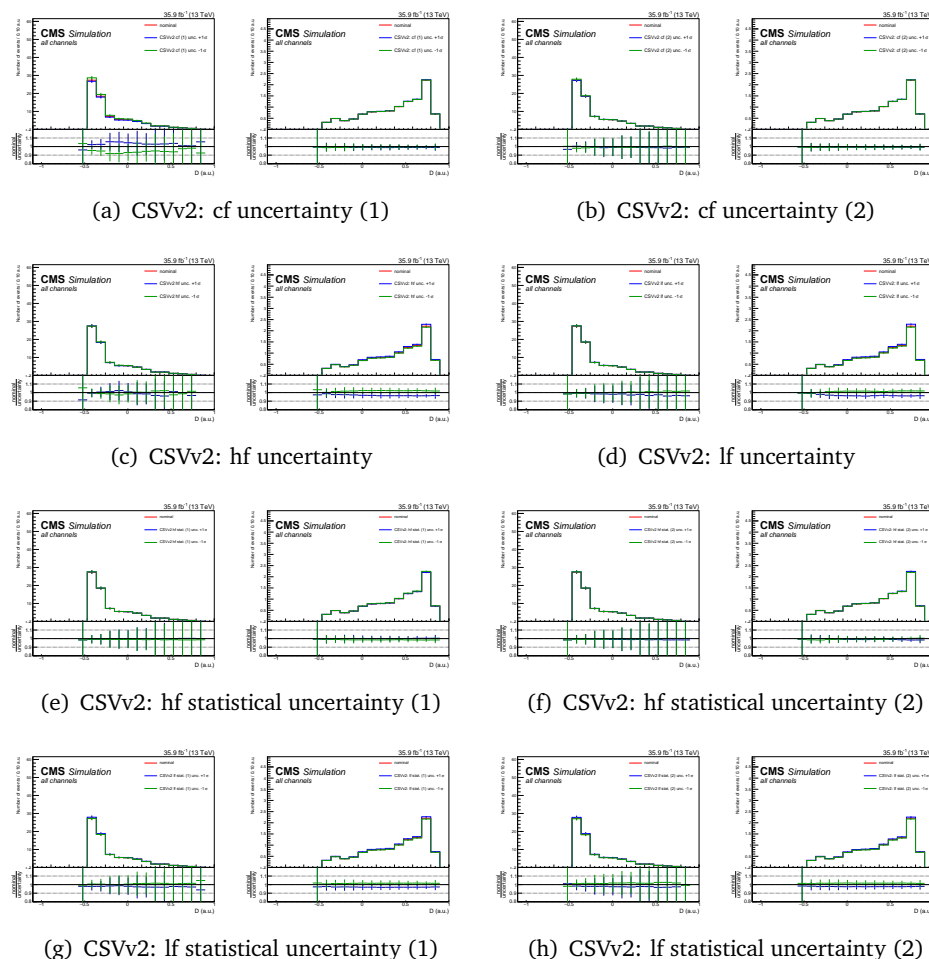


Figure 6.12: Distribution of the nominal values and shift due to systematic uncertainties for the transverse mass of the W boson in the STSR for the WZ process and FCNC signal involving a tZu vertex. All lepton channels summed. Part two.

6.3 Limit setting procedure validation

The analysis strategy has been established using a blinded strategy. Through the use of a pseudo dataset, the limit setting procedure has been validated. Signal injection tests for which the signal strength from a pseudo dataset with a pre-set signal strength is estimated are performed and shown in [Figure 6.13](#).

NOTE: Besprek plottjes

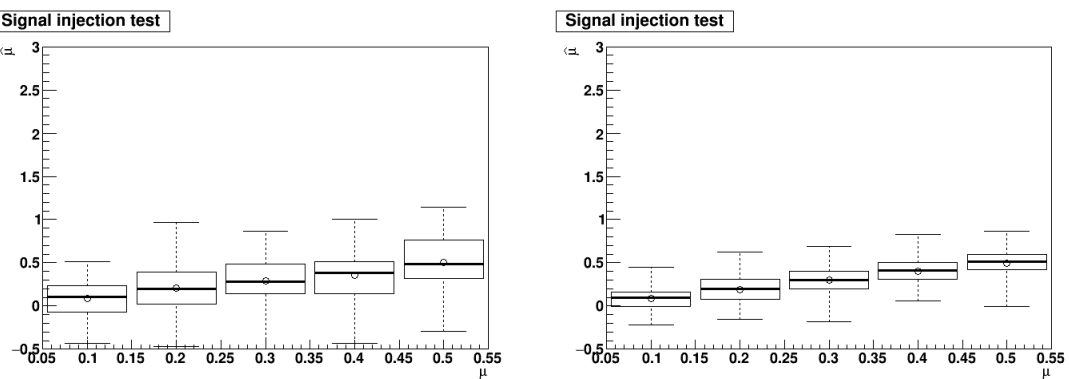


Figure 6.13: The obtained signal strength with the Maximum Likelihood method is in agreement with the signal strength used to generate the Asimov data set for the tZu (left) and tZc (right) couplings.

Another validation has been done by performing a Maximum Likelihood fit in the WZCR only, considering all lepton channels. A simultaneous fit of the signal strength of the NPe, NP μ and the WZ+jets backgrounds is done by using the multi-dimensional fit in Higgs Combine Tool. The resulting signal strengths can then be applied on the distribution of the transverse mass of the W boson to verify data/MC agreement, as can be seen in [Figure 6.15](#). Furthermore, a goodness of fit test is performed, resulting in a p-value of 0.3 (see [Figure 6.14](#)).

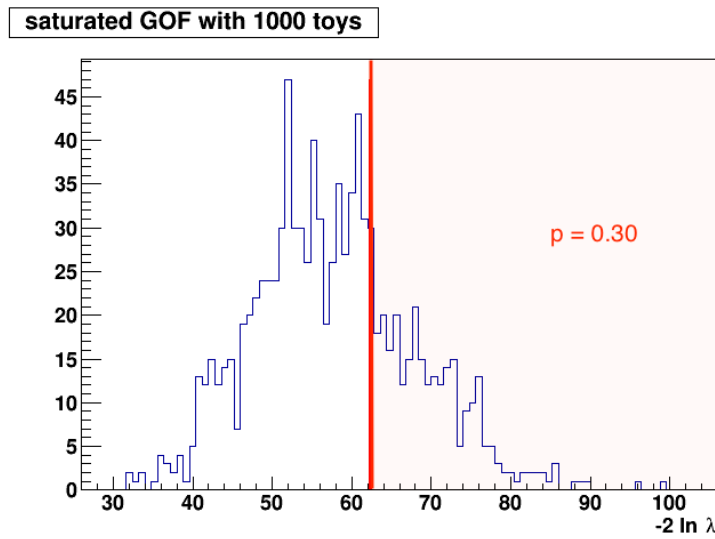


Figure 6.14: Goodness of fit testing in the WZCR with 1000 toys. The likelihood ratio is denoted as λ .

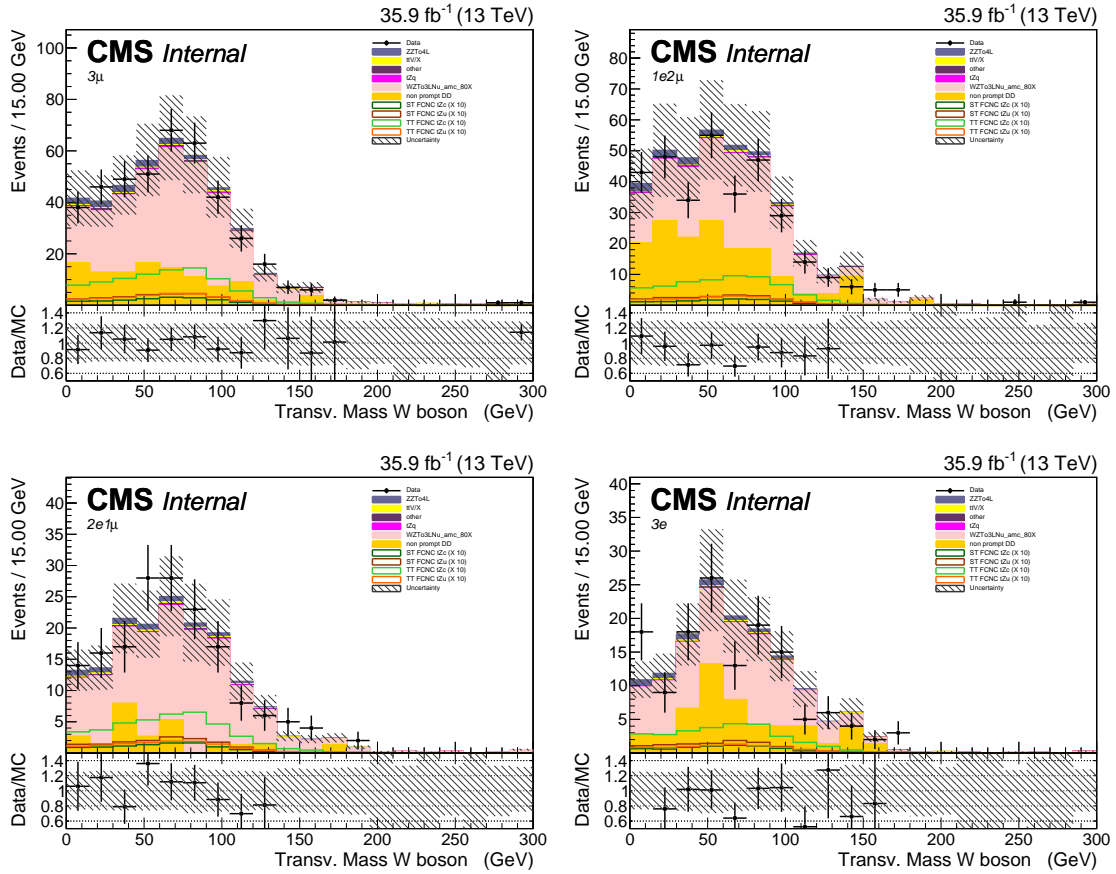


Figure 6.15: The transverse mass of the W boson in the WZCR for the 3μ channel (left, upper), $1e2\mu$ channel (right, upper), $2e1\mu$ channel (left, lower), and $3e$ channel (right, lower). The uncertainty band does not include theoretical uncertainties.

6.4 Results and discussion

The limit setting procedure explained in [Section 3.4](#) is applied and results are obtained for each lepton channel separately as well as the combination. For both the tZu and tZc coupling, the maximum likelihood estimator of their signal strengths $\hat{\mu}$ is compatible with zero. This is shown in [Figure 6.16](#). One can see that the $3e$ lepton channel has the largest uncertainty. This is due to the fact that this channel is the most influences by the lack of statistics for this search.

The maximum likelihood estimators for the nuisance parameters $\hat{\theta}$ are shown in [Figure 6.17](#) for the tZc interaction and in the Appendix ([Figure D.13](#)) for the tZu interaction. Their values obtained from the signal plus background or background only fits are in agreement. The transfer factors have an initial value different than one and have small uncertainties. The normalisation uncertainties on the yields of the simulated backgrounds get constrained by the fit.

In [Figure 6.18](#) and [Figure 6.19](#), one can see that the nuisance parameters related to the NPL normalisations are shifted with respect to their initial values. This is to be expected since their initial normalisation is arbitrary. Furthermore, the effect of the uncertainties on the maximum

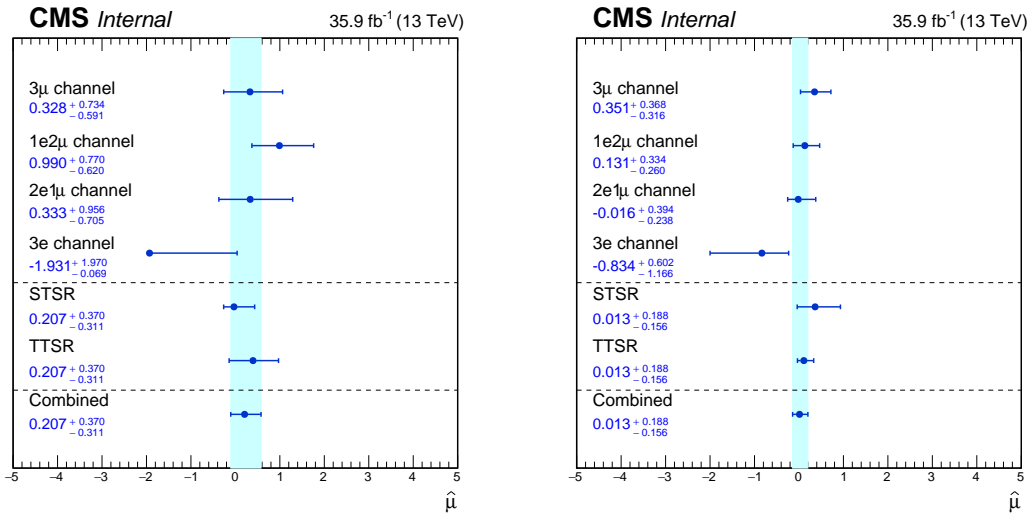


Figure 6.16: The maximum likelihood estimators for the signal strengths for the tZu vertex (right) and tZc vertex (left) per lepton channel as well as the combination in the STSR, TTSR, and all regions combined.

likelihood estimate of the signal strength is shown. The search is limited by lack of data, as can be seen from [Figure 6.26](#) and [Figure 6.27](#). After the limited data statistics, the most important systematic uncertainty are the $t\bar{t}Z$ normalisation, JES uncertainty and the NPL normalisation uncertainty.

The distributions of multivariate discriminating variables as well as the distribution of the transverse mass of the W boson are recreated with the maximum likelihood estimations of the nuisance parameters. The resulting distributions are shown in [Figure 6.20](#), [Figure 6.21](#), [Figure 6.22](#), [Figure 6.23](#), and [Figure 6.24](#). The post-fit distributions of the inputvariables for the BDTs are given in [Appendix D.3](#).

NOTE:
MAKE
THESE

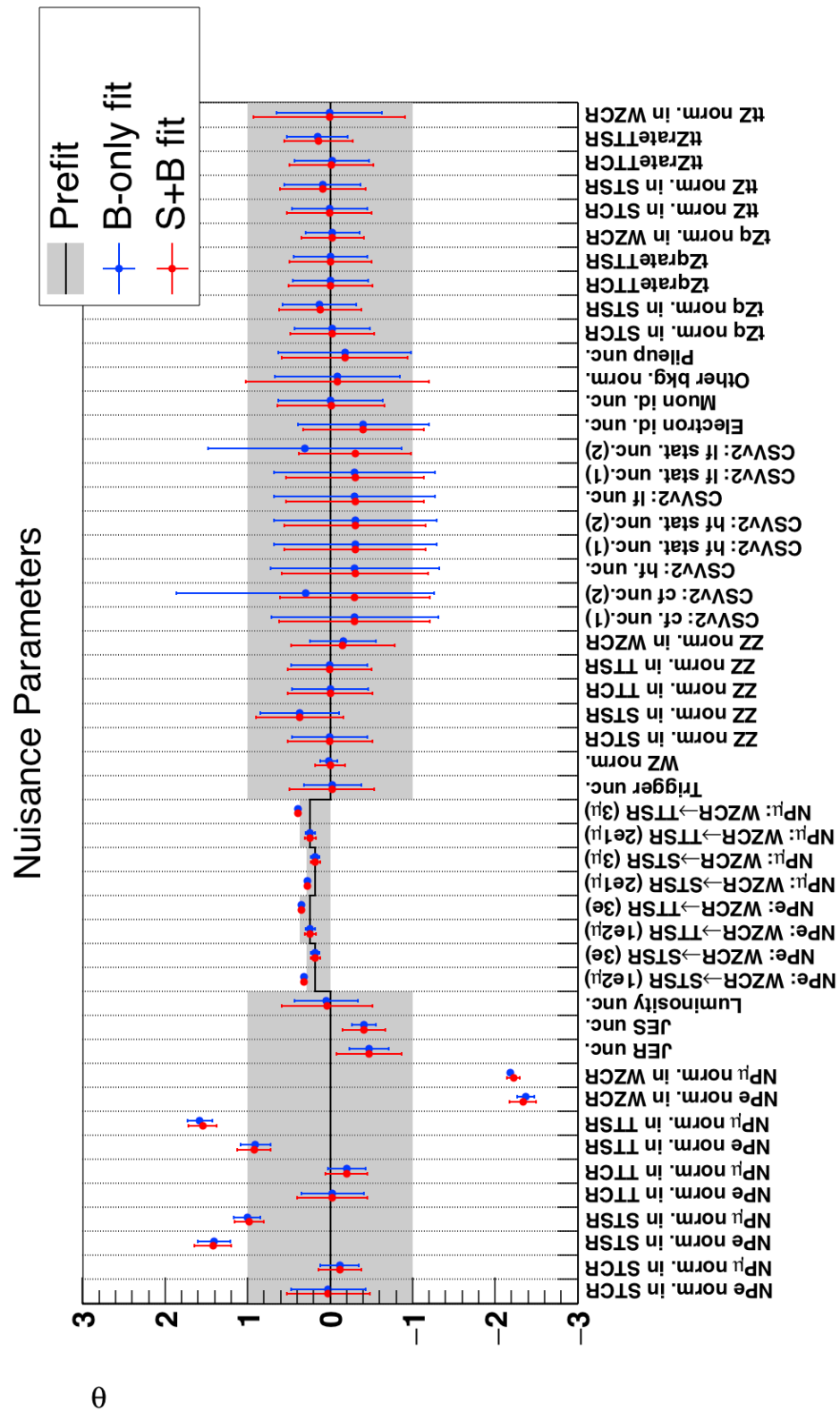


Figure 6.17: Maximum likelihood estimators for the tZc vertex.

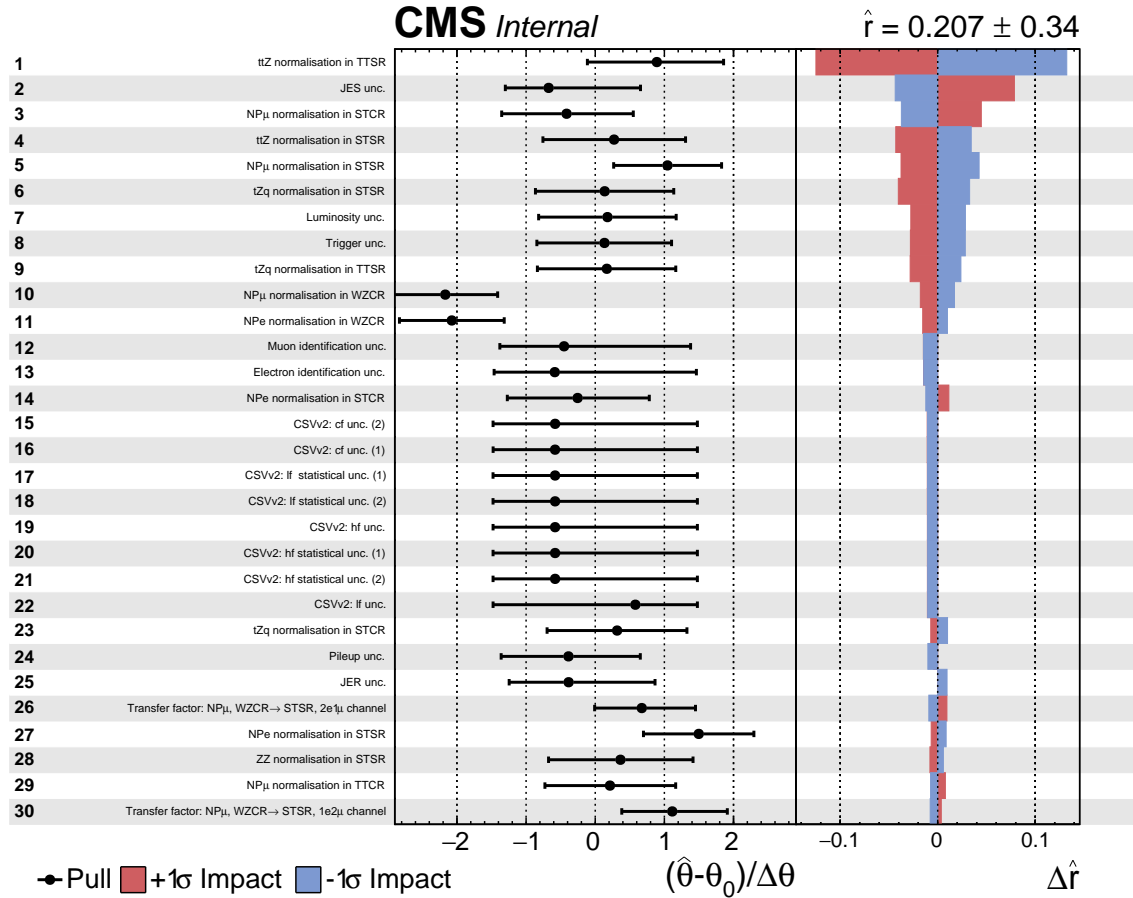


Figure 6.18: The pulls of the most influential each nuisance parameter and the influence of their uncertainty on the maximum likelihood estimation of the signal strength \hat{r} for the tZu vertex, part one.

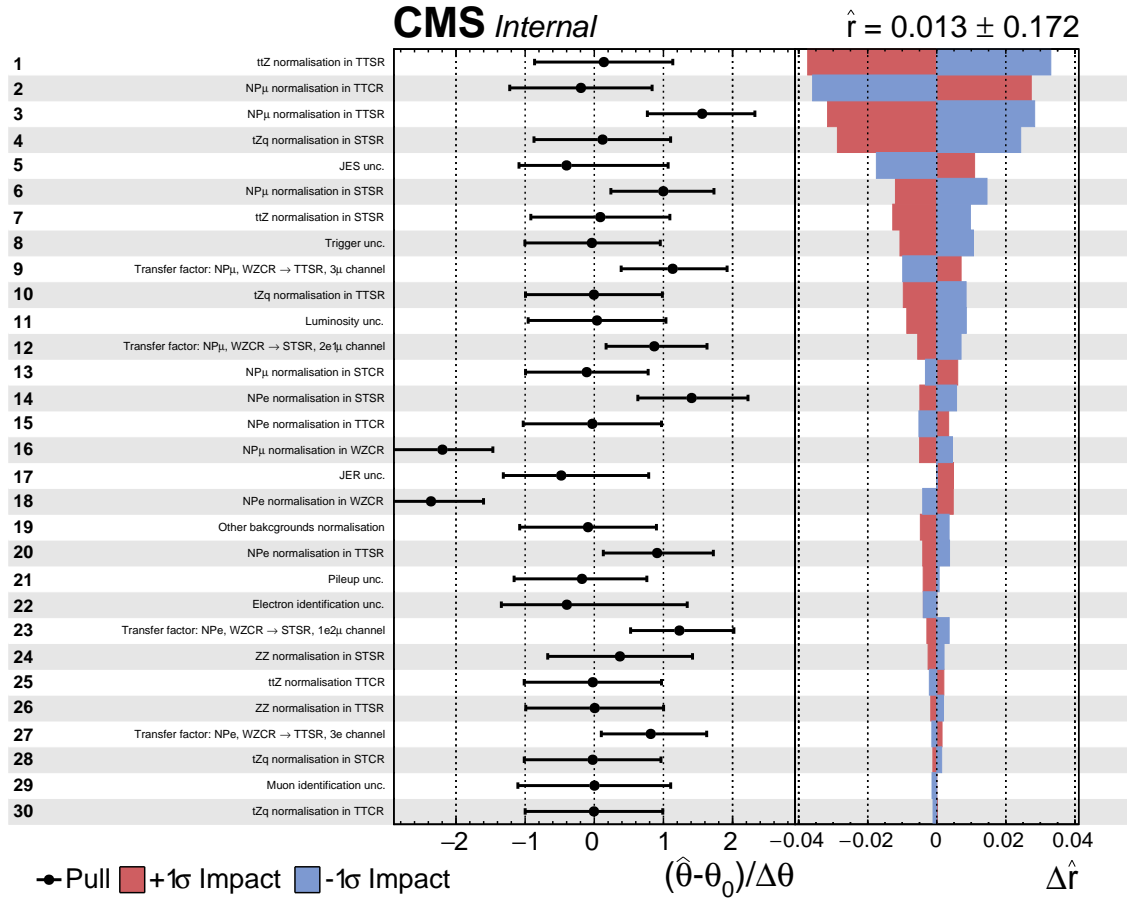


Figure 6.19: The pulls of the most influential nuisance parameter and the influence of their uncertainty on the maximum likelihood estimation of the signal strength \hat{r} for the tZc vertex, part one.

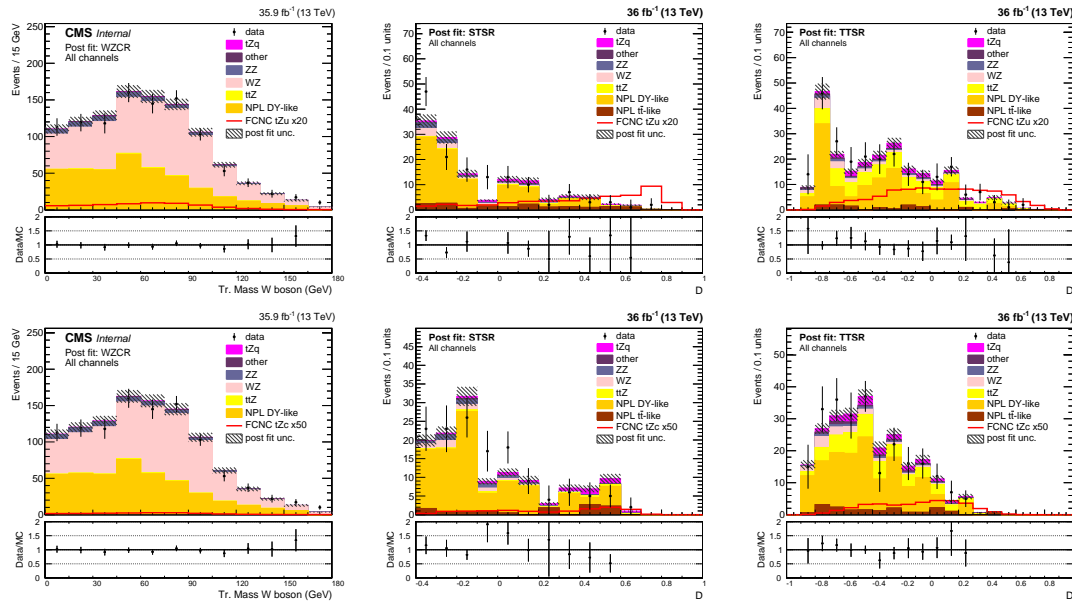


Figure 6.20: Post fit distributions for the all lepton channels of the transverse mass of the W boson in the WZCR (left), the multivariate discriminating variable in the STSR (middle), and the multivariate discriminating variable in the TTSR (right) for the tZu (top) and tZc (bottom) couplings.

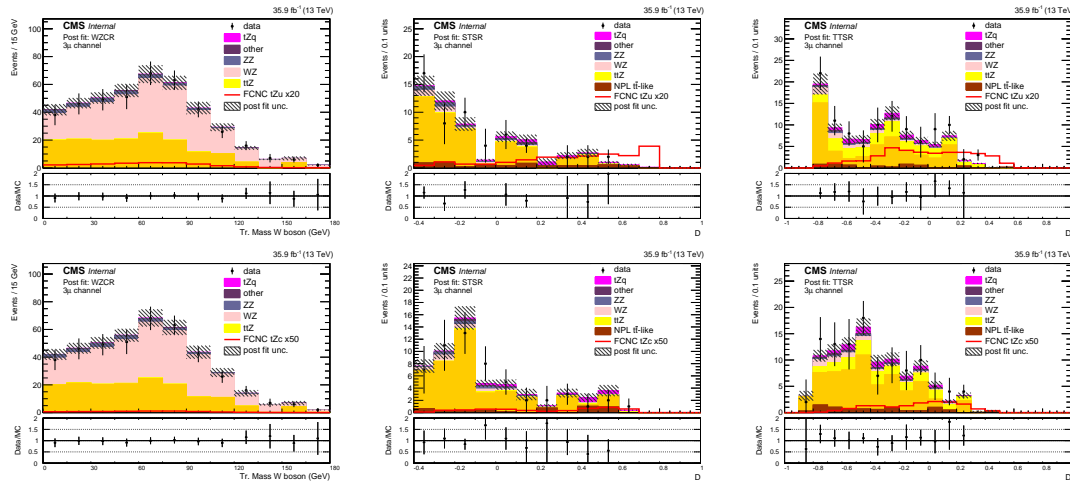


Figure 6.21: Post fit distributions for the 3μ lepton channel of the transverse mass of the W boson in the WZCR (left), the multivariate discriminating variable in the STSR (middle), and the multivariate discriminating variable in the TTSR (right) for the tZu (top) and tZc (bottom) couplings.

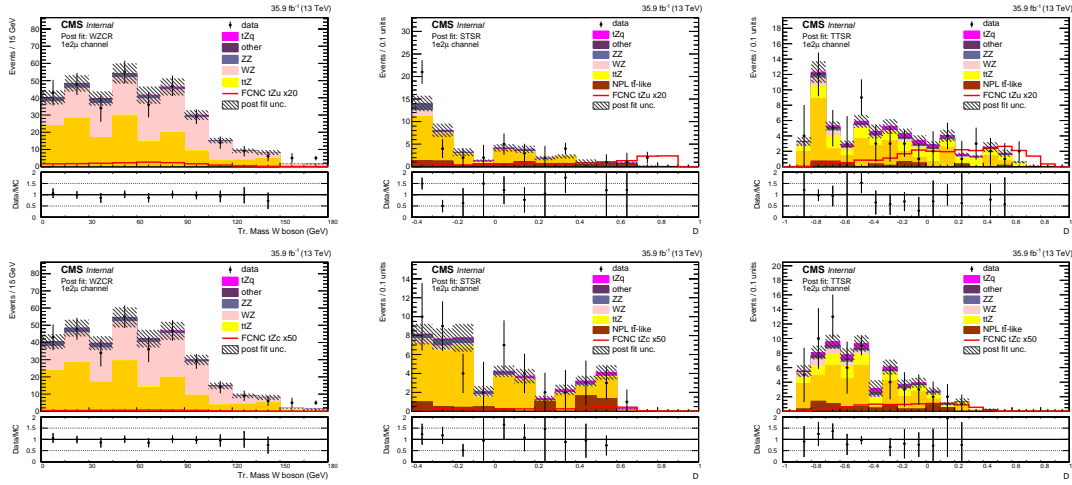


Figure 6.22: Post fit distributions for the $1e2\mu$ lepton channel of the transverse mass of the W boson in the WZCR (left), the multivariate discriminating variable in the STSR (middle), and the multivariate discriminating variable in the TTSR (right) for the tZu (top) and tZc (bottom) couplings.

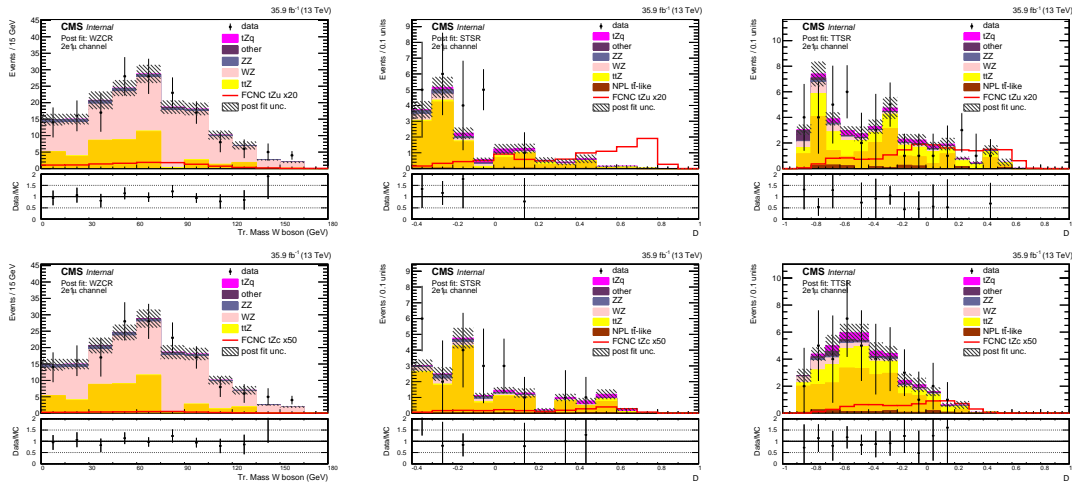


Figure 6.23: Post fit distributions for the $2e1\mu$ lepton channel of the transverse mass of the W boson in the WZCR (left), the multivariate discriminating variable in the STSR (middle), and the multivariate discriminating variable in the TTSR (right) for the tZu (top) and tZc (bottom) couplings.

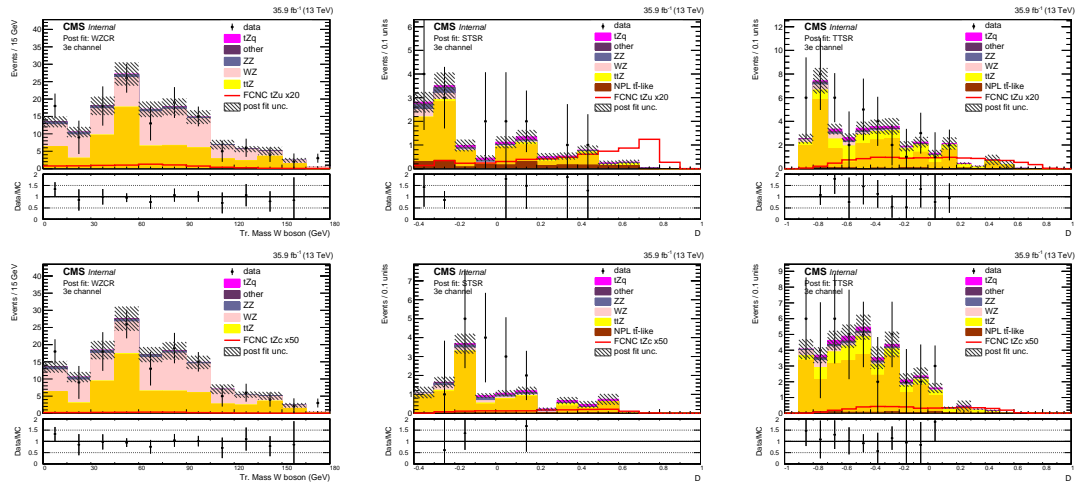


Figure 6.24: Post fit distributions for the 3e lepton channel of the transverse mass of the W boson in the WZCR (left), the multivariate discriminating variable in the STSR (middle), and the multivariate discriminating variable in the TTSR (right) for the tZu (top) and tZc (bottom) couplings.

6.4.1 One dimensional limits

The limit setting procedure used in this search returns limits on the signal strength modifier which can be translated to signal cross sections. These limits are translated to a limit on the branching fraction using Equation 1.39. Additionally, the limit on the couplings are extracted using the fact that the cross sections are quadratically dependent on the couplings. In Figure 6.25, the resulting limits at 95% CL on the branching fraction and couplings related to the tZu vertex is shown. This observed (expected) limit amounts to $\mathcal{B} < 0.024\%$ (0.015%) when $\kappa_{tZu}/\Lambda \neq 0$ and $\kappa_{tZc}/\Lambda = 0$. The expected limit surpasses the CMS search at a centre-of-mass of 8 TeV expected limits of 0.027% [10]. The observed limit of 0.024% for the tZu interaction doesn't surpass the CMS 8 TeV observed limit of 0.022% [10]. The ATLAS collaboration has set limits 95% CL at a centre-of-mass of 13 TeV [47] with observed (expected) limits of 0.017% (0.024%) for the tZu coupling. The expected limit presented in this analysis surpasses the expected limit for tZu.

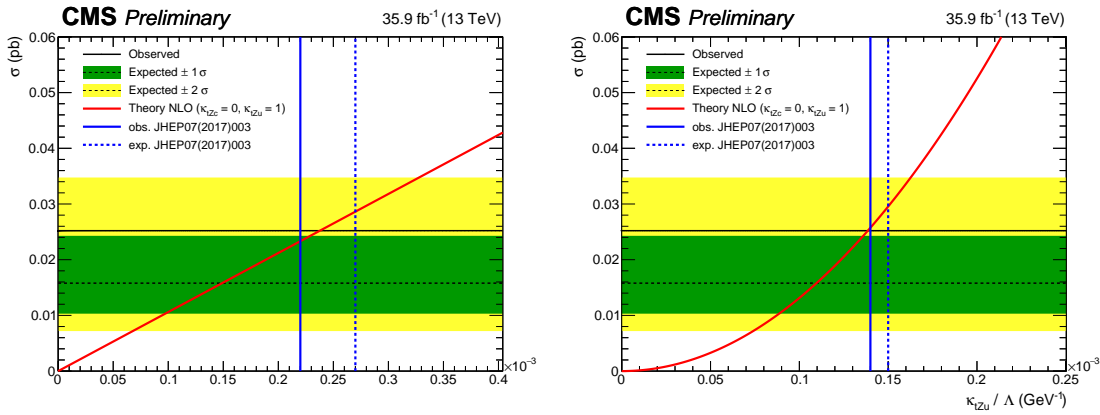


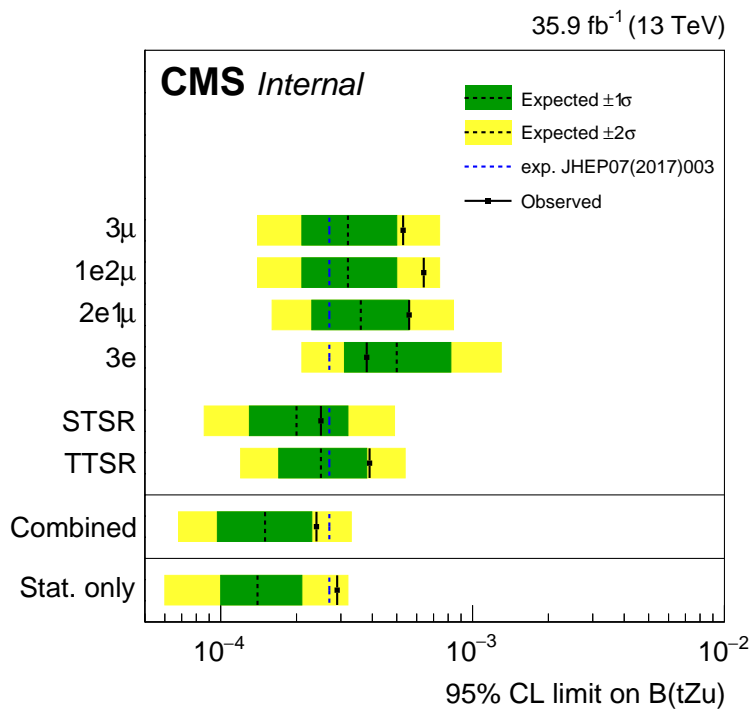
Figure 6.25: Exclusion limits at 95% CL on the FCNC branching fractions (left) and couplings (right) as a function of the cross section of the FCNC process, considering only the tZu vertex. The CMS observed (expected) limit at 95% CL at a centre-of-mass of 8 TeV [10] is given with a blue line (dashed line).

In Figure 6.26 and Table 6.2, the limits for each lepton channel separate as well as their combined limits are shown for the tZu vertex. The lepton channels are in agreement with each other, where the presence of a muon helps pushing the limit further. The STSR is the most sensitive region because of the higher presence of the targeted single top quark signal. Further, one can see that by combining signle top quark and top quark pair signals, one gains in sensitivity.

In Figure 6.27, the resulting limits at 95% CL on the branching fraction and couplings related to the tZc vertex is shown. For this coupling, the observed (expected) limit at 95% CL is $\mathcal{B} < 0.045\%$ (0.037%) when $\kappa_{tZc}/\Lambda \neq 0$ and $\kappa_{tZu}/\Lambda = 0$. The expected limit surpasses the CMS search at a centre-of-mass of 8 TeV expected limits of 0.118% [10]. This also the case for the observed limit of 0.045% for the tZc interaction, which surpasses the CMS 8 TeV observed limit of 0.049% [10]. The observed (expected) limit set by the ATLAS collaboration at a centre-of-mass of 13 TeV [47] is 0.023% (0.032%) for the tZc coupling. The expected limit presented in this analysis is in accordance with this limit.

Table 6.2: Expected limits on the branching fractions at 95% CL for the tZu coupling [10, 47].

	expected	+2 σ	+1 σ	-1 σ	-2 σ	observed
3 μ	0.032%	0.074%	0.050%	0.021%	0.014%	0.053%
1e2 μ	0.032%	0.074%	0.050%	0.021%	0.014%	0.064%
2e1 μ	0.036%	0.084%	0.056%	0.023%	0.016%	0.056%
3e	0.050%	0.13%	0.082%	0.031%	0.021%	0.038%
STSR only	0.020%	0.049%	0.032%	0.013%	0.0086%	0.025%
TTSR only	0.025%	0.054%	0.038%	0.025%	0.017%	0.039%
combined	0.015%	0.033%	0.023%	0.0097%	0.0068%	0.024%
8 TeV CMS (19.7 fb^{-1})	0.027%	-%	0.42%	0.018%	-%	0.022%
13 TeV ATLAS (36 fb^{-1})	0.024%	-%	0.35%	0.017%	-%	0.017%

**Figure 6.26:** Exclusion limits at 95% CL for each lepton channel and signal region on the FCNC tZu branching fractions considering one non-vanishing coupling at a time. The CMS observed (expected) limit at 95% CL at a centre-of-mass of 8 TeV [10] is given with a blue line (dashed line).

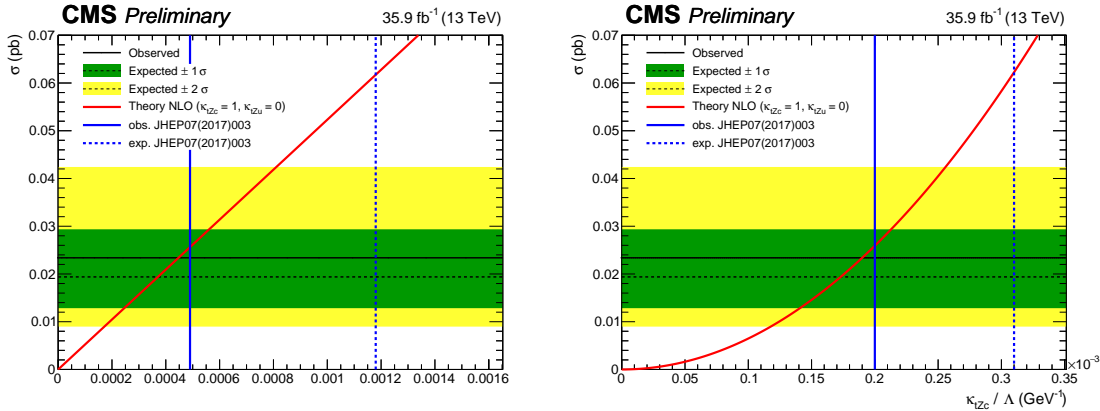


Figure 6.27: Exclusion limits at 95% CL on the FCNC branching fractions (left) and couplings (right) as a function of the cross section of the FCNC process, considering only the tZc vertex. The CMS observed (expected) limit at 95% CL at a centre-of-mass of 8 TeV [10] is given with a blue line (dashed line).

The limits for each lepton channel separate as well as their combined limits are shown for the tZc vertex in Figure 6.28 and Table 6.3. The lepton channels are in agreement with each other, and the presence of a muon helps the sensitivity. For the tZc vertex, the TTSR is the most sensitive region and by combining single top quark and top quark pair signals, one also gains in sensitivity.

Table 6.3: Expected limits on the branching fractions at 95% CL for the tZc coupling [10, 47].

	expected	+2σ	+1σ	-1σ	-2σ	observed
3μ	0.070%	0.15%	0.10%	0.046%	0.032%	0.12%
1e2μ	0.079%	0.18%	0.12%	0.052%	0.036%	0.096%
2e1μ	0.089%	0.20%	0.14%	0.058%	0.040%	0.099%
3e	0.12%	0.29%	0.19%	0.075%	0.050%	0.095%
STSR only	0.10%	0.2%	0.16%	0.066%	0.045%	0.17%
TTSR only	0.044%	0.094%	0.066%	0.029%	0.020%	0.043%
combined	0.037%	0.081%	0.056%	0.025%	0.017%	0.045%
8 TeV CMS (19.7 fb^{-1})	0.118%	-%	0.222%	0.071%	-%	0.049%
13 TeV ATLAS (36 fb^{-1})	0.032%	-%	0.046%	0.022%	-%	0.023%

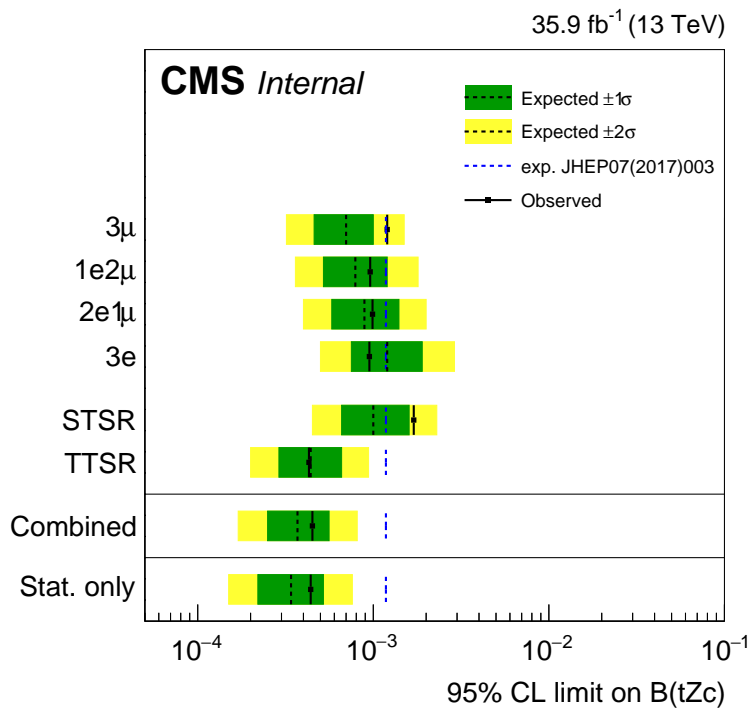


Figure 6.28: Exclusion limits at 95% CL for each lepton channel and signal region on the FCNC tZ_c branching fractions considering one non-vanishing coupling at a time. The CMS observed (expected) limit at 95% CL at a centre-of-mass of 8 TeV [10] is given with a blue line (dashed line).

6.4.2 Two-dimensional limits

One can interpolate the one dimensional limits λ_{tZq}^{1D} to a scenario where both couplings are on-vanishing. The interpolation is taken from Ref. [49], where an experimental extrapolation formulae

$$\kappa_{tZ_c}/\Lambda = \lambda_{tZ_c}^{1D} \sqrt{1 - \frac{\kappa_{tZ_u}/\Lambda}{\lambda_{tZ_u}^{1D}}}, \quad (6.1)$$

is found from 100 benchmark scenarios. These scenarios are constructed from existing signal samples as

$$\text{Signal yield} = (\kappa_{tZ_u}/\Lambda)^2 (\text{ST Zut yield} + \text{TT Zut yield}) + (\kappa_{tZ_c}/\Lambda)^2 (\text{ST Zct yield} + \text{TT Zct yield}). \quad (6.2)$$

For each scenario a dedicated BDT training is performed and the expected limit at 95% CL are calculated. The resulting two-dimensional limits are shown in Figure 6.29.

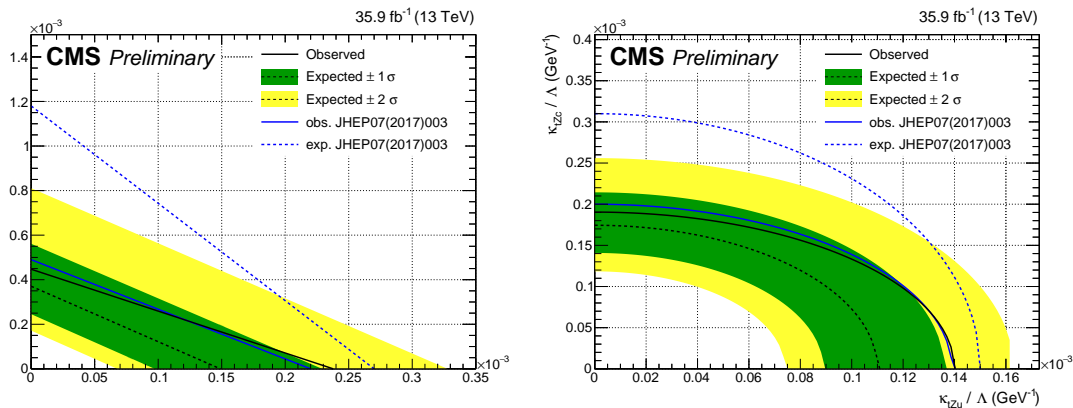


Figure 6.29: Two-dimensional limits on the branching fractions (left) and couplings (right) for FCNC interactions involving a tZq vertex. The CMS observed (expected) limit at 95% CL at a centre-of-mass of 8 TeV [10] is given with a blue line (dashed line).

Conclusion and prospects

7

7.1 Conclusion

The Standard Model of particle physics is the best theoretical framework so far to describe the nature around us. Although severely experimentally tested, this theory has its shortcomings and can not explain phenomena such as neutrino masses, dark matter, or dark energy. The heaviest particles in the Standard Model is the top quark , leading to the believe that it has an enhanced sensitivity to various new particles and interactions suggested by beyond the Standard Model theories. The top quark decays almost exclusively to a W boson and a bottom quark with a very short lifetime, making it escape from any bound states. This makes it possible to directly study the top quark properties by analysing its decay products. New physics phenomena are probed by measuring the production rate of top quarks and studying the Wtb vertex. The Large Hadron Collider is a top quark factory, producing a large number of events containing top quarks. At the proton collision points, experiments are placed to study the collisions. The search presented in this thesis is performed on data collected by the Compact Muon Solenoid experiment at a centre-of-mass energy of 13 TeV, resulting in 35.9 fb^{-1} of integrated luminosity.

Flavour changing neutral currents are forbidden at tree level and highly suppressed at higher order in the Standard Model. Nonetheless, many beyond the Standard Model theories enhance their probability. In this thesis, a search in three lepton final states is performed for the production of single top quarks via the tZq vertex, with $q = c, u$, or the top quark pair processes where one of the top quarks decay through this vertex. No significant deviation with respect to the predicted background is observed and upper limits at 95% confidence level are placed. The observed (expected) upper limits at 95% confidence level on the branching fractions of top quark decays are: $\mathcal{B}(t \rightarrow uZ) < 0.024\%$ (0.015%) and $\mathcal{B}(t \rightarrow cZ) < 0.045\%$ (0.037%), assuming one non-vanishing coupling at a time. A summary of the observed (expected) limits on the FCNC tZq vertex is shown in [Figure 7.1](#).

Significant improvements are developed with respect to previous searches, namely by using other kinematic variables as input into the BDT as well as a better handle on the NPL background. The expected limit for the FCNC tZu interaction is more stringent than the expected limit of 0.024% for the current most stringent observed limit of 0.017%, set at a centre-of-mass energy of 13 TeV by the ATLAS collaboration [47]. The observed (expected) limit on the tZc interaction

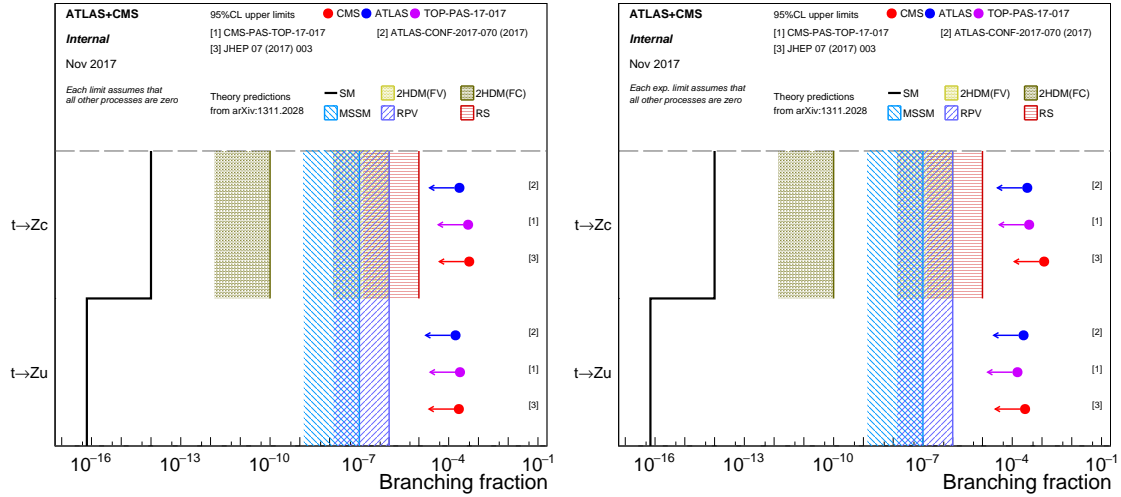


Figure 7.1: Summary of the most stringent observed (left) and expected (right) upper limits on FCNC tZq at 95% CL upper limits from CMS (red) and ATLAS (blue) at a centre-of-mass of 8 and 13 TeV. The results from this thesis are shown in purple. A comparison between theory predictions and experimental limits is shown. Figure adapted from [34].

set by ATLAS is 0.023% (0.032%) and its expected limit is comparable with the expected limit presented in this search. For the FCNC interactions with a tZq vertex, the branching fractions predicted within the Standard Model or beyond the Standard Model theories are still out of reach.

7.2 Prospects

This statistically limited search is expected to have an improvement when performed on a larger dataset. By extrapolating the current analysis to a dataset of 100 fb^{-1} , keeping the systematic uncertainties as is, the expected upper limits at 95% CL are $\mathcal{B}(t \rightarrow uZ) < 0.0051\%$ and $\mathcal{B}(t \rightarrow cZ) < 0.014\%$, assuming one non-vanishing coupling at a time. These limits, with respect to the result obtained in the presented search, are shown in Figure 7.2. An improvement with a factor 0.3 for the tZu , and 0.4 for the tZc vertex is expected. This milestone is expected to be reached with Run 2. Setting statistical limitations aside, the largest systematic uncertainty is coming from the jet energy scale uncertainty. This uncertainty can be decreased by more precise measurements of the jet energy respond with more data as well as better methodologies. Also a more precise measurement from the calorimeter could help reducing the uncertainty.

The recently developed charm tagging algorithm could help the lesser sensitive FCNC signal with a tZc vertex from its backgrounds. Additionally, a new pixel detector is installed in March 2017 and this is expected to enhance the performance of heavy-flavour tagging which should help improve the analysis.

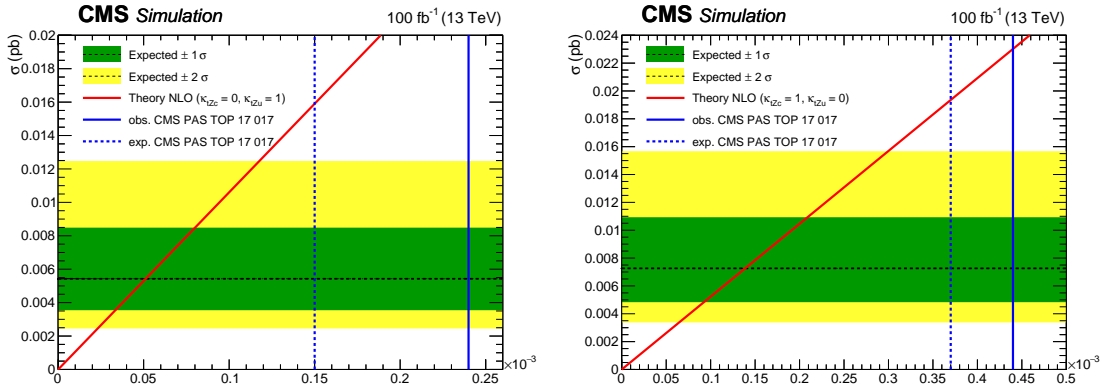


Figure 7.2: The expected limit at 95% CL for the tZu (left) and tZc interaction for an integrated luminosity of 100 fb^{-1} , extrapolated from the result obtained in this thesis, indicated with the blue (dashed) lines.

Future colliders should be able to reach meaningful sensitivity for top-FCNC couplings. In Figure 7.3, the sensitivity of the LHC at a centre-of-mass energy of 14 TeV and 3000 fb^{-1} integrated luminosity (HL-LHC) [186], as well as ILC/CLIC at a centre-of-mass energy of 500 GeV and 500 fb^{-1} of integrated luminosity [187], the future circular hadron colliders at a centre-of-mass of 100 TeV with an integrated luminosity of 10 ab^{-1} (FCC-hh) [186], the future electron positron colliders at a centre-of-mass of 500 GeV with an integrated luminosity of 10 ab^{-1} (FCC-ee) [188], and the future Large hadron electron collider with a centre-of-mass of 14 TeV and an integrated luminosity of 200 fb^{-1} [189] are shown. The sensitivities are originating from official projections as well as sensitivity studies based on the changes in luminosity, energy, and trigger thresholds.

The HL-LHC is not expected to have significant improvements for the limits of the top-Z FCNC interactions. Instead of hadron colliders, one could also look at future lepton colliders such as the FCC-ee, where the signal $e^+e^- \rightarrow Z\gamma \rightarrow t\bar{q}(\bar{t}q)$ can occur. The FCC-ee would be one of the high luminosity and high precision machines and would be able to perform precise measurements of the top quark, Higgs, Z and W bosons. Its large expected number of data and large production rates is expected to create an excellent environment for precise studies in the top quark section of the Standard Model. In Ref. [188] a study of the FCNC tZq single top quark production is done at different centre-of-mass energies and for different integrated luminosities. In Figure 7.3, their most stringent results are shown.

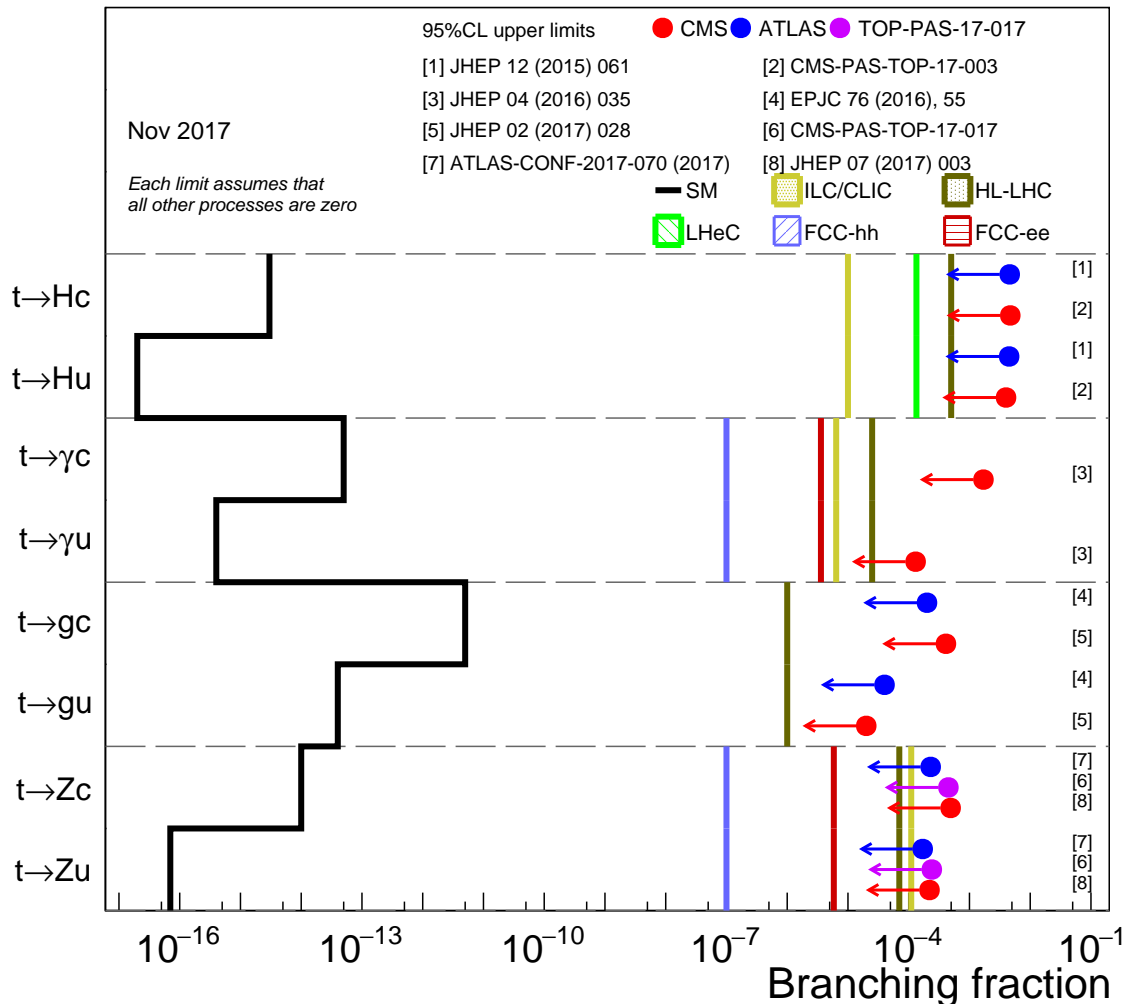
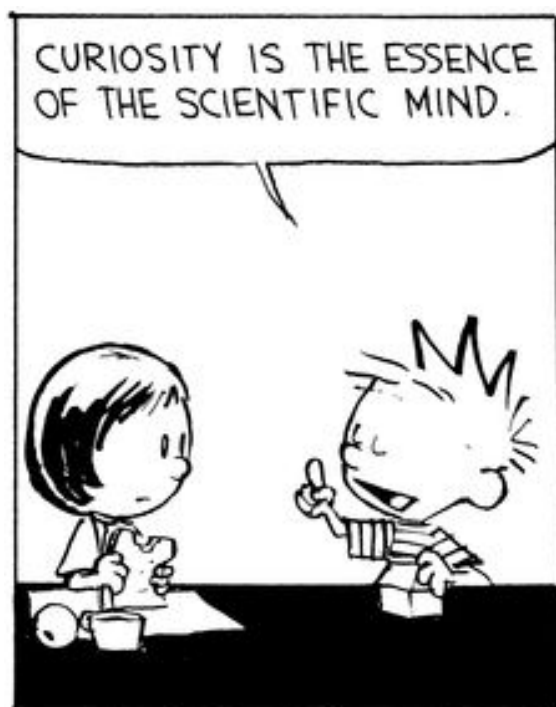


Figure 7.3: Summary of the most stringent upper limits on top-FCNC interactions at 95% CL upper limits from CMS (red) and ATLAS (blue) at a centre-of-mass of 8 and 13 TeV. The results from this thesis are shown in purple. A comparison between the projections for future colliders and the current experimental limits is shown. Figure adapted from [34]. The projections are taken from [186–189].

Appendix



A

Trigger scale factors

The trigger scale factors measured as a function of lepton p_T , using the dataset collected by E_T^{miss} triggers and WZ simulation, after a 3 lepton and jets selection, in the Z mass window. All corrections to simulation are applied.

Table A.1: Trigger efficiencies on data events selected with E_T^{miss} triggers and WZ simulation for all lepton channels together. The unweighed number of events is quoted. When there are no events passing the cuts, it is indicated with N/A. The uncertainties are statistical uncertainties.

ALL CHANNEL	data		WZ simulations	
	Efficiency	unc.	Efficiency	unc.
3 lep, at least one jet	117/118 = 99.15 %	12.94%	18047/18055 = 99.96%	1.05%
STS R	6/6 = 100.00%	57.74%	1541/1541 = 100.00%	3.60%
TTS R	26/27 = 96.30%	26.46%	1791/1792 = 99.94%	3.34%
WZCR	69/69 = 100.00 %	17.03%	14405/14412=99.95%	1.18%

Table A.2: Trigger efficiencies on data events selected with E_T^{miss} triggers and WZ simulation for 3 μ lepton channel together. The unweighed number of events is quoted. When there are no events passing the cuts, it is indicated with N/A. The uncertainties are statistical uncertainties.

3 μ CHANNEL	data		WZ simulations	
	Efficiency	unc.	Efficiency	unc.
3 lep, at least one jet	40/40 = 100.00 %	22.36 %	7814/7814 = 100.00%	1.60%
STS R	N/A	N/A	687/687 = 100%	5.40%
TTS R	13/13 = 100.00%	39.22%	763/763 = 100.00%	5.12%
WZCR	22/22 = 100.00 %	30.15%	6238/6238=100.00%	1.79%

Table A.3: Trigger efficiencies on data events selected with E_T^{miss} triggers and WZ simulation for 3e lepton channel together. The unweighted number of events is quoted. When there are no events passing the cuts, it is indicated with N/A. The uncertainties are statistical uncertainties.

3e CHANNEL	data		WZ simulations	
	Efficiency	unc.	Efficiency	unc.
3 lep, at least one jet	20/21 = 95.24%	29.76%	2211/2215 = 99.82 %	3.00%
STS R	4/4 = 100.00%	70.71%	176/176 = 100.00%	10.66%
TTS R	2/3 = 66.67%	60.86%	242/242 = 100.00%	9.09%
WZCR	14/14 = 100.00 %	37.80%	1744/1748=99.77%	3.38%

Table A.4: Trigger efficiencies on data events selected with E_T^{miss} triggers and WZ simulation for 2e1 μ lepton channel together. The unweighted number of events is quoted. When there are no events passing the cuts, it is indicated with N/A. The uncertainties are statistical uncertainties.

2e1 μ CHANNEL	data		WZ simulations	
	Efficiency	unc.	Efficiency	unc.
3 lep, at least one jet	32/32 = 100.00 %	25.00 %	3116/3118 = 99.94%	2.53%
STS R	1/1 = 100.00%	141.42%	255/255 = 100%	8.86%
TTS R	9/9 = 100.00%	47.14%	291/291 = 100.00%	8.29%
WZCR	14/14 = 100.00 %	37.80%	2529/2531=99.92%	2.81%

Table A.5: Trigger efficiencies on data events selected with E_T^{miss} triggers and WZ simulation for 1e2 μ lepton channel together. The unweighted number of events is quoted. When there are no events passing the cuts, it is indicated with N/A. The uncertainties are statistical uncertainties.

1e2 μ CHANNEL	data		WZ simulations	
	Efficiency	unc.	Efficiency	unc.
3 lep, at least one jet	25/25 = 100.00%	28.28%	4906/4908 = 99.96 %	2.02%
STS R	1/1 = 100.00%	141.42%	423/423 = 100.00%	6.88%
TTS R	2/2 = 100.00%	100.00%	495/496 = 99.80%	6.34%
WZCR	19/19 = 100.00 %	32.44%	3894/3895 =99.97%	2.27%

Transfer factors

B

Table B.1: Transfer factors for all lepton channels for going from WZCR to the signal regions. The transfer factors $Tr_{TTCR \rightarrow TTSR}$ and $Tr_{STCR \rightarrow STSR}$ are 0.33.

	$Tr_{WZCR \rightarrow STSR}$	$Tr_{WZCR \rightarrow TTSR}$
κ_{tZu}/Λ	0.22 ± 0.00	0.46 ± 0.00
κ_{tZc}/Λ	0.39 ± 0.01	0.76 ± 0.01
Z/ γ^* + jets	0.08 ± 0.09	0.10 ± 0.10
t̄t	0.54 ± 0.31	0.70 ± 0.31
WZ	0.10 ± 0.00	0.15 ± 0.00
tZq	0.36 ± 0.02	0.67 ± 0.03
t̄tZ	0.14 ± 0.02	0.61 ± 0.05
ZZ	0.10 ± 0.00	0.13 ± 0.00
other	0.16 ± 0.03	0.30 ± 0.03

Table B.2: Event yields for the t̄t background in all lepton channels. The yields below the dashed lines should be compared with the two first rows.

Region	t̄t event yield
STSR	13.1 ± 2.5
TTSR	9.7 ± 2.1
TTCR	22.3 ± 3.1
STCR	33.7 ± 3.8
.....	
TTSR (TTCR)	7.44 ± 1.02
STSR (STCR)	11.24 ± 1.28

Table B.3: Event yields for all lepton channels. The last two columns represent the predicted event yield after applying the transfer factors. The regions between brackets correspond to the region from which the prediction is made.

	STSR	TTSR	WZCR	TTCR	STCR	STSR (WZCR)	TTSR (WZCR)
κ_{tZu}/Λ	3.9 ± 0.0	11.2 ± 0.0	7.3 ± 0.0	0.6 ± 0.0	0.3 ± 0.0	1.57 ± 0.02	3.33 ± 0.04
κ_{tZc}/Λ	14.1 ± 0.1	30.9 ± 0.1	15.5 ± 0.1	1.7 ± 0.0	1.2 ± 0.0	6.12 ± 0.08	11.77 ± 0.13
$Z/\gamma^* + \text{jets}$	-4.6 ± 21.7	22.3 ± 14.3	136.9 ± 48.5	-14.0 ± 22.2	-15.9 ± 11.3	10.61 ± 11.31	13.69 ± 14.68
$t\bar{t}$	13.1 ± 2.5	9.7 ± 2.1	8.5 ± 1.9	22.3 ± 3.1	33.7 ± 3.8	4.61 ± 2.37	5.89 ± 2.96
WZ	60.9 ± 1.6	83.0 ± 1.7	552.7 ± 4.6	11.9 ± 0.6	8.5 ± 0.6	55.86 ± 1.57	83.80 ± 2.30
tZq	8.0 ± 0.2	16.9 ± 0.2	7.3 ± 0.2	2.2 ± 0.1	1.0 ± 0.1	2.66 ± 0.14	4.86 ± 0.25
$t\bar{t}Z$	3.5 ± 0.3	42.5 ± 0.9	9.6 ± 0.5	6.8 ± 0.4	0.5 ± 0.1	1.37 ± 0.18	5.90 ± 0.59
ZZ	4.6 ± 0.1	4.8 ± 0.1	46.2 ± 0.3	0.8 ± 0.0	0.6 ± 0.0	4.48 ± 0.16	6.06 ± 0.21
other	1.2 ± 0.3	5.6 ± 0.3	6.8 ± 0.5	7.5 ± 0.7	2.4 ± 0.5	1.09 ± 0.18	2.05 ± 0.24

C

Details about the BDTs

The boosted decision trees are trained without the NPL background. In the following figures, the correlation matrices for the background and signal samples are shown. Furthermore, the resulting discriminating variables for background (red) and signal (blue) are shown. The ROC curves, illustrating the discriminating power of each discriminator is also shown for the training samples. At the bottom of each figure, the input variables used to train that discriminator are shown, where the background is shown in red and the signal in blue.

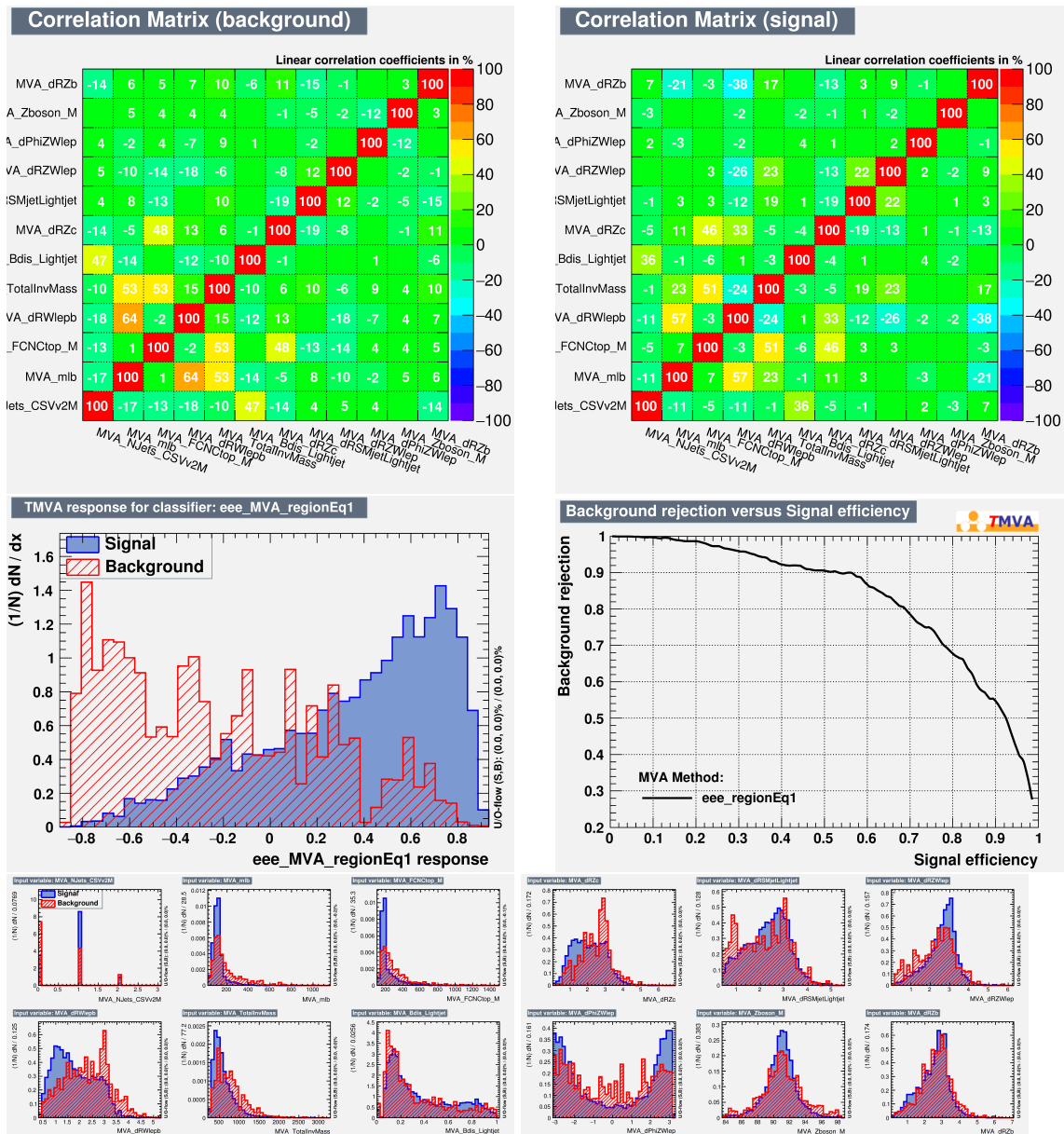
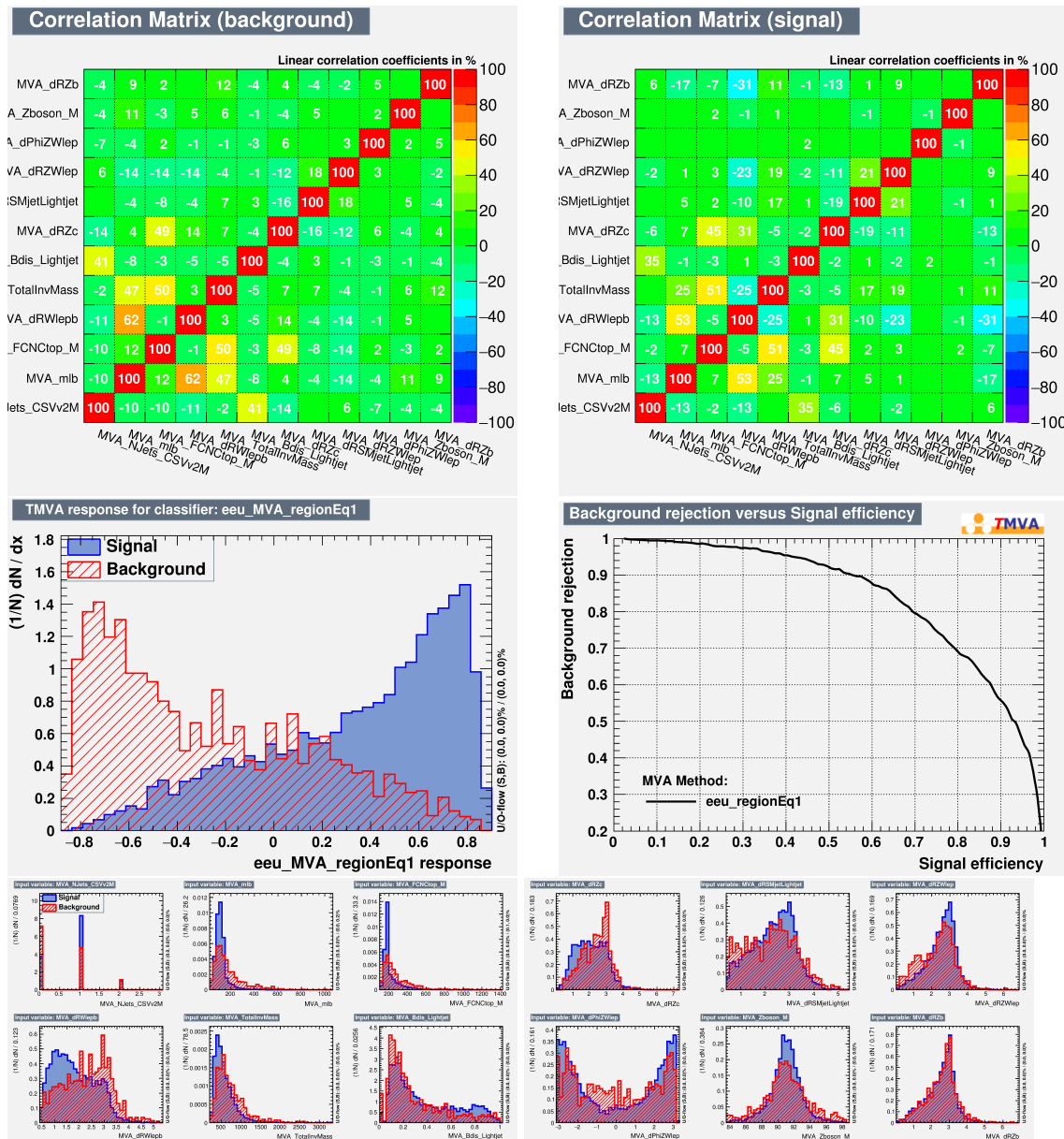


Figure C.1: 3e channel. TTSR: tZc vertex

Figure C.2: 2e1 μ channel. TTSR: tZc vertex

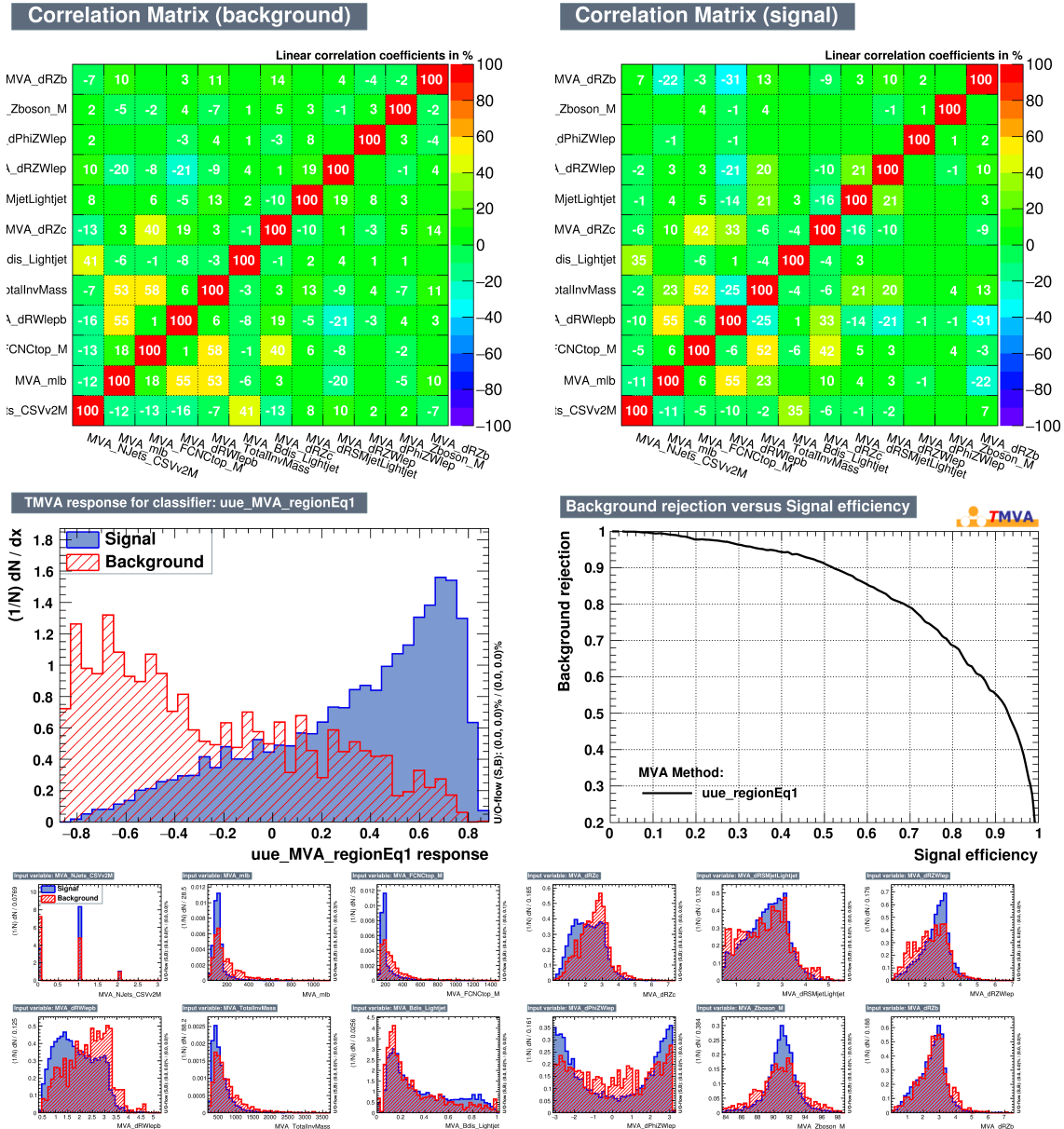
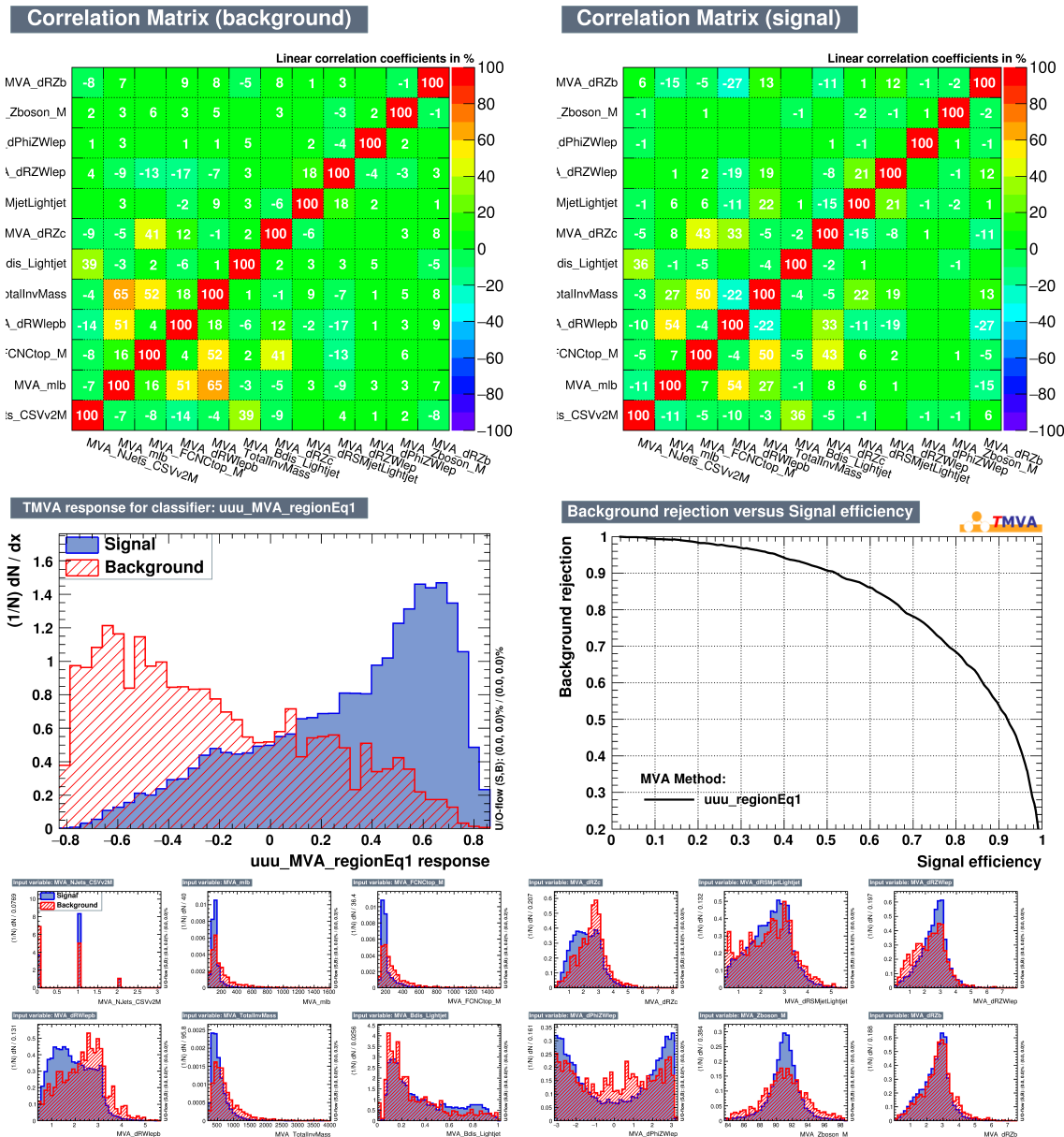


Figure C.3: 1e2μ channel. TTSR: tZc vertex

Figure C.4: 3 μ channel. TTSR: TzC vertex

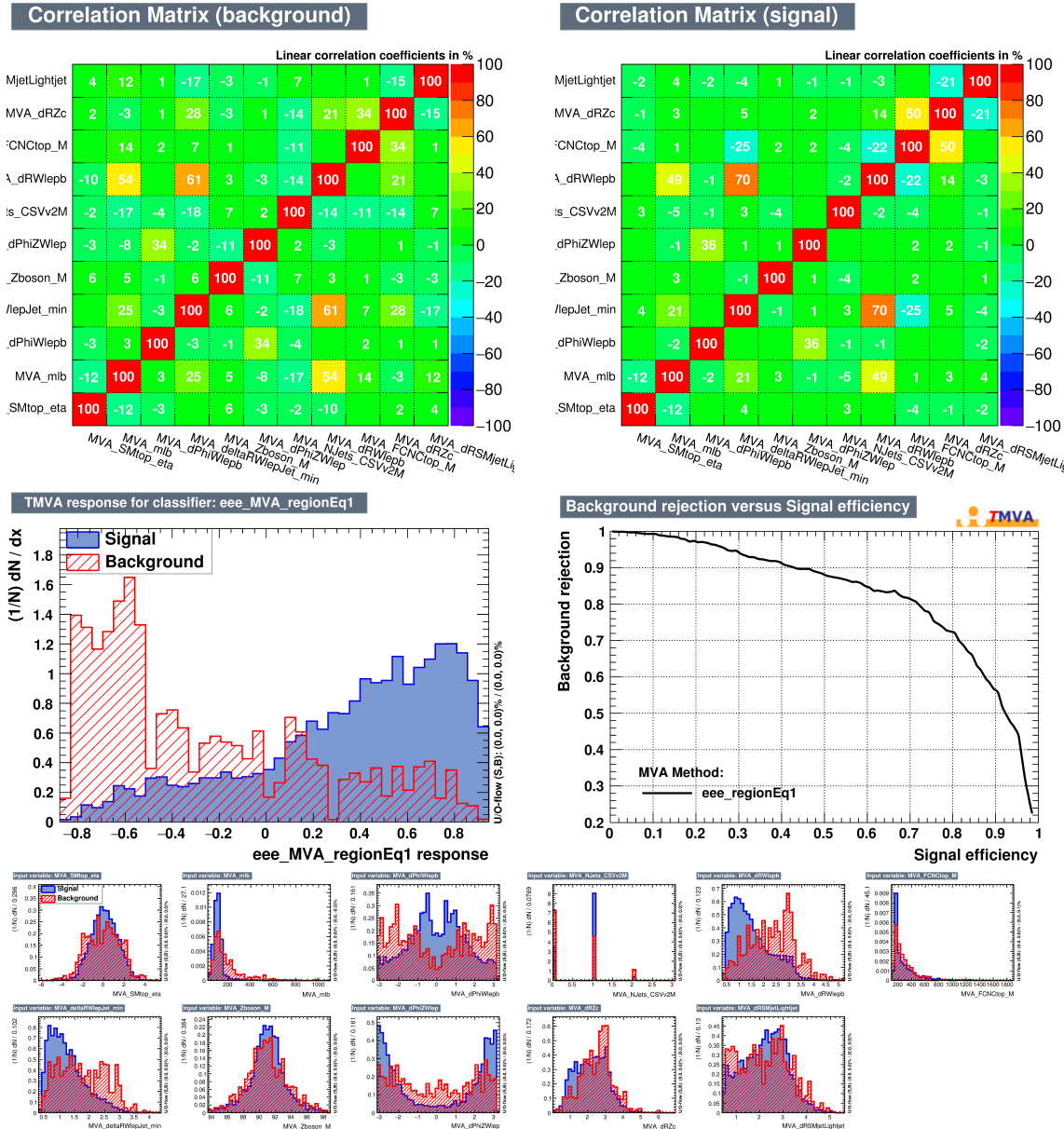
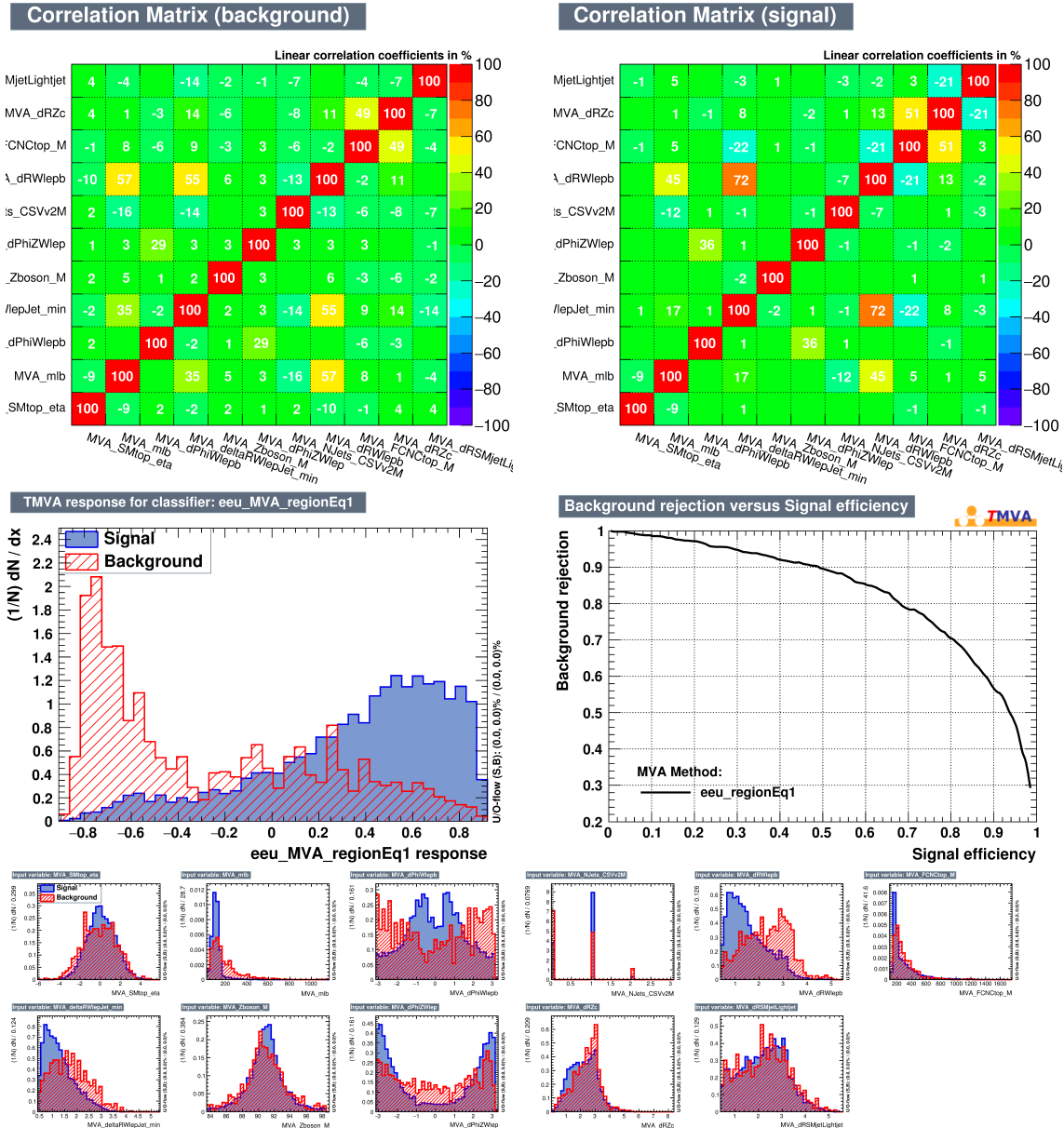


Figure C.5: 3e channel. TTSR: tZu vertex

Figure C.6: 2e1 μ channel. TTSR: tZu vertex

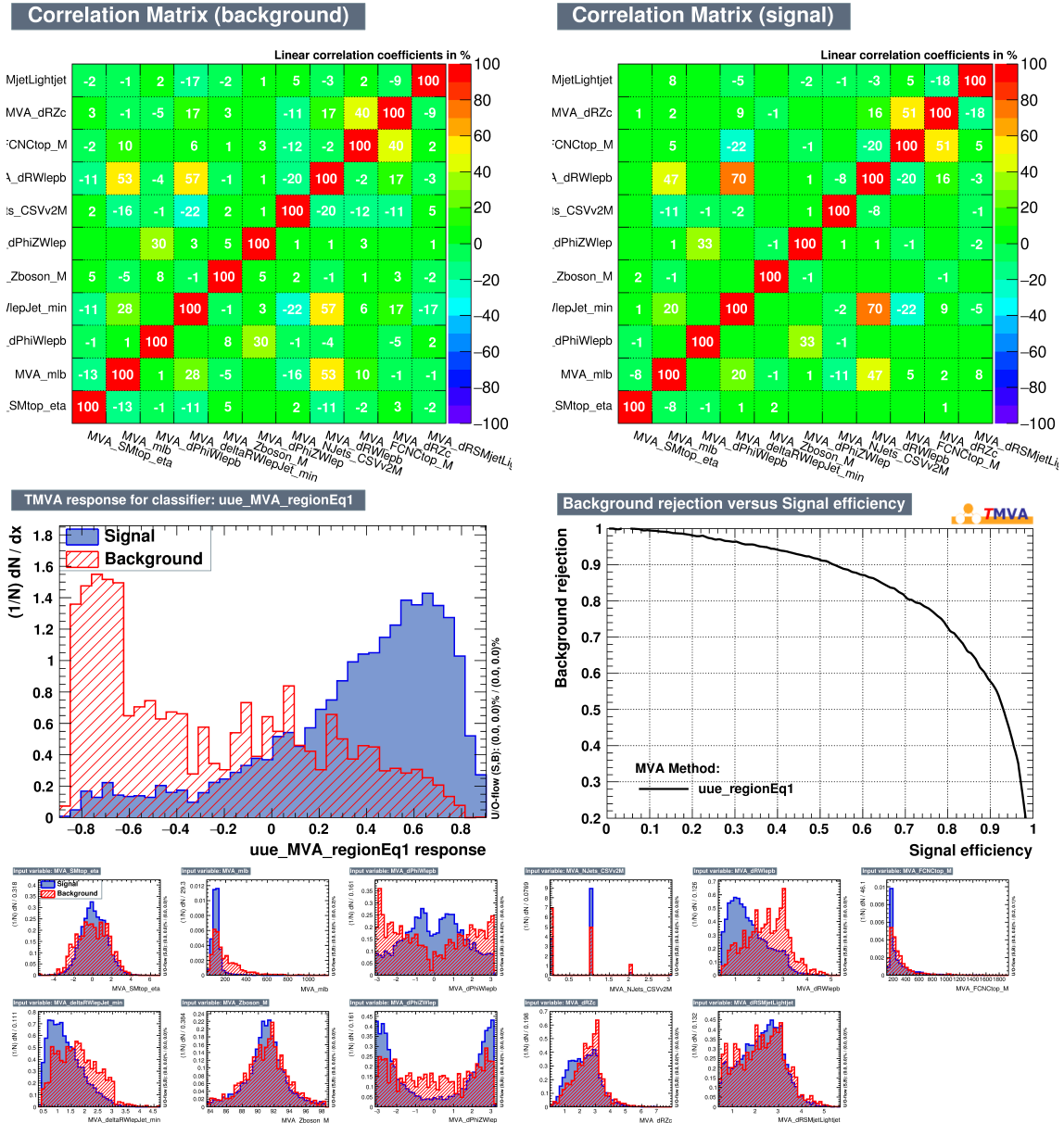
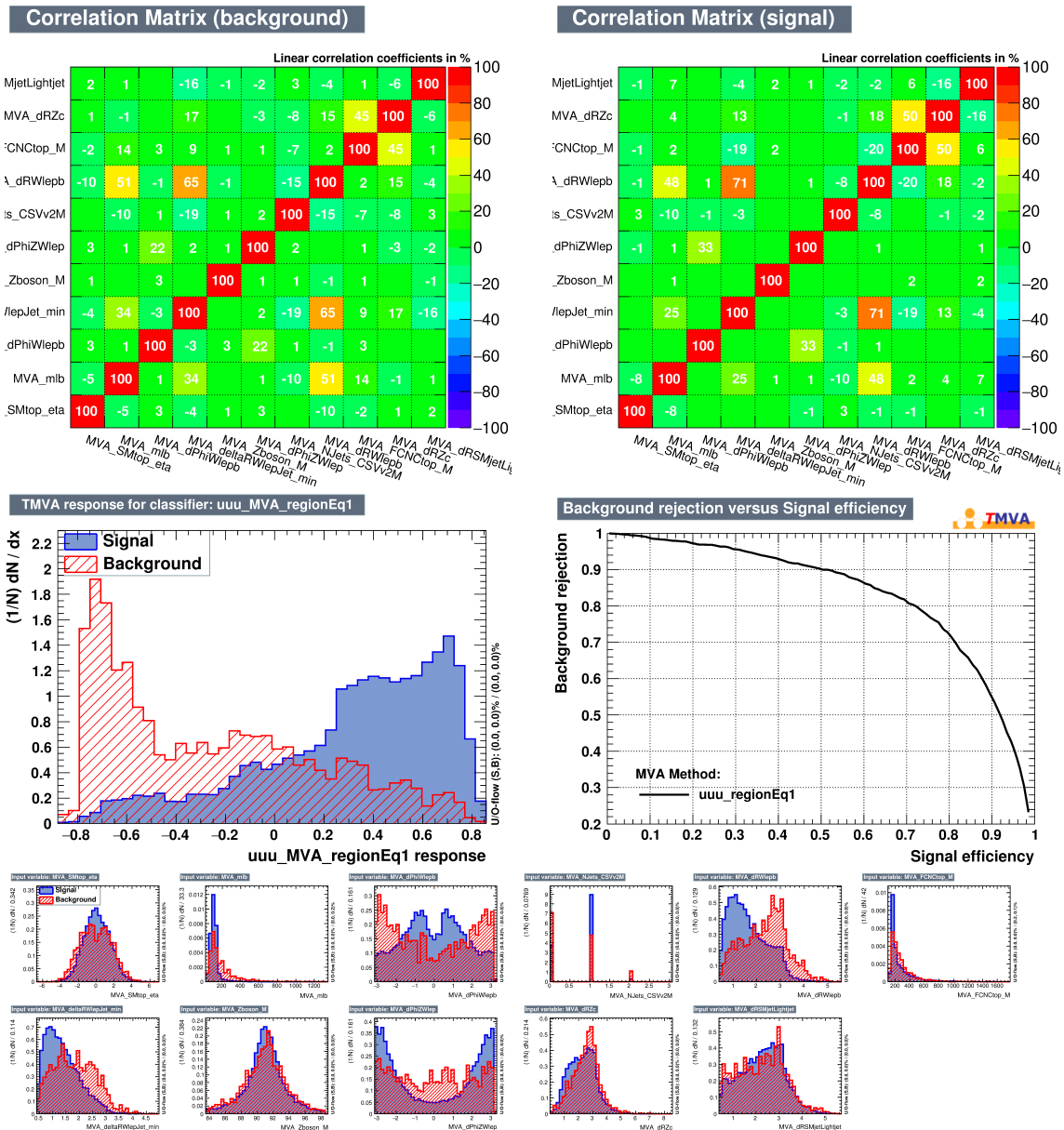


Figure C.7: 1e2μ channel. TTSR: tZu vertex

Figure C.8: 3 μ channel. TTSR: tZu vertex

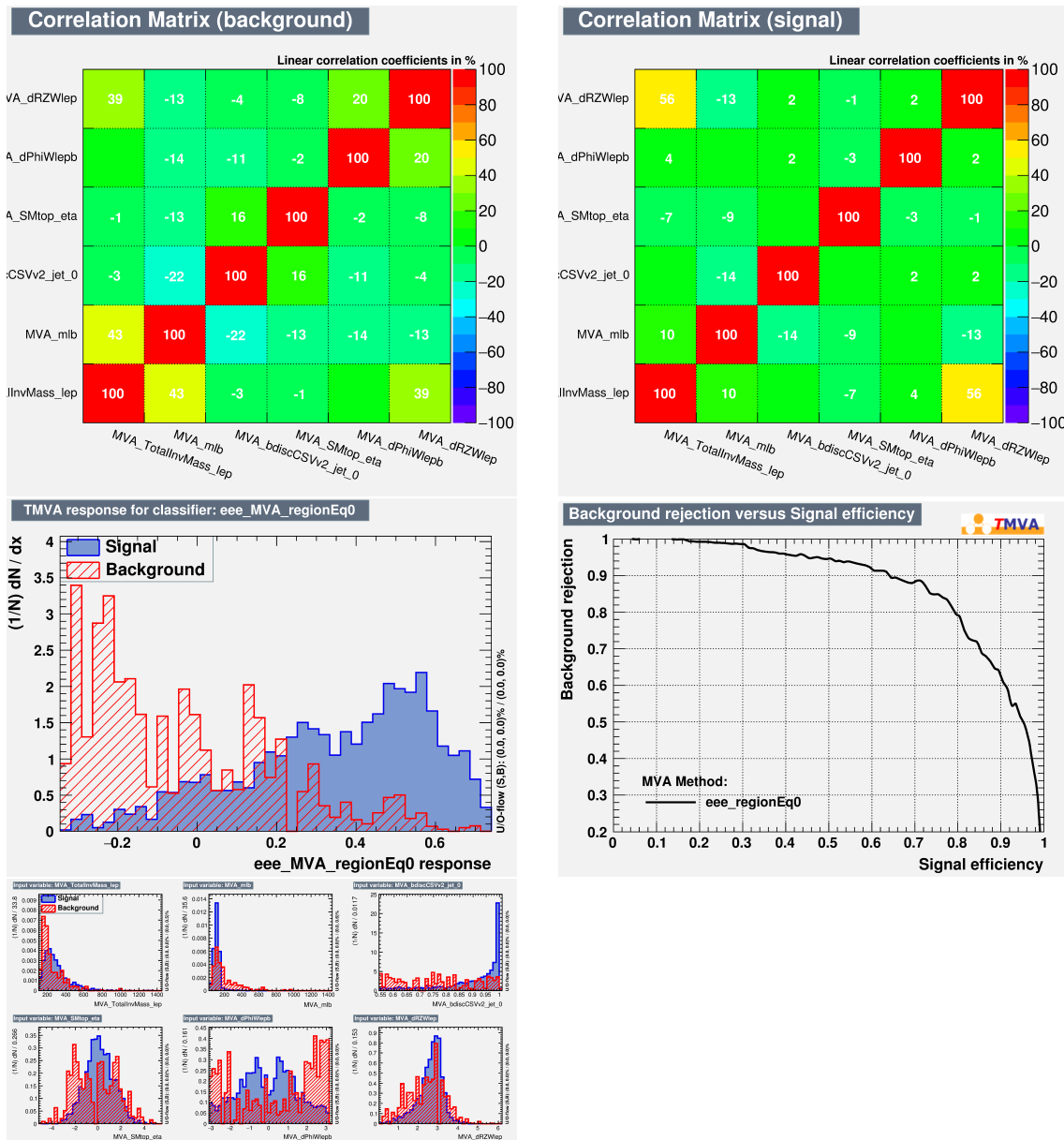
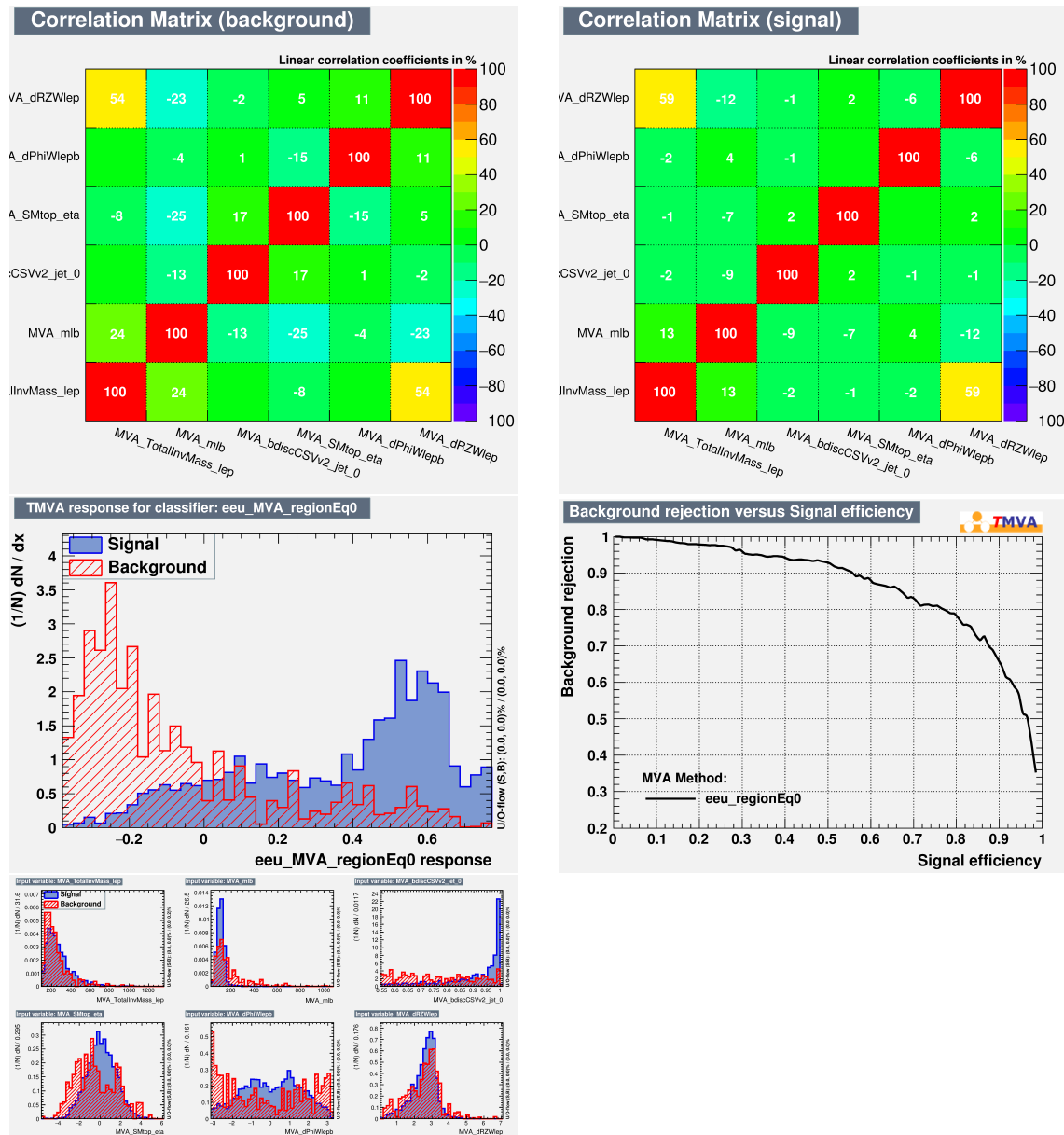
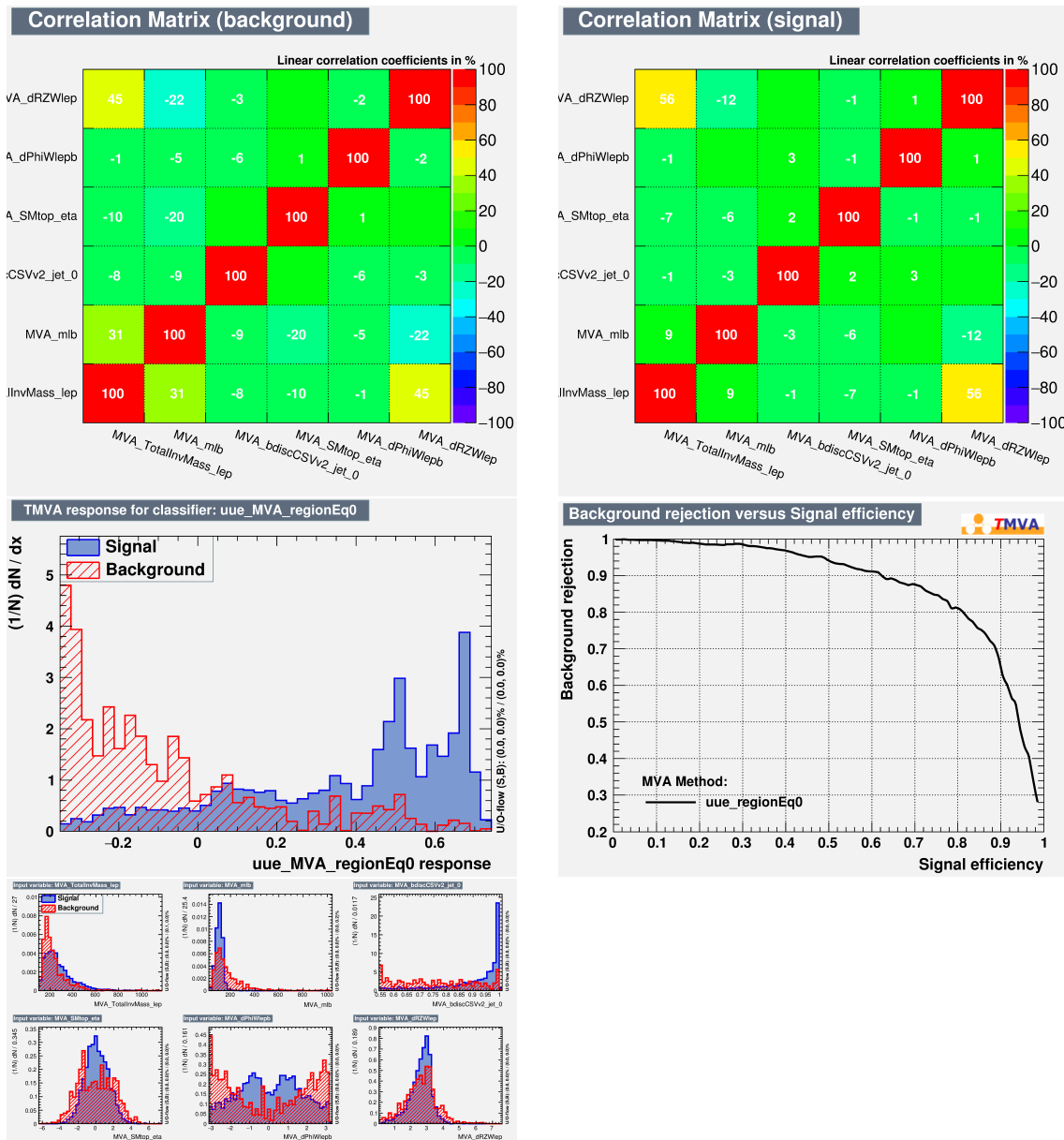
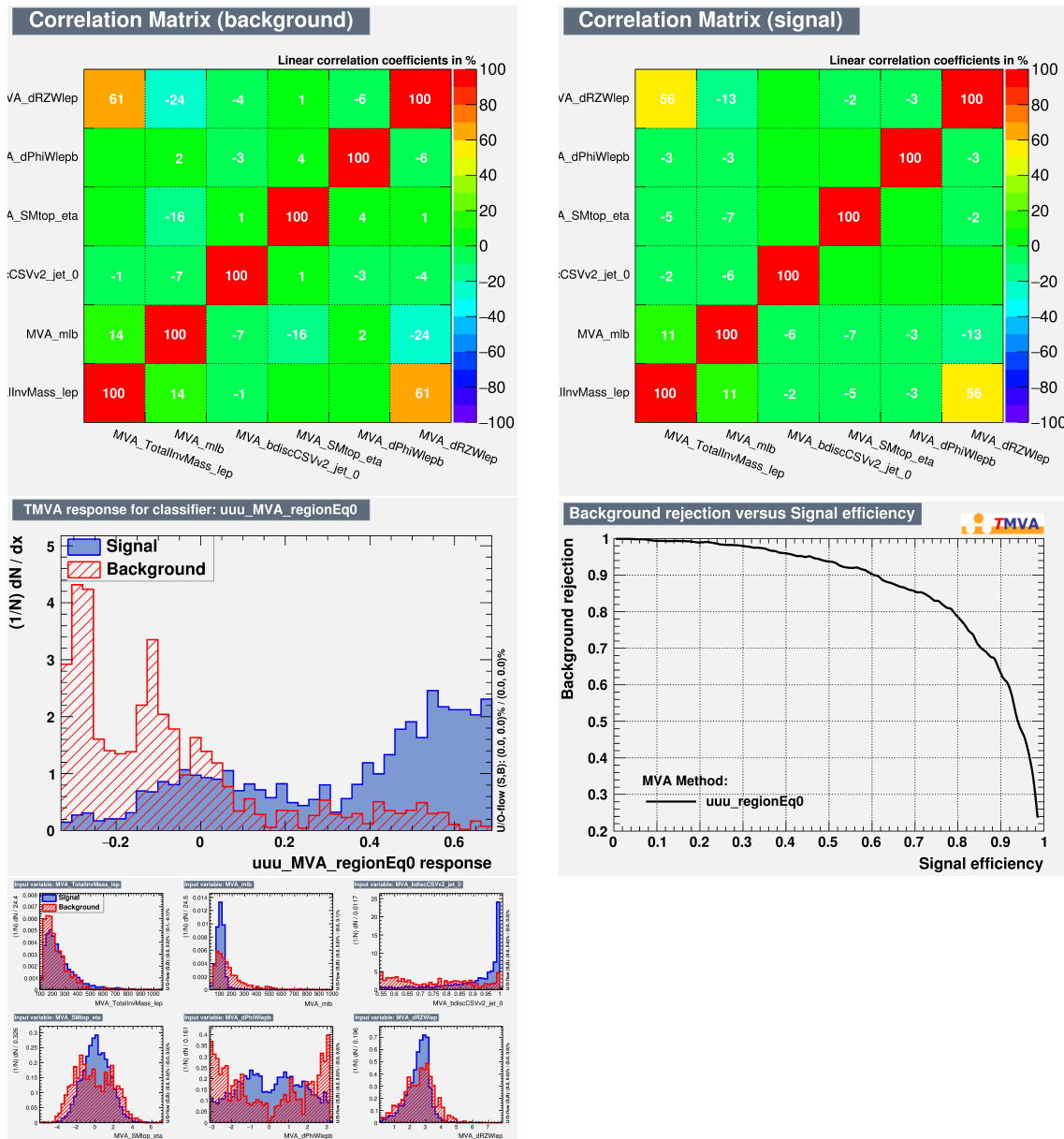


Figure C.9: 3e channel. STSR: tZc vertex

Figure C.10: 2e1 μ channel. STSR: tZc vertex

Figure C.11: 1e2 μ channel. STSR: tZc vertex

Figure C.12: 3 μ channel. STSR: tZc vertex

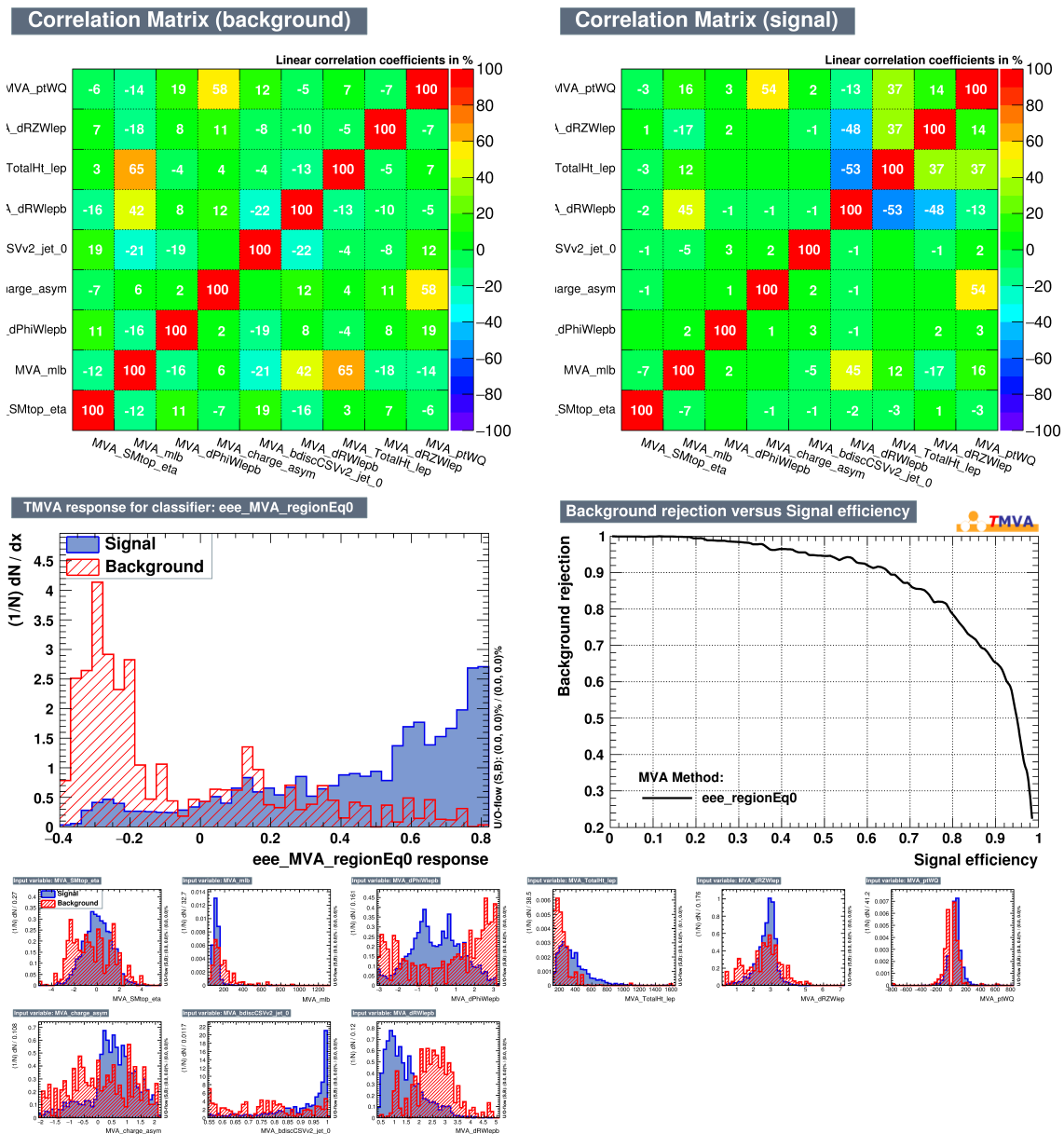
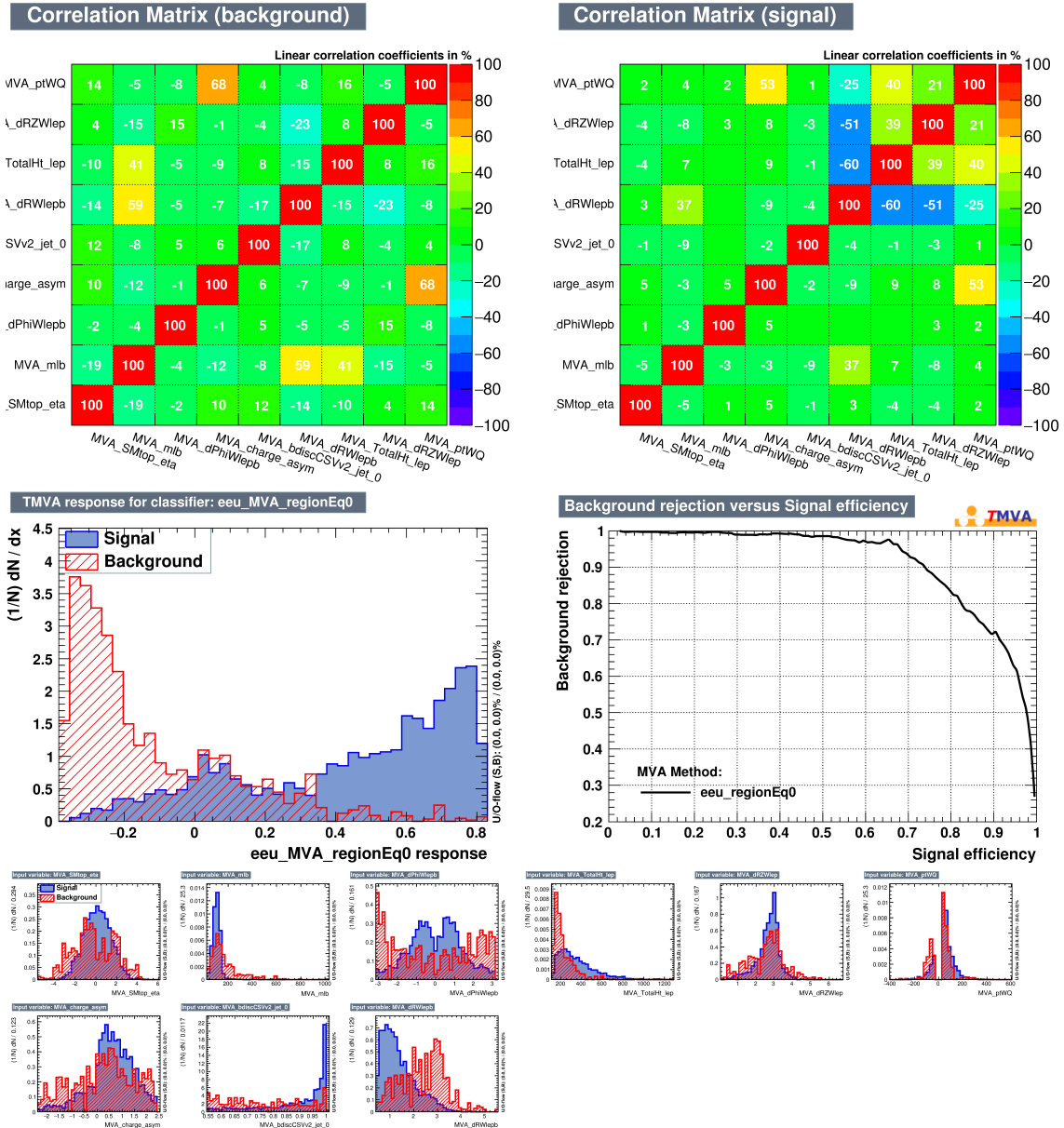
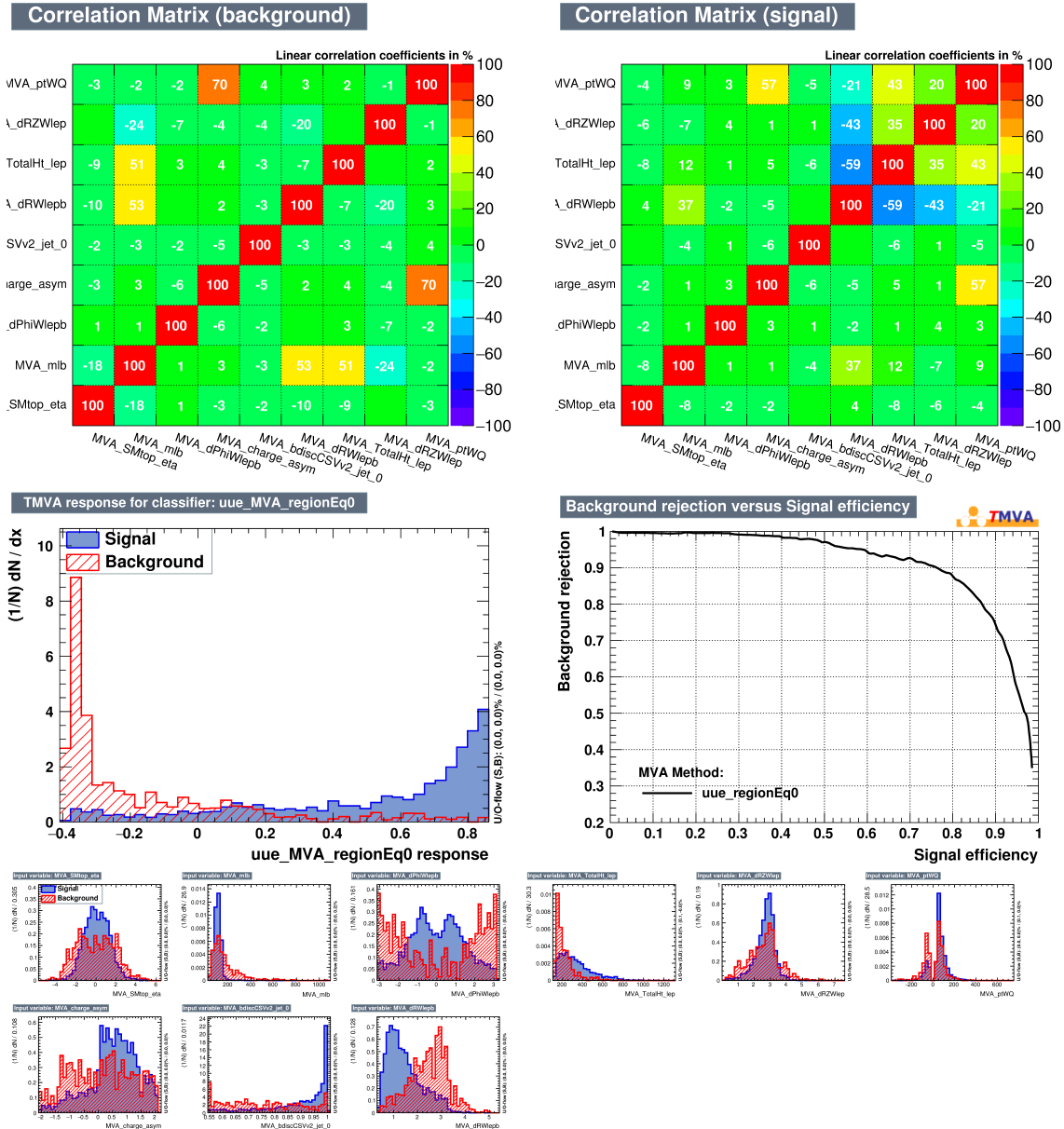
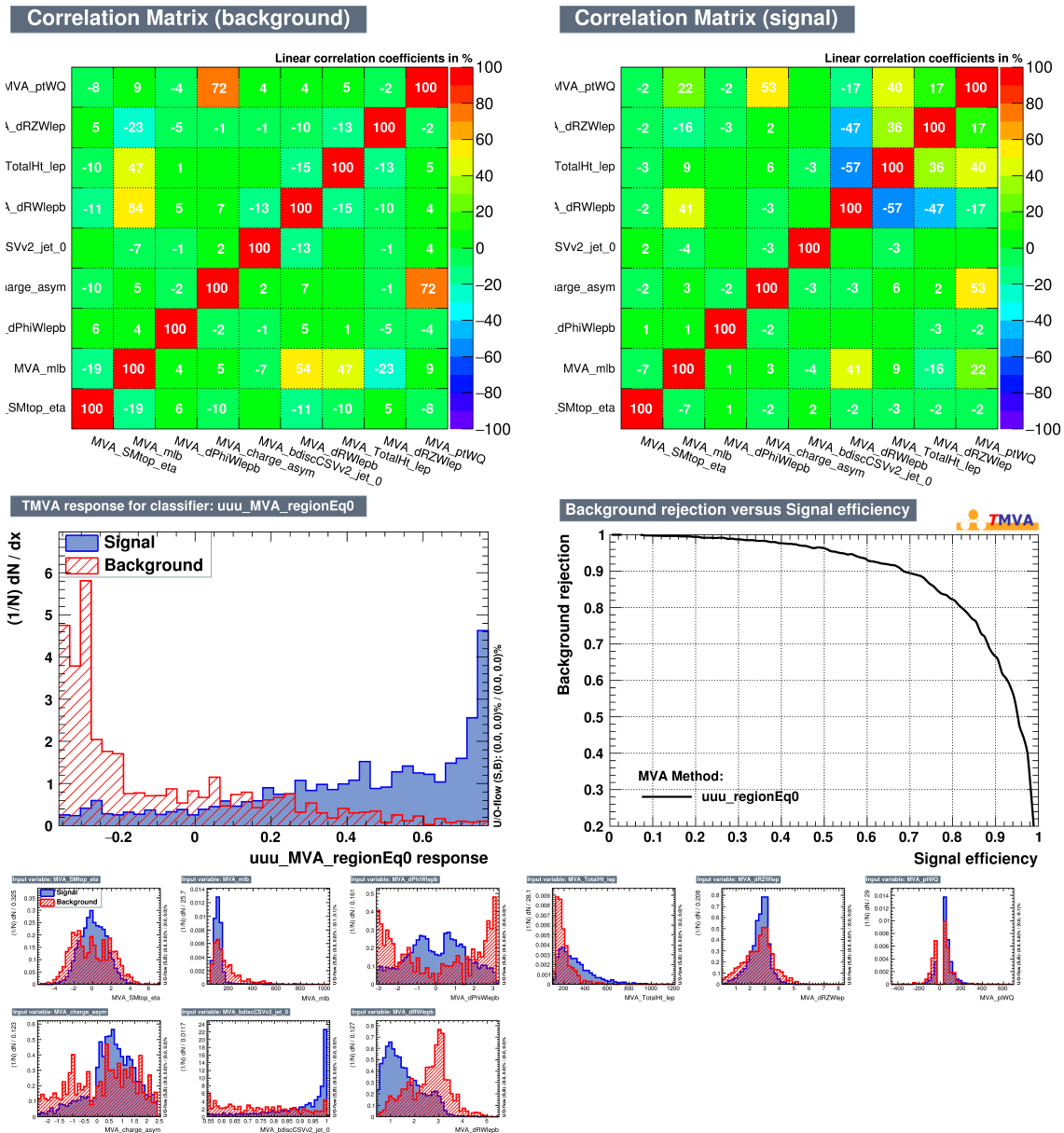


Figure C.13: 3e channel. STSR: tZu vertex

Figure C.14: 2e1 μ channel. STSR: tZu vertex

Figure C.15: 1e2 μ channel. STSR: tZu vertex

Figure C.16: 3 μ channel. STSR: tZu vertex

Limit setting details

D

D.1 BDT input variables for the tZc interaction

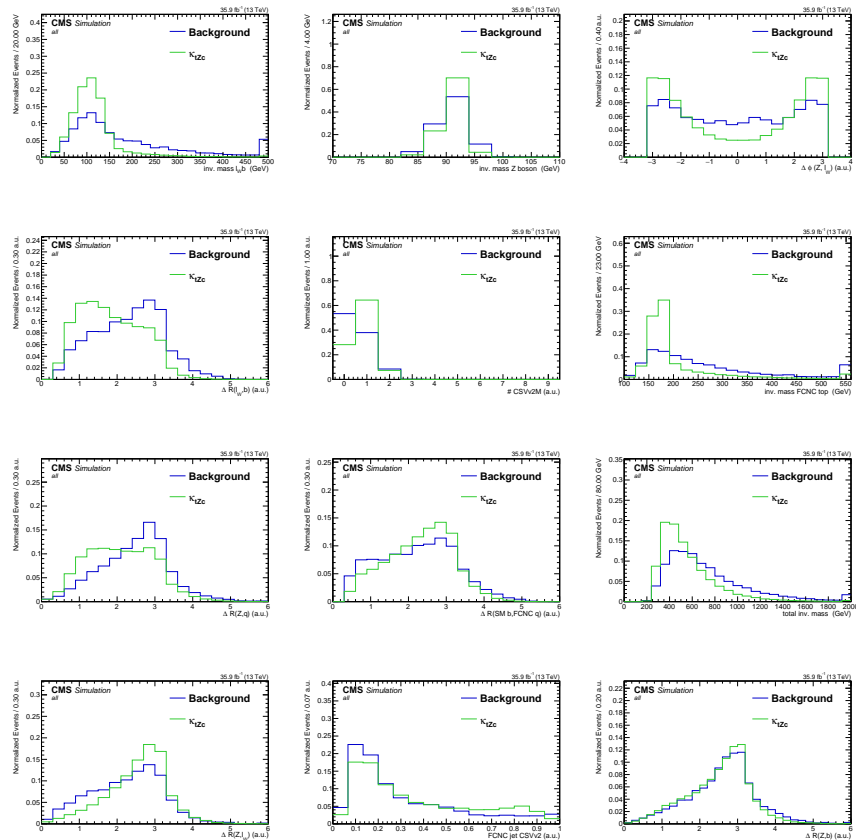


Figure D.1: The normalised input variables for reconstructing the multivariate discriminator in the TTSR for the tZc vertex.

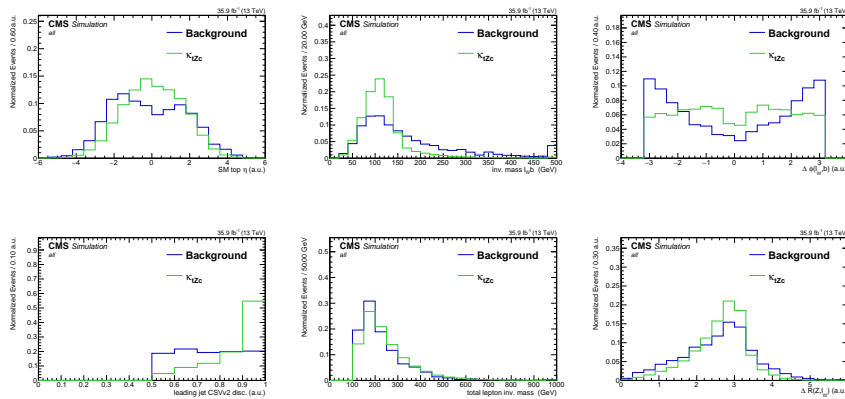


Figure D.2: The normalised input variables for reconstructing the multivariate discriminator in the STSR for the tZc vertex.

D.2 Effect of the systematic uncertainties

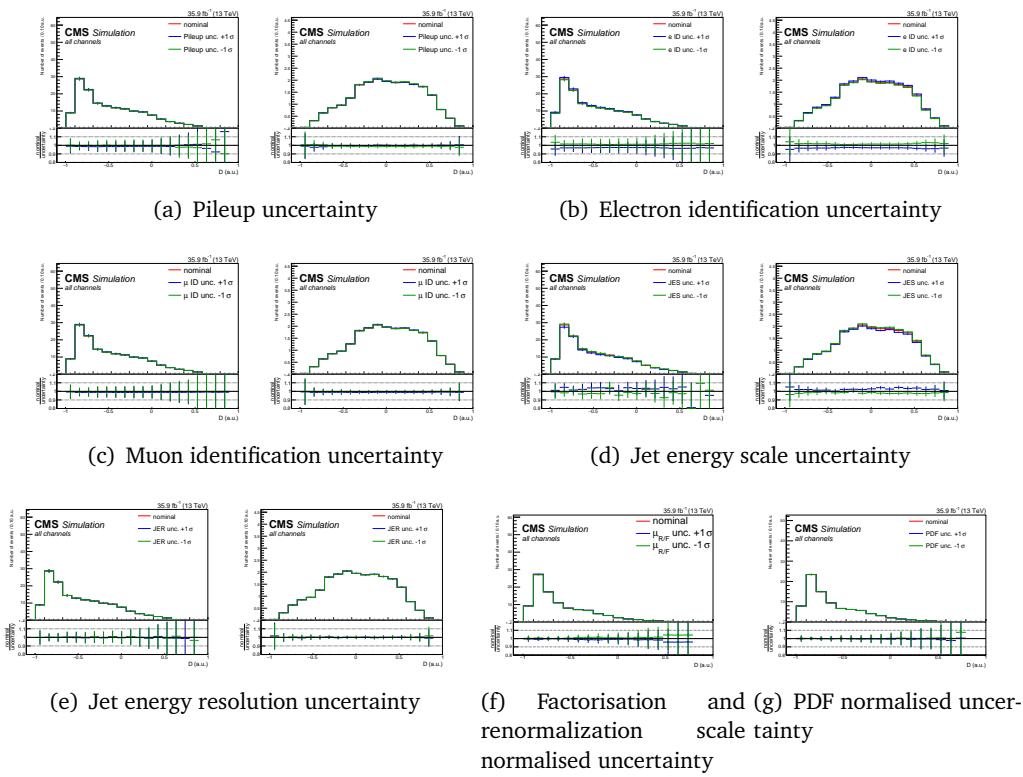


Figure D.3: Distribution of the nominal values and shift due to systematic uncertainties for the transverse mass of the W boson in the TTSR for the WZ process and FCNC signal involving a tZu vertex. All lepton channels summed. Part one.

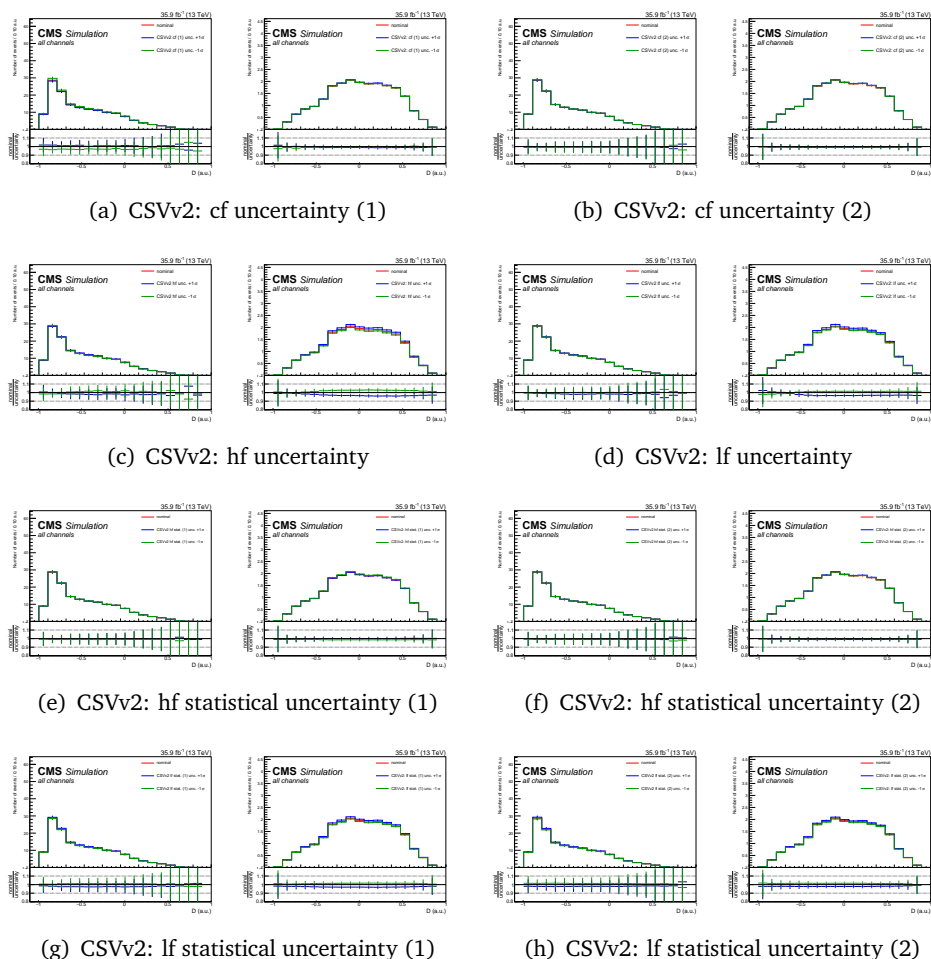


Figure D.4: Distribution of the nominal values and shift due to systematic uncertainties for the transverse mass of the W boson in the TTSR for the WZ process and FCNC signal involving a tZu vertex. All lepton channels summed. Part two.

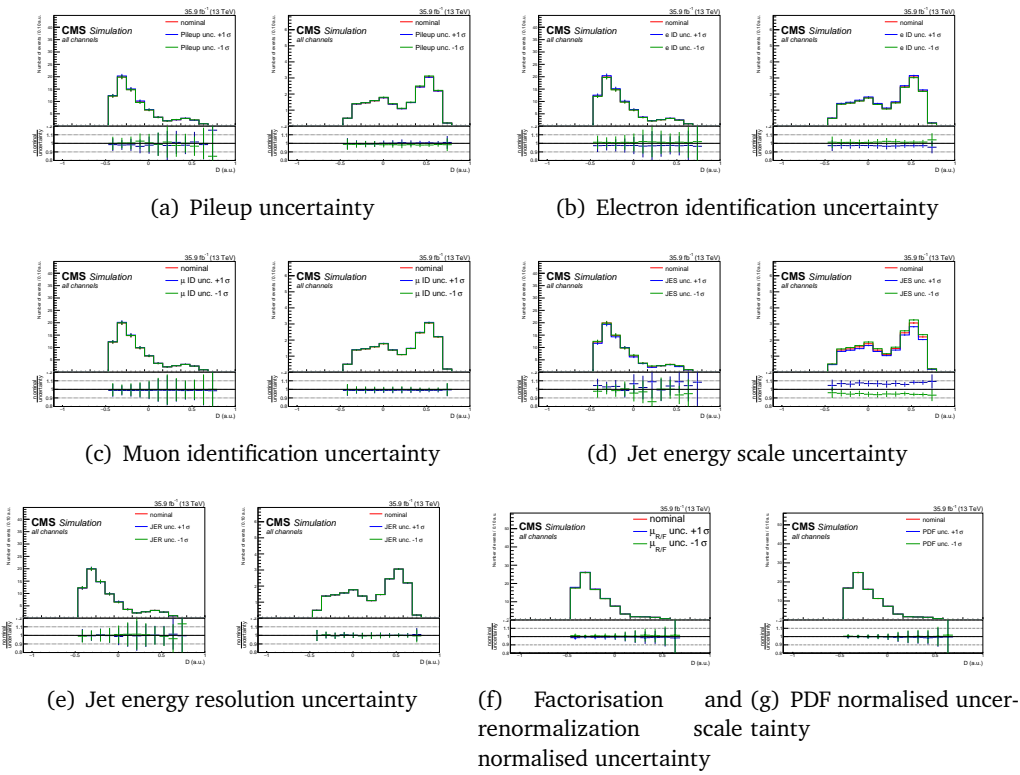


Figure D.5: Distribution of the nominal values and shift due to systematic uncertainties for the transverse mass of the W boson in the STSR for the WZ process and FCNC signal involving a tZc vertex. All lepton channels summed. Part one.

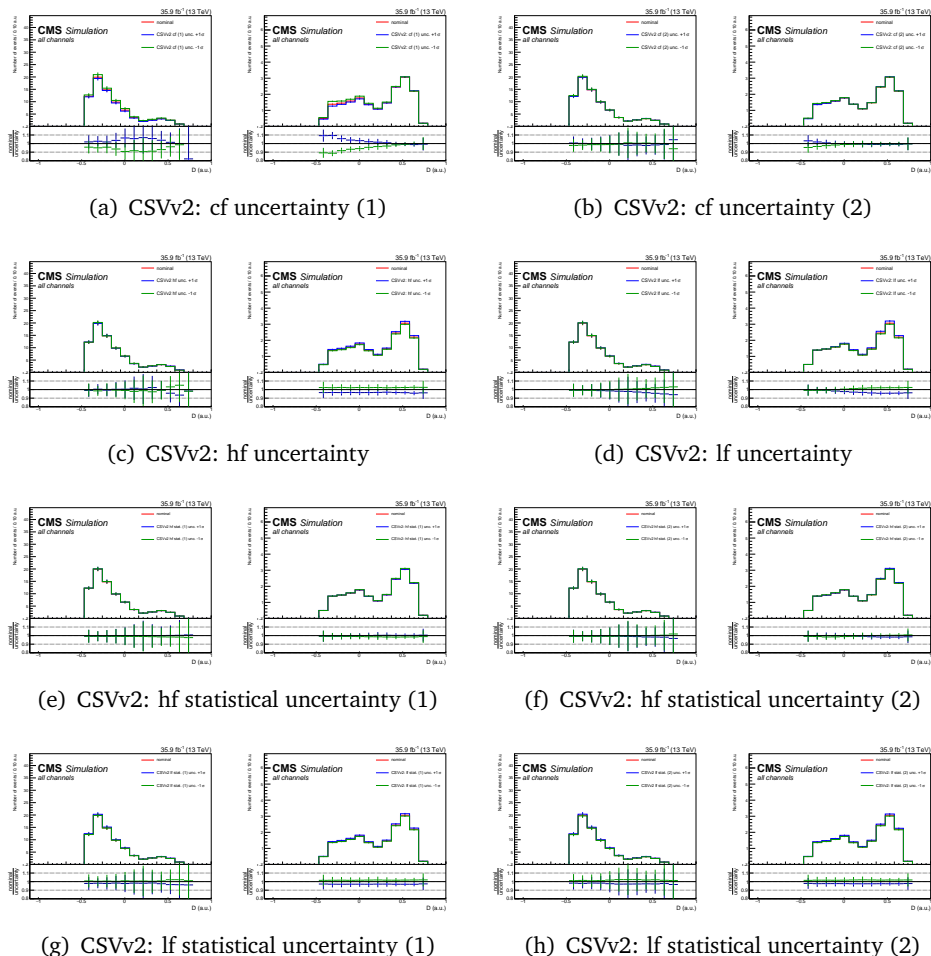


Figure D.6: Distribution of the nominal values and shift due to systematic uncertainties for the transverse mass of the W boson in the STSR for the WZ process and FCNC signal involving a tZc vertex. All lepton channels summed. Part two.

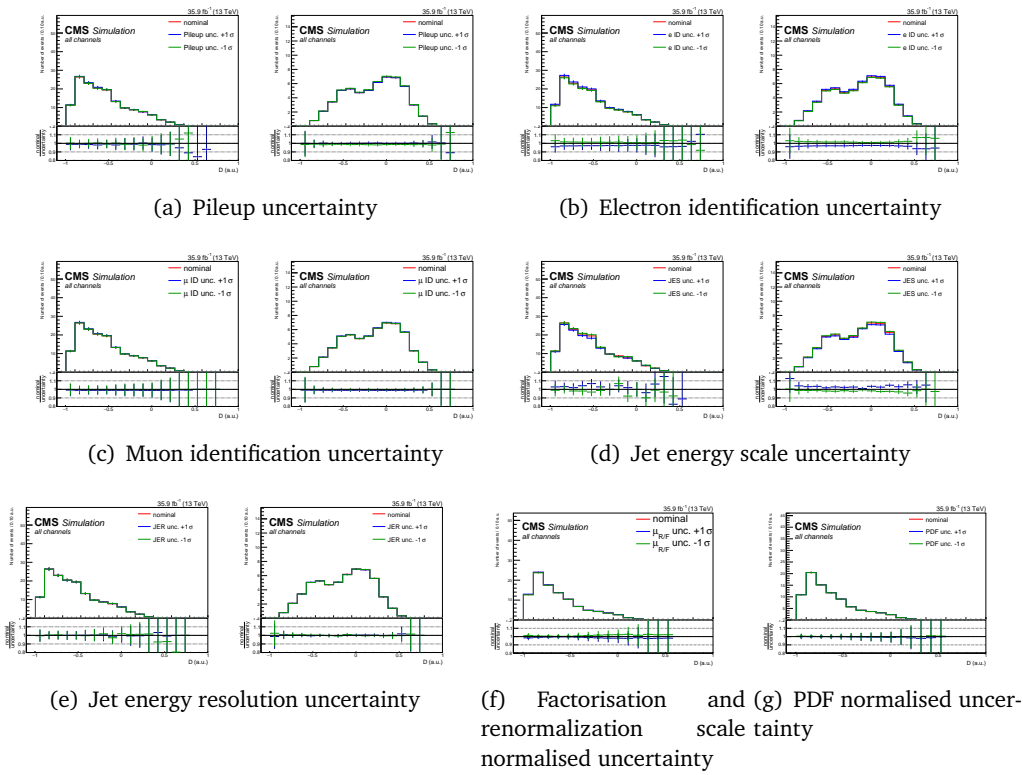


Figure D.7: Distribution of the nominal values and shift due to systematic uncertainties for the transverse mass of the W boson in the TTSR for the WZ process and FCNC signal involving a tZc vertex. All lepton channels summed. Part one.

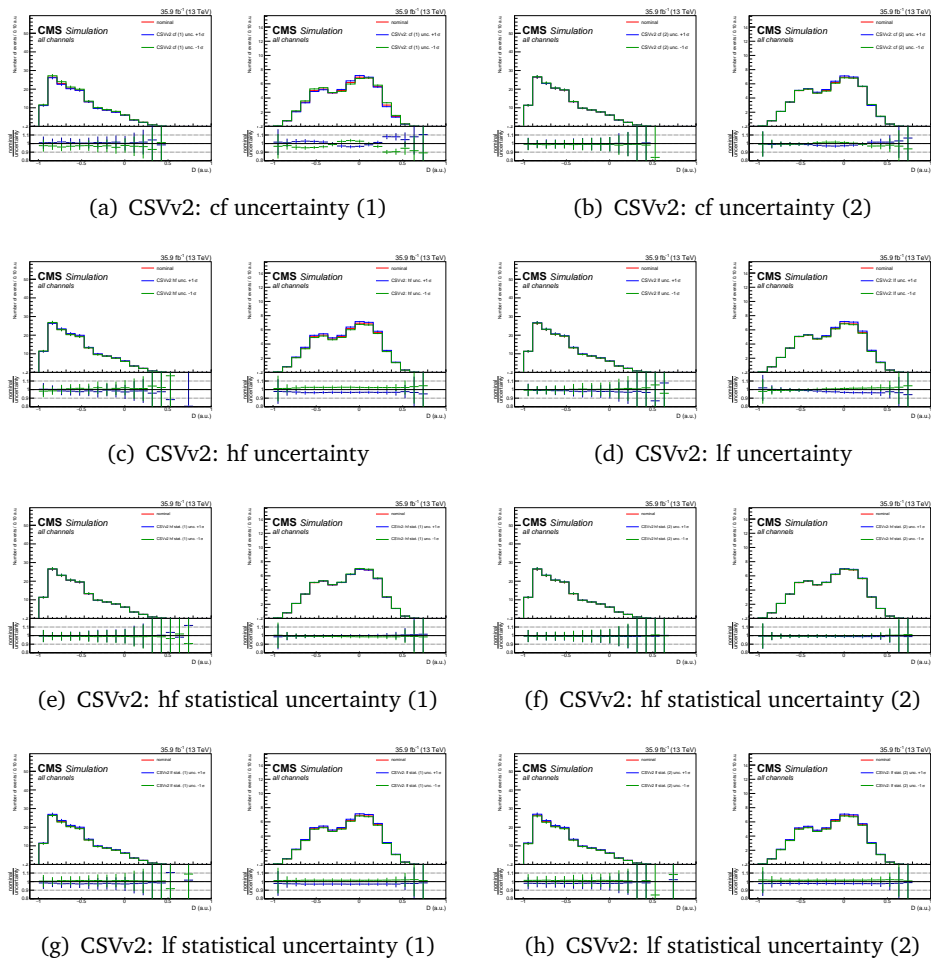


Figure D.8: Distribution of the nominal values and shift due to systematic uncertainties for the transverse mass of the W boson in the TTSR for the WZ process and FCNC signal involving a tZc vertex. All lepton channels summed. Part two.

D.3 Postfit distributions

D.3.1 Nuisance parameters

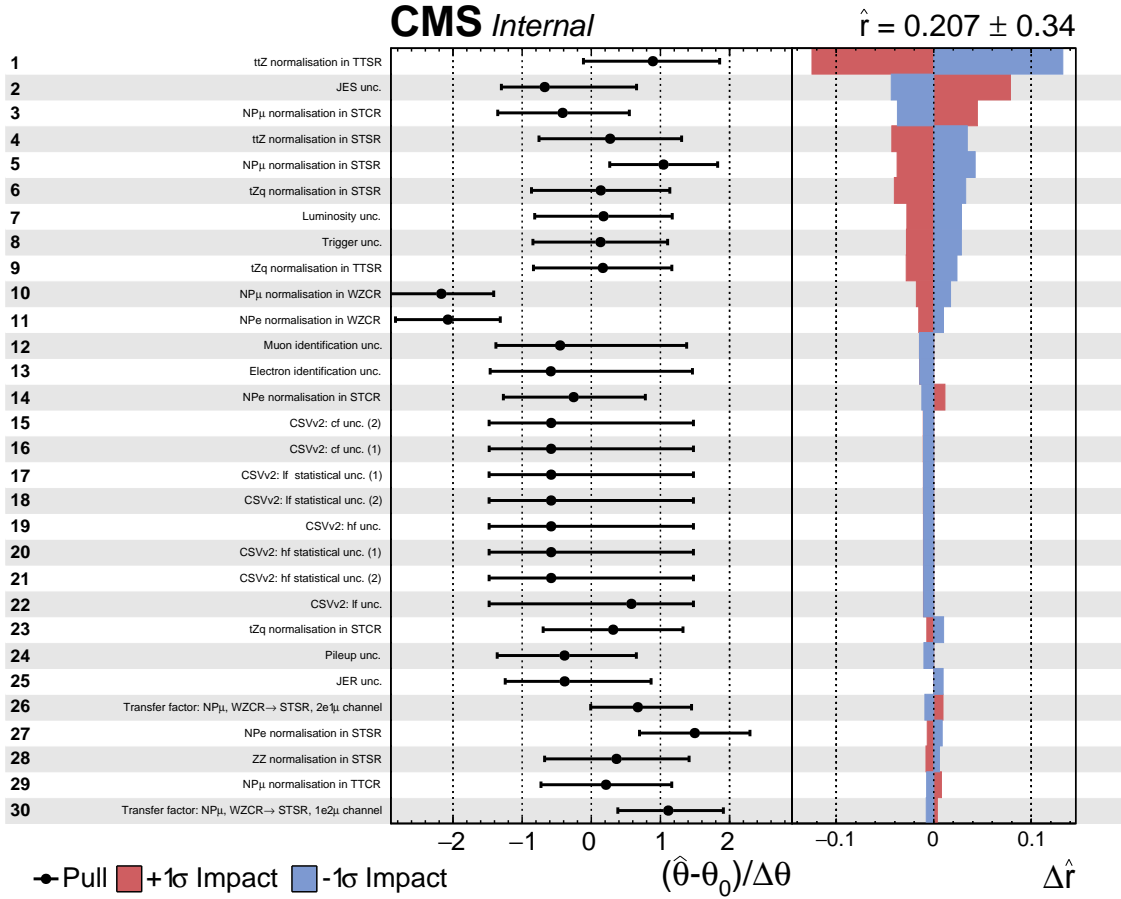


Figure D.9: The pulls of each nuisance parameter and the influence of their uncertainty on the maximum likelihood estimation of the signal strength \hat{r} for the tZ vertex, part one.

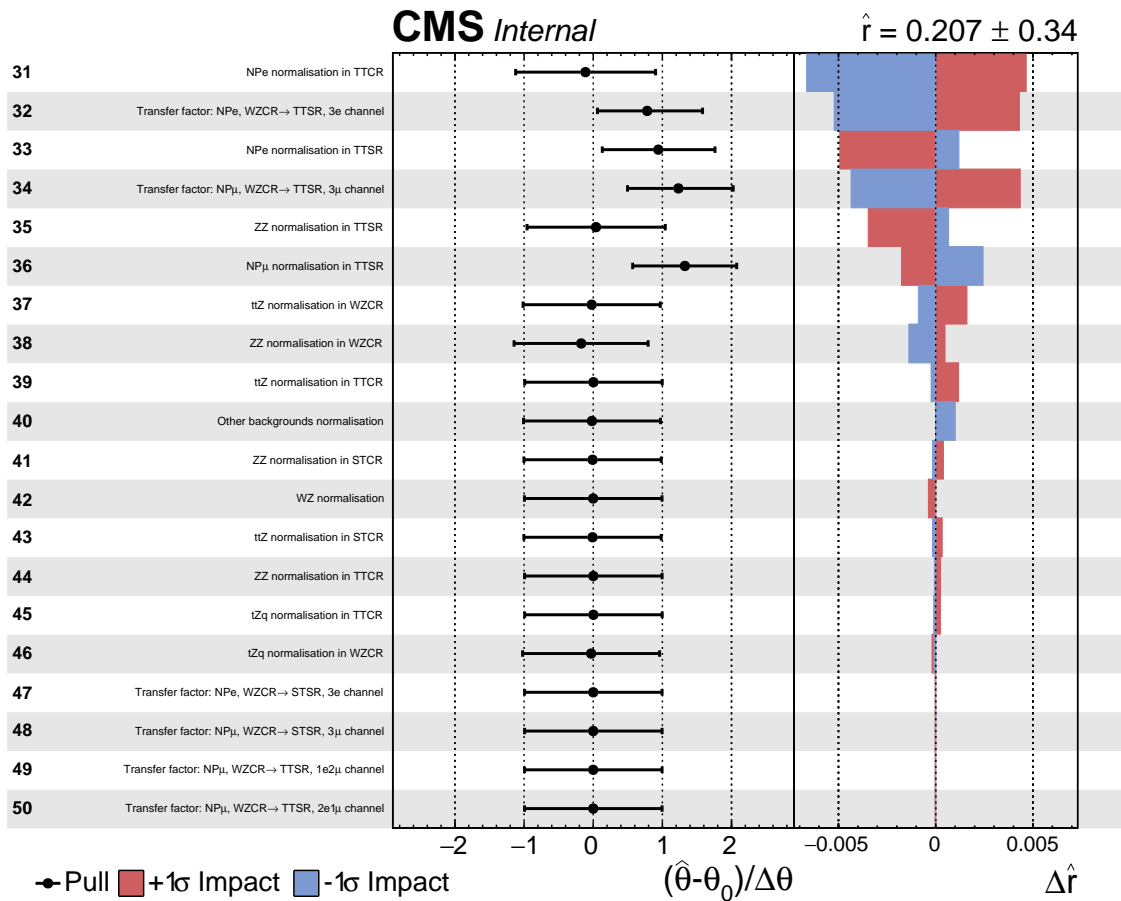


Figure D.10: The pulls of each nuisance parameter and the influence of their uncertainty on the maximum likelihood estimation of the signal strength \hat{r} for the tZu vertex, part two.

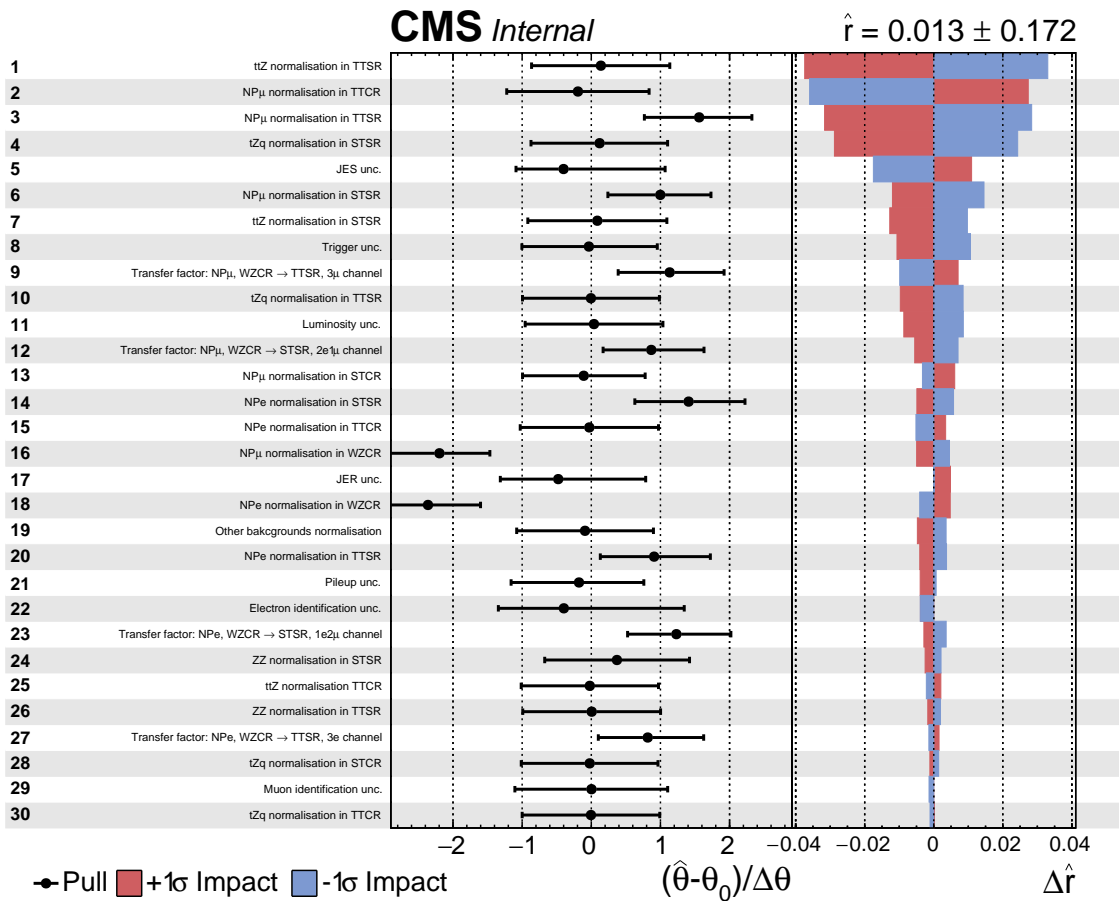


Figure D.11: The pulls of each nuisance parameter and the influence of their uncertainty on the maximum likelihood estimation of the signal strength \hat{r} for the tZc vertex, part one.

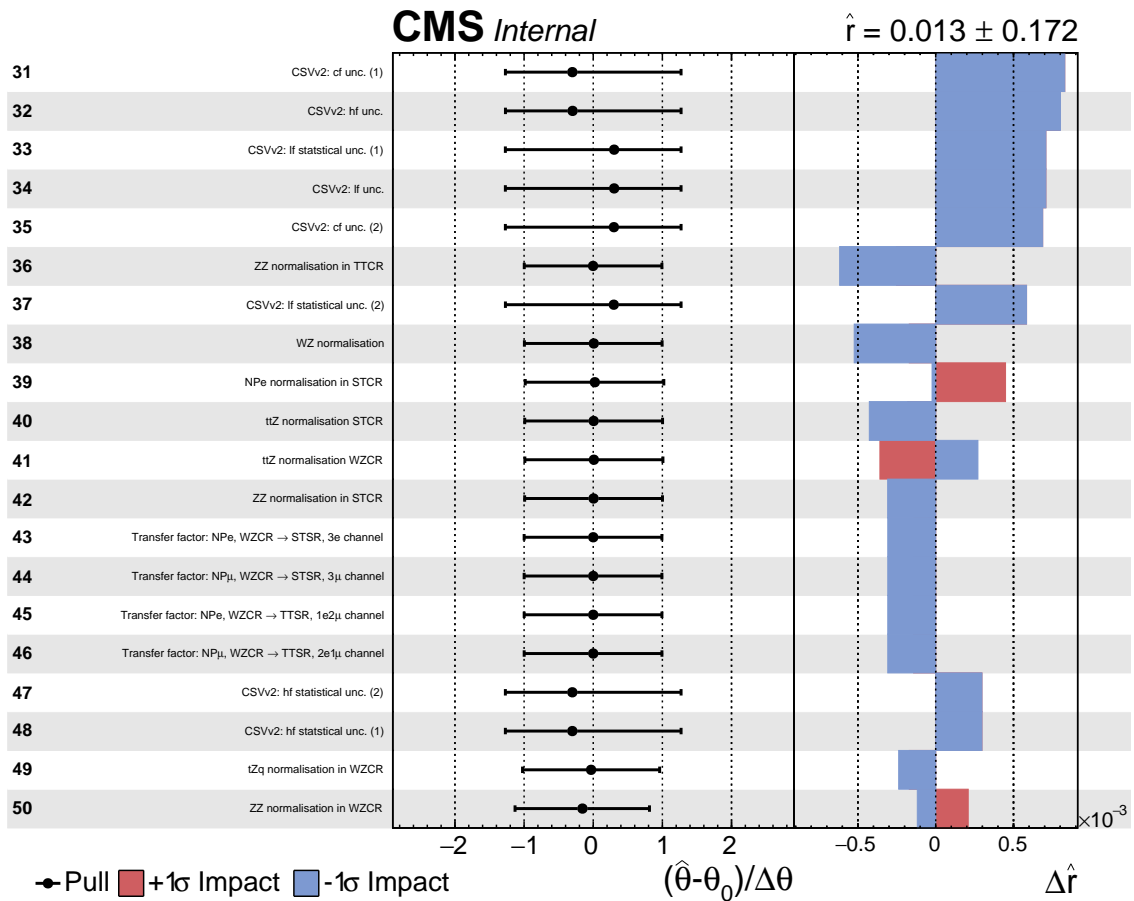


Figure D.12: The pulls of each nuisance parameter and the influence of their uncertainty on the maximum likelihood estimation of the signal strength \hat{r} for the tZc vertexg, part two.

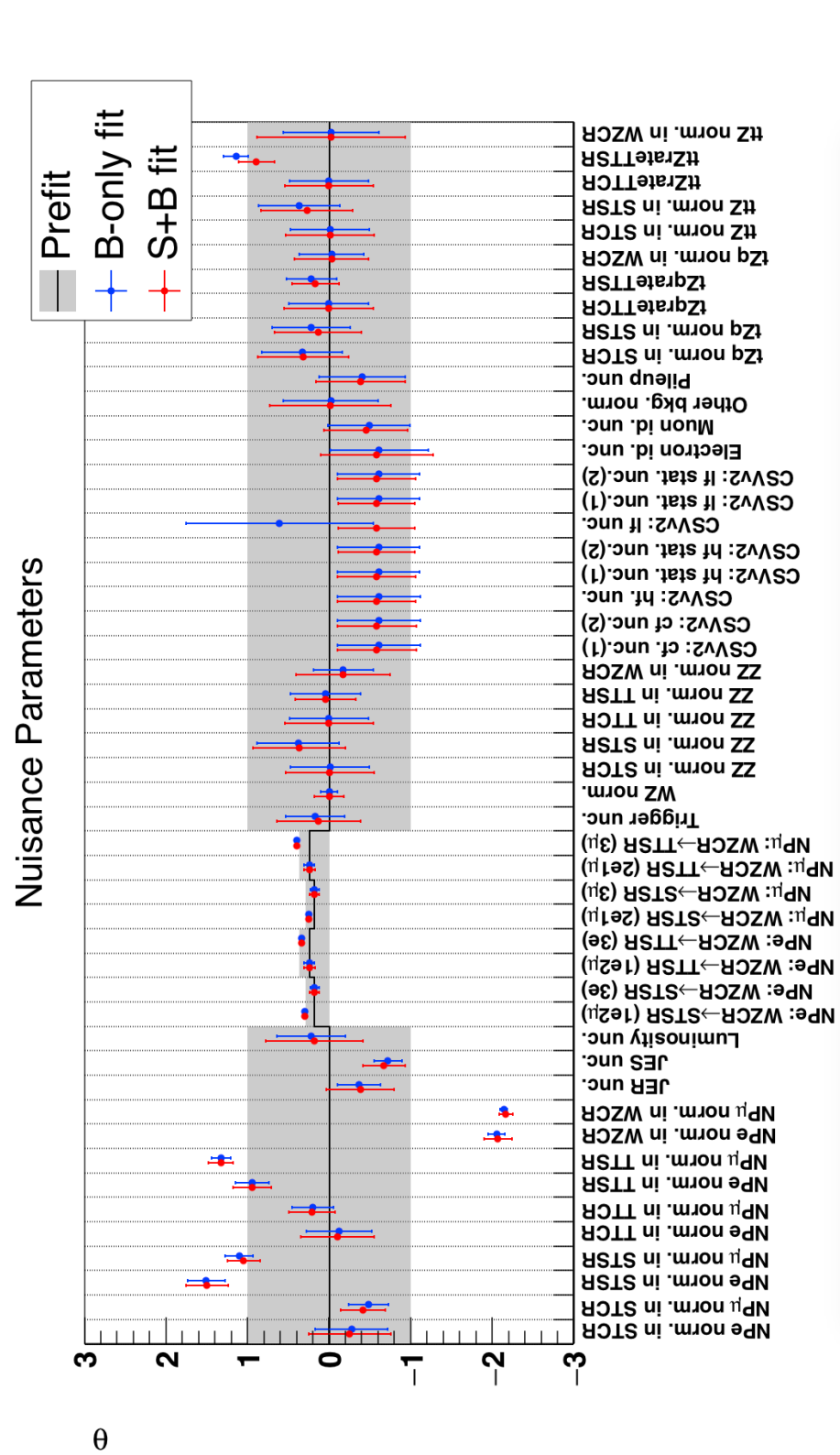


Figure D.13: Maximum likelihood estimators for the tZu vertex.

D.3.2 Postfit yields

Table D.1: Event yields for the tZc vertex in the STCR, all lepton channels summed.

Process	Prefit yield	Postfit yield	Factor (Post/pre)
NPL t̄t-like	33.00 ± 8.48	23.60 ± 3.11	0.72
t̄tZ	0.18 ± 0.21	0.24 ± 1.66	1.36
WZ	3.52 ± 0.25	3.66 ± 0.26	1.04
ZZ	0.31 ± 0.10	0.34 ± 0.07	1.09
Other backgrounds	1.66 ± 0.91	1.95 ± 1.01	1.17
tZq	0.31 ± 0.06	0.30 ± 0.04	0.95
κ_{tZc}/Λ	0.32 ± 0.03	0.00 ± 0.03	0.01
Data	32.00 ± 3.28	32.00 ± 3.28	1.00
Total background.	38.98 ± 8.67	30.09 ± 3.76	0.77

Table D.2: Event yields for the tZc vertex in the STSR, all lepton channels summed.

Process	Prefit yield	Postfit yield	Factor (Post/pre)
NPL Z/ γ^* + jets-like	6.12 ± 1.41	92.81 ± 4.27	15.17
t̄tZ	3.51 ± 0.34	3.70 ± 0.25	1.05
WZ	6.10 ± 0.66	7.02 ± 0.35	1.15
ZZ	4.60 ± 0.53	5.56 ± 0.47	1.21
Other backgrounds	1.25 ± 0.25	1.25 ± 0.13	1.00
tZq	8.03 ± 0.47	8.73 ± 0.28	1.09
NPL t̄t-like	9.33 ± 1.55	11.31 ± 0.61	1.21
κ_{tZc}/Λ	18.52 ± 0.30	0.24 ± 0.46	0.01
Data	138.00 ± 14.97	138.00 ± 14.97	1.00
Total background.	38.94 ± 2.70	130.38 ± 4.38	3.35

Table D.3: Event yields for the tZc vertex in the TTCR, all lepton channels summed.

Process	Prefit yield	Postfit yield	Factor (Post/pre)
NPL tt-like	29.00 ± 9.62	31.71 ± 4.07	1.09
t̄Z	2.85 ± 0.44	2.85 ± 0.27	1.00
WZ	3.98 ± 0.63	4.24 ± 0.69	1.07
ZZ	0.32 ± 0.08	0.33 ± 0.05	1.05
Other backgrounds	3.88 ± 0.66	3.79 ± 0.80	0.98
tZq	0.79 ± 0.13	0.78 ± 0.07	1.00
κ_{tZc}/Λ	0.59 ± 0.05	0.01 ± 0.05	0.01
Data	43.50 ± 3.28	43.50 ± 3.28	1.00
Total background.	40.81 ± 9.87	43.72 ± 4.15	1.07

Table D.4: Event yields for the tZc vertex in the TTSR, all lepton channels summed.

Process	Prefit yield	Postfit yield	Factor (Post/pre)
NPL Z/ γ^* + jets-like	9.36 ± 1.62	134.88 ± 5.19	14.41
t̄Z	42.55 ± 2.28	47.79 ± 1.40	1.12
WZ	12.46 ± 1.12	14.20 ± 0.62	1.14
ZZ	4.84 ± 0.35	5.05 ± 0.26	1.04
Other backgrounds	5.62 ± 0.82	5.62 ± 0.85	1.00
tZq	16.93 ± 0.89	17.57 ± 0.51	1.04
NPL tt-like	8.00 ± 1.07	17.45 ± 0.91	2.18
κ_{tZc}/Λ	56.85 ± 0.57	0.72 ± 1.32	0.01
Data	243.00 ± 19.21	243.00 ± 19.21	1.00
Total background.	99.76 ± 4.05	242.56 ± 5.58	2.43

Table D.5: Event yields for the tZc vertex in the WZCR, all lepton channels summed.

Process	Prefit yield	Postfit yield	Factor (Post/pre)
NPL Z/ γ^* + jets-like	204.00 ± 22.12	413.95 ± 12.56	2.03
t̄Z	9.57 ± 0.69	9.97 ± 0.55	1.04
WZ	551.63 ± 29.26	589.05 ± 12.67	1.07
ZZ	46.19 ± 2.40	44.25 ± 1.59	0.96
Other backgrounds	6.75 ± 0.99	6.86 ± 0.85	1.02
tZq	7.30 ± 0.45	7.36 ± 0.21	1.01
κ_{tZc}/Λ	26.34 ± 0.51	0.34 ± 0.64	0.01
Data	1053.00 ± 34.45	1053.00 ± 34.45	1.00
Total background.	825.44 ± 37.24	1071.45 ± 20.64	1.30

Table D.6: Event yields for the tZ_u vertex in the STCR, all lepton channels summed.

Process	Prefit yield	Postfit yield	Factor (Post/pre)
NPL tt-like	33.00 ± 9.88	25.33 ± 3.66	0.77
t̄Z	0.18 ± 0.23	0.38 ± 0.59	2.12
WZ	3.52 ± 0.27	3.82 ± 0.20	1.09
ZZ	0.31 ± 0.08	0.38 ± 0.05	1.22
Other backgrounds	1.66 ± 1.05	2.50 ± 0.42	1.51
tZq	0.31 ± 0.05	0.29 ± 0.04	0.92
κ_{tZu}/Λ	0.42 ± 0.03	0.09 ± 0.01	0.20
Data	32.00 ± 3.28	32.00 ± 3.28	1.00
Total background.	38.98 ± 10.28	32.70 ± 3.78	0.84

Table D.7: Event yields for the tZ_u vertex in the STSR, all lepton channels summed.

Process	Prefit yield	Postfit yield	Factor (Post/pre)
NPL Z/ γ^* + jets-like	6.12 ± 1.58	80.64 ± 4.44	13.18
t̄Z	3.53 ± 0.37	3.91 ± 0.23	1.11
WZ	6.10 ± 0.71	7.79 ± 0.15	1.28
ZZ	4.60 ± 0.60	6.21 ± 0.40	1.35
Other backgrounds	1.25 ± 0.30	1.31 ± 0.08	1.04
tZq	8.03 ± 0.45	8.92 ± 0.27	1.11
NPL tt-like	9.33 ± 1.39	16.13 ± 0.88	1.73
κ_{tZu}/Λ	11.25 ± 0.17	2.43 ± 0.09	0.22
Data	138.50 ± 14.19	138.50 ± 14.19	1.00
Total background.	38.97 ± 2.84	124.91 ± 4.61	3.21

Table D.8: Event yields for the tZ_u vertex in the TTCR, all lepton channels summed.

Process	Prefit yield	Postfit yield	Factor (Post/pre)
NPL tt-like	29.00 ± 9.99	28.92 ± 3.47	1.00
t̄Z	2.85 ± 0.48	2.93 ± 0.25	1.03
WZ	3.98 ± 0.65	4.71 ± 0.43	1.18
ZZ	0.32 ± 0.07	0.36 ± 0.04	1.14
Other backgrounds	3.88 ± 0.81	4.05 ± 0.31	1.04
tZq	0.79 ± 0.13	0.79 ± 0.07	1.01
κ_{tZu}/Λ	0.61 ± 0.05	0.13 ± 0.01	0.22
Data	44.00 ± 3.28	44.00 ± 3.28	1.00
Total background.	40.81 ± 10.34	41.76 ± 3.44	1.02

Table D.9: Event yields for the tZu vertex in the TTSR, all lepton channels summed.

Process	Prefit yield	Postfit yield	Factor (Post/pre)
NPL Z/ γ^* + jets-like	9.36 ± 1.67	113.23 ± 5.31	12.10
t \bar{t} Z	42.56 ± 2.31	62.23 ± 1.23	1.46
WZ	12.45 ± 1.06	15.70 ± 0.27	1.26
ZZ	4.84 ± 0.38	5.49 ± 0.12	1.13
Other backgrounds	5.62 ± 0.99	5.89 ± 0.44	1.05
tZq	16.92 ± 0.87	18.54 ± 0.24	1.10
NPL t \bar{t} -like	8.00 ± 1.03	10.93 ± 0.54	1.37
κ_{tZu}/Λ	21.76 ± 0.25	4.66 ± 0.15	0.21
Data	244.00 ± 19.96	244.00 ± 19.96	1.00
Total background.	99.75 ± 4.05	232.02 ± 5.65	2.33

Table D.10: Event yields for the tZu vertex in the WZCR, all lepton channels summed.

Process	Prefit yield	Postfit yield	Factor (Post/pre)
NPL Z/ γ^* + jets-like	204.00 ± 23.02	408.84 ± 13.11	2.00
t \bar{t} Z	9.57 ± 0.72	10.22 ± 0.36	1.07
WZ	551.63 ± 27.62	591.52 ± 11.22	1.07
ZZ	46.19 ± 2.42	44.46 ± 1.25	0.96
Other backgrounds	6.75 ± 1.11	7.40 ± 0.47	1.10
tZq	7.30 ± 0.44	7.47 ± 0.20	1.02
κ_{tZu}/Λ	14.12 ± 0.23	2.97 ± 0.13	0.21
Data	1053.00 ± 34.45	1053.00 ± 34.45	1.00
Total background.	825.44 ± 36.98	1069.91 ± 20.08	1.30

Vulgarising summaries



Summary

The Standard Model of particle physics is a theory of fundamental particles and their interactions. This theory has been experimentally confirmed and all particles predicted by this theory have been found. Nonetheless, this theory has its shortcomings and can not explain phenomena such as neutrino masses or gravity. The heaviest particle of the Standard Model is the top quark and physicists believe that it has an enhanced sensitivity to various new particles and interactions suggested by beyond the Standard Model theories. The top quark has a very short lifetime, so short that it doesn't form bound states and it can be used to study the bare quark. Furthermore, it has distinct signature since it almost exclusively decays to a W boson and a bottom quark. This makes the top quark an ideal candidate for the study of quark properties. Also, many beyond the Standard Model physics phenomena are researched by measuring the production rate of top quarks for studying the Wtb vertex, and interactions that are heavily suppressed in the Standard Model can be investigated. The Large Hadron Collider is a top quark factory, producing a large number of events containing top quarks. At the proton collision points, experiments are placed to study the collisions. The search presented in this thesis is performed on data collected by the Compact Muon Solenoid experiment at a centre-of-mass energy of 13 TeV, resulting in 35.9 fb^{-1} of integrated luminosity.

Flavour changing neutral currents are highly suppressed in the Standard Model. However, many beyond the Standard Model theories enhance their probability. In this thesis, a search in three lepton final states is performed for the production of single top quarks via the tZq vertex, with $q = c, u$, or the top quark pair processes where one of the top quarks decay through this vertex. No significant deviation with respect to the predicted background is observed and upper limits at 95% confidence level are placed. The observed (expected) upper limits at 95% confidence level on the branching fractions are: $\mathcal{B}(t \rightarrow uZ) < 0.024\% (0.015\%)$ and $\mathcal{B}(t \rightarrow cZ) < 0.045\% (0.037\%)$, assuming one non-vanishing coupling at a time.

Significant improvements are developed with respect to previous searches, namely by using other kinematic variables as input into the BDT as well as a better handle on the not prompt lepton background. The expected limit at 95% CL for the FCNC tZu interaction is more stringent than the expected limit (0.024%) of the current best observed limit (0.017%) set at a centre-of-mass energy of 13 TeV by ATLAS. The observed (expected) limit on the tZc interaction set by ATLAS is 0.023% (0.032%) and its expected limit is comparable with the expected limit presented in this search. For the FCNC interactions with a tZq vertex, the branching fractions

predicted within the Standard Model or beyond the Standard Model theories are still out of reach.

Samenvatting

“Een zoektocht naar kleurveranderende neutrale stromen gerelateerd met een top quark en een Z boson, gebruik makend van de data gecollecteerd door het CMS experiment met een middelpuntsmassaenergie van 13 TeV.”

Het Standaard Model van de deeltjes fysica is een theorie handelend over fundamentele deeltjes en hun interacties. Tot op heden is dit de beste theorie om de natuur om ons heen te beschrijven. Het is experimenteel geconfermeerd en al de deeltjes die deze theorie voorspelt zijn ook daadwerkelijk gevonden. Ondanks zijn vele successen heeft deze theorie echter ook zijn tekortkomingen. De fenomenen zoals neutrino massa's of zwaartekracht blijven onverklaard. De top quark is het zwaarste deeltje in het Standaard Model en doet fysici geloven dat het een verhoogde gevoeligheid heeft voor nieuwe deeltjes en interacties voorspeld door theoriën van nieuwe fysica. De top quark heeft zo'n korte levensduur, dat het onsnapt van de formatie van gebonden toestanden en het mogelijk is om rechtstreeks de top quark eigenschappen te onderzoeken. Veel nieuwe fysica theoriën worden onderzocht door naar de productie snelheid van top quarks te kijken en zo het Wtb interactiepunt onder de loep te nemen. Verder kunnen ook interacties die beperkt worden in het Standaard Model zo worden geanalyseerd. De “Large Hadron Collider” (LHC) is een zogenaamde top quark “fabriek” en produceert een zeer groot aantal interacties die resulteren in top quarks. Dit maakt de LHC een ideale plek om top quark fenomenen te onderzoeken en op elk proton collisie punt zijn experimenten geplaatst om de collisies te onderzoeken. Het onderzoek gepresenteerd in deze thesis omvat de data verzameld door het “Compact Muon Solenoid” (CMS) experiment aan een massamiddelpuntsenergie van 13 TeV, resulerend in een geïntegreerde luminositeit van 35.9 fb^{-1} .

Smaakveranderende neutral stromen zijn erg beperkt in het Standaard Model, tot op de mate dat deze niet waarneembaar zijn. Desondanks, vele nieuwe fysica theoriën verhogen hun waarschijnlijkheid en maken de observatie mogelijk. Het onderzoek gepresenteerd in de thesis kijkt naar interacties resulterend in eindtoestand met drie leptonen veroorzaakt door de productie van enkelvoudige top quarks door middel van een tZq interactiepunt, of door het verval via een tZq interactiepunt van een top quark komende van een top quark paar productie. De additionele quark kan ofwel een charm quark, ofwel een up quark zijn. Er is geen significante afwijking ten op zicht van de achtergronden gevonden en bovenlimieten met 95% betrouwbaarheidsinterval zijn geplaatst. De geobserveerde (verwachte) bovenlimieten met een 95% betrouwbaarheidsinterval op de vertakkingsfractie zijn: $\mathcal{B}(t \rightarrow uZ) < 0.024\%$

(0.015%) en $\mathcal{B}(t \rightarrow cZ) < 0.045\%$ (0.037%), waarbij verondersteld wordt dat er enkel één niet nulle koppeling aanwezig is.

De vooruitgang ten opzichte van vroegere onderzoeken komt door het gebruik van andere kinematische variabelen alsook een betere grip op de NPL achtergrond. De verwachte limiet op de FCNC tZu interactie is sterker dan deze van de huidige sterkste waargenomen (verwachte) limiet van 0.017% (0.024%) aan een massamiddelpuntsenergie van 13 TeV door ATLAS [47]. De waargenomen (verwachte) limiet voor de tZc interactie verkregen door ATLAS is 0.023% (0.032%) en is vergelijkbaar met de verwachte limiet van het onderzoek in deze thesis. Voor FCNC interacties, waar een tZq interactie plaatsvindt, blijven de vertakkingsfractie voorspeld door het Standaard Model en nieuwe fysica theoriën nog buiten het bereik van ontdekking of uitsluiting.

Bibliography

- [1] LUCIANO MAIANI: **The GIM Mechanism: origin, predictions and recent uses.** 2013. arXiv: [1303.6154 \[hep-ph\]](https://arxiv.org/abs/1303.6154) (see pp. vii, 5).
- [2] J. J. AUBERT et al.: **Experimental Observation of a Heavy Particle J .** In: *Phys. Rev. Lett.*, **33**: (1974). doi: [10.1103/PhysRevLett.33.1404](https://doi.org/10.1103/PhysRevLett.33.1404) (see p. vii).
- [3] CDF COLLABORATION, D. ACOSTA et al.: **First evidence for $B_s^0 \rightarrow \phi\phi$ decay and measurements of branching ratio and A_{CP} for $B^+ \rightarrow \phi K^+$.** In: *Phys. Rev. Lett.*, **95**: (2005). doi: [10.1103/PhysRevLett.95.031801](https://doi.org/10.1103/PhysRevLett.95.031801). arXiv: [hep-ex/0502044 \[hep-ex\]](https://arxiv.org/abs/hep-ex/0502044) (see p. vii).
- [4] LHCb and CMS COLLABORATION, VARDAN KHACHATRYAN et al.: **Observation of the rare $B_s^0 \rightarrow \mu^+\mu^-$ decay from the combined analysis of CMS and LHCb data.** In: *Nature*, **522**: (2015). doi: [10.1038/nature14474](https://doi.org/10.1038/nature14474). arXiv: [1411.4413 \[hep-ex\]](https://arxiv.org/abs/1411.4413) (see p. vii).
- [5] WOLFGANG ALTMANNSHOFER and DAVID M. STRAUB: **New Physics in $B \rightarrow K^*\mu\mu?$** In: *Eur. Phys. J. C*, **73**: (2013). doi: [10.1140/epjc/s10052-013-2646-9](https://doi.org/10.1140/epjc/s10052-013-2646-9). arXiv: [1308.1501 \[hep-ph\]](https://arxiv.org/abs/1308.1501) (see p. viii).
- [6] CDF COLLABORATION, T. ET AL. AALTONEN: **Search for the Flavor-Changing Neutral-Current Decay $t \rightarrow Zq$ in $p\bar{p}$ Collisions at $\sqrt{s} = 1.96$ TeV.** In: *Phys. Rev. Lett.*, **101**: (19 2008). doi: [10.1103/PhysRevLett.101.192002](https://doi.org/10.1103/PhysRevLett.101.192002) (see pp. viii, 15).
- [7] D0 COLLABORATION, VICTOR MUKHAMEDOVICH ABAZOV et al.: **Search for flavour changing neutral currents via quark-gluon couplings in single top quark production using 2.3 fb^{-1} of $p\bar{p}$ collisions.** In: *Phys. Lett. B*, **693**: (2010). doi: [10.1016/j.physletb.2010.08.011](https://doi.org/10.1016/j.physletb.2010.08.011). arXiv: [1006.3575 \[hep-ex\]](https://arxiv.org/abs/1006.3575) (see pp. viii, 15).
- [8] ATLAS COLLABORATION, GEORGES AAD et al.: **Search for flavour-changing neutral current top-quark decays to qZ in pp collision data collected with the ATLAS detector at $\sqrt{s} = 8$ TeV.** In: *Eur. Phys. J. C*, **76**:1 (2016). doi: [10.1140/epjc/s10052-015-3851-5](https://doi.org/10.1140/epjc/s10052-015-3851-5). arXiv: [1508.05796 \[hep-ex\]](https://arxiv.org/abs/1508.05796) (see pp. viii, 15).
- [9] ATLAS COLLABORATION, GEORGES AAD et al.: **Search for single top-quark production via flavour-changing neutral currents at 8 TeV with the ATLAS detector.** In: *Eur. Phys. J. C*, **76**:2 (2016). doi: [10.1140/epjc/s10052-016-3876-4](https://doi.org/10.1140/epjc/s10052-016-3876-4). arXiv: [1509.00294 \[hep-ex\]](https://arxiv.org/abs/1509.00294) (see pp. viii, 15, 19).

- [10] CMS COLLABORATION, ALBERT M SIRUNYAN et al.: **Search for associated production of a Z boson with a single top quark and for tZ flavour-changing interactions in pp collisions at $\sqrt{s} = 8$ TeV.** In: (2017). arXiv: [1702.01404 \[hep-ex\]](https://arxiv.org/abs/1702.01404) (see pp. viii, 15, 19, 111–115).
- [11] CMS COLLABORATION, SERGUEI CHATRCHYAN et al.: **Search for Flavor-Changing Neutral Currents in Top-Quark Decays $t \rightarrow Zq$ in pp Collisions at $\sqrt{s} = 8$ TeV.** In: *Phys. Rev. Lett.*, **112**:17 (2014). doi: [10.1103/PhysRevLett.112.171802](https://doi.org/10.1103/PhysRevLett.112.171802). arXiv: [1312.4194 \[hep-ex\]](https://arxiv.org/abs/1312.4194) (see pp. viii, 15).
- [12] CMS COLLABORATION, VARDAN KHACHATRYAN et al.: **Search for anomalous single top quark production in association with a photon in pp collisions at $\sqrt{s} = 8$ TeV.** In: *JHEP*, **04**: (2016). doi: [10.1007/JHEP04\(2016\)035](https://doi.org/10.1007/JHEP04(2016)035). arXiv: [1511.03951 \[hep-ex\]](https://arxiv.org/abs/1511.03951) (see pp. viii, 15, 19).
- [13] J. A. AGUILAR-SAAVEDRA: **Top flavor-changing neutral interactions: Theoretical expectations and experimental detection.** In: *Acta Phys. Polon. B*, **35**: (2004). arXiv: [hep-ph/0409342 \[hep-ph\]](https://arxiv.org/abs/hep-ph/0409342) (see pp. viii, 6, 15–17).
- [14] S. L. GLASHOW, J. ILIOPoulos, and L. MAIANI: **Weak Interactions with Lepton-Hadron Symmetry.** In: *Phys. Rev. D*, **2**: (7 1970). doi: [10.1103/PhysRevD.2.1285](https://doi.org/10.1103/PhysRevD.2.1285) (see pp. viii, 5).
- [15] MICHAEL E PESKIN and DANIEL V SCHROEDER: **An introduction to quantum field theory; 1995 ed.** Boulder, CO: Westview, 1995. URL: <https://cds.cern.ch/record/257493> (see pp. 1, 6, 12, 17).
- [16] C. P. BURGESS: **Introduction to Effective Field Theory.** In: *Ann. Rev. Nucl. Part. Sci.*, **57**: (2007). doi: [10.1146/annurev.nucl.56.080805.140508](https://doi.org/10.1146/annurev.nucl.56.080805.140508). arXiv: [hep-th/0701053 \[hep-th\]](https://arxiv.org/abs/hep-th/0701053) (see p. 1).
- [17] NADIA ROBOTTI: **The discovery of the electron: I.** In: *European Journal of Physics*, **18**:3 (1997). URL: <http://stacks.iop.org/0143-0807/18/i=3/a=002> (see p. 2).
- [18] Super-Kamiokande COLLABORATION, Y. FUKUDA et al.: **Evidence for oscillation of atmospheric neutrinos.** In: *Phys. Rev. Lett.*, **81**: (1998). doi: [10.1103/PhysRevLett.81.1562](https://doi.org/10.1103/PhysRevLett.81.1562). arXiv: [hep-ex/9807003 \[hep-ex\]](https://arxiv.org/abs/hep-ex/9807003) (see pp. 2, 14).
- [19] Double Chooz COLLABORATION, Y. ABE et al.: **Indication of Reactor $\bar{\nu}_e$ Disappearance in the Double Chooz Experiment.** In: *Phys. Rev. Lett.*, **108**: (13 2012). doi: [10.1103/PhysRevLett.108.131801](https://doi.org/10.1103/PhysRevLett.108.131801) (see pp. 2, 14).
- [20] Particle Data Group, C. PATRIGNANI et al.: **Review of Particle Physics.** In: *Chin. Phys. C*, **40**:10 (2016). doi: [10.1088/1674-1137/40/10/100001](https://doi.org/10.1088/1674-1137/40/10/100001) (see pp. 2–3, 6–8, 10, 42–43).
- [21] D0 COLLABORATION, S. ABACHI et al.: **Observation of the top quark.** In: *Phys. Rev. Lett.*, **74**: (1995). doi: [10.1103/PhysRevLett.74.2632](https://doi.org/10.1103/PhysRevLett.74.2632). arXiv: [hep-ex/9503003 \[hep-ex\]](https://arxiv.org/abs/hep-ex/9503003) (see p. 2).
- [22] CDF COLLABORATION, F. ABE et al.: **Observation of top quark production in $\bar{p}p$ collisions.** In: *Phys. Rev. Lett.*, **74**: (1995). doi: [10.1103/PhysRevLett.74.2626](https://doi.org/10.1103/PhysRevLett.74.2626). arXiv: [hep-ex/9503002 \[hep-ex\]](https://arxiv.org/abs/hep-ex/9503002) (see p. 2).
- [23] **First combination of Tevatron and LHC measurements of the top-quark mass.** In: (2014). arXiv: [1403.4427 \[hep-ex\]](https://arxiv.org/abs/1403.4427) (see p. 2).

- [24] CMS COLLABORATION, SERGUEI CHATRCHYAN et al.: **Observation of a new boson at a mass of 125 GeV with the CMS experiment at the LHC.** In: *Phys. Lett. B*, **716**: (2012). doi: [10.1016/j.physletb.2012.08.021](https://doi.org/10.1016/j.physletb.2012.08.021). arXiv: [1207.7235 \[hep-ex\]](https://arxiv.org/abs/1207.7235) (see pp. 2, 23).
- [25] ATLAS COLLABORATION, GEORGES AAD et al.: **Observation of a new particle in the search for the Standard Model Higgs boson with the ATLAS detector at the LHC.** In: *Phys. Lett. B*, **716**: (2012). doi: [10.1016/j.physletb.2012.08.020](https://doi.org/10.1016/j.physletb.2012.08.020). arXiv: [1207.7214 \[hep-ex\]](https://arxiv.org/abs/1207.7214) (see pp. 2, 23).
- [26] NICOLA CABIBBO: **Unitary Symmetry and Leptonic Decays.** In: *Phys. Rev. Lett.*, **10**: (12 1963). doi: [10.1103/PhysRevLett.10.531](https://doi.org/10.1103/PhysRevLett.10.531) (see p. 5).
- [27] B.J. BJØRKEN and S.L. GLASHOW: **Elementary particles and SU(4).** In: *Physics Letters*, **11**:3 (1964). doi: [10.1016/0031-9163\(64\)90433-0](https://doi.org/10.1016/0031-9163(64)90433-0) (see p. 5).
- [28] PATRICK KOPPENBURG and SEBASTIEN DESCOTES-GENON: **The CKM Parameters.** In: (2017). arXiv: [1702.08834 \[hep-ex\]](https://arxiv.org/abs/1702.08834) (see p. 6).
- [29] D0 COLLABORATION, S. ABACHI et al.: **Observation of the top quark.** In: *Phys. Rev. Lett.*, **74**: (1995). doi: [10.1103/PhysRevLett.74.2632](https://doi.org/10.1103/PhysRevLett.74.2632). arXiv: [hep-ex/9503003 \[hep-ex\]](https://arxiv.org/abs/hep-ex/9503003) (see p. 7).
- [30] CDF COLLABORATION, F. ABE et al.: **Observation of top quark production in $\bar{p}p$ collisions.** In: *Phys. Rev. Lett.*, **74**: (1995). doi: [10.1103/PhysRevLett.74.2626](https://doi.org/10.1103/PhysRevLett.74.2626). arXiv: [hep-ex/9503002 \[hep-ex\]](https://arxiv.org/abs/hep-ex/9503002) (see p. 7).
- [31] LHCTop WORKING GROUP: **LHCTopWG Summary plots.** 2017. URL: <https://twiki.cern.ch/twiki/bin/view/LHCPhysics/LHCTopWGSummaryPlots> (see pp. 9, 22).
- [32] CMS COLLABORATION, ANDREA GIAMMANCO and JEANNINE WAGNER-KUHR: **Measurement of the t-channel single Top-quark production rates in pp collisions at 7 TeV.** 2011. URL: <http://cms.web.cern.ch/news/measurement-t-channel-single-top-quark-production-rates-pp-collisions-7-tev> (see p. 9).
- [33] LHCTop WORKING GROUP: **ATLAS-CMS recommended predictions for single top cross sections using the Hathor v2.1 program.** 2017. URL: https://twiki.cern.ch/twiki/bin/view/LHCPhysics/SingleTopRefXsec#Predictions_at_7_8_13_and_14_TeV (see p. 10).
- [34] CMS COLLABORATION: **Summaries of CMS cross section measurements.** 2017. URL: <https://twiki.cern.ch/twiki/bin/view/CMSPublic/PhysicsResultsCombined> (see pp. 11, 20–21, 50, 118, 120).
- [35] CÉLINE DEGRANDE: **Effective field theories in the Standard Model and beyond.** Thesis. Université Catholique de Louvain, 2011. URL: <https://cp3.irmp.ucl.ac.be/upload/theses/phd/degrande.pdf> (see pp. 10–11).
- [36] ENRICO FERMI: **Tentativo di una Teoria Dei Raggi β .** In: *Il Nuovo Cimento (1924–1942)*, **11**:1 (20, 2008). doi: [10.1007/BF02959820](https://doi.org/10.1007/BF02959820) (see p. 10).
- [37] B. GRZADKOWSKI, M. ISKRZYNSKI, M. MISIAK, and J. ROSIEK: **Dimension-Six Terms in the Standard Model Lagrangian.** In: *JHEP*, **1010**: (2010). doi: [10.1007/JHEP10\(2010\)085](https://doi.org/10.1007/JHEP10(2010)085). arXiv: [1008.4884 \[hep-ph\]](https://arxiv.org/abs/1008.4884) (see pp. 12–13, 16).

- [38] J.A. AGUILAR SAVVEDRA, C. DEGRANDE, G. DURIEUX, et al.: **Constraining the MSMEFT in the top sector at the LHC.** 2017. URL: http://www.desy.de/~durieux/topbasis/basis_note.pdf (see p. 12).
- [39] ANDY BUCKLEY, CHRISTOPH ENGLERT, JAMES FERRANDO, et al.: **Constraining top quark effective theory in the LHC Run II era.** In: *JHEP*, **04**: (2016). DOI: [10.1007/JHEP04\(2016\)015](https://doi.org/10.1007/JHEP04(2016)015). arXiv: [1512.03360 \[hep-ph\]](https://arxiv.org/abs/1512.03360) (see p. 13).
- [40] YORIKIYO NAGASHIMA: **Beyond the standard model of elementary particle physics.** Weinheim, Germany: Wiley-VCH Verlag, 2014. URL: <http://www-spires.fnal.gov/spires/find/books/www?cl=QC793.2.N34::2014> (see p. 14).
- [41] Planck COLLABORATION, P. A. R. ADE et al.: **Planck 2015 results. XIII. Cosmological parameters.** In: *Astron. Astrophys.*, **594**: (2016). DOI: [10.1051/0004-6361/201525830](https://doi.org/10.1051/0004-6361/201525830). arXiv: [1502.01589 \[astro-ph.CO\]](https://arxiv.org/abs/1502.01589) (see p. 14).
- [42] P. J. E. PEEBLES and BHARAT RATRA: **The Cosmological constant and dark energy.** In: *Rev. Mod. Phys.*, **75**: (2003). DOI: [10.1103/RevModPhys.75.559](https://doi.org/10.1103/RevModPhys.75.559). arXiv: [astro-ph/0207347 \[astro-ph\]](https://arxiv.org/abs/astro-ph/0207347) (see p. 14).
- [43] A. D. SAKHAROV: **Violation of CP Invariance, c Asymmetry, and Baryon Asymmetry of the Universe.** In: *Pisma Zh. Eksp. Teor. Fiz.*, **5**: (1967). DOI: [10.1070/PU1991v034n05ABEH002497](https://doi.org/10.1070/PU1991v034n05ABEH002497) (see p. 14).
- [44] GUSTAVO BURDMAN: **New solutions to the hierarchy problem.** In: *Braz. J. Phys.*, **37**: (2007). DOI: [10.1590/S0103-97332007000400006](https://doi.org/10.1590/S0103-97332007000400006). arXiv: [hep-ph/0703194 \[hep-ph\]](https://arxiv.org/abs/hep-ph/0703194) (see p. 14).
- [45] ATLAS COLLABORATION, GEORGES AAD et al.: **Search for flavour-changing neutral current top quark decays $t \rightarrow Hq$ in pp collisions at $\sqrt{s} = 8$ TeV with the ATLAS detector.** In: *JHEP*, **12**: (2015). DOI: [10.1007/JHEP12\(2015\)061](https://doi.org/10.1007/JHEP12(2015)061). arXiv: [1509.06047 \[hep-ex\]](https://arxiv.org/abs/1509.06047) (see p. 15).
- [46] ATLAS COLLABORATION, MORAD AABOUD et al.: **Search for top quark decays $t \rightarrow qH$, with $H \rightarrow \gamma\gamma$, in $\sqrt{s} = 13$ TeV pp collisions using the ATLAS detector.** In: *submitted to JHEP*, (2017). arXiv: [1707.01404 \[hep-ex\]](https://arxiv.org/abs/1707.01404) (see pp. 15, 19).
- [47] ATLAS COLLABORATION, **Search for flavour-changing neutral current top quark decays $t \rightarrow qZ$ in proton-proton collisions at $\sqrt{s} = 13$ TeV with the ATLAS Detector.** Tech. rep. ATLAS-CONF-2017-070. CERN, 2017. URL: <https://cds.cern.ch/record/2285808> (see pp. 15, 19, 111–113, 117, 168).
- [48] CMS COLLABORATION, VARDAN KHACHATRYAN et al.: **Search for top quark decays via Higgs-boson-mediated flavor-changing neutral currents in pp collisions at $\sqrt{s} = 8$ TeV.** In: *JHEP*, **02**: (2017). DOI: [10.1007/JHEP02\(2017\)079](https://doi.org/10.1007/JHEP02(2017)079). arXiv: [1610.04857 \[hep-ex\]](https://arxiv.org/abs/1610.04857) (see p. 15).
- [49] CMS COLLABORATION, **Search for the flavor-changing interactions of the top quark with the Higgs boson in $H \rightarrow b\bar{b}$ channel at $\sqrt{s} = 13$ TeV.** Tech. rep. CMS-PAS-TOP-17-003. 2017. URL: <https://cds.cern.ch/record/2284743> (see pp. 15, 114).
- [50] M. BENEKE et al.: **Top quark physics.** 2000. arXiv: [hep-ph/0003033 \[hep-ph\]](https://arxiv.org/abs/hep-ph/0003033). URL: <http://weblib.cern.ch/abstract?CERN-TH-2000-100> (see p. 17).

- [51] JUN GAO, CHONG SHENG LI, and HUA XING ZHU: **Top Quark Decay at Next-to-Next-to Leading Order in QCD**. In: *Phys. Rev. Lett.*, **110**:4 (2013). doi: [10.1103/PhysRevLett.110.042001](https://doi.org/10.1103/PhysRevLett.110.042001). arXiv: [1210.2808 \[hep-ph\]](https://arxiv.org/abs/1210.2808) (see pp. 18, 47).
- [52] STEPHEN MYERS: **The LEP Collider, from design to approval and commissioning**. John Adams' Lecture. CERN, 1991. URL: <http://cds.cern.ch/record/226776> (see p. 23).
- [53] STEPHEN HOLMES, RONALD S MOORE, and VLADIMIR SHILTSEV: **Overview of the Tevatron collider complex: goals, operations and performance**. In: *JINST*, **6**:08 (2011). URL: <http://stacks.iop.org/1748-0221/6/i=08/a=T08001> (see p. 23).
- [54] OPAL, DELPHI, LEP Working Group for Higgs boson searches, ALEPH, L3 COLLABORATION, R. BARATE et al.: **Search for the standard model Higgs boson at LEP**. In: *Phys. Lett. B*, **565**: (2003). doi: [10.1016/S0370-2693\(03\)00614-2](https://doi.org/10.1016/S0370-2693(03)00614-2). arXiv: [hep-ex/0306033 \[hep-ex\]](https://arxiv.org/abs/hep-ex/0306033) (see p. 23).
- [55] CDF and D0 COLLABORATION, KENNETH HERNER: **Higgs Boson Studies at the Tevatron**. In: *Nucl. Part. Phys. Proc.*, **273-275**: (2016). doi: [10.1016/j.nuclphysbps.2015.09.131](https://doi.org/10.1016/j.nuclphysbps.2015.09.131) (see p. 23).
- [56] ABDELHAK DJOUADI: **The Anatomy of electro-weak symmetry breaking. I: The Higgs boson in the standard model**. In: *Phys. Rept.*, **457**: (2008). doi: [10.1016/j.physrep.2007.10.004](https://doi.org/10.1016/j.physrep.2007.10.004). arXiv: [hep-ph/0503172 \[hep-ph\]](https://arxiv.org/abs/hep-ph/0503172) (see p. 23).
- [57] LYNDON EVANS and PHILIP BRYANT: **LHC Machine**. In: *JINST*, **3**:08 (2008). URL: <http://stacks.iop.org/1748-0221/3/i=08/a=S08001> (see p. 23).
- [58] LHC Study Group, THOMAS SVEN PETTERSSON and P LEFÈVRE: **The Large Hadron Collider: conceptual design**. Tech. rep. CERN-AC-95-05-LHC. 1995. URL: [https://cds.cern.ch/record/291782](http://cds.cern.ch/record/291782) (see p. 23).
- [59] JORG WENNINGER and EZIO TODESCO: **Large Hadron Collider momentum calibration and accuracy**. Tech. rep. CERN-ACC-2017-0007. CERN, 2017. URL: <https://cds.cern.ch/record/2254678> (see p. 24).
- [60] CINZIA DE MELIS: **The CERN accelerator complex. Complexe des accélérateurs du CERN**. 2016. URL: <https://cds.cern.ch/record/2197559> (see p. 24).
- [61] CMS COLLABORATION, J. A. MURILLO QUIJADA: **Recent upgrades and results from the CMS experiment**. In: *J. Phys. Conf. Ser.*, **912**:1 (2017). doi: [10.1088/1742-6596/912/1/012005](https://doi.org/10.1088/1742-6596/912/1/012005) (see p. 24).
- [62] ANTONELLA DEL ROSSO: **HL-LHC updates in Japan. Projet HL-LHC : une réunion fait le point au Japon**. In: BUL-NA-2014-272. 51/2014 (2014). URL: <https://cds.cern.ch/record/1975962> (see p. 25).
- [63] OLIVER SIM BRÜNING, PAUL COLLIER, P LEBRUN, et al.: **LHC Design Report**. CERN Yellow Reports: Monographs. CERN, 2004. URL: <https://cds.cern.ch/record/782076> (see p. 25).
- [64] ATLAS COLLABORATION, G. AAD et al.: **The ATLAS Experiment at the CERN Large Hadron Collider**. In: *JINST*, **3**: (2008). doi: [10.1088/1748-0221/3/08/S08003](https://doi.org/10.1088/1748-0221/3/08/S08003) (see p. 25).

- [65] CMS COLLABORATION, S. CHATRCHYAN et al.: **The CMS Experiment at the CERN LHC**. In: *JINST*, 3: (2008). doi: [10.1088/1748-0221/3/08/S08004](https://doi.org/10.1088/1748-0221/3/08/S08004) (see pp. 25, 33–35).
- [66] ALICE COLLABORATION, K. AAMODT et al.: **The ALICE experiment at the CERN LHC**. In: *JINST*, 3: (2008). doi: [10.1088/1748-0221/3/08/S08002](https://doi.org/10.1088/1748-0221/3/08/S08002) (see p. 25).
- [67] LHCb COLLABORATION, A. AUGUSTO ALVES JR. et al.: **The LHCb Detector at the LHC**. In: *JINST*, 3: (2008). doi: [10.1088/1748-0221/3/08/S08005](https://doi.org/10.1088/1748-0221/3/08/S08005) (see p. 25).
- [68] M. BONGI et al.: **Astroparticle physics at LHC: The LHCf experiment ready for data taking**. In: *Nucl. Instrum. Meth. A*, 612: (2010). doi: [10.1016/j.nima.2009.08.039](https://doi.org/10.1016/j.nima.2009.08.039) (see p. 26).
- [69] TOTEM COLLABORATION, G. ANELLI et al.: **The TOTEM experiment at the CERN Large Hadron Collider**. In: *JINST*, 3: (2008). doi: [10.1088/1748-0221/3/08/S08007](https://doi.org/10.1088/1748-0221/3/08/S08007) (see p. 26).
- [70] MoEDAL COLLABORATION, B. ACHARYA et al.: **The Physics Programme Of The MoEDAL Experiment At The LHC**. In: *Int. J. Mod. Phys. A*, 29: (2014). doi: [10.1142/S0217751X14300506](https://doi.org/10.1142/S0217751X14300506). arXiv: [1405.7662 \[hep-ph\]](https://arxiv.org/abs/1405.7662) (see p. 26).
- [71] JAMES GILLIES: **Luminosity? Why don't we just say collision rate?** 2011. URL: <http://cds.cern.ch/record/1997001> (see p. 26).
- [72] HARRIET JARLETT and HARRIET KIM JARLETT: **LHC pushes limits of performance**. 2016. URL: <http://cds.cern.ch/record/2212301> (see p. 26).
- [73] CMS COLLABORATION: **Public Luminosity results**. 2017. URL: https://twiki.cern.ch/twiki/bin/view/CMSPublic/LumiPublicResults#Online_Luminosity_AN2 (see p. 27).
- [74] **Technical proposal**. LHC Tech. Proposal. CERN, 1994. URL: <https://cds.cern.ch/record/290969> (see p. 27).
- [75] CMS COLLABORATION, G. L. BAYATIAN et al.: **CMS physics: Technical design report**. In: (2006) (see p. 27).
- [76] CMS COLLABORATION, G L BAYATIAN, S CHATRCHYAN, G HMAYAKYAN, et al.: **CMS Physics: Technical Design Report Volume 1: Detector Performance and Software**. Technical Design Report CMS. CERN, 2006. URL: <https://cds.cern.ch/record/922757> (see pp. 27, 32, 57).
- [77] CMS COLLABORATION: **Detector Drawings**. 2012. URL: <https://cds.cern.ch/record/1433717> (see p. 28).
- [78] CMS COLLABORATION, S CHATRCHYAN, V KHACHATRYAN, A M SIRUNYAN, et al.: **Performance of the CMS Drift Tube Chambers with Cosmic Rays**. In: *JINST*, 5:CMS-CFT-09-012 (2009). arXiv: [0911.4855](https://arxiv.org/abs/0911.4855). URL: <http://cds.cern.ch/record/1223944> (see pp. 30–31).
- [79] CMS COLLABORATION: **News from the CMS experimental site: 22 November 2013**. URL: <http://cms.web.cern.ch/news/news-point-5-22-november-2013> (see p. 31).
- [80] INSTITUTE OF RESEARCH INTO THE FUNDAMENTAL LAWS THE UNIVERSE: **The CMS detector superconducting solenoid**. 2006. URL: http://irfu.cea.fr/en/Phocea/Vie_des_labos/Ast/ast_visu.php?id_ast=839 (see p. 33).

- [81] FERGUS WILSON: **Experimental Particle Physics**. 2012. URL: <http://slideplayer.com/slide/794631/> (see p. 33).
- [82] EMRAH TIRAS, BURAK BILKI, and YASAR ONEL: **Commissioning of CMS Forward Hadron Calorimeters with Upgraded Multi-anode PMTs and μ TCA Readout**. In: *PoS, ICHEP2016*: (2017). arXiv: [1611.05232 \[physics.ins-det\]](https://arxiv.org/abs/1611.05232).
- [83] LUCAS TAYLOR: **Experimental Particle Physics**. 2011. URL: <http://cms.web.cern.ch/news/electromagnetic-calorimeter> (see p. 34).
- [84] **Proceedings, 34th International Conference on High Energy Physics**. 2008. URL: <http://www.slac.stanford.edu/econf/C080730> (see p. 34).
- [85] L. BRIANZA: **Precision crystal calorimetry in LHC Run II with the CMS ECAL**. In: *JINST*, **12**:01 (2017). URL: <http://stacks.iop.org/1748-0221/12/i=01/a=C01069> (see pp. 35, 38).
- [86] CMS COLLABORATION, SERGUEI CHATRCHYAN, KHACHATRYAN, et al.: **Description and performance of track and primary-vertex reconstruction with the CMS tracker**. In: *JINST*, **9**:CERN-PH-EP-2014-070. CMS-TRK-11-001 (2014). arXiv: [1405.6569](https://arxiv.org/abs/1405.6569). URL: <http://cds.cern.ch/record/1704291> (see pp. 35, 58).
- [87] CHRISTINE SUTTON: **Chronicles of CMS: the saga of LS1**. 2015. URL: <http://cds.cern.ch/record/2024986> (see p. 36).
- [88] **A beautiful barrel for CMS**. 2014. URL: <http://cds.cern.ch/record/1998635> (see p. 36).
- [89] CMS COLLABORATION, VARDAN KHACHATRYAN et al.: **The CMS trigger system**. In: *JINST*, **12**:01 (2017). doi: [10.1088/1748-0221/12/01/P01020](https://doi.org/10.1088/1748-0221/12/01/P01020). arXiv: [1609.02366 \[physics.ins-det\]](https://arxiv.org/abs/1609.02366) (see p. 37).
- [90] CORINNE PRALAVORIO and CORINNE PRALAVORIO: **Major work to ready the LHC experiments for Run 2**. 2015. URL: <http://cds.cern.ch/record/2024977> (see p. 37).
- [91] CMS COLLABORATION, LUIGI GUIDUCCI: **CMS muon system towards LHC Run 2 and beyond**. Tech. rep. CMS-CR-2014-333. CERN, 2014. URL: <https://cds.cern.ch/record/1966038> (see p. 38).
- [92] CMS COLLABORATION, CARLO BATTILANA: **The CMS muon system status and upgrades for LHC run-2 and performance of muon reconstruction with 13 TeV data**. Tech. rep. CMS-CR-2016-437. CERN, 2016. URL: <http://cds.cern.ch/record/2239185> (see p. 38).
- [93] CMS COLLABORATION, SERGUEI CHATRCHYAN et al.: **Energy Calibration and Resolution of the CMS Electromagnetic Calorimeter in pp Collisions at $\sqrt{s} = 7$ TeV**. In: *JINST*, **8**: (2013). doi: [10.1088/1748-0221/8/09/P09009](https://doi.org/10.1088/1748-0221/8/09/P09009). arXiv: [1306.2016 \[hep-ex\]](https://arxiv.org/abs/1306.2016) (see p. 38).
- [94] CMS COLLABORATION: **Cool running for CMS tracker**. 2014. URL: <http://cds.cern.ch/record/1998606> (see p. 38).
- [95] L. CADAMURO: **The CMS Level-1 trigger system for LHC Run II**. In: *JINST*, **12**:03 (2017). URL: <http://stacks.iop.org/1748-0221/12/i=03/a=C03021> (see p. 38).

- [96] CMS COLLABORATION, DAVID AARON MATZNER DOMINGUEZ, D. ABBANEO, K. ARNDT, et al.: **CMS Technical Design Report for the Pixel Detector Upgrade**. 2012 (see p. 39).
- [97] CMS COLLABORATION, HANNO CHRISTOPHER PERREY: **Plans and Status of the Phase I Upgrade of the CMS Pixel Tracker**. Tech. rep. CMS-CR-2014-005. CERN, 2014. URL: <http://cds.cern.ch/record/1644757> (see p. 39).
- [98] CMC COLLABORATION, CLAUDIO GRANDI, DAVID STICKLAND, LUCAS TAYLOR, ACHILLE PETRILLI, and ALAIN HERVÉ: **CMS Computing Model: The "CMS Computing Model RTAG"**. Tech. rep. CMS-NOTE-2004-031. CERN-LHCC-2004-035. LHCC-G-083. 2004. URL: <http://cds.cern.ch/record/814248> (see p. 39).
- [99] CHRISTOPH ECK, J KNOBLOCH, LESLIE ROBERTSON, et al.: **LHC computing Grid: Technical Design Report. Version 1.06 (20 Jun 2005)**. Technical Design Report LCG. CERN, 2005. URL: <https://cds.cern.ch/record/840543> (see p. 39).
- [100] WORLDWIDE LHC COMPUTING GRID: **WorldWide LHC Computing Grid**. 2017. URL: <http://wlcg-public.web.cern.ch> (see p. 40).
- [101] JOHN C. COLLINS, DAVISON E. SOPER, and GEORGE F. STERMAN: **Factorization of Hard Processes in QCD**. In: *Adv. Ser. Direct. High Energy Phys.*, 5: (1989). DOI: [10.1142/9789814503266_0001](https://doi.org/10.1142/9789814503266_0001). arXiv: [hep-ph/0409313 \[hep-ph\]](https://arxiv.org/abs/hep-ph/0409313) (see p. 41).
- [102] RINGAILE PLACAKYTE: **Parton Distribution Functions**. In: 2011. arXiv: [1111.5452 \[hep-ph\]](https://arxiv.org/abs/1111.5452). URL: <https://inspirehep.net/record/954990/files/arXiv:1111.5452.pdf> (see p. 41).
- [103] RICHARD D. BALL, VALERIO BERTONE, STEFANO CARRAZZA, et al.: **Parton distributions for the LHC run II**. In: *JHEP*, 2015:4 (2015). DOI: [10.1007/JHEP04\(2015\)040](https://doi.org/10.1007/JHEP04(2015)040) (see p. 41).
- [104] JON BUTTERWORTH et al.: **PDF4LHC recommendations for LHC Run II**. In: *J. Phys. G*, 43: (2016). DOI: [10.1088/0954-3899/43/2/023001](https://doi.org/10.1088/0954-3899/43/2/023001). arXiv: [1510.03865 \[hep-ph\]](https://arxiv.org/abs/1510.03865) (see pp. 41–42).
- [105] H. ABRAMOWICZ and A. CALDWELL: **HERA collider physics**. In: *Rev. Mod. Phys.*, 71: (1999). DOI: [10.1103/RevModPhys.71.1275](https://doi.org/10.1103/RevModPhys.71.1275). arXiv: [hep-ex/9903037 \[hep-ex\]](https://arxiv.org/abs/hep-ex/9903037) (see p. 42).
- [106] STEPHEN HOLMES, RONALD S. MOORE, and VLADIMIR SHILTSEV: **Overview of the Tevatron Collider Complex: Goals, Operations and Performance**. In: *JINST*, 6: (2011). DOI: [10.1088/1748-0221/6/08/T08001](https://doi.org/10.1088/1748-0221/6/08/T08001). arXiv: [1106.0909 \[physics.acc-ph\]](https://arxiv.org/abs/1106.0909) (see p. 42).
- [107] JUAN ROJO et al.: **The PDF4LHC report on PDFs and LHC data: Results from Run I and preparation for Run II**. In: *J. Phys. G*, 42: (2015). DOI: [10.1088/0954-3899/42/10/103103](https://doi.org/10.1088/0954-3899/42/10/103103). arXiv: [1507.00556 \[hep-ph\]](https://arxiv.org/abs/1507.00556) (see p. 42).
- [108] ALAN D. MARTIN: **Proton structure, Partons, QCD, DGLAP and beyond**. In: *Acta Phys. Polon. B*, 39: (2008). arXiv: [0802.0161 \[hep-ph\]](https://arxiv.org/abs/0802.0161) (see p. 42).
- [109] J. PUMPLIN, D. STUMP, R. BROCK, et al.: **Uncertainties of predictions from parton distribution functions. 2. The Hessian method**. In: *Phys. Rev. D*, 65: (2001). DOI: [10.1103/PhysRevD.65.014013](https://doi.org/10.1103/PhysRevD.65.014013). arXiv: [hep-ph/0101032 \[hep-ph\]](https://arxiv.org/abs/hep-ph/0101032) (see p. 42).

- [110] FRANZ MANDL and GRAHAM G SHAW: **Quantum field theory; 2nd ed.** New York, NY: Wiley, 2010. URL: <https://cds.cern.ch/record/1236742> (see p. 44).
- [111] S BANERJEE: **CMS Simulation Software**. In: *Journal of Physics: Conference Series*, **396**:2 (2012). URL: <http://stacks.iop.org/1742-6596/396/i=2/a=022003> (see p. 44).
- [112] M HILDRETH, V N IVANCHENKO, D J LANGE, and M J KORTELAINEN: **CMS Full Simulation for Run-2**. In: *Journal of Physics: Conference Series*, **664**:7 (2015). URL: <http://stacks.iop.org/1742-6596/664/i=7/a=072022> (see p. 44).
- [113] S. AGOSTINELLI, J. ALLISON, K. AMAKO, et al.: **Geant4-a simulation toolkit**. In: *Nuclear Instruments and Methods in Physics Research Section A: Accelerators, Spectrometers, Detectors and Associated Equipment*, **506**:3 (2003). doi: [https://doi.org/10.1016/S0168-9002\(03\)01368-8](https://doi.org/10.1016/S0168-9002(03)01368-8) (see pp. 44, 46).
- [114] MICHAEL H. SEYMOUR and MARILYN MARX: **Monte Carlo Event Generators**. In: 2013. doi: 10.1007/978-3-319-05362-2_8. arXiv: [1304.6677 \[hep-ph\]](1304.6677) (see p. 44).
- [115] TORBJORN SJÖSTRAND: **Monte Carlo Tools**. In: 2009. doi: <10.1201/b11865-14>. arXiv: [0911.5286 \[hep-ph\]](0911.5286) (see p. 44).
- [116] STEFAN HÖCHE: **Introduction to parton-shower event generators**. In: 2015. doi: 10.1142/9789814678766_0005. arXiv: [1411.4085 \[hep-ph\]](1411.4085) (see pp. 44–45).
- [117] ADAM ALLOUL, NEIL D. CHRISTENSEN, CÉLINE DEGRANDE, CLAUDE DUHR, and BENJAMIN FUKS: **FeynRules 2.0 - A complete toolbox for tree-level phenomenology**. In: *Comput. Phys. Commun.*, **185**: (2014). doi: <10.1016/j.cpc.2014.04.012>. arXiv: [1310.1921 \[hep-ph\]](1310.1921) (see p. 44).
- [118] CELINE DEGRANDE, CLAUDE DUHR, BENJAMIN FUKS, et al.: **UFO - The Universal FeynRules Output**. In: *Comput. Phys. Commun.*, **183**: (2012). doi: <10.1016/j.cpc.2012.01.022>. arXiv: [1108.2040 \[hep-ph\]](1108.2040) (see p. 44).
- [119] JOHAN ALWALL, MICHEL HERQUET, FABIO MALTONI, OLIVIER MATTELAER, and TIM STELZER: **MadGraph 5 : Going Beyond**. In: *JHEP*, **06**: (2011). doi: [10.1007/JHEP06\(2011\)128](10.1007/JHEP06(2011)128). arXiv: [1106.0522 \[hep-ph\]](1106.0522) (see p. 45).
- [120] MICHELANGELO L. MANGANO, MAURO MORETTI, FULVIO PICCININI, and MICHELE TRECANI: **Matching matrix elements and shower evolution for top-quark production in hadronic collisions**. In: *JHEP*, **01**: (2007). doi: <10.1088/1126-6708/2007/01/013>. arXiv: [hep-ph/0611129 \[hep-ph\]](hep-ph/0611129) (see p. 45).
- [121] TORBJORN SJÖSTRAND, STEPHEN MIRENNA, and PETER Z. SKANDS: **PYTHIA 6.4 Physics and Manual**. In: *JHEP*, **0605**: (2006). doi: <10.1088/1126-6708/2006/05/026>. arXiv: [hep-ph/0603175 \[hep-ph\]](hep-ph/0603175) (see pp. 45–46).
- [122] TORBJORN SJÖSTRAND, STEFAN ASK, JESPER R. CHRISTIANSEN, et al.: **An Introduction to PYTHIA 8.2**. In: *Comput. Phys. Commun.*, **191**: (2015). doi: <10.1016/j.cpc.2015.01.024>. arXiv: [1410.3012 \[hep-ph\]](1410.3012) (see pp. 45–46, 49).
- [123] JOHAN ALWALL et al.: **Comparative study of various algorithms for the merging of parton showers and matrix elements in hadronic collisions**. In: *Eur. Phys. J. C*, **53**: (2008). doi: <10.1140/epjc/s10052-007-0490-5>. arXiv: [0706.2569 \[hep-ph\]](0706.2569) (see p. 45).

- [124] J. ALWALL, R. FREDERIX, S. FRIXIONE, et al.: **The automated computation of tree-level and next-to-leading order differential cross sections, and their matching to parton shower simulations.** In: *JHEP*, **07**: (2014). DOI: [10.1007/JHEP07\(2014\)079](https://doi.org/10.1007/JHEP07(2014)079). arXiv: [1405.0301 \[hep-ph\]](https://arxiv.org/abs/1405.0301) (see p. 45).
- [125] STEFANO FRIXIONE and BRYAN R. WEBBER: **Matching NLO QCD computations and parton shower simulations.** In: *JHEP*, **06**: (2002). DOI: [10.1088/1126-6708/2002/06/029](https://doi.org/10.1088/1126-6708/2002/06/029). arXiv: [hep-ph/0204244 \[hep-ph\]](https://arxiv.org/abs/hep-ph/0204244) (see p. 45).
- [126] RIKKERT FREDERIX and STEFANO FRIXIONE: **Merging meets matching in MC@NLO.** In: *JHEP*, **12**: (2012). DOI: [10.1007/JHEP12\(2012\)061](https://doi.org/10.1007/JHEP12(2012)061). arXiv: [1209.6215 \[hep-ph\]](https://arxiv.org/abs/1209.6215) (see p. 45).
- [127] SIMONE ALIOLI, PAOLO NASON, CARLO OLEARI, and EMANUELE RE: **A general framework for implementing NLO calculations in shower Monte Carlo programs: the POWHEG BOX.** In: *JHEP*, **2010**:6 (2010). DOI: [10.1007/JHEP06\(2010\)043](https://doi.org/10.1007/JHEP06(2010)043) (see p. 45).
- [128] SIMONE ALIOLI, PAOLO NASON, CARLO OLEARI, and EMANUELE RE: **NLO single-top production matched with shower in POWHEG: s - and t -channel contributions.** In: *JHEP*, **2009**:09 (2009). URL: <http://stacks.iop.org/1126-6708/2009/i=09/a=111> (see p. 45).
- [129] STEFANO FRIXIONE, PAOLO NASON, and CARLO OLEARI: **Matching NLO QCD computations with parton shower simulations: the POWHEG method.** In: *JHEP*, **2007**:11 (2007). URL: <http://stacks.iop.org/1126-6708/2007/i=11/a=070> (see p. 45).
- [130] SIMONE ALIOLI, PAOLO NASON, CARLO OLEARI, and EMANUELE RE: **A general framework for implementing NLO calculations in shower Monte Carlo programs: the POWHEG BOX.** In: *JHEP*, **06**: (2010). DOI: [10.1007/JHEP06\(2010\)043](https://doi.org/10.1007/JHEP06(2010)043). arXiv: [1002.2581 \[hep-ph\]](https://arxiv.org/abs/1002.2581) (see p. 45).
- [131] STEFANO FRIXIONE, PAOLO NASON, and CARLO OLEARI: **Matching NLO QCD computations with Parton Shower simulations: the POWHEG method.** In: *JHEP*, **11**: (2007). DOI: [10.1088/1126-6708/2007/11/070](https://doi.org/10.1088/1126-6708/2007/11/070). arXiv: [0709.2092 \[hep-ph\]](https://arxiv.org/abs/0709.2092) (see p. 45).
- [132] PAOLO NASON: **A New method for combining NLO QCD with shower Monte Carlo algorithms.** In: *JHEP*, **11**: (2004). DOI: [10.1088/1126-6708/2004/11/040](https://doi.org/10.1088/1126-6708/2004/11/040). arXiv: [hep-ph/0409146 \[hep-ph\]](https://arxiv.org/abs/hep-ph/0409146) (see p. 45).
- [133] ANDREI V. GRITSAN, RAOUL RÖNTSCH, MARKUS SCHULZE, and MENG XIAO: **Constraining anomalous Higgs boson couplings to the heavy flavor fermions using matrix element techniques.** In: *Phys. Rev. D*, **94**:5 (2016). DOI: [10.1103/PhysRevD.94.055023](https://doi.org/10.1103/PhysRevD.94.055023). arXiv: [1606.03107 \[hep-ph\]](https://arxiv.org/abs/1606.03107) (see p. 45).
- [134] IAN ANDERSON et al.: **Constraining anomalous HVV interactions at proton and lepton colliders.** In: *Phys. Rev. D*, **89**:3 (2014). DOI: [10.1103/PhysRevD.89.035007](https://doi.org/10.1103/PhysRevD.89.035007). arXiv: [1309.4819 \[hep-ph\]](https://arxiv.org/abs/1309.4819) (see p. 45).
- [135] SARA BOLOGNESI, YANYAN GAO, ANDREI V. GRITSAN, et al.: **On the spin and parity of a single-produced resonance at the LHC.** In: *Phys. Rev. D*, **86**: (2012). DOI: [10.1103/PhysRevD.86.095031](https://doi.org/10.1103/PhysRevD.86.095031). arXiv: [1208.4018 \[hep-ph\]](https://arxiv.org/abs/1208.4018) (see p. 45).
- [136] YANYAN GAO, ANDREI V. GRITSAN, ZIJIN GUO, et al.: **Spin determination of single-produced resonances at hadron colliders.** In: *Phys. Rev. D*, **81**: (2010). DOI: [10.1103/PhysRevD.81.075022](https://doi.org/10.1103/PhysRevD.81.075022). arXiv: [1001.3396 \[hep-ph\]](https://arxiv.org/abs/1001.3396) (see p. 45).

- [137] PIERRE ARTOISENET, RIKKERT FREDERIX, OLIVIER MATTELAER, and ROBBERT RIETKERK: **Automatic spin-entangled decays of heavy resonances in Monte Carlo simulations**. In: *JHEP*, **03**: (2013). DOI: [10.1007/JHEP03\(2013\)015](https://doi.org/10.1007/JHEP03(2013)015). arXiv: [1212.3460 \[hep-ph\]](https://arxiv.org/abs/1212.3460) (see p. 46).
- [138] V. KHACHATRYAN and ETAL: **Event generator tunes obtained from underlying event and multiparton scattering measurements**. In: *Eur. Phys. J. C*, **76**:3 (2016). DOI: [10.1140/epjc/s10052-016-3988-x](https://doi.org/10.1140/epjc/s10052-016-3988-x) (see p. 46).
- [139] RICHARD D. BALL et al.: **Parton distributions with LHC data**. In: *Nucl. Phys. B*, **867**: (2013). DOI: [10.1016/j.nuclphysb.2012.10.003](https://doi.org/10.1016/j.nuclphysb.2012.10.003). arXiv: [1207.1303 \[hep-ph\]](https://arxiv.org/abs/1207.1303) (see p. 46).
- [140] YUE ZHANG, BO HUA LI, CHONG SHENG LI, JUN GAO, and HUA XING ZHU: **Next-to-leading order QCD corrections to the top quark associated with γ production via model-independent flavor-changing neutral-current couplings at hadron colliders**. In: *Phys. Rev. D*, **83**: (2011). DOI: [10.1103/PhysRevD.83.094003](https://doi.org/10.1103/PhysRevD.83.094003). arXiv: [1101.5346 \[hep-ph\]](https://arxiv.org/abs/1101.5346) (see p. 47).
- [141] J ALWALL, R FREDERIX, S FRIXIONE, et al.: **The automated computation of tree-level and next-to-leading order differential cross sections, and their matching to parton shower simulations**. In: *JHEP*, **07**: (2014). arXiv: [1405.0301](https://arxiv.org/abs/1405.0301). URL: <http://cds.cern.ch/record/1699128>.
- [142] CMS Monte Carlo Generator Group. URL: <https://twiki.cern.ch/twiki/bin/view/CMS/GeneratorMain> (see pp. 48–49).
- [143] T. GEHRMANN, M. GRAZZINI, S. KALLWEIT, et al.: **W^+W^- Production at Hadron Colliders in Next to Next to Leading Order QCD**. In: *Phys. Rev. Lett.*, **113**:21 (2014). DOI: [10.1103/PhysRevLett.113.212001](https://doi.org/10.1103/PhysRevLett.113.212001). arXiv: [1408.5243 \[hep-ph\]](https://arxiv.org/abs/1408.5243) (see p. 49).
- [144] A. HOECKER, P. SPECKMAYER, J. STELZER, et al.: **TMVA - Toolkit for Multivariate Data Analysis**. 2007. eprint: [physics/0703039](https://arxiv.org/abs/physics/0703039) (see p. 50).
- [145] R. BRUN and F. RADEMAKERS: **ROOT: An object oriented data analysis framework**. In: *Nucl. Instrum. Meth. A*, **389**: (1997). DOI: [10.1016/S0168-9002\(97\)00048-X](https://doi.org/10.1016/S0168-9002(97)00048-X) (see p. 50).
- [146] A. MAYR, H. BINDER, O. GEFELLER, and M. SCHMID: **The Evolution of Boosting Algorithms - From Machine Learning to Statistical Modelling**. In: (2014). arXiv: [1403.1452 \[stat.ME\]](https://arxiv.org/abs/1403.1452) (see p. 51).
- [147] OLAF BEHNKE, KEVIN KRONINGER, GREGORY SCHOTT, and THOMAS SCHORNER-SADENIUS: **Data Analysis in High Energy Physics: A Practical Guide to Statistical Methods**. 1st. Wiley-VCH, 2013 (see p. 51).
- [148] CHRISTIAN BÖSER, SIMON FINK, and STEFFEN RÖCKER: **Introduction to Boosted Decision Trees: A multivariate approach to classification problems**. 2014. URL: <https://indico.scc.kit.edu/indico/event/48/session/4/contribution/35/material/slides/0.pdf> (see p. 51).
- [149] CMS COLLABORATION, SERGUEI CHATRHYAN et al.: **Combined results of searches for the standard model Higgs boson in pp collisions at $\sqrt{s} = 7$ TeV**. In: *Phys. Lett. B*, **710**: (2012). DOI: [10.1016/j.physletb.2012.02.064](https://doi.org/10.1016/j.physletb.2012.02.064). arXiv: [1202.1488 \[hep-ex\]](https://arxiv.org/abs/1202.1488) (see p. 52).

- [150] GLEN COWAN, KYLE CRANMER, EILAM GROSS, and OFER VITELLS: **Asymptotic formulae for likelihood-based tests of new physics**. In: *Eur. Phys. J. C*, **71**: (2011). doi: [10.1140/epjc/s10052-011-1554-0](https://doi.org/10.1140/epjc/s10052-011-1554-0), [10.1140/epjc/s10052-013-2501-z](https://doi.org/10.1140/epjc/s10052-013-2501-z). arXiv: [1007.1727 \[physics.data-an\]](https://arxiv.org/abs/1007.1727) (see pp. 52–53).
- [151] CMS COLLABORATION, **Observation of a new boson with a mass near 125 GeV**. Tech. rep. CMS-PAS-HIG-12-020. CERN, 2012. URL: <https://cds.cern.ch/record/1460438> (see p. 52).
- [152] The ATLAS COLLABORATION, The CMS COLLABORATION, The LHC Higgs Combination Group, **Procedure for the LHC Higgs boson search combination in Summer 2011**. Tech. rep. CMS-NOTE-2011-005. ATL-PHYS-PUB-2011-11. CERN, 2011. URL: <http://cds.cern.ch/record/1379837> (see p. 52).
- [153] HIGGS WORKING GROUP: **Documentation of the RooStats based statistics tools for Higgs PAG**. 2017. URL: <https://twiki.cern.ch/twiki/bin/viewauth/CMS/SWGuideHiggsAnalysisCombinedLimit> (see p. 52).
- [154] LORENZO MONETA, KEVIN BELASCO, KYLE S. CRANMER, et al.: **The RooStats Project**. In: *PoS, ACAT2010*: (2010). arXiv: [1009.1003 \[physics.data-an\]](https://arxiv.org/abs/1009.1003) (see p. 52).
- [155] THOMAS JUNK: **Confidence level computation for combining searches with small statistics**. In: *Nuclear Instruments and Methods in Physics Research Section A: Accelerators, Spectrometers, Detectors and Associated Equipment*, **434**:2 (1999). doi: [10.1016/S0168-9002\(99\)00498-2](https://doi.org/10.1016/S0168-9002(99)00498-2) (see p. 52).
- [156] A L READ: **Presentation of search results: the CL s technique**. In: *Journal of Physics G: Nuclear and Particle Physics*, **28**:10 (2002). URL: <http://stacks.iop.org/0954-3899/28/i=10/a=313> (see p. 52).
- [157] CMS COLLABORATION, A. M. SIRUNYAN et al.: **Particle-flow reconstruction and global event description with the CMS detector**. In: *JINST*, **12**: (2017). doi: [10.1088/1748-0221/12/10/P10003](https://doi.org/10.1088/1748-0221/12/10/P10003). arXiv: [1706.04965 \[physics.ins-det\]](https://arxiv.org/abs/1706.04965) (see pp. 56–60, 62).
- [158] R. FRÜHWIRTH: **Application of Kalman filtering to track and vertex fitting**. In: *Nuclear Instruments and Methods in Physics Research Section A: Accelerators, Spectrometers, Detectors and Associated Equipment*, **262**:2 (1987). doi: [http://dx.doi.org/10.1016/0168-9002\(87\)90887-4](http://dx.doi.org/10.1016/0168-9002(87)90887-4) (see p. 57).
- [159] PIERRE BILLOIR: **Progressive track recognition with a Kalman like fitting procedure**. In: *Comput. Phys. Commun.*, **57**: (1989). doi: [10.1016/0010-4655\(89\)90249-X](https://doi.org/10.1016/0010-4655(89)90249-X) (see p. 57).
- [160] CMS COLLABORATION, SERGUEI CHATRHYAN et al.: **Performance of CMS muon reconstruction in pp collision events at $\sqrt{s} = 7$ TeV**. In: *JINST*, **7**: (2012). doi: [10.1088/1748-0221/7/10/P10002](https://doi.org/10.1088/1748-0221/7/10/P10002). arXiv: [1206.4071 \[physics.ins-det\]](https://arxiv.org/abs/1206.4071) (see p. 57).
- [161] W ADAM, R FRÜHWIRTH, A STRANDLIE, and T TODOROV: **Reconstruction of electrons with the Gaussian-sum filter in the CMS tracker at the LHC**. In: *Journal of Physics G: Nuclear and Particle Physics*, **31**:9 (2005). URL: <http://stacks.iop.org/0954-3899/31/i=9/a=N01> (see p. 57).

- [162] **Performance of electron reconstruction and selection with the CMS detector in proton-proton collisions at $\sqrt{s} = 8\text{TeV}$.** In: *JINST*, **10**:06 (2015). URL: <http://stacks.iop.org/1748-0221/10/i=06/a=P06005> (see p. 58).
- [163] CMS COLLABORATION: **Electron and photon performance in CMS with the full 2016 data sample.** 2017. URL: <http://cds.cern.ch/record/2255497> (see pp. 58, 62–63).
- [164] K. Rose: **Deterministic annealing for clustering, compression, classification, regression, and related optimization problems.** In: *Proceedings of the IEEE*, **86**:11 (1998). DOI: [10.1109/5.726788](https://doi.org/10.1109/5.726788) (see p. 58).
- [165] CMS COLLABORATION, WOLFGANG WALTENBERGER: **Adaptive Vertex Reconstruction.** Tech. rep. CMS-NOTE-2008-033. CERN, 2008. URL: <https://cds.cern.ch/record/1166320> (see p. 58).
- [166] CMS COLLABORATION, ANDREAS KORN Mayer: **The CMS Pixel Luminosity Telescope.** Tech. rep. CMS-CR-2015-121. CERN, 2015. URL: <https://cds.cern.ch/record/2039978> (see p. 59).
- [167] CMS COLLABORATION, **CMS Luminosity Measurements for the 2016 Data Taking Period.** Tech. rep. CMS-PAS-LUM-17-001. CERN, 2017. URL: <http://cds.cern.ch/record/2257069> (see p. 59).
- [168] CMS COLLABORATION, **Measurement of the inelastic proton-proton cross section at $\sqrt{s} = 13\text{ TeV}$.** Tech. rep. CMS-PAS-FSQ-15-005. CERN, 2016. URL: <https://cds.cern.ch/record/2145896> (see p. 60).
- [169] CMS COLLABORATION: **Muon Identification and Isolation efficiency on full 2016 dataset.** 2017. URL: <http://cds.cern.ch/record/2257968> (see pp. 60–61).
- [170] CMS COLLABORATION: **Effective areas used for Summer16 samples.** 2017. URL: https://indico.cern.ch/event/482673/contributions/2187022/attachments/1282446/1905912/talk_electron_ID_spring16.pdf (see p. 63).
- [171] MATTEO CACCIARI, GAVIN P. SALAM, and GREGORY SOYEZ: **The Anti-k(t) jet clustering algorithm.** In: *JHEP*, **04**: (2008). DOI: [10.1088/1126-6708/2008/04/063](https://doi.org/10.1088/1126-6708/2008/04/063). arXiv: [0802.1189 \[hep-ph\]](https://arxiv.org/abs/0802.1189) (see p. 63).
- [172] CMS COLLABORATION, **Jet algorithms performance in 13 TeV data.** Tech. rep. CMS-PAS-JME-16-003. CERN, 2017. URL: <http://cds.cern.ch/record/2256875> (see p. 63).
- [173] V. KHACHATRYAN et al.: **Jet energy scale and resolution in the CMS experiment in pp collisions at 8 TeV.** In: *JINST*, **12**:02 (2017). URL: <http://stacks.iop.org/1748-0221/12/i=02/a=P02014> (see pp. 64–65).
- [174] CMS COLLABORATION: **Jet energy scale and resolution performances with 13 TeV data.** 2016. URL: <http://cds.cern.ch/record/2160347> (see pp. 64–66).
- [175] CMS COLLABORATION: **Identification of b-quark jets with the CMS experiment.** In: *JINST*, **8**:04 (2013). URL: <http://stacks.iop.org/1748-0221/8/i=04/a=P04013> (see p. 66).

- [176] CMS COLLABORATION, **Identification of b quark jets at the CMS Experiment in the LHC Run 2**. Tech. rep. CMS-PAS-BTV-15-001. CERN, 2016. URL: <http://cds.cern.ch/record/2138504> (see pp. 66–68).
- [177] NAZAR BARTOSIK: **Diagram showing the common principle of identification of jets initiated by b-hadron decays**. 2016. URL: http://bartosik.pp.ua/hep_sketches/btagging (see p. 67).
- [178] CMS COLLABORATION, **Identification of b quark jets at the CMS Experiment in the LHC Run 2**. Tech. rep. CMS-PAS-BTV-16-001. CERN, 2017 (see p. 68).
- [179] CMS COLLABORATION, **Performance of missing energy reconstruction in 13 TeV pp collision data using the CMS detector**. Tech. rep. CMS-PAS-JME-16-004. CERN, 2016. URL: <http://cds.cern.ch/record/2205284> (see pp. 68, 74–75).
- [180] JORDAN DAMGOV: **Missing Et Optional Filters Run 2**. 2017. URL: <https://twiki.cern.ch/twiki/bin/viewauth/CMS/MissingETOptionalFiltersRun2> (see p. 74).
- [181] CMS COLLABORATION: **EGM corrections for Moriond17**. 2017. URL: https://indico.cern.ch/event/613162/contributions/2472046/attachments/1410308/2156822/EGMSmearerAndRegression_PPD_022017.pdf (see p. 78).
- [182] ARIE BODEK, JIYEON HAN, and WILLIS SAKUMOTO: **Misalignment and Muon Scale corrections**. 2012. URL: https://www-cdf.fnal.gov/~jyhan/cms_momscl/rochcor_cmsnote.pdf (see p. 78).
- [183] CMS COLLABORATION: **Rochestor Correction**. 2017. URL: <https://twiki.cern.ch/twiki/bin/viewauth/CMS/RochcorMuon> (see p. 78).
- [184] CMS Collaboration, **Evidence for the standard model production of a Z boson with a single top quark in pp collisions at $\sqrt{s} = 13$ TeV**. Tech. rep. CMS-PAS-TOP-16-020. CERN, 2017. URL: <http://cds.cern.ch/record/2284830> (see p. 97).
- [185] NNPDF COLLABORATION, RICHARD D. BALL et al.: **Parton distributions from high-precision collider data**. In: *Eur. Phys. J. C*, 77: (2017). DOI: [10.1140/epjc/s10052-017-5199-5](https://doi.org/10.1140/epjc/s10052-017-5199-5). arXiv: [1706.00428 \[hep-ph\]](https://arxiv.org/abs/1706.00428) (see p. 97).
- [186] Top Quark Working Group, K. AGASHE et al.: **Working Group Report: Top Quark**. In: 2013. arXiv: [1311.2028 \[hep-ph\]](https://arxiv.org/abs/1311.2028) (see pp. 119–120).
- [187] M. L. MANGANO et al.: **Physics at a 100 TeV pp collider: Standard Model processes**. In: *CERN Yellow Report*, 3 (2017). DOI: [10.23731/CYRM-2017-003.1](https://doi.org/10.23731/CYRM-2017-003.1). arXiv: [1607.01831 \[hep-ph\]](https://arxiv.org/abs/1607.01831) (see pp. 119–120).
- [188] HAMZEH KHANPOUR, SARA KHATIBI, MORTEZA KHATIRI YANEHSARI, and MOJTABA MOHAMMADI NAJAFABADI: **Single top quark production as a probe of anomalous $tq\gamma$ and tqZ couplings at the FCC-ee**. In: *Phys. Lett. B*, 775: (2017). DOI: [10.1016/j.physletb.2017.10.047](https://doi.org/10.1016/j.physletb.2017.10.047). arXiv: [1408.2090 \[hep-ph\]](https://arxiv.org/abs/1408.2090) (see pp. 119–120).
- [189] WEI LIU, HAO SUN, XIAOJUAN WANG, and XUAN LUO: **Probing the anomalous FCNC top-Higgs Yukawa couplings at the Large Hadron Electron Collider**. In: *Phys. Rev. D*, 92:7 (2015). DOI: [10.1103/PhysRevD.92.074015](https://doi.org/10.1103/PhysRevD.92.074015). arXiv: [1507.03264 \[hep-ph\]](https://arxiv.org/abs/1507.03264) (see pp. 119–120).

Acknowledgements



